XFEL.EU TR-2013-004

TECHNICAL DESIGN REPORT

Scientific Instrument Single Particles, Clusters, and Biomolecules (SPB)

August 2013

A.P. Mancuso, A. Aquila,

G. Borchers, and K. Giewekemeyer,

Scientific Instrument SPB (WP84);

N. Reimers, Central Instrumentation Engineering (CIE)

European X-Ray Free-Electron Laser Facility GmbH

Albert-Einstein-Ring 19

22761 Hamburg

Germany

Contents

Disclaimer

On occasion throughout this report, products and/or services of commercial entities are mentioned by their respective brand names, or described in more detail. These references are purely for illustrative purposes, to communicate that commercially available, off-the-shelf solutions to some of the engineering challenges SPB faces are at hand. The explicit mention of a product in this document, or lack thereof, does not imply endorsement or rejection of any particular product, nor any particular product's applicability to or likely inclusion in the SPB instrument.

Part I

TECHNICAL DESIGN

1 Introduction

1.1 Purpose of this document

This technical design report (TDR) of the Single Particles, Clusters, and Biomolecules (SPB) scientific instrument builds on the preceding conceptual design report (CDR) [57] and outlines technical specifications and designs for many of the components of the SPB instrument. More detailed design and modelling has been undertaken for certain long-lead-time components, in particular the X-ray optics, as these require specification for procurement in the near future. For most other components, the level of detail described will not be as high, reflecting the timeline of the project with earliest beam expected to arrive late in 2015.

1.2 Scope of this document

The SPB instrument is more than just the apparatus in the hutches on the experiment floor. We of the SPB team are firmly of the opinion that, to perform state-of-the-art single-particle imaging experiments on the kinds of samples we describe below, we need to care about not just the X-ray instrumentation, but the sample delivery and support, and the subsequent analysis of the data collected. The whole process—from what kind of X-ray beam is produced in the undulator, through the observation, delivery, and focusing of that beam, through delivering the sample to the interaction region, collecting diffraction data and its analysis—is near and dear to our hearts, and something we pursue with the specialist European XFEL (XFEL.EU) groups such as the X-Ray Optics and Beam Transport group (WP73), the X-Ray Photon Diagnostics group (WP74), the Detector Development group (WP75), the DAQ and Control Systems group (WP76), the Optical Laser group (WP78), and the Sample Environment group (WP79).

Nevertheless, the body of this document is concerned with the key X-ray systems and those interacting directly with them, such as the focusing systems, the sample delivery technology, and the two-dimensional detectors. Other “separable” topics of keen interest to the SPB group, and of no less importance, are described in appendices. The goal of this structure is to group like instrumentation together, while still providing information about the breadth of development undertaken by the SPB group.

In this chapter, we briefly describe elements of the scientific case that support the

instrument requirements—in particular, the chosen focal spot sizes and photon energy range. In Chapter 2, “Advisory review team”, and Chapter 3, “Acknowledgements”, Acknowledgements, we note the many colleagues who have contributed to this document in many and varied ways. In Chapter 4, “Overview of the SPB instrument”, we describe briefly the broad features of the SPB instrument and its key components. In Chapter 5, “Photon beam properties”, the properties of the free-electron laser (FEL) radiation as produced are described, before the necessary X-ray optics are discussed in Chapter 6, “X-ray optics layout”. The necessary diagnostics for our beam are discussed in Chapter 7, “Instrument diagnostics”. Progressing further downstream in the instrument, the sample chamber is discussed in Chapter 8, “Sample chamber”, and the intimately linked detector is described in Chapter 9, “Detector integration”. Essential aspects of sample delivery are discussed in Chapter 10, “Sample delivery techniques”, while the pump optical laser and its conditioning are discussed in Chapter 11, “Optical laser for pump–probe experiments”. Other aspects of instrumentation and software are discussed in the appendices.

1.3 Science case summary

The SPB instrument is primarily concerned with three-dimensional imaging, or three-dimensional structure determination, of micrometre-scale and smaller objects. A particular emphasis is placed on biological objects—including viruses, biomolecules, and protein crystals—though the instrument will also be capable of investigating non-biological samples using similar techniques.

The science case for the SPB instrument was first documented explicitly in the SPB Workshop held in 2008 in Uppsala, Sweden [58], and has since been refined in light of recent work at the SLAC Linac Coherent Light Source (LCLS) in Menlo Park, California [18, 11, 60]. Importantly, we note the length scale of samples to be investigated. This includes sub-micrometre–sized specimens—such as nanocrystals of hundreds of nanometres in diameter—as well as small cells of similar sizes. Furthermore, biological macromolecules on the scale of tens of nanometres are also of interest. For a review, see, for example, reference [93]. These classes of samples lead to the instrument’s desired focal spot sizes of order 1 µm and 100 nm—a core element of the instrument design.

Below, we outline a limited set of examples to help elucidate the breadth of application and requirements to the instrumentation.

1.3.1 Biological samples

The goal of the SPB instrument is to support the imaging and structure determination of biological specimens of approximately 1 µm in size and smaller using a variety of related X-ray techniques. One of the key principles of FEL biological structure determination is the idea that one can outrun, or at worst mitigate, radiation damage through the use of ultrabright, ultrashort pulses of FEL X-rays [64, 73, 6]. We describe a few such examples below.

1.3.1.1 Reproducible samples

Arguably one of the most exciting classes of samples for structure determination at an X-ray free-electron laser (XFEL) facility encompasses those samples where each individual sample exhibits the same, or markedly similar, structure as each other individual. A so-called “reproducible” sample allows for the collection of data from many copies of such samples. Naively, each individual sample illuminated with the XFEL beam scatters two-dimensional data into a two-dimensional detector at the instrument. Reproducible samples allow the aggregation of that data from many copies of the sample into a single piece of three-dimensional information about the sample [64].

Reproducible bio-samples potentially include biomolecules, macromolecular complexes, and viruses, whose sizes range from tens of nanometres (biomolecules) to hundreds of nanometres (viruses and large complexes), and which are thus well illuminated by the order 1 µm and 100 nm spot sizes at SPB.

Crystalline samples are also reproducible, and benefit from this as the non-crystalline samples described above.

1.3.1.2 Nanocrystallography

The recent advent of structure determination from small micrometre– and sub-micrometre–sized crystals of biomolecules using XFEL sources [18, 11, 76] represents an opportunity to use the SPB instrument to investigate the structure of macromolecules that do not form the larger crystals amenable to be investigated at third-generation synchrotron sources. Nanocrystallography (NX) represents both a practical extension of crystallography at XFELs and an important step towards the successful XFEL-based imaging of non-crystalline, reproducible samples (see Figure 1.1 on the following page). Multiple examples of its success at LCLS [18, 11]

and the existence of mature, accessible analysis software [108] make nanocrystals a very promising class of samples.

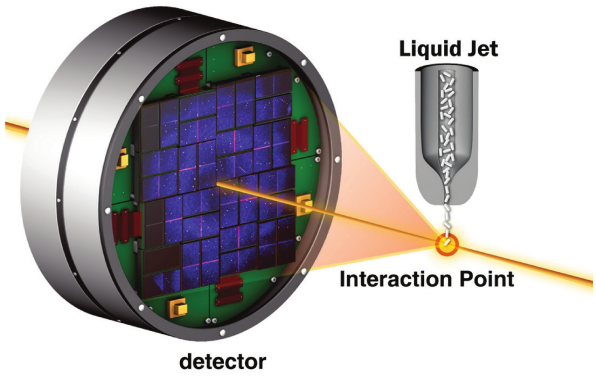

Figure 1.1: Schematic of a nanocrystallographic experiment. Figure adapted from Boutet et al., Science (2012) [11].

Furthermore, a consortium of users, led by Henry Chapman of the Center for Free-Electron Laser Science (CFEL) in Hamburg, Germany, has proposed to build a second interaction region and its ancillary instrumentation within the SPB hutch for the purpose of performing nanocrystallography with the "spent"' XFEL beam, or screening crystals simultaneously with an experiment in the SPB interaction region. This Serial Femtosecond Crystallography (SFX) project would significantly enhance the nanocrystallographic capabilities of the SPB instrument and the European XFEL facility. The project is described later in this chapter and elsewhere in this document.

1.3.1.3 Non-reproducible samples

Non-reproducible samples include biological cells, for example, which, while exhibiting many similarities between individuals, are not reproducible in a way to make them amenable to three-dimensional structure determination from many copies. Nevertheless, there is community interest to examine some such systems. The advantage of XFEL sources—particularly the European XFEL—is the ability to image many such systems to moderate resolution (today tens of nanometres, potentially better in the future) and explore the properties of populations by observing their two-dimensional projections. (For an example diffraction pattern, see Figure 1.2 on the next page).

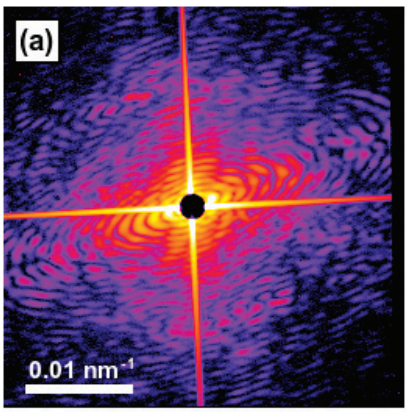

Figure 1.2: Example of a coherent diffraction pattern from a single-celled organism with strong signal spanning orders of magnitude of dynamic range. Figure originally published in A.P. Mancuso et al., New J. Phys. **12**, 035003 (2010).

1.3.1.4 Time-resolved biological experiments

In addition to determining the structure of static biological systems, the short-pulsed nature of XFELs allows the examination of dynamic biological systems [4, 63]. The dominant paradigm for performing time-resolved experiments at XFELs is by initiating a process in a sample with a short pulse from an optical laser—a so-called pump laser—and then probing that same sample some time Δt later to measure the structural change in that sample (see Figure 1.3 on the following page for a schematic of such an experiment). Again, these experiments require reproducible samples, as one wishes to observe the same system with different time delays to understand its evolution. The processes investigated, however, do not need to be reversible. The fast sample replacement common to XFELs, and the ultrabright pulses used, mean that irreversible processes in reproducible samples can be explored, opening up a wealth of opportunity unable to be observed by other methods.

As an example, plants and fungi contain photoreceptors, which play a key role in these organisms' environmental adaptation, survival, and reproductive success. These photoreceptors "serve to optimize plant growth or fungal spore dispersal by triggering phototropic responses and, by entraining their respective circadian systems, control daily or seasonal timing of asexual and sexual development" [38]. All manner of biological functions arise from the interaction of light—from the ultraviolet to the infrared—with photoreceptors in these systems, and the structural ramifications of these interactions are in many cases not understood. By examining photosensitive macromolecules illuminated with an optical laser as a function of time, one can hope to understand the structural changes that occur in such photoreceptor systems.

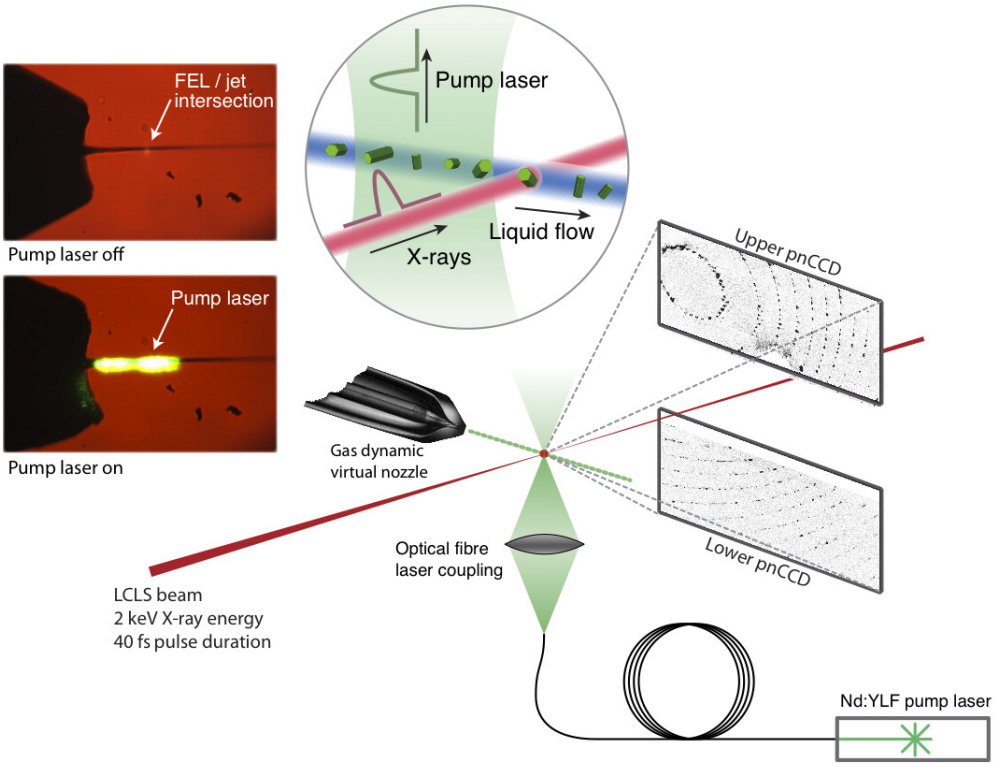

Figure 1.3: Example pump–probe experimental setup. A pump laser illuminates a stream of crystals some time before they are illuminated by the XFEL beam. Figure originally appeared in A. Aquila et al., Optics Express, **20** (3) pp. 2706-2716, 2012. ©OSA (2012).

Another approach to time-resolved methods is through the use of caged compounds [25, 53]. Caged compounds are “light-sensitive probes that functionally encapsulate biomolecules in an inactive form” [25]. Upon illumination, these cages release the contained compound, allowing for a controlled temporal “start” of a dynamic, biological process. This technology potentially offers the possibility to examine the dynamics of biomolecules that themselves are not light-sensitive, thus generalizing the class of specimens amenable to time series investigation.

1.3.2 Non-biological samples

The SPB instrument is also well suited to forward scattering, or coherent diffractive imaging, experiments on non-biological samples of 1 µm or smaller. These include metal nanocrystals, quantum dots, and other finite-sized inorganic samples. The technique of coherent diffraction imaging from forward scattered signal is the same as for biological samples, with the added benefit of a higher signal level due to the typical composition of these samples containing heavier elements than the bio-samples.

1.3.2.1 Example: Nanostructured materials

Examples of non-biological samples include quantum dots [103] or other nanostructured materials, such as nanowires [36] and metal nanocrystals [78, 70], all of which have important technological potential. While many of these samples are explored in Bragg geometry (which will be available at the Materials Imaging and Dynamics (MID) instrument of the European XFEL), many are also investigated in the forward scattering geometry or grazing incidence geometry.

Samples that grow on surfaces, such as metal aggregates on oxide surfaces [31, 104] are also of potential interest.

Perhaps of greatest interest are dynamic, fast processes in materials that can be studied in pump–probe modalities. For example, catalytic particles on surfaces in grazing incidence geometry responding to a femtosecond laser probe could be studied in the geometries available at SPB with tens of femtoseconds time resolution and single-digit nanometre spatial resolutions, offering unprecedented insight into their function.

1.4 Basic instrument parameters

To address the science described above, the SPB instrument is designed as a 3–16 keV instrument located behind the SASE1 undulator of the European XFEL. Its basic parameters are described here in Table 1.1 on the next page. An overview of the undulator source that delivers these parameters is described more fully in Chapter 5, “Photon beam properties”.

Table 1.1: Parameters of the SPB instrument

Parameter	Value (range)	Unit
Photon energy	3–16	keV
Pulse energy (max)	ca. 1–5	mJ
Photons per pulse (max)	ca. 1–8	10^{12} photons
Focal spot size	approx. 0.1 & 1.0	µm
Repetition rate	10×1350 (max. at highest pulse energy) 10×2700 (max. at lower pulse energies)	s^{-1}
Pulse duration (range)	few–100	fs
Detector pixel size (AGIPD)	200×200	μm^2
Upstream detector	4 independent quadrants ($4 \times 512 \times 512$ pixels)	n.a.
Downstream detector	2 independent quadrants ($2 \times 512 \times 128$ pixels)	n.a.
Single-photon sensitivity	Yes	n.a.
Detector dynamic range at 12 keV	$> 10^4$	photons
Detector frame rate (burst)	4.5	MHz
Sample–detector distances	approx. 0.13 – 5 (upstream) approx. 7–12 (downstream)	m
Sample delivery options	Liquid jet Aerosol jet Fixed targets	n.a.
Miscellanea	Pump–probe laser	n.a.

1.5 User consortia proposals

In 2011, European XFEL issued a call for expressions of interest to user consortia (UC) to deliver instrumentation to the project [29].

From the call:

"The Council of the European XFEL decided to welcome contributions by User Consortia to the construction of scientific instruments, to the ancillary instrumentation and to the technical infrastructure."

In response to this call, a number of expressions of interest, and subsequently complete proposals, were received. Of these proposals, three have a very close interaction with the SPB instrument: the SFX proposal mentioned above, the dataXpress proposal, and the user consortium for XFEL-based Integrated Biology Infrastructure (XBI) proposal. In particular, the SFX proposal involves the addition of instrumentation to the SPB experiment hutch, and therefore requires a very close cooperation and integration to succeed. The main aims and contributions of these proposals are described below, and their integration into the SPB instrument and infrastructure is presented in the relevant chapters and appendices of this TDR. For a more comprehensive account of each UC proposal, readers are referred to the respective spokespersons named in the sections below.

1.5.1 SFX proposal

The Serial Femtosecond Crystallography (SFX) consortium proposes to deliver instrumentation that will allow one to perform nanocrystallography with the so-called "spent" beam at the SPB instrument. This will involve the installation of refocusing optics downstream of the SPB sample chamber (for details, see Section 6.5, "Refocusing option"), an additional sample chamber in which NX can be performed, and an additional 4 megapixel (Mpx) Adaptive Gain Integrating Pixel Detector (AGIPD) for measuring crystallographic diffraction patterns.

The SFX consortium is led by Henry Chapman of the Center for Free-Electron Laser Science (CFEL), Deutsches Elektronen-Synchrotron (DESY), and the University of Hamburg. To date, the technical design of the required refocusing optics and rail system, and the identification of space and technical constraints have been performed by the SPB team. Due to the highly integrated nature of the instrumentation involved, a very close cooperation with the SFX team is anticipated, including having the SFX scientist(s) and engineer(s) physically located at European XFEL for a large fraction

of their time during the construction phase. Needless to say, the presence of SFX personnel at the experiment hall will be required during the operation phase.

Throughout this document, elements of the SFX cooperation are addressed. For the reader's convenience and clarity, we refer to the user consortium proposal as SFX, and to the *method* of illuminating small crystals with an XFEL beam as nanocrystallography, abbreviated as "NX" where appropriate.

1.5.2 dataXpress proposal

The aptly named "dataXpress" user consortium proposal aims to contribute to making sense of the "deluge of data" coherent imaging and nanocrystallographic experiments expect to produce at the European XFEL. Through determining sensible veto signals and using data reduction techniques to minimize the amount of data that must be stored, the dataXpress proposal plans to make working with the approximately 15 TB / day[1] that may be collected at the European XFEL possible and to ensure the phrase "data, data everywhere and not a thought to think" will be just a perversion of Coleridge [21] and not a reality.

Led by Anton Barty of CFEL, DESY, who is also a member of the SPB instrument's advisory review team, the dataXpress consortium comprises a variety of institutions across Europe. The CFEL team have already begun work on algorithms and data reduction techniques that may be applied at the SPB instrument, and the dataXpress consortium also aims to contribute compatible computing hardware for the efficient use of these algorithms.

1.5.3 XBI proposal

The user consortium for XFEL-based Integrated Biology Infrastructure (XBI) plans to contribute to both what comes before the SPB instrument (biological sample preparation, including, for example, crystal growth) as well as what comes after the SPB instrument, including data interpretation, modelling, and validation.

Led by Victor Lamzin of the European Molecular Biology Laboratory (EMBL), Hamburg, who is also a member of the SPB instrument's advisory review team, the XBI consortium comprises members from a variety of institutions across Europe, representing different facets of the structural biology community.

[1] 2 MB / frame, 350 frames / train max., 12 hour shift, 50% utilization, 10% hit rate

Perhaps the most noticeable contribution proposed by the XBI consortium is a greater than 460 m^2 biology laboratory to be housed in the European XFEL main building on the laboratory level—one floor above the instruments. This will allow for sample preparation techniques including crystal growth, cell culturing, and more. This laboratory space and support are proposed to be available to users awarded beamtime who wish to prepare samples on site.

2 Advisory review team

This chapter describes the role of the advisory review team (ART) and lists its members.

2.1 Role

The ART is a panel of experts in diverse matters related to single-particle imaging. The ART advises on the design of the SPB instrument and also provides a review function to give feedback on the SPB design and implementation. The ART has already reviewed the instrument's conceptual design and is responsible for reviewing the subsequent technical design, as well as providing advice and feedback continuously until the instrument's final delivery.

2.2 Members

Prof. Dr Franz Pfeiffer
Physics Department (E17) and Institute of Medical Engineering (IMETUM)
Technische Universität München
James-Franck-Straße
85748 Garching
Germany
Phone: +49 89 289 12552
Fax: +49 89 289 12548
franz.pfeiffer@ph.tum.de

Prof. Dr David Stuart (Scientific Advisory Committee (SAC) representative)
MRC Professor of Structural Biology
Division of Structural Biology
Henry Wellcome Building for Genomic Medicine
Oxford, OX3 7BN
UK
Phone: +44 1865 287546
stuart-pa@strubi.ox.ac.uk

Dr Sebastien Boutet
CXI Instrument Scientist
LCLS, SLAC National Accelerator Laboratory
2575 Sand Hill Rd
Menlo Park, CA 95205
USA
Phone: +1 650 926 8676
Fax: +1 650 926 3600
sboutet@slac.stanford.edu

Dr Garth Williams
CXI Instrument Scientist
LCLS, SLAC National Accelerator Laboratory
2575 Sand Hill Rd
Menlo Park, CA 95205
USA
Phone: +1 650 926 2682
Fax: +1 650 926 3600
gjwillms@slac.stanford.edu

Dr Anton Barty
Project Leader, dataXpress User Consortium
Member, Serial Femtosecond Crystallography (SFX) User Consortium
Member, User Consortium for XFEL-based Integrated Biology Infrastructure (XBI)
Center for Free-Electron Laser Science (CFEL)
Deutsches Elektronen-Synchrotron (DESY)
Notkestraße 85
22607 Hamburg
Germany
Phone: +49 40 8998 5783
Fax: +49 40 8998 1958
anton.barty@desy.de

Dr Dan DePonte
SLAC National Accelerator Laboratory
2575 Sand Hill Rd
Menlo Park, CA 95205
USA
Phone: +1 650 926 2368
Fax: +1 650 926 4695
daniel.deponte@desy.de

Prof. Dr Ilme Schlichting
Director, Dept. of Biomolecular Mechanisms, Max Planck Institute for Medical Research
Jahnstraße 29
69120 Heidelberg
Germany
Phone: +49 6221 486-500
Fax: +49 6221 486-351
ilme.schlichting@mpimf-heidelberg.mpg.de

Prof. Dr Victor Lamzin
Project Leader, User Consortium for XFEL-based Integrated Biology Infrastructure (XBI)
Member, Serial Femtosecond Crystallography (SFX) User Consortium
Deputy Head of Outstation and Senior Scientist
European Molecular Biology Laboratory (EMBL) Hamburg
Deutsches Elektronen-Synchrotron (DESY)
Notkestraße 85
22603 Hamburg
Germany
Phone: +49 40 8990 2121
Fax: +49 40 8990 2149
victor@embl-hamburg.de

3 Acknowledgements

In an endeavour such as designing a scientific instrument for a facility as novel as the European XFEL, the knowledge of a small team can go only so far. Many colleagues from around the globe have graciously, and without want of reward, contributed their knowledge to help make the SPB instrument design as good as it can be.

The SPB optics design was greatly assisted by Harald Sinn and Liubov Samoylova of the X-Ray Optics and Beam Transport group of the European XFEL. Very profitable discussions about the feasibility of various optical designs were held with Yamauchi-sensei of Osaka University, Ueda-san of JTEC corporation, and Riccardo Signorato of Bruker Corporation. Frank Siewert of Helmholtz-Zentrum Berlin provided invaluable advice on metrology technologies for mirror characterization, and Cameron Kewish of Synchrotron Soleil in France provided sound advice on the feasibility of various optical designs. Thanks to Regina Souffli of Lawrence Livermore National Laboratory for providing valuable information on roughness measurements and coatings, and to Eric Gullikson of Lawrence Berkeley National Laboratory for useful discussions on slope errors and scatter.

Liubov Samoylova, Oleg Chubar of Brookhaven National Laboratory, and Alexey Buzmakov of the Shubnikov Institute of Crystallography are thanked for their efforts in delivering and assistance with SRW code for propagation of wavefields.

We would also like to thank JJ X-Ray A/S in Denmark for providing models of standard components.

The discussion of instrument diagnostics has benefitted enormously from the experience of Jan Grünert and his X-Ray Photon Diagnostics group at European XFEL, including Cigdem Ozkan, Jens Buck, and Wolfgang Freund.

Substantial contributions, especially regarding sample delivery, came from Joachim Schulz, Sadia Bari, and Charlotte Uetrecht of the Sample Environment group at European XFEL.

We are very grateful for the valuable insights provided by the European XFEL Detector Development group led by Markus Kuster and supported by Jola Sztuk-Dambietz, Monica Turcato, Andreas Koch, and Steffen Hauf. The Adaptive Gain Integrating Pixel Detector (AGIPD) consortium—led by Heinz Graafsma with the assistance of Julian Becker, Helmut Hirsemann, and many more—have delivered us

much information about and images of the AGIPD system. The DSSC consortium, led by Matteo Porro, is similarly thanked for its efforts in developing the Depleted P-Channel Field Effect Transistor (DEPFET) Sensor with Signal Compression (DSSC) and communicating those developments with us. Georg Weidenspointer is particularly thanked for valuable discussions.

Chris Youngman, Nicola Coppola, Krzysztof Wrona, and Burkhard Heisen of the DAQ and Control Systems group at European XFEL are thanked for their contributions to control, data acquisition, data management, and scientific computing. Without these essential structures, we would not be able to control or measure anything. Chun Hong Yoon is thanked for his contribution to scientific software, including data structures, algorithm implementation and software coordination.

Haiou Zhang, Raùl Villanueva, and Martin Dommach, all at the European XFEL, are thanked for their advice on vacuum technology.

Ryan Coffee of the Linac Coherent Light Source (LCLS) is thanked for taking the time to give a detailed course in state-of-the-art timing systems at XFEL sources and pointing out the roads open to future improvements.

Holger Fleckenstein and Lars Gumprecht of the Center for Free-Electron Laser Science (CFEL), Deutsches Elektronen-Synchrotron (DESY), are thanked for their insights into sample chamber design for FEL experiments.

Our user consortia partners are thanked for their collaborative spirit and valuable discussions. In particular, Henry Chapman as the spokesperson of the SFX consortium, Victor Lamzin as spokesperson of the XBI consortium, and Anton Barty for the dataXpress consortium. Your contributions will allow us to make an even better user experience.

Particular commendation is reserved for the staff of the CXI instrument at LCLS, particularly Sebastien Boutet and Garth Williams, who have been an invaluable and generous source of advice and experience throughout our design process.

One should not and cannot forget the countless members of the imaging and crystallographic community who have contributed ideas, feedback, dinner discussions, and more at workshops, conferences, and in-house meetings. This instrument is for all of you.

Valuable feedback on this text was provided by Thomas Tschentscher of European XFEL as well as Massimo Altarelli, Andreas Schwarz, and Serguei Molodtsov, all

of whom are members of the European XFEL Management Board. Michael Meyer, Anders Madsen, Christian Bressler, and Andreas Scherz are leading scientists at the European XFEL. They and their groups are also thanked for their continued feedback and valuable discussions.

Finally, the SPB ART and the Scientific Advisory Committee (SAC) of the European XFEL have contributed review comments and insights at each stage of design of the SPB instrument. Their diligent work in providing advice and feedback—often on short notice and in considerable detail—is thoroughly appreciated and highly valued. The instrument will be better because of their generosity in providing scientific input, critical feedback, and specialist knowledge.

4 Overview of the SPB instrument

4.1 Requirements and constraints of the SPB instrument

4.1.1 Requirements

The SPB instrument is characterized by two focal spot sizes of just larger than 1 µm and 100 nm, which may be separately brought to focus in a common focal plane, inside a single sample chamber. Sample is delivered to this focal plane, most likely through a form of injection, where it interacts with the focused FEL beam. The diffraction from the sample is collected in a two-dimensional detector downstream of this interaction region, and is recorded for on-the-fly analysis, subsequent analysis, or both. Figure 4.2 gives an iconographic overview of the key components. Figures 4.3 and 4.4 show a simplified drawing of the key components.

The science cases, partially outlined in Section 1.3, “Science case summary”, provide the key requirements to the realization of the SPB instrument.

In summary, the instrument should:

- Operate between 3 keV and 16 keV photon energy
- Transmit the maximum number of photons possible to the focal spots
- Minimally perturb the wavefront of the FEL beam (i.e. the number of optical elements in the beam must be minimized)
- Accommodate injected samples, both from liquid jets and aerosols (and potentially other sources)
- Allow a two-dimensional detector to be placed very close (≈ 100 mm) to the interaction region and up to 10 m away (to cater to different sample sizes, in an almost continuous fashion between these positions; see, for example, Appendix A of reference [58]).

To satisfy the second and third point, we chose to use mirror optics, particularly in light of their superior transmission in the lower energy range (3 keV to 5 keV) when compared to beryllium lenses or zone plates. For a more complete discussion, see Chapter 5, "Optical layout", and Appendix B of reference [58].

The injection of samples is dealt with in Chapter 10, “Sample delivery techniques”, and the progress to date on detector integration is discussed in Chapter 9, “Detector integration”.

4.1.2 Constraints

Additional constraints to the instrument design arise from the physics of the beam (the FEL beam can, in many cases, be destructive), good experimental work practices, and competing vacuum environments in close proximity.

Specifically:

- The instrument operates behind the SASE1 undulator, limiting the minimum photon energy of the instrument to 3 keV.
- It is desirable to be able to isolate the sample chamber’s vacuum from the rest of the instrument. This allows a minimal volume to be pumped after an intervention to the sample chamber, and protects the detector and upstream optics from contamination due to exposure to ambient pressure.
- Special care needs to be taken when designing a beam dump for the FEL beam, due to its potentially destructive nature. The same is true for any opaque element that may be inserted into the direct beam (e.g. diagnostics screens).
- Beam conditioning components need to be designed to cope with the high average intensity XFEL beam. This typically leads to larger longitudinal distances for these components than for comparable components at synchrotrons or lower repetition rate XFELs. For example, slit systems—which are normally quite thin—can be on the order of 0.5 m in length at the European XFEL.
- X-ray optics require vacuum pressures of approximately 1×10^{-9} mbar and lower. The sample chamber will utilize liquid jets, which may, in extreme cases, produce a background vacuum poorer than 1×10^{-4} mbar. These regions need to be suitably isolated, without having a window between them when the beam is on.

4.1.3 Goal of the SPB instrument design

The goal of the SPB instrument design is to create an instrument that meets the scientific requirements outlined above, respecting the constraints demanded by physics and the operation environment, both in a timely manner and within the fiscal constraints of the project.

Within all of these boundary conditions, we aim to design an instrument that is

capable of world-leading single-particle imaging, with the highest possible photon flux in each of the instrument's focal spots, and with supporting instrumentation to utilize the high repetition rate of the European XFEL. We aim to make design decisions that not only deliver beyond-state-of-the-art instrumentation, but also control the associated risks and deliver an instrument that can be used well in practice—not just on paper.

In the remainder of this report, we describe the proposed instrument design, first in general and then in increasing detail for each component or subsystem. For a quick overview, a schematic of the entire instrument is shown in Figure 4.2 on page 35.

4.2 Overview of the instrument design

4.2.1 Optical system

The optical system of the SPB instrument produces an approximately 100 nm focus and a slightly larger than 1 µm focus from two independent focusing mirror systems.

The 100 nm–scale focusing system comprises two Kirkpatrick-Baez (KB), elliptical focusing mirrors placed at a distance of 3 m for the horizontal focusing mirror and 1.9 m for the vertical focusing mirror, upstream of the focal plane and within the experiment hutch. While this is a much larger working distance than one may be accustomed to at most light source facilities, or even existing FEL sources [10] (owing to the large distance from source to sample at the European XFEL), one still needs to take care when designing the interface between the optics and the sample chamber—in particular regarding the management of the very different vacua between these sections and a careful appreciation of the window valve between optics and sample chamber, and precisely when it may be used. A perspective drawing of the 100 nm–scale focusing system within the experimental hutch is shown in Figure 4.4 on page 37.

The micrometre-scale focusing system comprises four mirrors—two focusing and two flat. These are to be arranged in two pairs—a flat horizontal mirror and a focusing horizontal mirror, followed by a focusing vertical mirror and a flat vertical mirror. The benefits of such a design are twofold. These pairs of mirrors are much more robust to vibrations over the greater than 20 m distance between optics and focus, and they can be readily upgraded so that the flat mirrors can be adaptive optics that may be used to correct wavefront aberrations [61]. This adds a wealth of flexibility in the optical design on top of creating a high-quality wavefront necessary for imaging. This design will still produce a high-transmission optical system and would be a world-leading optics even

without the proposed adaptive upgrade. A perspective view of the micrometre-scale mirror hardware is shown in Figure 4.3 on page 36.

As a historical note, in the conceptual design of the SPB instrument, a two-mirror design was proposed [57], though this required a large translation of the sample chamber, detector, and any diagnostics downstream—as much as 300 mm both horizontally and vertically, in some cases. In addition to improved vibration properties, and the path for a wavefront-improving upgrade, the four-mirror design avoids the need for a large translation of downstream components, simplifying operation and switching between spot sizes. For a complete discussion of the performance of the four-bounce system, see Chapter 6, "X-ray optics layout". For a discussion of some alternate optical designs that have been considered in the design process, including the two-bounce solution, see Appendix C, "Additional optical considerations".

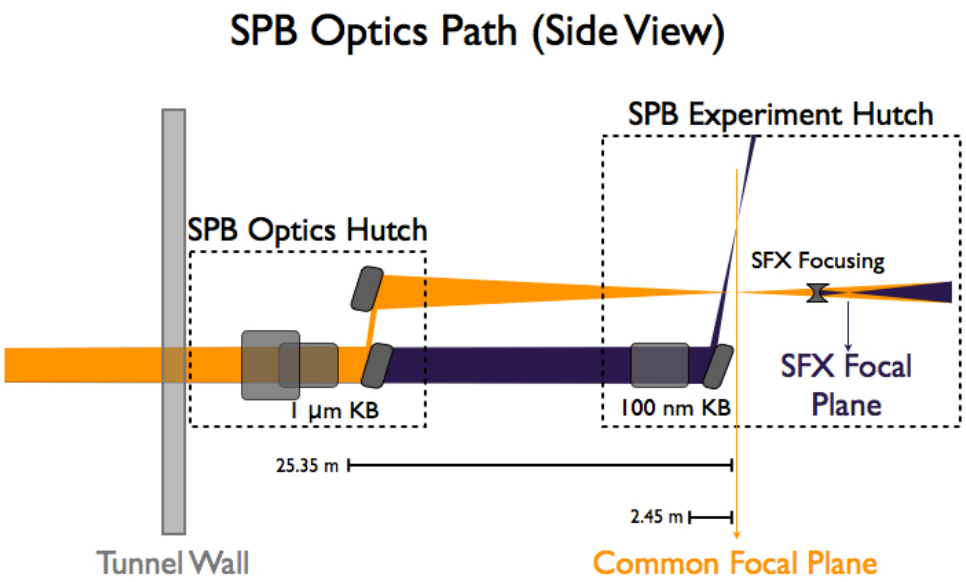

Figure 4.1: Pictorial side view showing the placement of the SPB optics and layout in the experiment hutch. Note that the horizontal optics are always upstream of the vertical optics. The details of the optical systems are described in Chapter 6, "X-ray optics layout".

These two foci are independent, meaning that a minimal number of optical elements are used to create each focal spot. For the 100 nm–scale optics, these are four mirrors—two offset mirrors upstream of the instrument (required for safety reasons—see Chapter 6, "X-ray optics layout") and the two focusing mirrors. For the micrometre-scale optics, we require six mirrors. For an overview, see Figure 4.1. Nevertheless, these solutions maximize the transmission of the instrument and minimize wavefront distortions by minimizing the number of optical elements as much

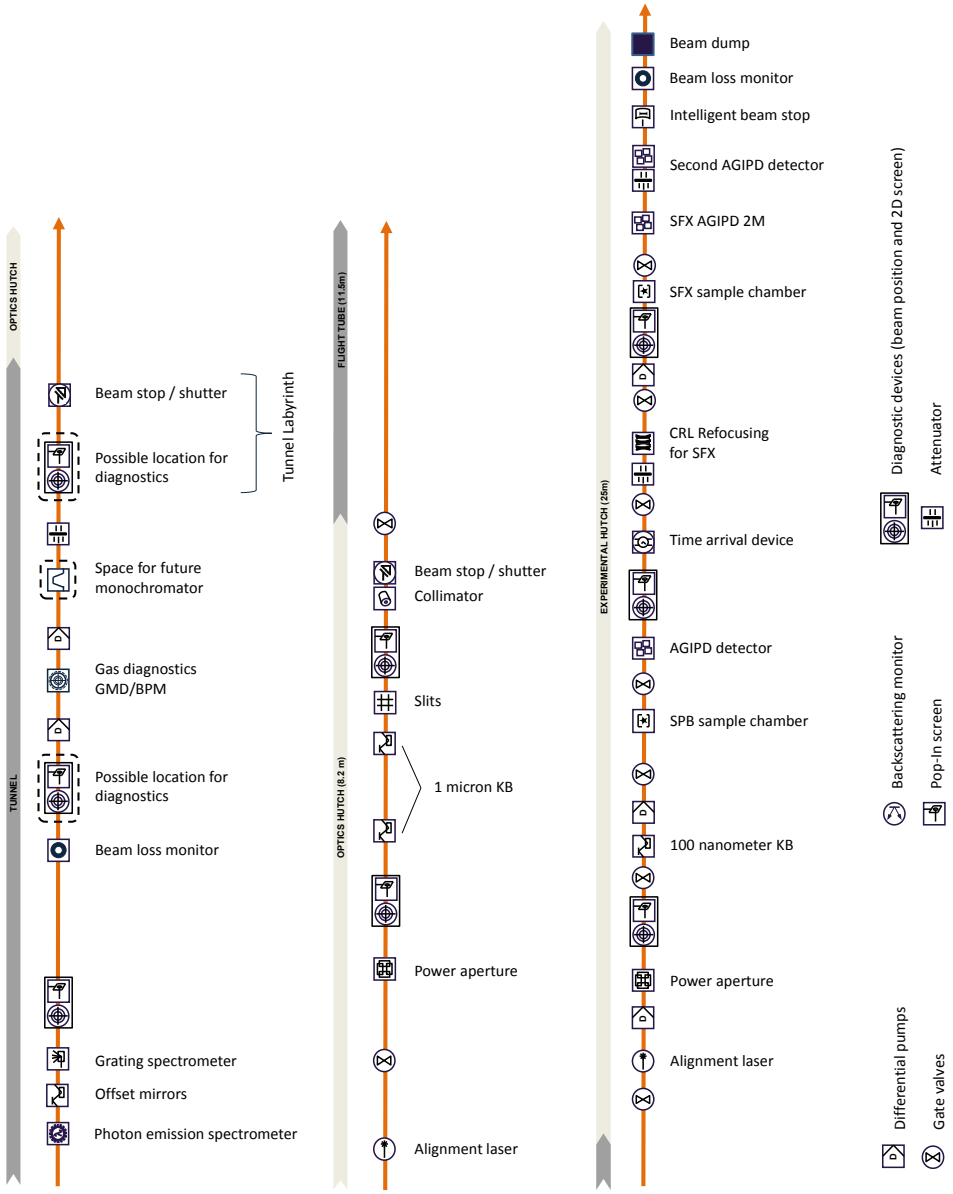

Figure 4.2: Iconographic overview of SPB instrumentation in the tunnel, optics hutch, and experiment hutch

as practicable. Furthermore, the upgrade scenario described in Section 6.3.6, “Future upgrades”, directly addresses mitigating wavefront distortions.

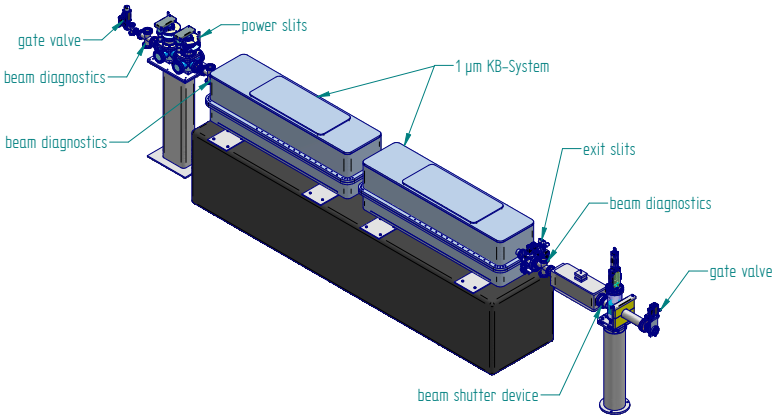

Figure 4.3: Optics hutch overview showing the two mirror chambers, the required diagnostic elements (screens, beam monitors) and the required slit systems. The beam propagates from top left to bottom right. The upstream mirror chamber contains a flat horizontally reflecting mirror, followed by a horizontally focusing KB mirror. The downstream mirror chamber contains a vertically focusing KB mirror followed by a flat vertically reflecting mirror. Each of these four mirrors is 1 m long with a 950 mm clear aperture on the surface. Each mirror tank is 2.2 m long.

4.2.2 Sample chamber and interaction region

Both focal spots are brought to a focus in a common focal plane, allowing the use of a single, common sample chamber, which minimizes cost and complexity. The interaction region foresees the injection of samples both in a liquid-jet form, or as an aerosol stream, as well as precision-controlled fixed-target samples on a removable stack of sample stages. The chamber has vacuum valves on both its upstream and downstream sides, and a door to one side, to allow easy access to the interaction region should intervention be required. This ability to vacuum-isolate the sample chamber protects the upstream X-ray optics from ambient pressure, but also the detector downstream. Furthermore, this minimizes the volume required to pump in the case of an intervention, minimizing any associated downtime.

In general, there are three main vacuum regions in the SPB instrument. The vacuum upstream of the sample chamber houses the X-ray optics and must be maintained at a pressure of 1×10^{-9} mbar or better. Downstream of the sample chamber, the

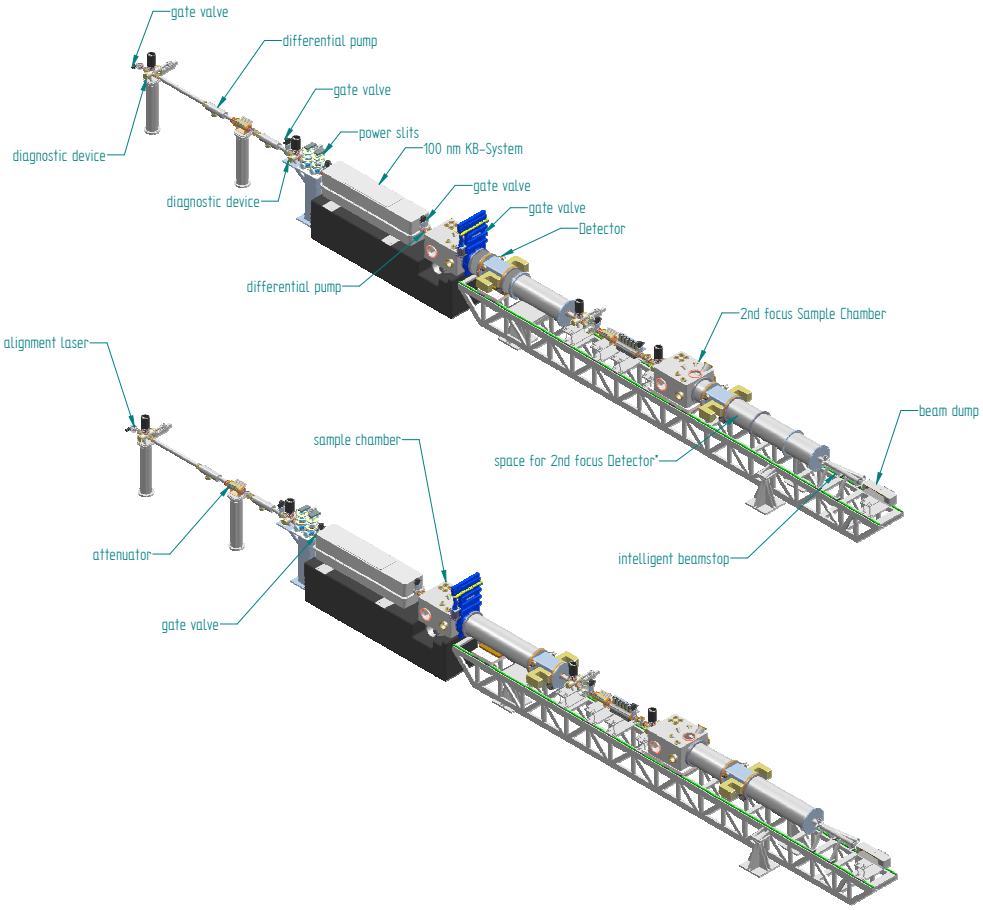

Figure 4.4: Experiment hutch overview in nanocrystallography configuration (above) and imaging configuration (below). The 100 nm–scale KB optics and the sample chamber are the most prominent features of the apparatus. The downstream elements of the instrument, including the detector, the SFX apparatus, and its detector, as well as the intelligent downstream diagnostics and beam dump, are located on a moveable rail. This allows for straightforward coarse alignment of the downstream components for the different beam positions and directions produced by the different focusing optics. The downstream elements may also be conveniently moved in the longitudinal direction, to allow for different sample–detector distances (needed for differently sized samples) or to adjust the refocused spot size in the SFX sample chamber.

vacuum requirement for the detectors and diagnostics devices therein is relaxed, and a vacuum of 1×10^{-5} to 1×10^{-6} mbar is sufficient. The sample chamber itself may also operate in a similar range, but in cases of liquid and aerosol injection, vacuum pressures as poor as 1×10^{-3} to 1×10^{-4} mbar have been observed in similar setups, and we plan to accommodate these challenging cases too.

Therefore, the most challenging vacuum interface is that between the upstream X-ray

optics and the sample chamber itself. In operation, it is implausible to use a window between these optics and the sample chamber, due to the destructive nature of the XFEL beam. Using a window is undesirable anyway, from an optical point of view, as we wish to minimize the number of elements that could perturb the wavefront of the XFEL beam. For this region, we propose a differential pumping system that is designed to accommodate this relatively large pressure difference within the available space. This is a key part of the successful operation of the instrument and is detailed in Section A.3.1, "Differential pump between 100 nm–scale KB and sample chamber".

4.2.3 Detection and downstream components

The scientific requirements and the detector pixel size (≈ 200 µm) lead to the detector needing to be positioned as close as physically possible to the interaction region (see Chapter 9, "Detector integration") and up to 10 m downstream to collect the low-angle scattering data from larger samples. This range will be satisfied by two detection planes, one upstream and a smaller detector downstream. The downstream plane is required due to the dead area at the centre of the detector, which in any case prohibits the collection of data at low scattering angles (see Section 9.1.5, "Preferred overall detector layout, including two detection planes"). The upstream detector needs to move as far as 5.5 m downstream to satisfy the sampling requirements of the largest expected samples.

All of the components downstream of the sample chamber are to be mounted on a rail system, which will allow their longitudinal position to be varied from experiment to experiment. This is particularly important for the detector, which needs an optimal sample–detector distance, especially given its limited total number of pixels. As the different optical geometries of the SPB instrument have slightly different optical paths, a rail system allows all of the downstream optical components to move in concert, and remain at least coarsely aligned between different settings. The rail system is described more fully in Section B.3, "Rail system".

4.2.4 SFX apparatus

The SFX apparatus consists of a compound refractive lens (CRL) stack for refocusing the micrometre-scale beam into a secondary sample chamber downstream. Both of these components are located on the rail. The CRL lens stack, for example, may then be positioned as far upstream as the SPB experiment's detector geometry allows, maximizing the acceptance of the refocusing optic. This optics may then still refocus to the same location in the SFX sample chamber, by the addition of CRL lenses, or

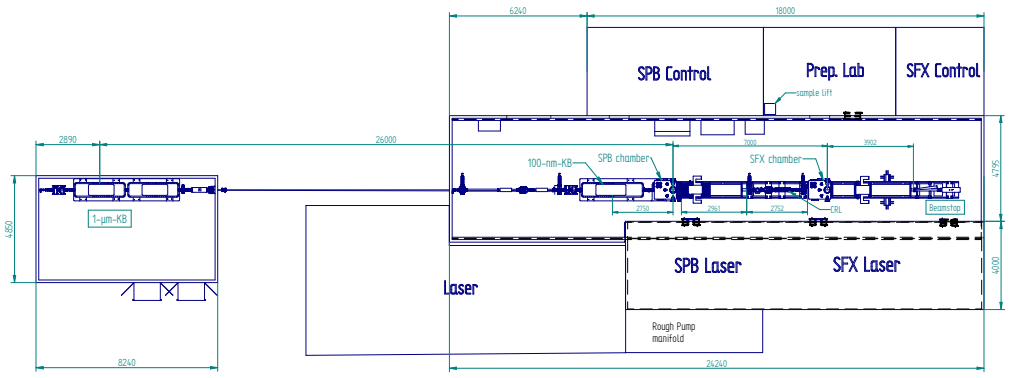

Figure 4.5: SPB instrument overview, top–down perspective. The SPB instrument is shown within the SASE1 area of the experiment hall. At the most upstream end of the hall is the SPB optics hutch, containing the micrometre-scale focusing optics. At the most downstream end is the SPB experiment hutch, containing the 100 nm–scale focusing optics, the sample chamber, and the SFX sample chamber and refocusing optics. Note the preparation area and the sample lift, which can be used to receive samples directly from the characterization laboratory on the floor above.

the SFX sample chamber may be moved a commensurate distance upstream to accommodate the lenses' movement. Importantly, all of the SFX apparatus can be "popped out" of the beam when imaging experiments require a long sample–detector distance. A 4 Mpx AGIPD detector is planned for the SFX setup.

Ideally, the SFX apparatus would be installed in a region of the SPB instrument that could be radiation-shielded from the SPB interaction region—allowing independent access to the SFX interaction region without interrupting the SPB experiment. Unfortunately, the physics of the XFEL beam thwart this idea by requiring a beam dump of 1.5 m length to stop the beam at the end of the experiment hutch. Imagining one can add such a device as a shutter within the experiment hutch would cause the necessary instrumentation to exceed the dimensions of the SPB experiment hutch. Furthermore, even this beam dump would not work in the location between the SPB and SFX interaction regions, as the XFEL beam size would be much smaller than at the end of the hutch and would cause the dump material to fail (damage and ablate) under its irradiation. For further details, see Appendix D, "Beam conditioning components". This technical limitation places even more stringent requirements of the dialogue between the SPB staff and the SFX user consortium, and in that vein, integration meetings between key SPB and SFX personnel have begun to address the issue of optimizing the collaboration.

4.3 Biosafety

The SPB instrument anticipates operating as a Bio-Safety Level 1 (BSL1) laboratory, mainly due to complex instrumentation, aerosolization of sample, etc., which make it difficult to realize a higher level of bio-containment during initial operation.

We propose that after initial experience of a BSL1 instrument at the European XFEL, one may consider a BSL2 outfitting for a future instrument, after an initial understanding of the required instrumentation is grounded in practice.

By providing a BSL1-compatible region, and a bio-sample lift that directly links the characterization lab (on the floor above) and the preparation area immediately adjacent to the instrument, we have created a seamless BSL1 environment for the efficient transport of sample material between the relevant laboratories and spaces at the European XFEL. In keeping with accepted safety guidelines, these spaces (labs, hutch, and preparation area) will be access control–limited to personnel with the appropriate safety training.

For an overview of the major components of the instrument, see Figure 4.5 on the preceding page for a top-down view of the of the optics hutch, the experiment hutch and the nearby support infrastructure.

5 Photon beam properties

For the reader's convenience, this chapter summarizes the photon beam properties of the SASE1 undulator, the source relevant to the SPB instrument, as described in [100] and in [83].

5.1 Radiation from the SASE1 undulator

The SPB instrument will be located in the centre beamline after the SASE1 undulator of the European XFEL, as shown in Figure 5.1.

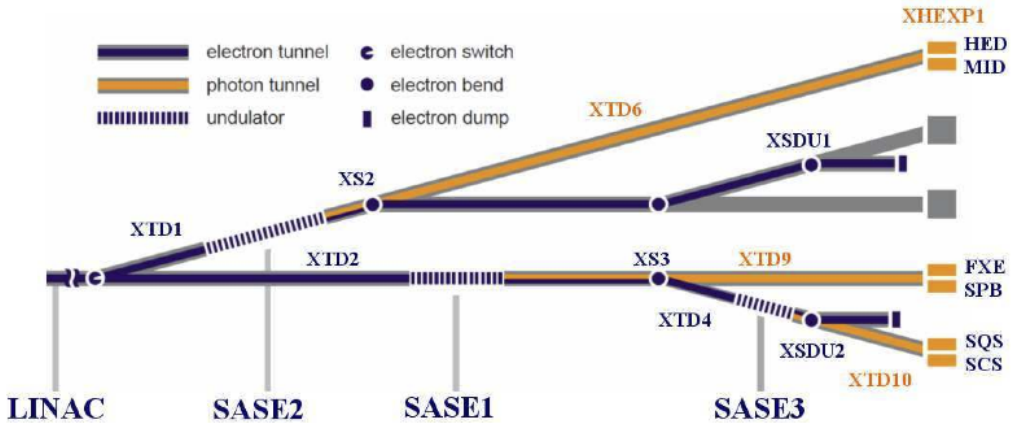

Figure 5.1: Layout of the European XFEL accelerator, undulator, and X-ray beam transport systems. Note that the SPB instrument is located after the SASE1 undulator. Figure sourced from [100].

Table 5.1: Fundamental operating parameters of the SPB instrument, as discussed at the SPB workshop [58] and modified from those tabulated in [100]

Scientific instrument	Photon energy [keV]	Bandwidth $\Delta\omega/\omega$	Beam size [µm]	Special optics
SPB	3–16	Natural	0.1–10	Extreme focusing

Table 5.1, from [100], lists the desired operating range of the SPB instrument, its proposed range of beam size as requested at the SPB workshop [58], and its proposed bandwidth. The proposed bandwidth to be used is the natural bandwidth of the FEL ($\Delta E/E \approx 1 \times 10^{-3}$); see also Table 5.2 on the next page. The SPB CDR document [57] outlines the possible addition of a monochromator in a future

upgrade in its Chapter 5, “Optical layout”. Note that a general discussion on the bandwidth requirements at the SPB instrument is given in Section 7.1.3.4 of this report, “Wavelength spectrum”.

Table 5.2: Parameters of the European XFEL SASE1 photon beam [83] relevant to the SPB instrument. All values are simulated values assuming saturation. Note that only those values for the minimum (0.02 nC) and maximum (1 nC) bunch charge of the electron beam are shown. The numbers in red indicate maximum pulse energies and photon numbers per pulse for each photon beam energy and bunch charge. It can be seen that the highest electron energy that is compatible with a given photon energy leads to the highest photon pulse energy. Note that the peak power here is calculated as the power during a pulse, not a bunch train.

Electron energy: 17.5 GeV										
Photon energy [keV]	2.76		4.96		8.27		12.4		15.5	
FWHM pulse length [fs]	–	–	–	–	1.68	107	1.68	107	1.68	107
FWHM bandwidth [%]	–	–	–	–	0.21	0.14	0.18	0.12	0.16	0.10
Bunch charge [nC]	–	–	–	–	0.02	1.00	0.02	1.00	0.02	1.00
RMS electron energy jitter [MeV]	–	–	–	–	4.10	2.00	4.10	2.00	4.10	2.00
Expected FWHM wavelength jitter[1] [%]	–	–	–	–	0.11	0.05	0.11	0.05	0.11	0.05
Photons per pulse [10^{12}]	–	–	–	–	0.06	2.29	0.032	0.91	0.02	0.58
Pulse energy [mJ]	–	–	–	–	8.09e-2	3.04	6.35e-2	1.80	5.36e-2	1.43
Peak power [GW]	–	–	–	–	48.1	28.4	37.8	16.8	31.9	13.3
Source size [µm]	–	–	–	–	28.6	43.0	27.3	42.7	26.5	46.5
Source divergence [µrad]	–	–	–	–	2.83	1.91	2.00	1.35	1.65	1.07
Coherence degree	–	–	–	–	0.96	0.941	0.96	0.82	0.96	0.71
Electron energy: 14.0 GeV										
Photon energy [keV]	2.76		4.96		8.27		12.4		15.5	
FWHM pulse length [fs]	–	–	1.68	107	1.68	107	1.68	107	1.68	107
FWHM bandwidth [%]	–	–	0.24	0.17	0.20	0.13	0.16	0.10	0.14	0.082
Bunch charge [nC]	–	–	0.02	1.00	0.02	1.00	0.02	1.00	0.02	1.00
RMS electron energy jitter [MeV]	–	–	4.10	2.00	4.10	2.00	4.10	2.00	4.10	2.00
Expected FWHM wavelength jitter[a] [%]	–	–	0.14	0.07	0.14	0.07	0.14	0.07	0.14	0.07
Photons per pulse [10^{12}]	–	–	0.098	4.5	0.045	1.6	0.022	0.64	0.014	0.40
Pulse energy [mJ]	–	–	7.82e-2	3.59	5.94e-2	2.10	4.41e-2	1.26	3.54e-2	0.99
Peak power [GW]	–	–	46.5	33.5	35.4	19.6	26.3	11.8	21.1	9.24
Source size [µm]	–	–	32.6	49.2	30.8	46.0	29.3	49.2	28.5	53.5
Source divergence [µrad]	–	–	4.11	2.79	2.66	1.78	1.87	1.27	1.54	1.00
Coherence degree	–	–	0.960	0.958	0.96	0.89	0.96	0.705	0.958	0.569
Electron energy: 10.5 GeV										
Photon energy [keV]	2.76		4.96		8.27		12.4		15.5	
FWHM pulse length [fs]	1.68	107	1.68	107	1.68	107	1.68	107	1.68	107
FWHM bandwidth [%]	0.28	0.22	0.23	0.17	0.18	0.13	0.14	0.08	0.11	0.056
Bunch charge [nC]	0.02	1.00	0.02	1.00	0.02	1.00	0.02	1.00	0.02	1.00
RMS electron energy jitter [MeV]	4.10	2.00	4.10	2.00	4.10	2.00	4.10	2.00	4.10	2.00
Expected FWHM wavelength jitter[a] [%]	0.18	0.09	0.18	0.09	0.18	0.09	0.18	0.09	0.18	0.09
Photons per pulse [10^{12}]	0.16	8.4	0.065	2.9	0.027	0.92	0.012	0.34	0.006	0.22
Pulse energy [mJ]	7.01e-2	3.70	5.20e-2	2.34	3.62e-2	1.21	2.28e-2	7.54e-1	1.50e-2	5.53e-1
Peak power [GW]	41.7	34.5	31.0	21.8	21.5	11.3	13.6	7.03	8.91	5.16
Source size [µm]	38.4	58.0	35.9	53.7	33.8	50.4	32.3	58.7	31.8	64.3
Source divergence [µrad]	6.26	4.26	3.79	2.55	2.44	1.78	1.70	1.17	1.38	0.92
Coherence degree	0.960	0.969	0.960	0.941	0.960	0.769	0.957	0.528	0.936	0.395

A detailed overview of essential simulated source parameters at the SASE1 undulator

for representative photon energies in the operating range of the SPB instrument (3–16 keV) is given in Table 5.2. The values have been extracted from [83], which is also the basis of [100]. They represent a good estimate of the expected performance of the XFEL source at the SPB instrument. Maximum values for pulse energy (and photons per pulse)—which represent the most demanding limit in terms of heat load on all components interacting with the beam—are indicated in red for every photon energy.

As visible in Table 5.2, the highest pulse energy (up to 3.7 mJ) is expected for the lowest photon energy (2.76 keV). This is especially important as, to a first approximation, the damage threshold for interaction of the (focused) XFEL beam with matter decreases with decreasing photon energy (and thus, decreasing penetration depth) [88].

In general, the beam is highly spatially coherent, with the degree of coherence decreasing for harder-energy X-rays or higher bunch charge in the accelerator (that is, higher photon flux). The source size is expected to be between about 30 and 50 µm FWHM across a range of different parameters.

The European XFEL is designed to produce pulses of less than 10 fs in duration for sub-100 pC bunch charges (see Table 5.2). In order to utilize the “diffract-and-destroy” principle for single particles to the highest resolutions, it is expected that pulse durations below 10 fs are necessary [64, 73]. For other applications, such as nanocrystallography, these duration constraints appear to be significantly reduced, with pulses of hundreds of femtoseconds duration viable in some cases [6]. However, for single particles and nanocrystals, the key parameter to maximize is pulse intensity, achieved with the highest pulse power. A peak power of 46 GW focused to a 0.1 µm diameter spot would give a maximum of 4.6×10^{20} W/cm^2.

6 X-ray optics layout

Chapter authors: A. Aquila[1], **A.P. Mancuso**[1]

6.1 Overview and layout

6.1.1 Goals of the optical layout

As stated in Section 1.3, "Science case summary" [57], the primary goals of the optical system of the SPB instrument are to produce:

- Maximum number of photons delivered to the sample, in spot sizes slightly larger than the sample sizes
- Flat, uniform, or characterizable wavefront in the focal plane
- Highest possible transmission of the optical system across the operating photon energy range of the instrument (3–16 keV)

The scientific cases described in Section 1.3, "100 nm–scale focusing optics", require two high-quality focal spots on the order of 100 nm and slightly larger than 1 µm to be produced. Both focal spots should ideally be located in the same focal plane and as close as feasible to each other within that plane. This allows a single detector and chamber geometry. Otherwise, many of the components would need to be duplicated along the beamline, increasing the cost and complexity of the instrument. This single sample chamber approach is outlined in Chapter 4, "Overview of the SPB instrument".

In this section, we present two world-beating focusing systems that satisfy the requirements listed above for a micrometre-scale focus and a 100 nm–scale focal size, across the photon energy range of the SPB instrument, in a mechanically plausible design with a clear path to future upgrades that will result in even further improved performance.

In the next section, we revisit the basic optical considerations that constrain the design, and then present the key elements of the two focusing systems. Detailed considerations of each optical system's performance are given in Section 6.3, "Micrometre-scale focusing optics", and Section 6.4, "100 nm–scale focusing optics".

[1]Scientific Instrument SPB group (WP84), European XFEL GmbH, Albert-Einstein-Ring 19, 22767 Hamburg, Germany

6.1.2 Basic optical considerations

Many factors contribute to the focal spot size of an optical system.

The critical factors are:

- System geometry: optics shapes and distances
- Numerical (clear) aperture of the optics
- Aberrations, and roughness of the optic's surface
- Wavelength
- Source size
- Source point and fluctuation around the source point
- Source shape, or number of spatial modes contained in the source

In this chapter, we discuss the first three items. The wavelength and source properties are adjustable quantities for which we will have to make certain approximations or selections. The wavelengths considered correspond to the desired 3–16 keV photon energy range. The source properties are perhaps the least well-known quantities that have a bearing on the optical system. We make estimates of the source properties where possible, and make educated estimates about fluctuations, source shape, and so on, as a best attempt to include these effects. In addition, the source point location is also addressed in Section C.5, "Ray tracing".

Many critical optical features and aspects of the SPB instrument can be demonstrated from paraxial geometric optics[2] and from simple diffraction theory. The instrument re-images and demagnifies the source point in the undulator into the focal point in the sample chamber. The SPB beamline's source point is estimated to be located in the third-to-last undulator [88] of SASE1, which is 932.6 m from the interaction region of the sample chamber. It is estimated that the source point will have a size of approximately 40 µm FWHM diameter across much of the SPB operation parameters (see Table 5.2), which varies only slightly with photon energy and decreases somewhat with reduced electron bunch charge [100]. The source size and the source-to-focus distance then fully determine the location of the focusing optical elements. Specifically, if we consider the geometric demagnification of a source size to obtain an image or focal size S, then we can determine L, the distance from the optics to the focus, for a fixed source–focus distance:

$$\frac{S}{40 \times 10^{-6}} = \frac{L}{932.6 - L} \tag{6.1}$$

[2]The optics are approximately 70 Rayleigh lengths from the source point.

Based on the above-mentioned criteria, to obtain the micrometre-scale and 100 nm–scale spots, the focusing optics will need to be 22.75 m and 2.33 m from the focus, respectively.

Two other critical features to note are the photon energy range covered by the instrument and the lateral size of the X-ray beam on the optics caused by the long working distances. The instrument is designed to work from 3 keV up to 16 keV. This wide photon energy range produces challenges for all focusing optics under consideration. The approx. 900 m propagation distance also leads to large lateral beam sizes at the optics, as show in Table 6.1 [88].

Table 6.1: Table of beam size at experiment hall as a function of photon energy. Reproduced from [88].

Photon energy [keV]	$FWHM_{upper}$ [mm]	$FWHM_{lower}$ [mm]	Divergence [µrad]
3	5.57	3.10	6.18
5	3.80	2.01	4.22
8	2.67	1.34	2.96
10	2.26	1.11	2.51
12	1.97	0.95	2.19
15	1.66	0.79	1.85

Ideally, an optic should have an aperture size of at least 4σ of the beam size, to minimize diffraction from the optics' aperture and best preserve the beam profile[3] and wavefront. The large transverse beam sizes expected in the experiment hall make it difficult to meet this requirement for all photon energies for realistic mirror lengths (that can also meet the stringent figure and roughness requirements detailed below). The clear-aperture requirement becomes most difficult at the lower energies of the beamline, in particular between 3 keV and 5 keV. If we consider the requirement of the transverse dimension of the mirror's clear aperture to accept 4σ (or $1.7\times$FWHM), then the desired lateral aperture (based on the upper bound from Table 6.1) is 9.46 mm (5.57 mm FWHM) for the 3 keV case.

The lateral or transverse clear aperture (C_A) of a grazing incidence mirror can be estimated using the relation:

$$C_A \approx L \times \theta \tag{6.2}$$

[3] $\pm 2\sigma$ from peak intensity or 91.1% of the intensity assuming a 2D square aperture.

where L is the mirror length, or mirror's clear aperture, and θ is the grazing incident angle of the mirror. Current mirror technology, which could be implemented at the European XFEL, provides for 1000 mm long mirrors with a 950 mm clear aperture. See Figure 6.1 for an estimate of the clear aperture as a function of photon energy. This scale of mirror is not so different from the 950 mm long offset mirrors with 800 mm long clear aperture that the X-Ray Optics and Beam Transport group is planning to implement. Furthermore, preliminary discussions with possible vendors have suggested that such mirrors can indeed be manufactured.

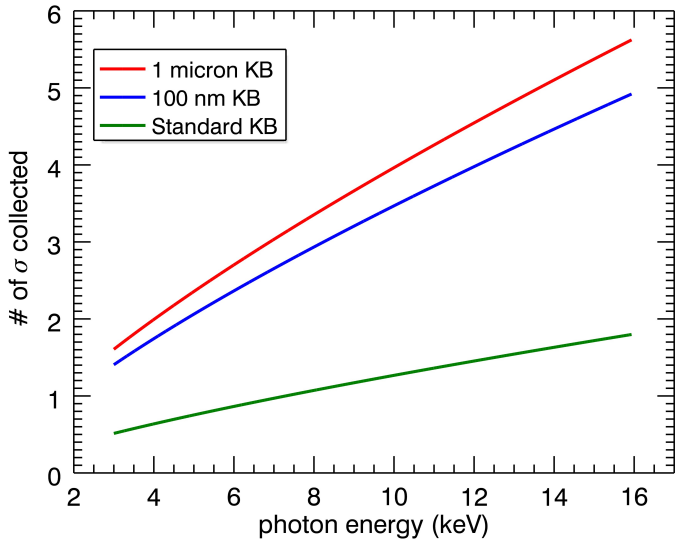

Figure 6.1: Fraction of beam collected as a function of photon energy for mirror parameters as discussed in the main text. This assumes a 2D Gaussian beam with largest beam sizes stated in the table of beam sizes, Table 6.1 on the preceding page. The standard KB is a 450 mm length, 2.7 mrad angle optics. The angle corresponds to the critical angle of silicon at 13.5 keV.

As stated in Chapter 5 of the SPB CDR [57], we will use KB mirrors for all SPB focusing elements. Grazing incidence mirrors were chosen as the only viable technology as they provide high efficiency, ultimately diffraction-limited spot sizes, the potential to survive intense X-ray pulses, and can suppress much of the third-order harmonic radiation over most of the photon energy range. Conveniently, and of particular importance from an operation standpoint, they are also achromatic. However, to obtain these goals, extensions to current mirror technology in both mirror figure and length with such high-quality figure are required.

Of critical note is that—even with perfect mirrors—we could be limited in focal size by the numerical or clear aperture of the optics. With the 950 mm clear aperture

and the 4 mrad reflection angle, we will obtain a lateral aperture of 3.8 mm. A similar calculation will provide a lateral aperture of 3.3 mm for the 100 nm KB. To demonstrate this effect, Figure 6.2 shows the minimal focal spot size due to the diffraction limits of our lateral aperture size. Figure 6.3 on the next page and Figure 6.4 on the following page show the expected focal spot sizes, under various FEL conditions, for the micrometre-scale and 100 nm–scale foci, respectively. As the planned SPB KB mirrors are to be the longest that have been made to such specifications, the only possible way to increase the numerical aperture is to increase the grazing angle of the mirrors. This technique is only possible at photon energies closer to the lower limit of the operating range of the specific coating, e.g. where the critical angle of the material is higher. This possibility will be discussed further in Section 6.3.6, "Future upgrades", on possible upgrades to the micrometre-scale optics.

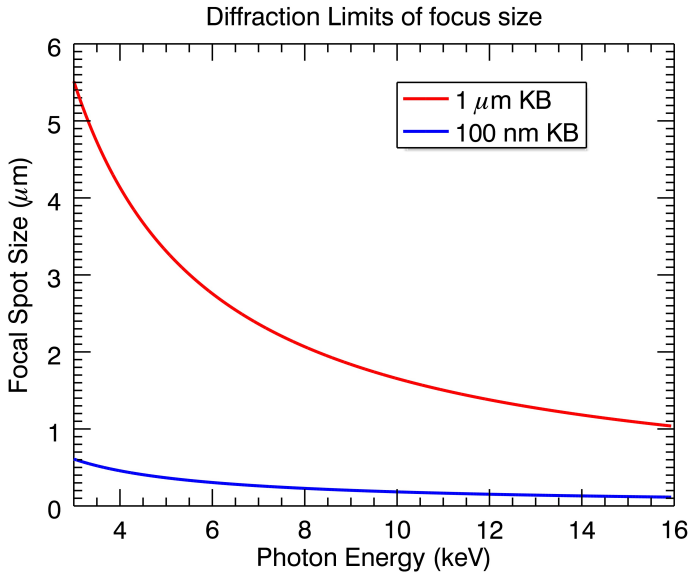

Figure 6.2: Expected diffraction-limited focal spot size due to the lateral numerical aperture size for the SPB instrument

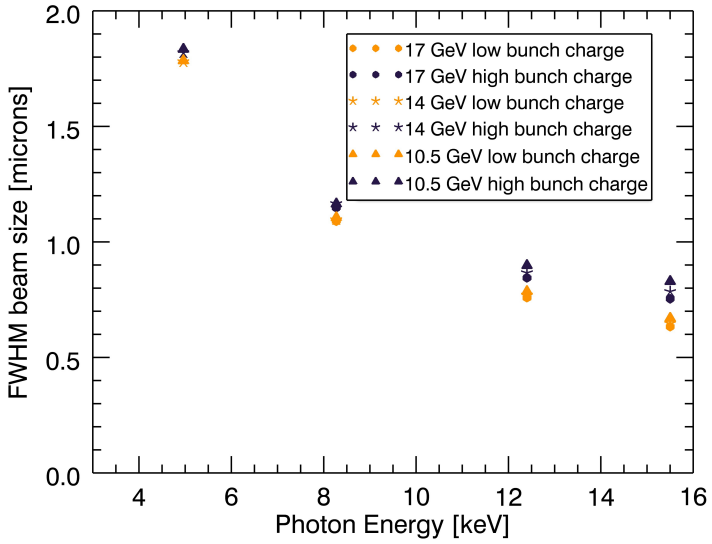

Figure 6.3: Expected focal spot size for the micrometre-scale KB focus using the FEL parameters provided in Table 5.2 on page 42. The model is an estimate based on a truncated Gaussian beam and takes into account the finite numerical aperture of the FEL.

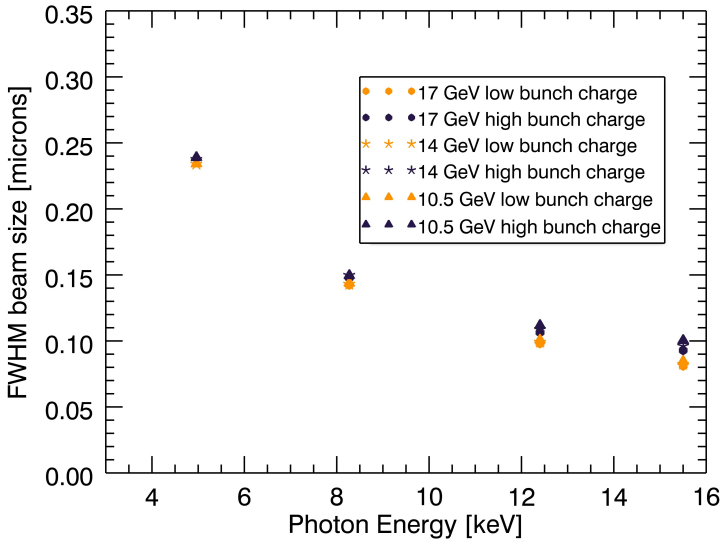

Figure 6.4: Expected focal spot size for the 100 nm–scale KB focus using the FEL parameters provided in Table 5.2 on page 42 using the same calculations as in Figure 6.3

The following sections describe all focusing and optical components starting with the

optics furthest upstream and ending with the optics furthest downstream. An overview of the placement of the mirrors in the SPB optics and experiment hutches is shown in Figure 4.1 on page 34. The properties and placement of each mirror are described individually below.

6.2 Horizontal offset mirrors

The first optics the SPB beam sees are the horizontal offset mirrors (HOMs). These are a pair of horizontally reflecting mirrors with 800 mm clear aperture each. The HOMs remove the high-energy Bremsstrahlung radiation co-propagating with the FEL radiation and are an essential part of radiation safety for all instruments. The mirror angles are adjustable in order to tailor their aperture for different photon energies (which implies different beam sizes). The second mirror of the pair is dynamically bendable, using piezoelectric transducers, to potentially focus and correct for abberated wavefronts in the horizontal direction only. These mirrors are described in the *Conceptual Design Report: X-Ray Optics and Beam Transport* [88] and are to be delivered by the X-Ray Optics and Beam Transport group. Of important operational note is the change in horizontal angle under different use conditions as shown in Figure 6.5. This translation (and corresponding rotation) is necessary to collect the full beam width as a function of photon energy. The angular motion of the HOMs translates into a 0.1 mrad offset angle in the front end of our optics hutch as shown in Figure 6.5. While this angle is small, it needs to be considered in the development of an alignment procedure for the beamline.

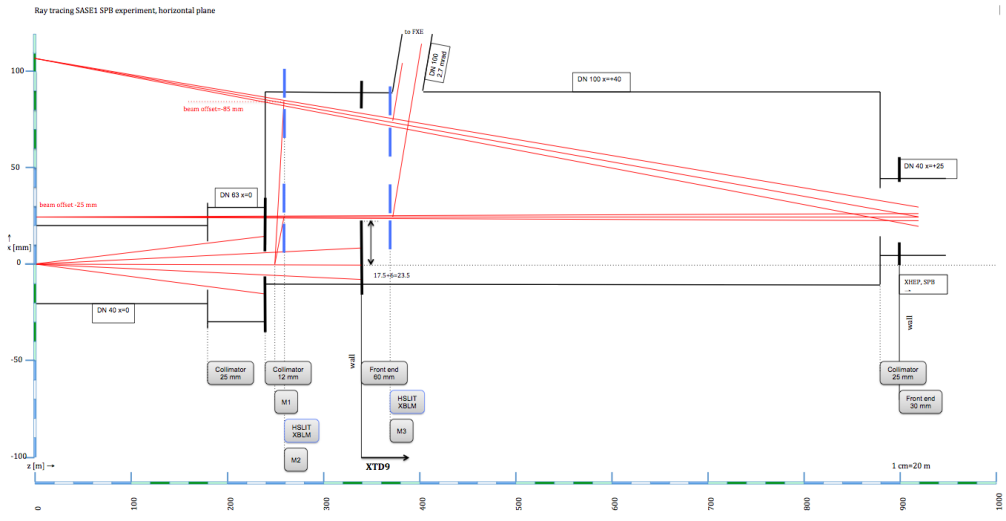

Figure 6.5: Horizontal offset mirrors provide a varying incident angle to the experiment hall [87], which needs to be taken into account for the SPB alignment procedure

The SPB instrument is located on the centre branch of the SASE1 undulator. This is by design to minimize the number of front-end optics needed to direct the beam, in order to preserve the wavefront entering the experiment floor from the tunnel. The only optics encountered by the SPB beamline are a pair of HOMs. The handoff for responsibility between the SPB team and the X-Ray Optics and Beam Transport group is located at the beam transport tunnel wall, where the beam shutter is situated. The only elements of responsibility for the SPB team upstream of the shutter are the SPB attenuators located just upstream of the beam shutter.

6.3 Micrometre-scale focusing optics

6.3.1 Physical considerations

Due to the required 22.75 m distance to obtain a diffraction-limited micrometre-scale focus, the SPB optics hutch is located as upstream as possible on the experiment hall floor as shown in Figure 4.5 on page 39. This is to minimize drift and vibrations, as the beam transport tunnel is in a separate, floating, concrete environment to the experiment hall. The SPB optics hutch is located approximately 900 m downstream of the expected source position, near the end of the SASE1 undulator. The optical solution chosen will refocus the 40 µm source spot to the focal location 26 m, 24.7 m (horizontal, vertical) downstream of the centre of the optics. This provides an ideal geometric demagnification on the order of 37, producing a spot slightly larger than 1 µm. In practice, the actual spot size will be slightly larger, depending on the final figure error of the optics and diffraction limit, and on the actual source size in the SASE1 undulator. The figure error is discussed in detail in Section 6.3.3.3, "Roughness, slope errors, and height errors", and depends on the achievable reduction of slope errors, which need to be a factor of two better than current technology.

One positive aspect of the long focal distance is the creation of very long Rayleigh lengths of 6.5 mm and 6.0 mm for the horizontal and vertical, respectively. These long lengths make aerosol injection easier, as the injector placement and spray angles mean that the sample should be in the focus even if the injection system is not perfectly aligned. Astigmatic effects from misalignment are also less of a concern.

6.3.2 Layout

With the 950 mm physical size limit for the clear aperture outlined in the previous section, we have chosen a 4 mrad reflection angle, θ, to maximize the clear aperture

while maintaining the photon energy range of the beamline. A traditional 1 µm KB pair located 26 m and 24.7 m upstream of the interaction region (horizontal and vertical, respectively), and 40.3 m and 39 m from the end of the beam stop would produce a beam deviation of order 300 mm at the sample chamber and 450 mm at the beam stop when compared to the straight-through beam.

Instead of implementing a traditional KB pair for the micrometre-scale focusing optics, we propose a four-bounce solution for two key reasons. First, a four-bounce system (with opposite facing mirrors in both the horizontal and vertical directions; see Figure 6.6) is much less sensitive to vibrations than a traditional KB system. In this geometry, variations in position do not map to variations in angle over the large optics-to-focus distance. Secondly, as two of the four mirrors are flats, these provide an excellent opportunity to be actuated and used to correct for any wavefront variations [61]—either those introduced by the optics or those inherent to the beam.

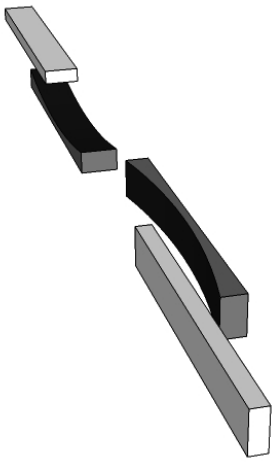

Figure 6.6: Visualization of the four-bounce micrometre-scale KB system with two steering optics. The view is from above and upstream towards the back of the optics hutch.

Furthermore, an added practical benefit is that the four-bounce design mitigates the large offset produced by a traditional KB design. The beam is steered back to a path parallel to the one it had prior to its interaction with the KB, mitigating the need to change the optical axis of the entire instrument markedly, which would otherwise lead to potentially very long delays in operation after changes in photon energy or spot size. The drawback is that this scheme introduces two additional optical elements, which may reduce transmission compared to a two-mirror system and contribute to wavefront degradation—though the proposed upgrade plans should alleviate the wavefront issue.

The four-bounce system for the micrometre-scale focus also preserves the luminosity of the 100 nm–scale KB system (described in Section 6.4, “100 nm–scale focusing optics”), which is a two-bounce system that receives the beam directly from the HOMs. As shown in Figure 4.1 on page 34, this solution also allows the 100 nm–scale KB system to remain approximately aligned when the micrometre-scale system is used.

For the interested reader, in the course of evaluating focusing solutions for the micrometre-scale focal spot, we have investigated in detail five possible optical solutions. These can be found in Appendix C, “Additional optical considerations”, along with a description of the benefits and drawbacks of each method. We consider the solution presented here in the main text as the most viable, and the reasons for rejecting the other possible alternative solutions are described in the appendix.

It is envisioned that this mirror design will consist of two chambers. From most upstream to downstream, the mirror layout is as follows: In the first chamber, there is a pair of horizontal optics, first the horizontally reflecting flat followed by the horizontal KB, as the incoming X-rays may need to be adjusted horizontally due to the possible 0.1 mrad offset from the HOMs. This is followed by a pair of vertically oriented optics in the second chamber. The first optics is the vertically reflecting KB ellipse reflecting the X-rays upward, followed by a vertically downward reflecting flat. There are two main reasons for this configuration: (1) With the two KB optics close together, astigmatic effects are minimized. (2) It is difficult to measure an inverted optics for sag due to gravity. Using a flat in this direction is less risky than attempting to compensate and accurately measure an ellipsoid in this inverted configuration. In both cases, due to space considerations, there is a longitudinal overlap of the mirrors by 30 cm. This is to reduce both the lateral offset of 5.6 mm from the unreflected X-ray beam and to reduce the longitudinal space required in the rather short SPB optics hutch. The exact coordinates of the mirrors with respect to the optics hutch, focal point, and each other are shown in Figure 6.7 on the next page and Figure 6.8 on page 56. These figures were produced by an adaptable ray-tracing simulator that we designed for the SPB instrument.

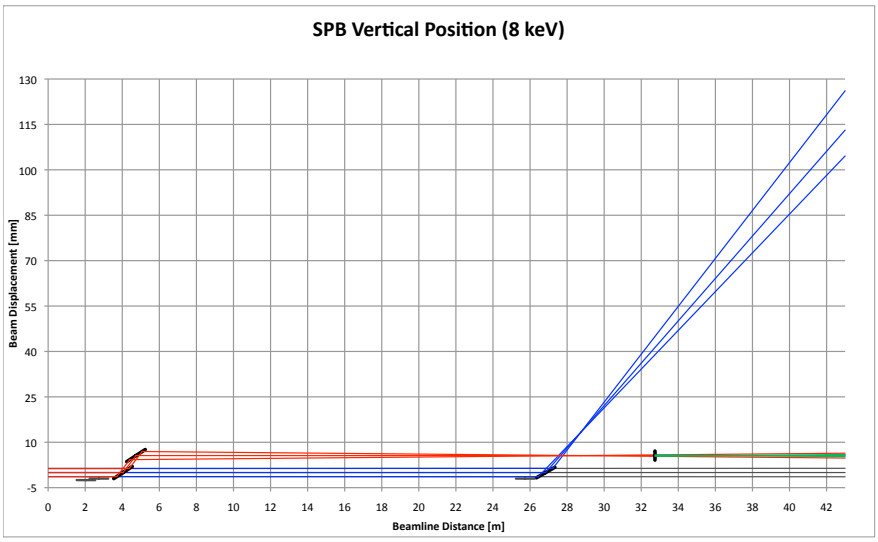

Figure 6.7: Geometrical ray-tracing simulation of the SPB beamline for the vertical direction, where the $Z = 0$ m marker is the tunnel wall. The three lines represent $\pm$ FWHM and the centre line. The three colors represent different focusing conditions: red for micrometre-scale optics, blue for 100 nm–scale, and green for SFX focal spots. Note that distances are shown in metres, while offsets (on the vertical axis) are in millimetres.

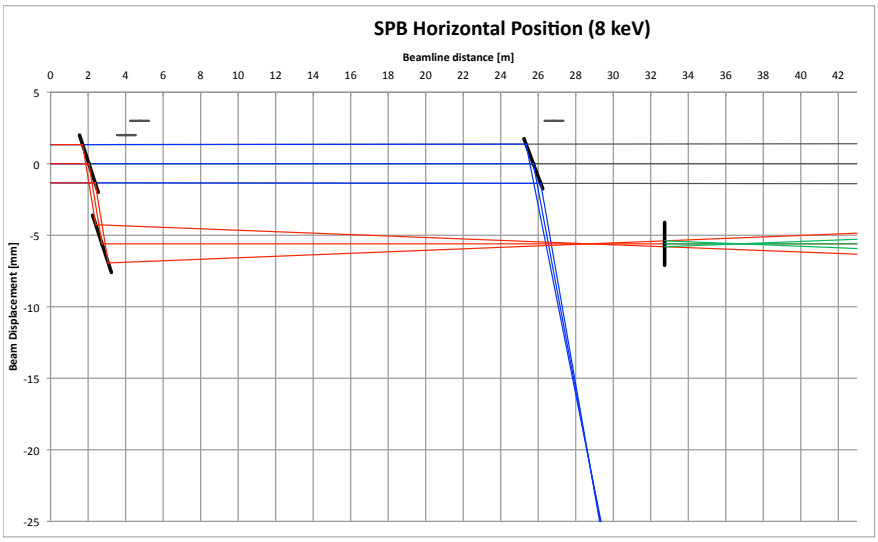

Figure 6.8: Equivalent horizontal ray tracing, with zoom in to see the focal plane at Z = 28.74 m and SFX with a 1 µm focal spot size (that is, a 1:1 focal geometry from the SPB focus). The SFX size and distances were chosen to make the beam sizes the same—with and without refocusing for SFX—at the beam dump. This ensures the heat load at the dump is not excessive. Note that distances are shown in metres, while offsets (on the vertical axis) are in millimetres.

6.3.3 Optical specifications

The basic optical specification for any KB system can be summed up with the geometric distance as shown in Figure 6.9 and Table 6.2. We have the added complexity that we plan a four-bounce KB system with flats preceding and following the KB optics. However, as the flats only reflect the real source point without ideally modifying the source, the path lengths and angles do not change. That is, the idealized source point becomes a symmetric line through the reflection and can be traced using the same distances and angles.

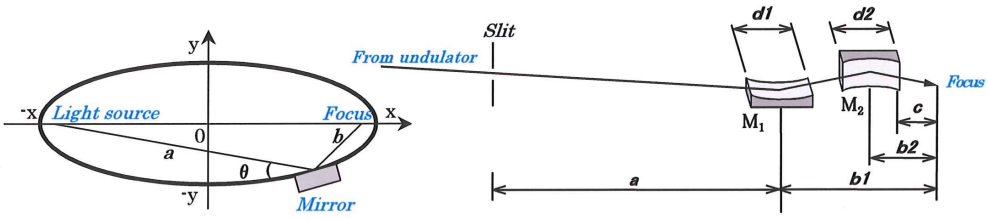

Figure 6.9: Geometrical specification for a KB system, adapted from JTEC

Table 6.2: Geometrical distances and angular specifications for the micrometre-scale KB system

Parameter	Value	Unit
Distance source to KB1 (a)	906.615	m
Distance KB1 to focus (b1)	26	m
Distance KB2 to focus (b2)	24.7	m
Distance end of KB2 to focus (c)	24.2	m
Length of KB1 (d1)	1000	mm
Clear aperture KB1	950	mm
Length of KB2 (d2)	1000	mm
Clear aperture KB2	950	mm
Incidence angles (θ)	4	mrad

6.3.3.1 Optic figure

Both KB optics are to be be polished into ellipses, as this is the ideal shape for point to point focusing. Table 6.3 provides information on the expected shape of the ellipse for both horizontal and vertical KB optics.

Table 6.3: Geometrical ellipse parameters for the micrometre-scale KB system

Parameter	KB1 (@4 mrad)	KB2 (@4 mrad)	Unit
KB plane	XZ	YZ	–
Major axis	466.3075	466.3075	m
Minor axis	0.614	0.599	m
Radius of curvature (centre)	12.7	12.1	km
Maximum incidence angle	4.04	4.04	mrad
Minimum incidence angle	3.96	3.96	mrad

6.3.3.2 Coatings

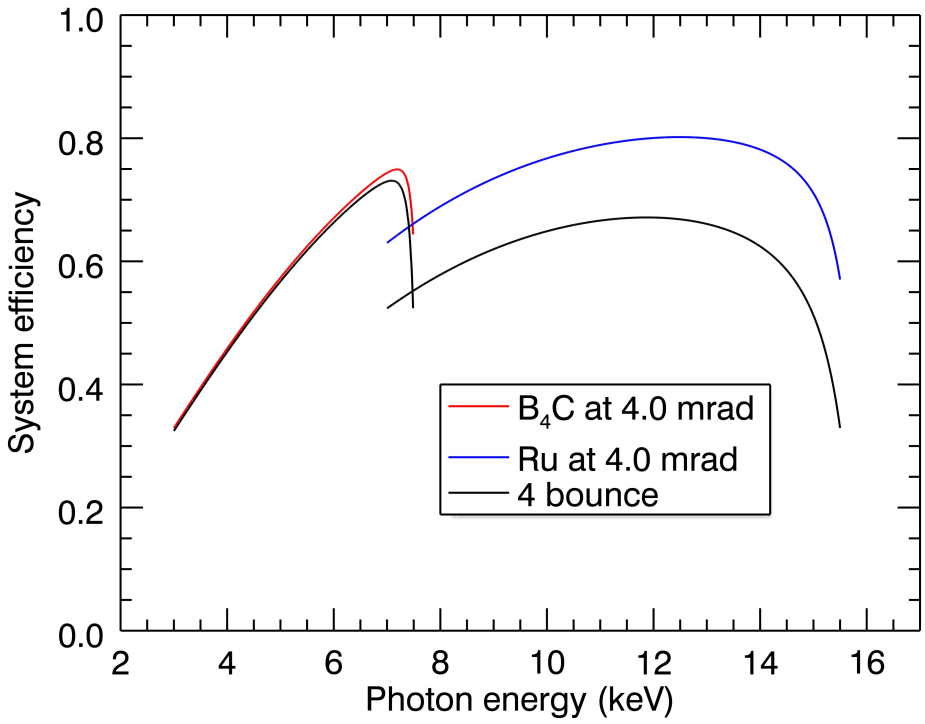

Figure 6.10: Effects of coating and collection angle on efficiency of the KB system. Note that surface errors are not included. Also, while we intend a four-bounce system for the micrometre-scale focus, the two-bounce system is also shown to demonstrate the reduction due to total reflectivity compared to the reductions due to aperture.

Table 6.4: Coating material specifications

Photon energy range	Material	Thickness
3 keV to 7 keV	B_4C	50 nm
7 keV to 16 keV	Ru	50 nm

Examining the reflectivity curves of various relevant optical materials, it is clear that the limit to the steepness of the grazing angle (and, hence, the aperture) is set by mirror efficiency. (That is, a poorly reflecting mirror will absorb too much of the FEL beam and will not only reduce the transmission of the instrument, but will also likely cause damage and fail). As stated, the grazing angle and the length of the mirror limit

the obtainable clear aperture. The effects of this limit on clear or numerical aperture have strongly influenced our decision to investigate metal coatings that have higher critical angles than the traditional low-Z materials used at existing FEL facilities [112]. The calculated reflectivity curves for 5, 10, and 15 keV, as a function of angle, for two candidate materials are shown in Figure 6.11. Specifically, we considers boron carbide (B_4C) and ruthenium (Ru). As previously stated, ablation and thermal damage of the optical coating are of more concern than reflectivity efficiency.

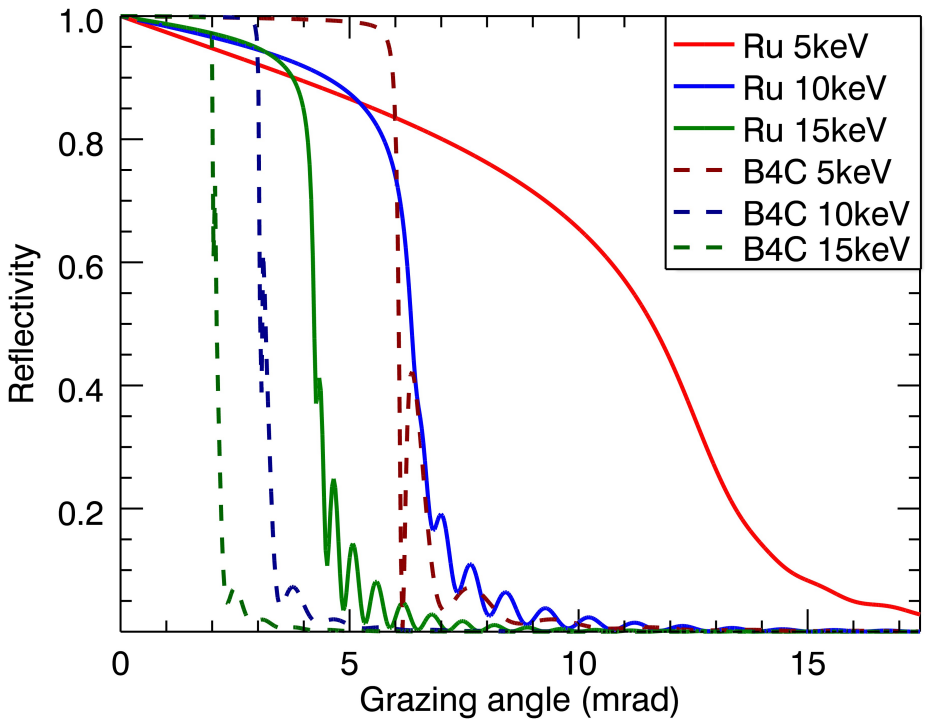

Figure 6.11: Reflectivity of 50 nm thin coating of B_4C and Ru as a function of angle for 5, 10, and 15 keV photon energies

While metal coatings provide higher critical angles (which implies a larger aperture for the same mirror length) and a less sharp loss of reflectivity at the critical angle, this comes at the cost of stronger absorption at the surface of the optics. Ru is a prime candidate in this energy range due to its high critical angle, its common use in synchrotron optics, and because it has no absorption edges over the working range of the beamline. However, for FEL radiation, one has to be careful to consider that the peak dose, as a function of fluence and angle, remains below the damage threshold. Figure 6.12 on the next page and Figure 6.13 on page 62 show the calculated response for a Ru-coated optics as a function of pulse power and angle.

It shows that the Ru coating is likely to survive 1 mJ pulses; however, if the FEL is operated in saturation > 1 mJ, then one may expect to exceed the estimated damage threshold of 0.7 eV/atom. To resolve this issue, experiments have also been conducted by the SPB group and collaborators at SACLA in Japan on various optical materials, including both B_4C and Ru. Current experimental dose estimates show that 0.7 eV/atom is very likely a conservative estimate[4], and one can expect a significantly higher threshold before damage occurs.

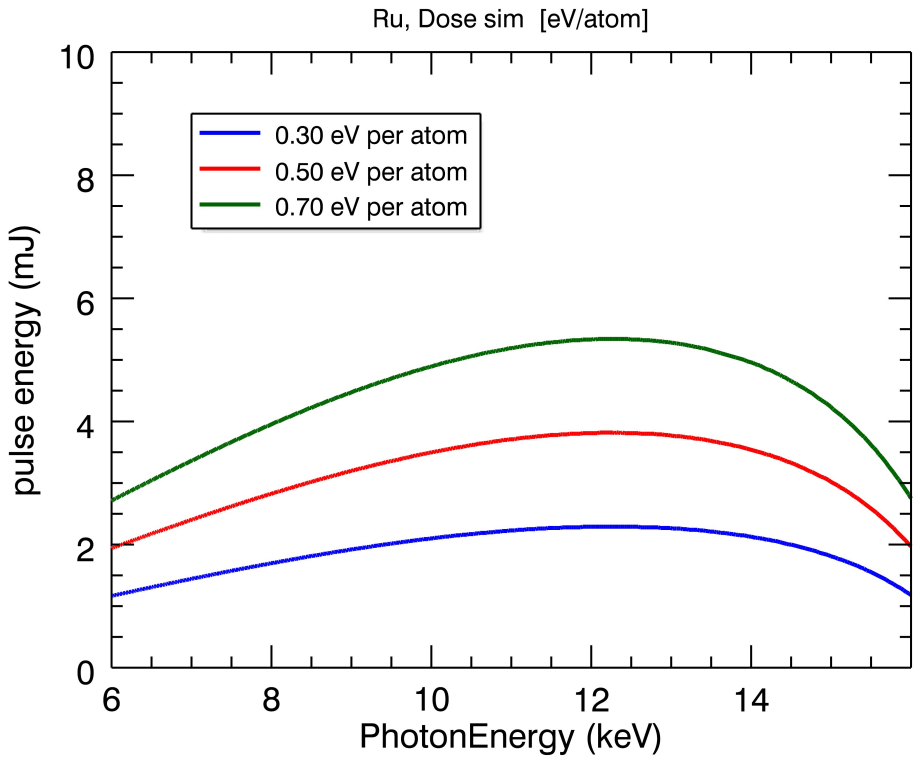

Figure 6.12: Expected dose levels for a Ru-coated optics at 4 mrad grazing angles. These simulation look at the peak of a 2D Gaussian pulse striking a grazing surface. No heat transfer or fast cooling is taken into account.

[4] A. Aquila et al., unpublished data, analysis in progress.

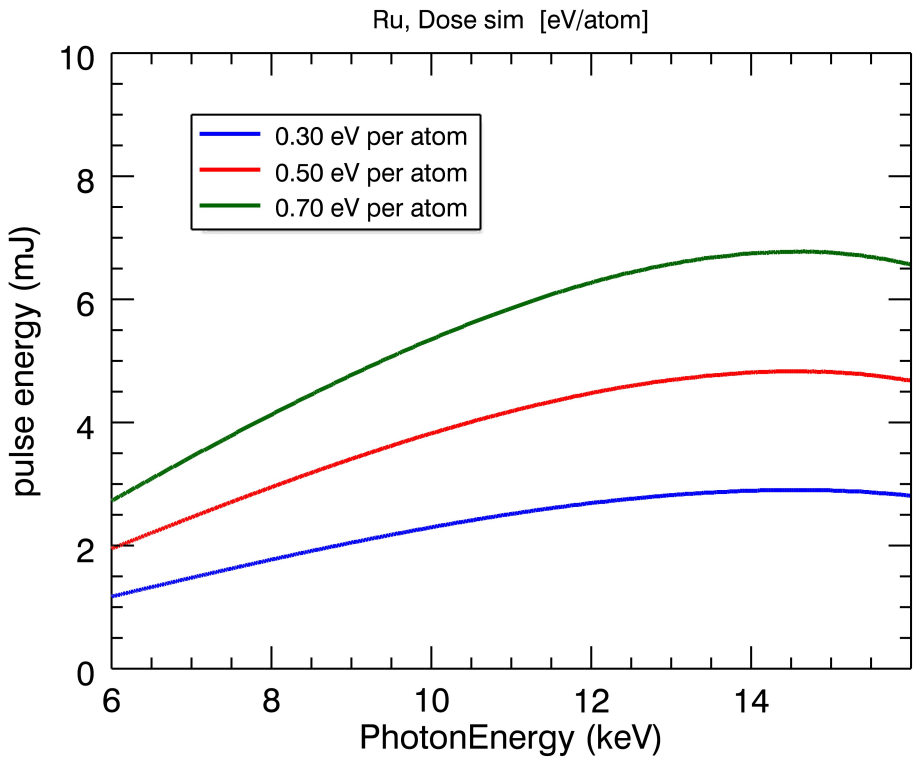

Figure 6.13: Same dose calculation as shown in Figure 6.12 on the preceding page, except shifting to 3.5 mrad grazing angles: changes in reflectivity and photon density are associated with the different grazing angle.

Simulations on the heat load of the Ru coating has also been conducted and are shown in Figure 6.14 on the next page. The concern is that while each pulse deposits only 50 µJ of energy in the mirror, the very small beam sizes and the pulse train bunch pattern might cause the surface to significantly deform or melt by the end of the pulse train, especially as the absorption length of Ru is significantly less than that of B_4C. Calculations for B_4C have also been conducted; however, as the reflectivity is nearly 99%, up to its critical angle, simulations have shown that the optics is expected to be far from melting or ablation/evaporation damage limits in the cases we envisage for the SPB instrument.

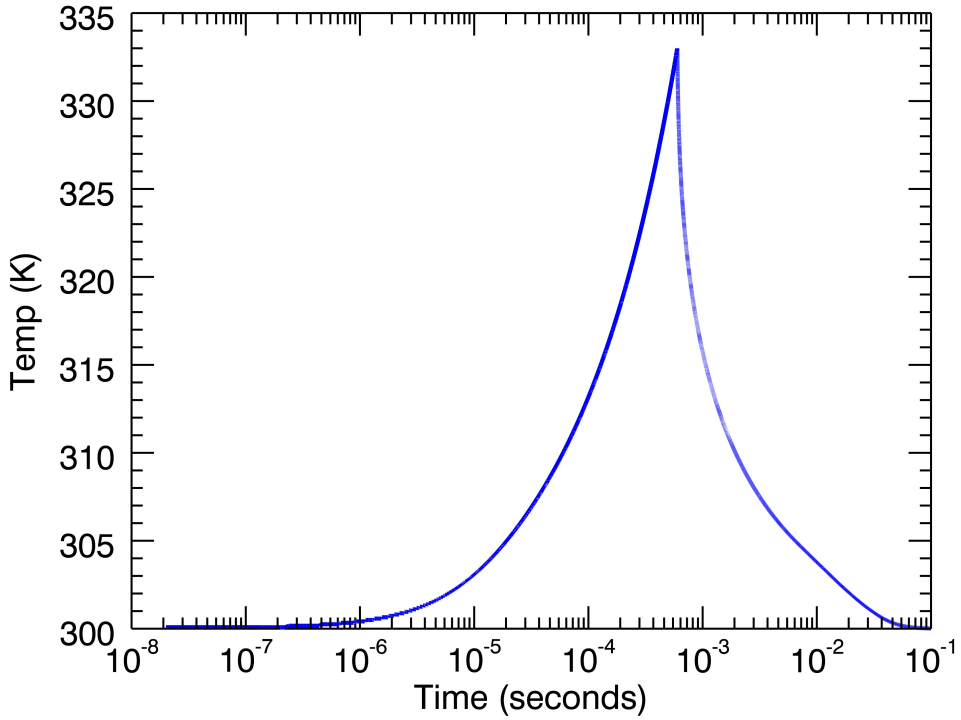

Figure 6.14: 3D finite difference analysis of the heat transport through the optical layer and the substrate. The plot shows the maximum temperature of the Ru, as a function of time, averaged over the centre 15 mm by 0.5 mm area. The simulation used a 50 nm thin Ru coating on a Si substrate. The Si voxels were of 32 mm^3 and covered the entire optics. The simulation used a full pulse train of 2700 pulses of 1 mJ. While the heat reached a peak of 33°C above room temperature, it cools back down within the 10 Hz pulse train window (time shown on a logarithmic scale). This assumes a heat bath surrounding the optics.

With these considerations in mind, we aim to balance the reflectivity with the desire to obtain a large clear aperture. We have chosen two coatings—each with the same working angle but different working energy ranges: B_4C for the lower photon energy range of 3 keV to 7 keV with a 4 mrad grazing angle, and, for the higher energies between 7 keV and 16 keV, we will use a Ru coating operating at 4 mrad (see Table 6.4 on page 59). The motivation for these two coatings is a balance between collecting a larger lateral dimension while keeping the cutoff from moving to a lower photon energy.

Figure 6.1 on page 48 shows the aperture, expressed as the number of σ collected, as a function of photon energy for both coatings. Figure 6.10 on page 59 shows the

overall system efficiency for a two-mirror and a four-mirror system including collection aperture. It is of note that at lower photon energies the drop in system efficiency between a two-mirror system and a four-mirror system is negligible, as reduction in numeric aperture is the dominant effect. Suppression effects for the third-order harmonics for the two- and four-mirror systems are shown in Figure 6.15.

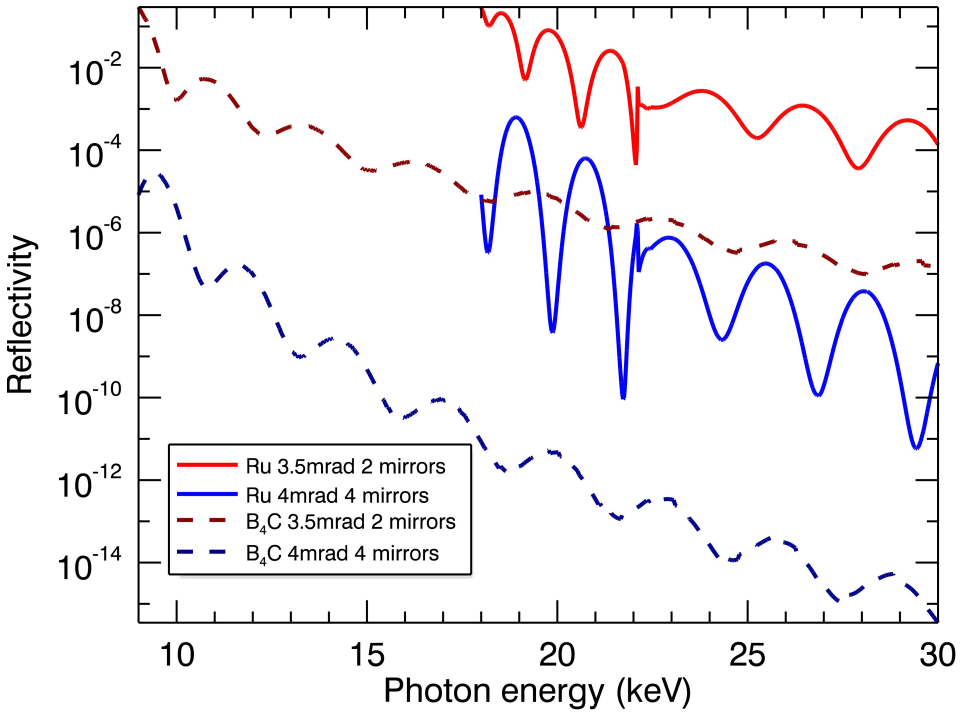

Figure 6.15: Rejection of the third-order harmonic for the FEL. Note that, while the 4 mrad angle is sufficient to remove effectively all harmonics, the 3.5 mrad coating may have a small fraction transmitted when working at the lower limit of the photon energy range of each coating.

Also of manufacturing importance, sputtered coatings are often of a density that is less than bulk density. This has the effect of reducing the critical photon energy for a given working angle. While the deposition parameters (sputtering gas pressure, voltage, target power, and so on) can change the materials' density and microstructure, they also have an effect on surface roughness. Based on measurements [92] of sputtered B_4C, the density is 2.2 g/cm^3. For Ru, we estimate 90% of the bulk density, which is typical for sputtered metals. However, a critical-angle measurement with a witness coating piece needs to be checked with a Cu K_α source to ensure proper density estimates and film thickness.

Regardless of optical design, the general specification to the power spectral density (PSD) of the mirror shape (slope/figure errors and roughness/finish), the mirror lengths, incidence angle, and mirror coatings are independent of the detailed shape of the mirror. These are the limiting factors in optical performance.

6.3.3.3 Roughness, slope errors, and height errors

The PSD will determine the mirrors' performance: focal spot size and wavefront. While the exact fractal dimension of the shape can be specified, often by the maximum slope error, r.m.s. height error as well as mid and high spatial frequency roughness are typically specified. Due to the long working distance of 26 m, the slope errors need to be better than 0.02 µrad [19]. Using the Strehl relation for the high spatial frequencies, roughness needs to be better than 1 nm r.m.s., while the Marechal criterion gives a required figure error of less than 0.6 nm r.m.s. for a four-bounce optical system [86]. If we include the two HOMs in the total mirror count, then there is an increase in specification of the r.m.s. height error. If the roughness specification is set to what is standard for current state-of-the-art synchrotron optics, this factor of 2.5 reduction has the effect of reducing the deterioration of peak intensity, caused by roughness, by 85% (a 10% loss compared to a 1.7% absolute loss in peak efficiency per optics). We note that the slope error specification will only reduce the peak brightness by 0.1% (per optics); however, slope errors cause the beam distribution and tails to deviate from a Gaussian profile and distort the wavefront. As the primary goal of our beamline is imaging, any deviation can potentially complicate reconstructions. A table of specifications is given in Table 6.5.

Table 6.5: Figure, slope error, and roughness specifications for all SPB optics

Error category	Spatial frequency	Corresponding wavelength	Specification
High spatial frequency	0.5 μm^{-1} to 50 μm^{-1}	20 nm to 2 µm	$<$ 0.4 nm r.m.s.
Mid spatial frequency	100 m^{-1} to 0.5 μm^{-1}	2 µm to 10 mm	$<$ 0.25 nm r.m.s.
Figure (slope errors)	1 m^{-1} to 100 m^{-1}	10 mm to 1 m	$<$ 20 nrad r.m.s.
Residual height errors	1 m^{-1} to 100 m^{-1}	10 mm to 1 m	$<$ 0.5 nm r.m.s.

6.3.3.4 Substrate

We plan on implementing single-crystalline Si as the substrate material. This is in line with the substrates used in the HOMs [87]. Each substrate, for both flats and KB

optics, will have dimensions of (L×W×H) 1000 mm × 120 mm × 70 mm. There will be two coating stripes on each substrate with clear-aperture dimensions of (L×W) 950 mm × 30 mm. However, it is noted that the polished surface needs to extend to the edge of the optics along the length direction. This is to minimize aberrations if the FEL beam extends slight outside of the clear aperture. It is also worth noting that, based on these dimensions and a bulk silicon density of 2.329 g/cm^3, each substrate will weigh 19.6 kg.

6.3.4 Environmental considerations

Due to the small micrometre-scale focal spot sizes and long lever arm working distance of the KB optics, special consideration needs to be paid to vibrations, drifts, and other environmental considerations, in particular to ensure that the optics vibrate less than the beam width.

6.3.4.1 Vibrations

Ground vibrations at the European XFEL experiment floor site have been measured[5] in the 1 Hz to 100 Hz range and have been shown to have moderate vibrations on the order of less than 50 nm r.m.s.[6]. However, events with 700 nm peak-to-valley displacement have also been recorded with displacement velocity on the order of 30 µm/s. This means that care must be taken to ensure that the focal spot does not vibrate or move a significant fraction of the beam width. There are three types of motion of concern: when the KB chamber moves or is displaced as a solid unit (lateral motion), when the floor beneath the KB chamber is uncorrelatedly tilting the optics (angular motion), and when the two mirrors of the KB system resonate or vibrate against each other (higher-order bending and torsion modes). Each of these motions has a different resonance frequency and deviates the beam in different ways.

As is stated in the *Technical Design Report: X-Ray Optics and Beam Transport* [87], we request the eigenfrequencies of the optics vacuum chamber be at a frequency larger than 90 Hz and mounted on a stiff granite block. This will reduce the higher-order bending and torsion modes. The four-bounce KB design also reduces the sensitivity to angular motion by a factor of 20 over that of a conventional two-mirror KB. If the optics have a 2 µm motion across the 2 m chamber, there is a 1 µm deviation in beam height and no angular deviation. Also, for the horizontal KBs, any angular motion does not displace the beam, but causes a slight aberration to the

[5] XFEL.EU TR-2012-005
[6] This depends on the time of day due to events in the local area.

wavefront and a very small focal shift. Supporting the chamber on a stiff granite block should reduce vertical chamber motion as well.

6.3.4.2 Thermal loads and cooling

It is also of note that, while local heating is of concern and has been discussed, the overall thermal power that needs to be removed from the optics is minimal. This is due to the focusing optics being downstream of the horizontal offset mirrors, and, as such, the only radiation incident upon the mirrors is the lasing component of the X-ray beam. With a full pulse train of 2700 pulses operating at 10 Hz, and 5 mJ per pulse, with 10% absorption, we estimate no more than 13.5 W of power absorbed on each mirror. This is for near-worst-case working conditions: running deep into saturation of the FEL, worse than expected reflectivity, and at a full bunch train. While this is a minimal amount of heat, we do see the possible need to actively cool the mirrors, or mirror mounts, to maintain thermal stability. This is due to concerns over heat deformation and heat buildup changing the focusing properties of the optics. Existing single copper blade designs—from synchrotrons, placed in indium–gallium liquid troughs along the back or side of the optic—should suffice. These designs give great thermal conductivity without distorting the optics by touching them. While the optics hutch is also thermally stabilized, it will be ideal to monitor the position and temperature of the optics to minimize drifts.

6.3.4.3 Drifts

The micrometre-scale KB chambers are located on the experiment floor to minimize long- and slow-scale motion drifts >1 s. This should have a dramatic effect on reducing long-scale drifts between the experiment and the micrometre-scale KB optics. However, the accelerator, undulators, and HOMs are located in the transport tunnel, which is on an independent concrete floor. These drifts cannot be compensated easily. However, as stated in the vibration section, due to the four-bounce KB design, pointing drifts of up to 1 µrad produce less than 1 µm shifts in beam position[7]. This stability means that we need to worry only about very long timescale drifts, such as shift or daily cycles. These drifts can be corrected with the planned diagnostic screens and tools.

6.3.4.4 Vacuum requirements

The FEL environment is a highly ionizing one; all volatile components[8] in the vacuum system will become free radicals. It is of great concern that these ions will bond or conduct surface chemistry on the mirrors' surface. This degradation effect needs to be minimized to preserve the lifetime of the mirrors and coatings. Based on the fact that the optics hutch is located 10 m upstream of the differential pumping, it is expected that the base pressure will be low, on the order of 10^{-9} mbar or better. However, as there is limited space usable for vacuum pumping, the two mirror chambers will each require ports for their own ion pump.

6.3.5 Mechanical mounting and motion

Ideally, we would like to control all six degrees of freedom for each of the four optics that make up the micrometre-scale focusing system, for example by mounting each optic on a six-axis strut-like device. The travel ranges of each degree of freedom will vary. The longest axis will be the axis that moves the mirrors laterally to the beam. This motion will be required to intersect both coatings and also move far enough to remove the optics from the beam path (120 mm). As each KB mirror combination is coupled, it is possible to remove a few degrees of freedom in each pair by mechanically linking the optics. However, this tradeoff is only acceptable if it provides better mechanical and vibrational stability for the KB system. Also of interest is whether a mechanical support system can be devised that minimizes cross talk such that moving one motor only moves a single spatial or rotational degree of freedom and not one of each at the same time. We would also like to utilize as many out-of-vacuum motors as possible to keep the vacuum system as clean as possible. However, vendor-provided finite element analysis (FEA) of the chamber will then be required, as feed-through-style bellow motors are susceptible to drifts caused by deformation of the vacuum chamber under different atmospheric conditions (for example, if the temperature or pressure in the optics hutch changes).

It is also required that the mounting attempt to prevent any sag, torsion, or bending motion especially when moving the optics. It has been shown that just mounting the optics can cause a change in the profile of the optics surface [86]. The motion of the optics mount should therefore not place any additional static stress on the optics.

The optical angular placement accuracy of the system needs to be on the order of the slope errors of 20 nrad. As the optics are 1 m long, this corresponds to a

[7] However, such drifts will change the focal position as the focal position is also sensitive to angle.
[8] Water vapour and hydrocarbons are the main concerns.

linear placement accuracy of better than 20 nm. Depending on the style and type of mounting, this linear placement accuracy might require a higher tolerance in motion and step size. It is recognized that moving a 19.6 kg mirror to much better than 1 µm is a difficult challenge. Another difficult mounting challenge is the inverted flat mirror. This mounting must minimize sag and other distortions due to the inverted nature of the mounting.

6.3.5.1 Alignment tools

Along with the mechanical and static design of the chamber, additional ports for glass windows and electronic feed-throughs will need to be implemented. These ports serve three important functions. The first is to provide a method for temperature measurements without touching the optical surface via an IR thermometer. For alignment purposes, we intend to add YAG clipping screens to see if we are passing along the ideal optical path. These screens may be looked at using off-axis long-range microscopes. The YAG screens might require linear motion control to prevent clipping during operation. Additionally, the X-Ray Optics and Beam Transport group is currently investigating utilizing pentaprisms for laser interferometery as discussed in their optics TDR [87]. If this technique proves successful, we plan to also implement it on our optics.

6.3.6 Future upgrades

As described earlier, an ideal future upgrade for the micrometre-scale focus is to replace the two flat mirrors with adaptive-optics bendable flats. These flats will allow for the correction of low spatial frequency aberrations, from the KBs or HOMs, or longitudinal motions of the source point. Piezoelectric adaptive mirrors have been demonstrated to correct the wavefront and obtain diffraction-limited spots in beamline geometries of similar length [62] [61]. These optics are also being investigated for the HOMs with the downstream mirror planned to contain four rows of piezoelectric transducer actuators along the sides of the mirror substrate. The adaptive optics are to remove aberrations in the beam and make it more uniform/Gaussian, and could also improve peak brightness of the focus depending on any aberrations in the KBs, HOMs, or flats themselves. Of critical note is the system's coherence length [20] of 20 mm[9]. If the pushers can modify the surface of a spatial frequency of this order, then all aberrations and distortions caused by slope errors could be removed.

Another use of these deformable flats is to provide an adjustable numerical aperture

[9] Calculated for 10 keV photon energy, 2.51 µrad divergence, and 4 mrad incidence angle.

to enable specific focal spot sizes. For example, at 4 keV, the critical angle of B_4C is 7 mrad, meaning that the focal spot for the micrometre-scale optics could be reduced from the present diffraction-limited size of 4.14 µm to 2.36 µm, just through increasing the aperture (through tilting the mirror) and correcting for the resultant aberrations. We currently implement a 4 mrad angle for the B_4C coating to cover the energy range of 3–7 keV, which is limiting at the lower energies of this range. That is, if we used higher angles, we would in principle achieve a smaller focus; however, the beam would then become aberrated as the KB shape is not designed to work at the higher angle. An adaptive optics would, in principle, be able to bend, thus correcting the curvature of the outgoing wavefront and producing an aberration-free, diffraction-limited spot of nearly half the size (which is four times the flux density).

6.3.7 Simulations

We have simulated the wave field of our micrometre-scale focusing optics using a phase screen to simulate phase distortions from our KB optics from the ideal wavefront. The phase screen correlates to the expected height errors and is based on real 800 mm superpolished optic flats after a smoothed fifth-order polynomial was subtracted. These height errors were then scaled to produced a slope errors of 50 nrad, which is the current technology employed at the CXI instrument at LCLS, and used in the phase screen. The beam was propagated for an approximately 1 Å wavelength, 12 keV, a clear aperture of 3.8 mm, which is the expected clear aperture of the beamline, and a divergence of 2.19 µrad FWHM. Figure 6.16 on the next page shows the focal plane and the expected intensity distribution line-outs. Figure 6.17 on page 72 shows the same wave field propagated 1 m out of focus into the far field[10]. These simulations also include expected slope errors. It is difficult to take into account the effects of the two flat mirrors in the micrometre-scale KB system; hence, we have also conducted additional simulations on a worst-case scenario, which can be found in Section C.3, “Wavefront simulations”.

[10] over 150 Rayleigh lengths

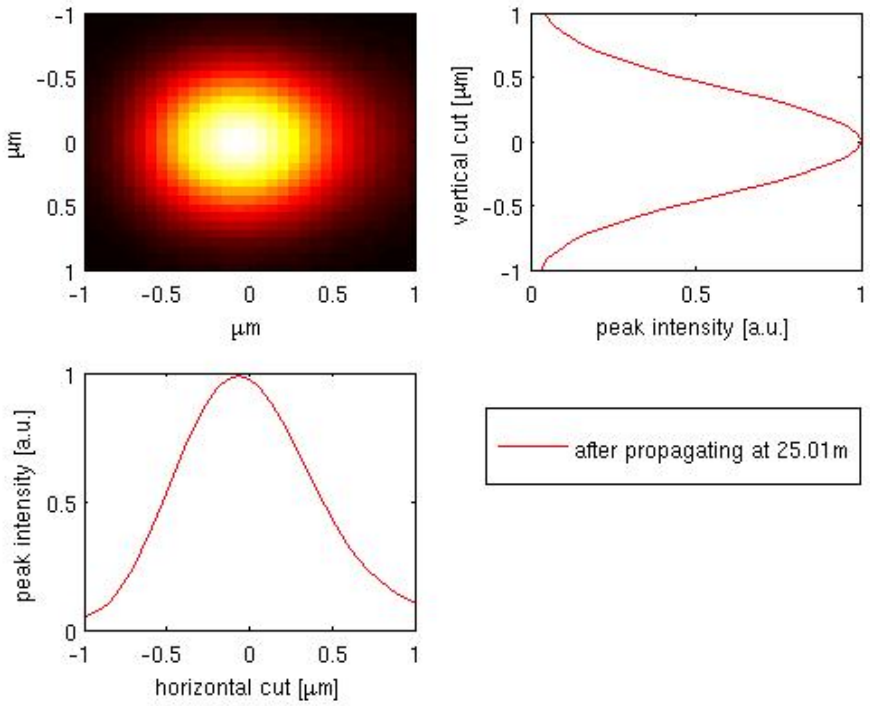

Figure 6.16: Intensity profile from a wave propagation for the micrometre-scale focus using an approximate, expected height error profile

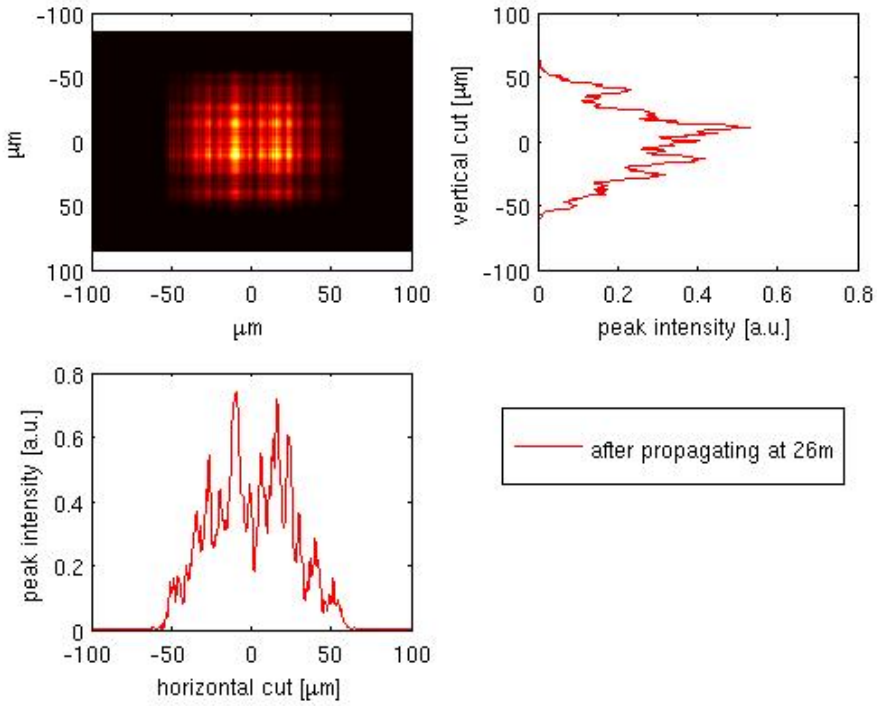

Figure 6.17: Same intensity profile from a wave propagation for the micrometre-scale focus, propagated 1 m out of focus into the far field

6.3.8 Metrology

Due to the high precision and demanding nature of the SPB micrometre-scale optics, we envision numerous metrologies, both in acceptance testing as well as commissioning characterization. As accurate knowledge of the wavefront may be necessary for many planned experiments, there may be a need for regular characterization of the focal properties along with possible shot-to-shot monitoring of the reflected wavefront. We list here the possible tools we plan on implementing to characterize our optical focus.

6.3.8.1 Nanometer optical component measuring machine

One of the most successful tools in characterizing the KB optics used on our sister beamline, CXI at LCLS, was a nanometre optical component measuring machine (NOM) [86]. This technique is useful for determination of gravitational sag as well as residual nanometre height and slope changes due to mounting of the optics. We

anticipate implementing this technique as an inspection tool prior to acceptance of the mirror.

6.3.8.2 Atomic force microscopy

Atomic force microscopy (AFM) is critical to obtain information on the high spatial frequencies of the mirror's figure. This technique provides information on the r.m.s. roughness of the optical surfaces. Roughness is important as the higher the roughness, the lower the specular reflectivity. This technique is implemented on a small subsection of the mirror often before and after coating of the mirror's surface. While the roughness does not contribute to the overall shape of the focal spot, it does contribute to the efficiency due to increasing out-of-focus scattering. This metrology is also planned in the acceptance testing.

6.3.8.3 Interferometry

To obtain information on the mid spatial frequencies, interferometric methods, such as white-light interferometry and Zygo optical profiling, are often used. These techniques provide PSD data that falls in the spatial frequency gap between the NOM and AFM techniques. Along with the afore-mentioned techniques, interferometry will enable good cross checks and overlap of the PSD for acceptance testing.

6.3.8.4 Wavefront measurements

A wavefront monitor is envisioned to ideally provide an online tool for daily feedback of the focal spot shape. For a full description of envisioned possibilities, see Section 7.2.5, "Wavefront".

6.3.8.5 Knife edge tests

Knife edge tests are often used to characterize the 1 µm focal spot sizes at SACLA [112]. While such tests do not give a full wavefront image of the beam, they can be easy to implement with a diode and a precision-controlled micrometre-thick wire. However, this method is also limited to attenuated beams and is often inaccurate in representing the beam tails. While these limitations make it impractical to consider as a real-time alignment tool, it could be useful as a cross check during commissioning.

6.3.8.6 Visible wavefront measurements

We intend to utilize a visible-light laser at the front of the optics hutch for alignment purposes. While the initial purpose of this laser is to coarsely align the optics with the known path of the FEL, we intend to use a single-mode (transverse electromagnetic mode, $TEM_{0,0}$) laser with the possibility of changing the divergence/collimation and utilizing various apertures. This laser could then be used as a visible-light wavefront sensor via a Talbot setup. While the visible limits of this approach mean that we only probe the longer spatial frequencies of our optical system, it can facilitate alignment without the use of the FEL and also be utilized to monitor long-term changes in the optics' sag/distortion. If we intend to upgrade to deformable flat mirrors, this technique will also enable the coarse shape alignment of the flats.

6.4 100 nm–scale focusing optics

This section describes the 100 nm–scale KB focusing system. To prevent duplication and to highlight the differences between the two focusing systems, all descriptions and discussions that are identical between the micrometre-scale and 100 nm–scale focusing systems will be omitted for this section.

6.4.1 Layout

The layout of the 100 nm–scale KB optics is a traditional two-mirror system that reflects in the same directions as the four-bounce micrometre-scale KB system (for example, positive *Y* or up, and negative *X* or away from the control room direction). Figure 6.7 on page 55 and Figure 6.8 on page 56 show the position and deflection of the 100 nm–scale KB system.

6.4.2 Optical specifications

As can be seen in Table 6.6 on the next page, the 100 nm–scale KB pair are nearly a factor of 10 closer to the focal point than the micrometre-scale focus. This has little effect on the requirements for slope errors, height errors, and roughness; however, it does have a significant impact on the nominal radius of curvature.

Table 6.6: Geometric distances and angles for the 100 nm–scale KB focusing system

Parameter	Value	Unit
Distance source to KB1 (a)	929.615	m
Distance KB1 to focus (b1)	3.0	m
Distance KB2 to focus (b2)	1.9	m
Distance end of KB2 to focus (c)	1.4	m
Length of KB1	1000 (d1)	mm
Clear aperture KB1	950	mm
Length of KB2 (d2)	1000	mm
Clear aperture KB2	950	mm
Incidence angles (θ)	3.5	mrad

6.4.2.1 Coatings

We plan to implement the same optical coating for the 100 nm–scale KB system as we do for the micrometre-scale KB optics. However, as seen in Table 6.7, the 100 nm–scale KB optics have a much steeper radius of curvature, and the maximum angle at the closest edge of the optics extends to 4 mrad. Due to these steeper angles, we plan to implement both materials in the KB at 3.5 mrad instead of having either coating at 4 mrad. This is to ensure that the edges of the KB optics do not exceed the critical angle, especially for the B_4C coating. Figure 6.18 on the next page shows the approximate efficiency for the 100 nm–scale KB system.

Table 6.7: KB figure parameters for 100 nm–scale focus

Parameter	KB1 (@3.5 mrad)	KB2 (@3.5 mrad)	Unit
KB plane	*XZ*	*YZ*	–
Major axis	466.3075	466.3075	m
Minor axis	0.185	0.147	m
Radius of curvature (centre)	1.72	1.09	km
Maximum incidence angle	3.84	4.08	mrad
Minimum incidence angle	3.24	3.11	mrad

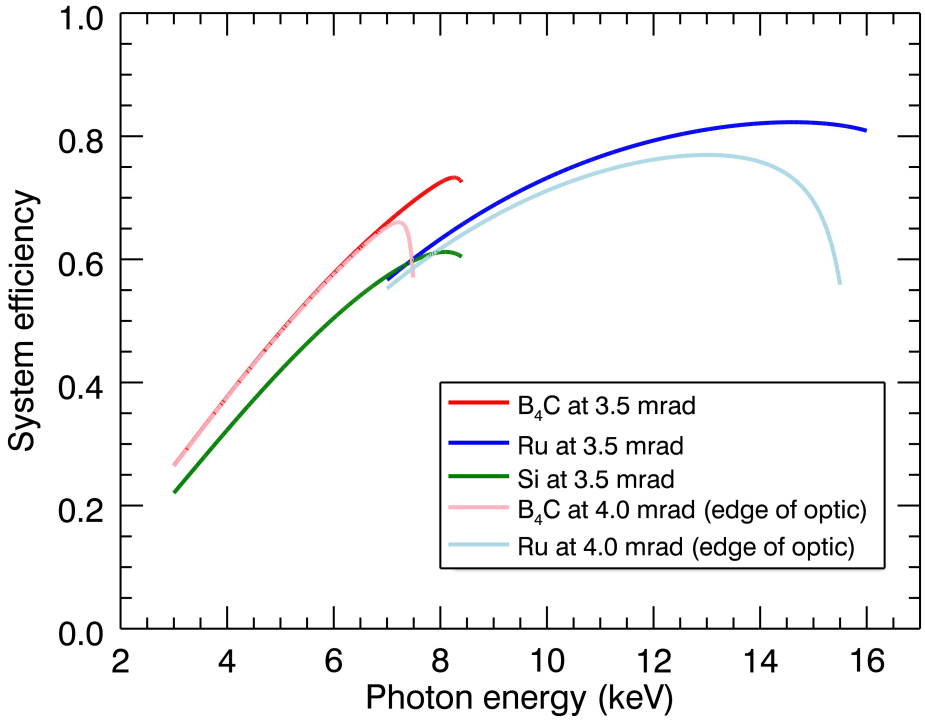

Figure 6.18: Effects of coating and collection angle on efficiency of the 100 nm–scale KB system. For comparison purposes, the uncoated Si substrate is also shown up to its critical angle. The gains in efficiency using B_4C are evident. Also shown is the efficiency at the edge of the optics. This is to locate the critical angle for the coating. Please note that surface errors are not included.

6.4.2.2 Optic figure

As the 100 nm–scale KB optics is much closer to the interaction region, the optics has a steeper curve than the micrometre-scale KB optics. We have adjusted the incidence angle to limit the steepness of the edge of the 100 nm–scale KB to be 4 mrad. The shape of the optics is describe in Table 6.7 on the preceding page.

6.4.3 Environmental considerations

6.4.3.1 Vacuum requirements and contamination

It is worth noting that the 100 nm–scale KB is very close to the sample chamber and only 1.4 m from the interaction region. As the majority of materials we will be experimenting on will involve either water and hydrocarbons, we will need to isolate the 100 nm–scale KB from the experiment chamber either with a diamond window valve or with a strong differential pumping aperture. This requirement is to protect the coating from building up carbon or significant oxide layer. A discussion of the limits and possibility of using a thin diamond vacuum window can be found in Section C.2, "CVD diamond windows", while the use of a short windowless differential pumping aperture is discussed in Appendix A, "Vacuum concept and design". It is of note that, if we utilize a windowless design, we will require a magnetic-bearing or other vibration-free turbomolecular pump on the differential and possibly the KB chamber.

6.4.3.2 Vibrations and drifts

As we would prefer the FEL beam to drift, from shot to shot, by less than a beam width, we recognize the need to minimize vibrations and drifts. As the KB chamber is close to the interaction region, the major contributor to drifts is thermal drifts. While the hutch has been specified to maintain thermal stability to better than 0.1°C, we expect this to vary with the number of people in the room and possibly the time of day. To compensate for these effects, we plan to enclose the KB chamber in a thermal shroud. This should maintain thermal stability to much better than 0.1°.

As the 100 nm–scale KB chamber is located in the experiment hutch, we anticipate the need to reduce vibrations in the entire hutch. To facilitate this, we intend to implement a vacuum manifold with the roughing pumps (which cause the most vibrations and noise) located outside of the experiment hutch, as described in Appendix A, "Vacuum concept and design". While this will reduce the vibrations, if we incorporate turbo pumps on the KB chamber, the differential pumping aperture, or both, there will be a possible vibration source located very close to the KB system. To reduce vibrations, these pumps can be isolated, via bellows and possibly the adjustment of the turbo pumps' speed, if it is evident that they are close to a resonance of the KB system; or magnetic-bearing turbo pumps can be used. Even with these precautions, we will still require a stiff granite block to mount the KB optics on. Due to size and motion requirements of the sample chamber, the 100 nm–scale KB will be on the same block as the sample chamber.

6.4.4 Mechanical mounting and motion

6.4.4.1 Required motion

One important aspect to note in the mechanical design of the KB chamber is shown in Figure 6.8 on page 56. Due to the motion of the FEL beam when the micrometre-scale KB is inserted and removed, the 100 nm–scale KB does not need to change position to prevent beam clipping. This is useful to maintain the rough alignment between experiments and reduces the time necessary to align when switching between the two focal sizes. Also worth noting is that this enforces certain size requirements on the entrance and exit ports for the KBs; however, a DN63 port is sufficient to admit the FEL in all conditions.

The ability to accurately position the KB mirrors is critical to the operation of the SPB instrument. We require all six degrees of freedom: three positional and three rotational for each of the mirrors. This may be implemented using a hexapod or other six-axis strut-like device. We would prefer a motion that minimizes cross talk between the motors, such that moving one motion does not change more than one degree of freedom. A similar setup to the motion control used in the micrometre-scale KB would be ideal to provide common backup parts, such as motors. As we only have two mirrors instead of four, a single large chamber is sufficient for both mirrors in this case.

6.5 Refocusing option

Adding a parasitic refocused nanocrystallography instrument has the potential to increase the throughput of the SPB instrument. This has been explicitly proposed for incorporation into the SPB experiment hutch by the SFX user consortium led by Henry Chapman of CFEL, DESY. As the refocused beam does not need to have the same beam quality, due to the nature of crystallography, compound refractive lenses (CRLs) become ideal candidates from a geometric and thermal point of view. While the SFX collaboration will ultimately contribute to the design of the optics layout for the refocusing options, we give a general overview assuming the use of CRLs.

6.5.1 Geometric layout

Ideally, the CRLs would be used in a 1:1 refocusing geometry with the primary SPB focal position used as an intermediate focus. The total system length will be four times the focal length and will need to fit into the 14 m between the SPB focus and

the beam stop. Critically, the spent FEL beam also requires space after the SFX instrument to expand; otherwise, there is the very real possibility of melting or ablating the beam stop with the small beam. A refocusing geometry other than 1:1 may be better suited for our beam stop. It is also envisioned that the SFX sample chamber and these refocusing optics will be situated on our instrument rail (see Figure B.1 on page 174). This allows for greater flexibility if a slightly larger secondary focal size is required. Also, as the CRLs come in unit number and are chromatic, this propagation direction flexibility ensures that the sample can always be in the focus. It is clear that this geometry becomes difficult, if not impossible, when the SPB instrument is operating with the 100 nm–scale KB focus. At 8 keV, the FWHM beam will be of the order of 6 mm in size at the entrance pupil of the CRLs depending on rail position. Current CRL technology is limited to around 2.8 mm in diameter. However, the micrometre-scale KB focus produces a smaller-sized beam at the entrance of the CRL lens stack.

Table 6.8 gives estimates on the number of pulses the lens stack can sustain without being heated by 300°C, which is half the recrystallization temperature of 600°C. Table 6.8 also gives an estimate on the number of lenses needed to achieve the 2.5 m focal length necessary for a 1:1 focus that fits within the constraints outlined above, and appraises the system efficiency for the given N lenses.

Table 6.8: CRL thermal thresholds and efficiencies, based on a 300°C thermal rise using a 1 mJ pulse energy

Photon energy [keV]	FWHM at entrance pupil [mm]	No. of pulses to raise temp. by 300°C	No. of lenses for a 2.5 m focus	Estimated system efficiency
5.0	0.79	900	3	28.1%
8.0	0.56	2100	8	55.3%
12.0	0.41	> 2700	17	79.5%

6.5.1.1 Number of CRLs

To calculate the maximum number of required lenses in Table 6.8, the formula $N = R/2f\delta$ was used, where N is the number of lenses, f is the focal length, and δ is the real part of the index of refraction. It is worth noting that δ is wavelength-dependent.

6.5.1.2 Thermal loads

For Table 6.8 on the preceding page, each lens was assumed to be made of Be and have a inner radius, R, of 200 µm and a $2R_0$ diameter of 1.5 mm. The thinnest point of the lens was assumed to be 30 µm thick. These specifications are currently near the limit of mass-produced lenses. For the thermal absorption simulation, a Gaussian beam was propagated through a single thin lens, and the system efficiency and the energy absorbed as a function of radius were calculated.

It is assumed that the material is thinner than the absorption length so that the energy deposited as a function of length remains constant. While this is always true in the centre of the lens, it is not true at the outer edges of the lens at energies below 8.0 keV. This effect needs to be investigated. However, modelling at both high photon energy and low photon energy gives similar results: the majority of the energy is absorbed in the centre of the lens; even though this location is the thinnest, it has the highest intensity.

To calculate the thermal rise as a function of position, the linear heat capacity is used:

$$\Delta T(x,y) = \frac{n \cdot A(x,y)}{m(x,y) \cdot C_p} \tag{6.3}$$

where ΔT is the rise in temperature, C_p is the heat capacity, n is the number of pulses, $A(x,y)$ is the absorbed energy, and $m(x,y)$ is the mass of the needle of volume $D \cdot (\Delta r)^2$.

It is also worth noting that the peak irradiance is 2.68 W/cm^2 at 8 keV, assuming a 10 fs pulse. More analysis needs to be conducted on the ablation threshold of Be in this energy and wavelength regime (that is, estimates on the amount of energy absorbed per atom needs to be worked out).

7 Instrument diagnostics

Chapter authors: K. Giewekemeyer[1], G. Borchers[1], A. Aquila[1], J. Buck[2], J. Grünert[2], C. Ozkan[2], A.P. Mancuso[1]

7.1 Diagnostic requirements

This chapter gives an overview of the essential parameters of the FEL source, as well as the planned beam geometries for different use cases at the SPB instrument. Following that, the resulting diagnostics requirements are discussed, both as an overview and in more detailed subsections considering each parameter to be monitored separately.

For an overview of essential simulated source parameters at the SASE1 undulator for representative photon energies in the operating range of the SPB instrument (3–16 keV), see Table 5.2 on page 42.

7.1.1 Beam geometries

An overview of the most important components at the SPB instrument with their respective coarse positions along the beam propagation direction is given in Figure 7.1 on the following page and Figure 7.2 on page 83. In addition, the beam geometry (FWHM size and lateral offset from the axis of the beam exiting the tunnel) is indicated for every component.

Representative configurations for the beam geometry at the SPB instrument are summarized in Table 7.1 on page 84. The beam size generally decreases with increasing photon energy, so that smallest and largest beam sizes are covered by the cases considered here. The beam offset and direction depends on the different focusing optics used and their configuration.

Note that the beam size substantially varies depending on photon energy and optical configuration, e.g. at the position of the beam dump between 0.8 mm (at 15 keV) and 24.5 mm (at 3 keV). The beam offset (as defined in Chapter 6, “X-ray optics layout”)

[1]Scientific Instrument SPB group (WP84), European XFEL GmbH, Albert-Einstein-Ring 19, 22767 Hamburg, Germany
[2]X-Ray Photon Diagnostics group (WP74), European XFEL GmbH, Albert-Einstein-Ring 19, 22767 Hamburg, Germany

is only a function of the focusing mirror incidence angle. This is 3.5 mrad for the 100 nm–scale focus and 4 mrad for the micrometre-scale focus. At the beam dump, the offset can be as large as about 100 mm.

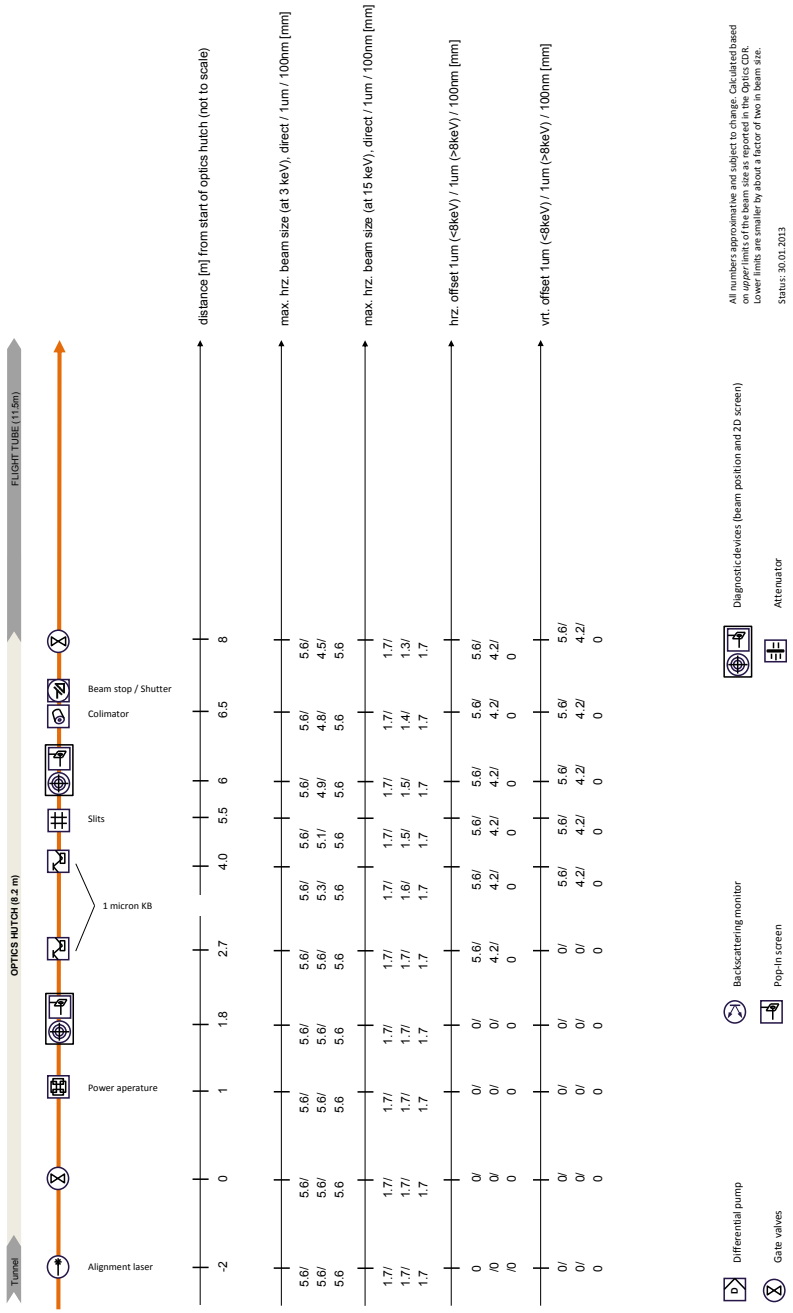

Figure 7.1: Schematic of the SPB instrument's optics hutch, including maximum beam size and offset for different longitudinal positions and photon energies

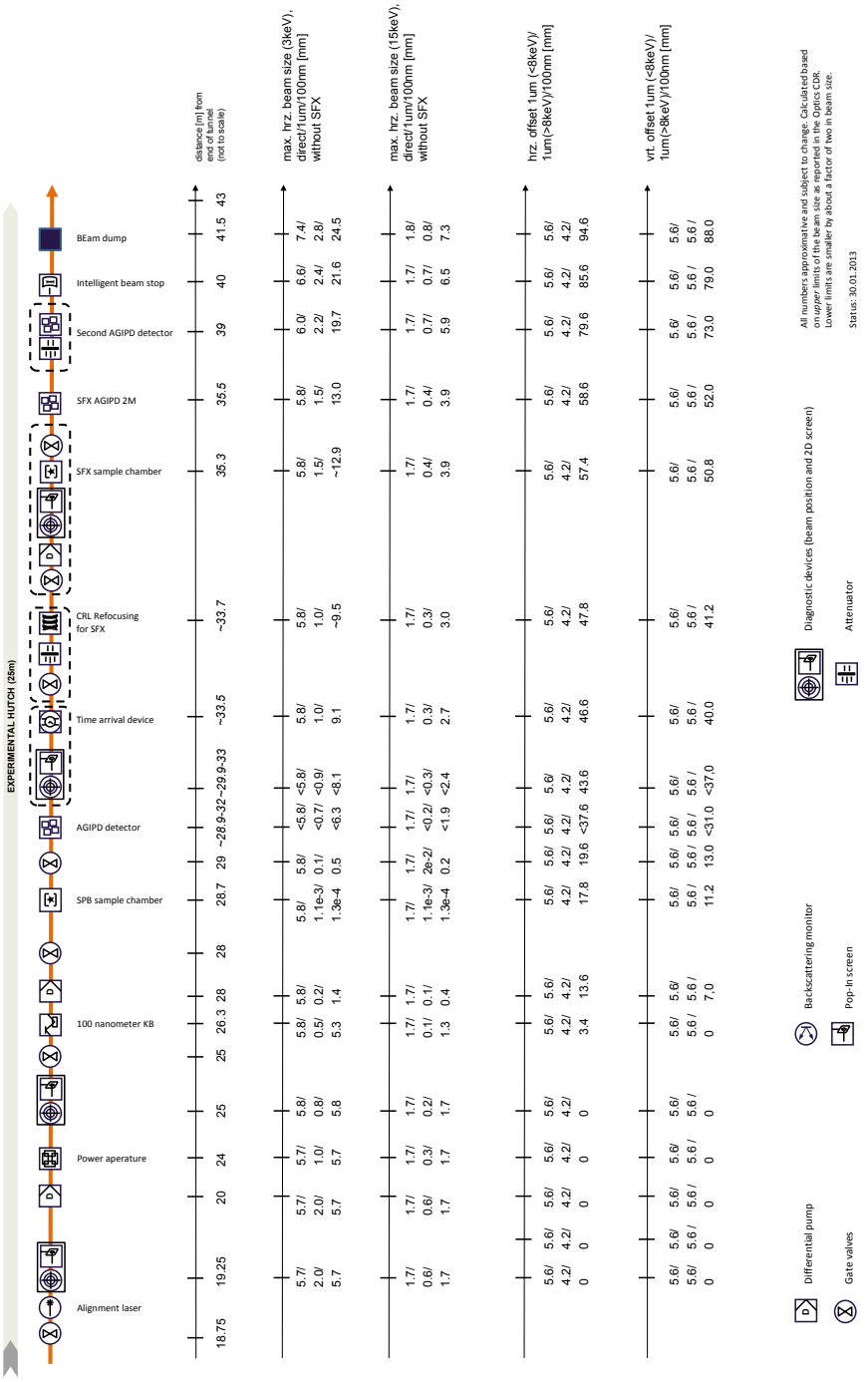

Figure 7.2: Schematic of the SPB instrument's experiment hutch, including maximum beam size and offset for different longitudinal positions and photon energies

When the SFX apparatus is being used, the beam size is further influenced behind the refractive refocusing lenses (not indicated in Figures 7.1 and 7.2). For a

Table 7.1: Typical optical configurations of the SPB instrument that span its whole energy range. Some cases are technically feasible (black circle) or very difficult or not feasible (white circle), due to damage thresholds on optics, geometrical restrictions, or both.

Beam energy	3 keV	8 keV	18 keV
Micrometre-scale focus without SFX	•	•	•
Micrometre-scale focus with SFX	○	•	•
100 nm–scale focus without SFX	•	•	•
100 nm–scale focus with SFX	○	○	○
Direct beam	•	•	•

magnification of $M = 1$, the SPB focus is imaged onto the SFX focus and is followed by a diverging beam that impinges onto the beam dump. However, the distances over which it diverges are smaller by about 2 m compared to the case without refocusing for nanocrystallography, which has important ramifications on the maximum radiation tolerance of the beam stop (see Section D.7, “Beam dump”).

7.1.2 Overview of diagnostic requirements

Essential parameters of the photon beam that—depending on the actual experiment—need to be continuously monitored at the SPB instrument are listed in Table 7.2 on the next page. Beyond the expected parameter range, the table also shows the requisite measurement accuracy and other requirements, such as the rate at which the measurement needs to be performed and the number of required devices at the beamline. Note that not all of these quantities need to be monitored for every experiment, every shot, or both.

In the table, the key quantities are in *italicized letters*. Due to the bunch structure of the European XFEL beam, the required measurement rate is either very high (4.5 MHz), to keep up with the 220 ns pulse separation within a pulse train, or low (10 Hz), i.e. equal to the train repetition rate. If the required rate is equal to the pulse repetition rate within a pulse train, all relevant diagnostic devices need to be synchronized with the FEL beam on a nanosecond timescale in order to not take data during the large “silent” bunch separation gaps of ca. 100 ms.

Table 7.2: Most important physical quantities of the photon beam, their respective ranges, and required measurement accuracies at the SPB instrument. Quantities for which monitoring is *mandatory* for beamline operation and experiments are *italicized*. Note that the 2D intensity profile and position of the beam change substantially along the optical axis. Unlike for the other parameters, several devices are required for these beam parameters to be measured.

Physical quantitiy	**Range**	**Accuracy**	**Absolute scaling?**	**Rate**	**Non-destructive?**	**No. of devices**	**Generally required?**	**Remarks**
Pulse energy	1 nJ – 1 mJ	< 1% (rel.) / < 10% (abs.)	Yes*	4.5 MHz	Yes	2	Yes	* 1 absolute / 1 relative
2D intensity profile	∅ of beam (FWHM): 0.1 mm (15 keV) up to 25 mm (3 keV) Parallel beam offset: up to 5.6 mm	–	No	10 Hz	No	5	Yes	1 non-destructive device at 4.5 MHz would be very beneficial (intelligent beam stop)
Beam centroid position	Ca. 2.5 x beam size	–	Yes	4.5 MHz*	Yes	5	Yes	* Rate depending on actual fluctuations
Central wavelength	3–15 keV	0.5 BW	Yes	4.5 MHz*	Yes	1	Yes	* Rate depending on actual fluctuations
Bandwidth (BW)	0.05% (keV) – 0.3% (3 keV)	0.1 BW	Yes	4.5 MHz*	Yes	1	Yes	* Rate depending on actual fluctuations
Wave-length spectrum	3–15 keV	0.01 BW	Yes	4.5 MHz	Yes	1	No	Potentially required for certain crystallography experiments
Phase aberrations in focal plan	TBD	TBD	Yes	10 Hz – 4.5 MHz*	Yes	1	No	Potentially required for certain coherent-imaging experiments * Rate depending on actual fluctuations
Relative delay optical, X-ray pulse	–	–	Yes	4.5 MHz	Yes	1	No	Pump–probe experiments only
Pulse duration	ca. 1–200 fs		Yes	4.5 MHz	Yes	1	Yes	–

7.1.3 Detailed diagnostic requirements

7.1.3.1 Pulse energy

The expected range for the SASE1 pulse energy in saturation, within the relevant photon energy range of the SPB instrument, starts at around 15 µJ (0.02 nC bunch charge, 15.5 keV photon energy) and increases up to ca. 3.7 mJ (1.0 nC bunch charge, 2.76 keV photon energy). Covering this energy range as the core range, the pulse energy monitor should also be able to measure pulse energies down to ca. 1 nJ and up to ca. 10 mJ with high enough precision (< 10% systematic measurement uncertainty [35]).

For experiment analysis and control, it is mandatory to measure the pulse energy on a shot-to-shot basis, i.e. with a rate of 4.5 MHz, and in a non-destructive way.

It is not necessary that each pulse energy monitor provide the pulse energy on an absolute scale. If relative monitors can be calibrated to a single absolute monitor, this information is sufficient. In order to calibrate attenuators and to measure the efficiency of optical components, it is necessary to have several pulse energy monitors throughout the beamline—which may be calibrated against an absolute measure.

7.1.3.2 Beam centroid position

Monitoring the beam centroid position at different locations along the beam path is very important for (real-time) control of the beam direction and potential beam loss. By design, the lateral beam centroid position varies within a certain nominal range, which can be as large as about 9 cm at the beam stop position when switching from the micrometre-scale focus to the the 100 nm–scale focus. In addition, the beam position and direction are subject to random fluctuations arising from the SASE process and optics vibrations. Lastly, long-term drift, mostly due to thermal effects, has an influence on positioning and pointing. By frequent monitoring of such drift effects, one could in the future—depending on the complexity of the alignment process—set up an active feedback system for beam positioning.

The field of view of a beam position monitor (BPM) should be chosen so that random beam position fluctuations are limited to the active sensor area. Positioning fluctuations on the order of 10–20% of the beam size (as observed at LCLS for 14 GeV electron energy [2]) are accounted for, though expectations are this will not be as severe at the European XFEL. The actual accuracy of the position monitor should be two orders of magnitude better, i.e. within 0.1–1% of the beam size. In

order to accurately measure the beam centroid position, the field of view should be at least twice the size (FWHM diameter) of the beam. For monitoring positioning drift, however, the field of view should be slightly larger still. Unlike fluctuations and drift, the large nominal changes in the lateral beam position for different optics configurations need to be followed by translations of the beam position monitors. In order to determine the beam position with respect to a fixed reference, e.g. the photon beam exiting the tunnel at a given set of parameters, those translations should be well-calibrated with respect to a fixed reference beamline coordinate system.

Ideally, all beam position monitors should be shot-to-shot, non-destructive devices. While this is feasible for the gas-based beam position monitors located in the photon tunnel (see below), space (and cost) constraints lead to the choice of solid-state-based position monitors in the optics and experiment hutch. Even though these may be able operate at 4.5 MHz, they almost certainly have an impact on the beam wavefront, the degradation of which cannot be tolerated for certain experiments. In addition, damage thresholds of BPM materials can prevent the devices being used at full repetition rate for certain beam sizes and energies.

As indicated in Figure 7.1 on page 82 and Figure 7.2 on page 83, beam position monitors and imaging screens are planned at six different locations along the beam path (excluding SFX), after entering the experiment hall. The respective beam size and offset values, in addition to the corresponding required accuracies, are given in Table 7.3.

Table 7.3: Geometrical beam parameters and resulting approximate field of view (FOV) and positioning accuracy requirements for BPMs throughout the beamline. Note that the beam size has been estimated based on the upper size limit of the source, as given in [88]. The range of beam positioning fluctuations to account for has been estimated based on experimental values from LCLS.

BPM name and approximate distance from start of optics hutch [m]	Beam diameter FWHM[1] [mm]	Beam position fluctuations [mm]	Beam offset (x/y) [mm]	Required BPM FOV [mm^2]	Required 0.1% – 1% FWHM resolution [µm]
BPM_1_OH / 2	1.7–5.6	0.2–1.1	0–5.6	11.2 x 11.2	2–20
BPM_2_OH / 6	1.5–5.6	0.2–1.1	0–5.6	11.2 x 11.2	2–20
BPM_1_EH / 19	0.6–5.7	0.06–1.1	0–5.6	11.4 x 11.4	0.6–6
BPM_2_EH / 25	0.2–5.8	0.02–1.2	0–5.6	11.6 x 11.6	0.2–2
BPM_3_EH / 30–33	0.1–8.1	0.01–1.6	0–26	16.2 x 16.2	0.1–1
BPM_4_EH / 40	0.7–21.6	0.1–4.3	0–79.0	43.2 x 43.2	0.7–7

Note that beam positioning monitors can be based on different technologies, so that not all devices need to be identical. The BPM close to the beam dump, for example, may be much simpler than those upstream, i.e. it may be designed as a beam loss monitor only.

7.1.3.3 2D intensity profile

The 2D intensity profile of the FEL beam needs to be monitored at different locations along the beam path mainly for two reasons. Firstly and most importantly, for optics and slit alignment, it is necessary to have visual feedback of the beam shape and position. Secondly, under certain circumstances, it is possible to reconstruct the complex wavefront, i.e. especially the phase aberrations of the FEL beam, after its intensity is known in two or more planes along the beam propagation direction [69].

For alignment of the KB mirrors, it is helpful to be able to monitor not only the focused beam but also the partly focused and unfocused components of the beam. This is especially true for alignment of the four-mirror system that is envisioned for producing the micrometre-scale focus. Therefore, the field of view of the imagers should generally be larger than that of the beam position monitors. On the other hand, it is sometimes desirable to image the internal structure of the beam itself so that, in general, a variable field of view and resolution are required for the 2D intensity imagers.

Expected beam diameters, position fluctuations, and offsets—together with the required field of view, resolution[2], and number of pixels within the beam FWHM—are summarized in Table 7.4 on the facing page. The required field of view has been calculated so that the maximum offset plus the maximum beam width is always smaller than the screen (except for the screen S_4_EH). In practice, the resolution will probably not be as high, i.e. an imaging system with a pixel pitch of 10 µm will be very good for most cases and sufficient for the limiting cases.

For alignment purposes, a frame rate of 10 Hz is sufficient. In this case, there is furthermore no need for a non-destructive device. There should ideally be one device, preferably at the position of the intelligent beam stop, i.e. in the far field of the focus, which allows measurement of the 2D beam intensity at (nearly) the full frame rate of 4.5 MHz. This should make it possible to monitor shot-to-shot fluctuations in the beam profile, which can influence diffraction data collected from a sample, especially in coherent X-ray diffractive imaging (CXDI) experiments. The fast 2D imager does not need to be non-destructive to the beam as it is only followed by the beam dump, but it

[2] Assuming a resolution of 1% of the beam FWHM

Table 7.4: Geometrical beam parameters and resulting approximate field of view (FOV) and positioning accuracy requirements for 2D intensity monitors (screens) throughout the beamline. Note that the beam size has been estimated based on the upper size limit of the source, as given in [88].

Screen name and approximate distance from start of optics hutch [m]	Beam diameter FWHM[3] [mm]	Beam position fluctuations [mm]	Beam offset (x/y) [mm]	Required FOV [mm^2]	1% FWHM resolution [µm]	Pixels in FWHM at 10 µm pixel pitch
S_1_OH / 2	1.7–5.6	0.2–1.1	0–5.6	15 x 15	17	170–560
S_2_OH / 6	1.5–5.6	0.2–1.1	0–5.6	15 x 15	15	150–560
S_1_EH/ 19	0.6–5.7	0.06–1.1	0–5.6	15 x 15	6	60–570
S_2_EH / 25	0.2–5.8	0.02–1.2	0–5.6	15 x 15	2	0–580
S_3_EH / 30–33	0.1–8.1	0.01–1.6	0–26	35 x 35	1	10–810
S_4_EH / 40	0.7–21.6	0.1–4.3	0–79.0	45 x 45	7	70–2160

needs to be especially radiation-hard in order to cope with high pulse repetition rates. This requirement could be met by a transparent device.

The dynamic range of the imagers should be around 12 bit, which is sufficient for alignment purposes. For wavefront reconstruction, a dynamic range as high as possible should be chosen, i.e. preferably higher than 12 bit. As this requirement usually compromises the possible frame rate and inter-frame distance, it will be necessary to find a compromise between speed and dynamic range.

7.1.3.4 Wavelength spectrum

In addition to a full wavelength spectrum, a number of summarizing parameters can be used to describe the spectroscopic characteristics of an FEL beam. These are the mean photon wavelength $\bar{\lambda}$, its experimental uncertainty $\sigma(\bar{\lambda})$, its relative jitter, and the bandwidth BW = $\Delta\lambda/\lambda$.

For the scientific methods applied at the SPB beamline, which are mainly nanocrystallography and variants of CXDI, it is often sufficient to know only the aforementioned summary parameters instead of the entire spectrum for each pulse. Before we discuss the limits up to which this holds, we summarize the expected spectroscopic parameter values at the European XFEL.

A summary of expected parameters for the SASE1 undulator radiation as derived from simulations is given in Table 5.2. The expected bandwidth BW for the SASE1 radiation from the European XFEL falls into a range of BW = 0.06–0.28%, depending on electron beam energy (between 14 and 17.5 GeV), electron bunch charge

(between 0.02 and 1.0 nC) and photon energy (between 2.76 and 15.5 keV) [83]. As a general rule, BW increases with decreasing pulse length and decreasing bunch charge, but BW is not expected to increase beyond 0.3% for the predicted beam parameters in the photon energy range of the SPB beamline (ca. 3–16 keV). The expected bandwidth is substantially larger for soft X-ray energies, but this does not concern the SPB beamline, which will not be able to access energies below 3 keV.

The relative wavelength jitter is expected to be about twice the relative electron energy jitter [82], i.e. within about 0.1–0.2% for the short-pulse/low-charge mode and within about 0.05–0.1% for the long-pulse/high-charge mode.

For a practical comparison, we note that LCLS typically provides femtosecond photon pulses with a FWHM bandwidth of BW = 0.2–0.5 % at 8.26 keV photon energy (“hard” X-rays), and values in the range of 0.2–1.0% at 0.5–2 keV (“soft” X-rays) [26, 89]. These values are reached for “standard-mode” bunch charges of 0.15 nC (0.25 nC) in the hard (soft) X-ray regime. The FWHM pulse lengths for these parameters are in the range of 50–250 fs in the hard and 70–400 fs in the soft X-ray range, respectively [89]. In addition, an ultrashort, low-charge mode with 20 pC bunch charge and pulse durations of 5–10 fs [3] is available. At 8.3 keV, this mode has a typical FWHM bandwidth of about 0.24% [3]. The measured relative LCLS wavelength jitter (FWHM) is on the order of 0.24% for hard X-rays and 0.47% for soft X-rays [26].

In conclusion, the measured bandwidth and wavelength jitter of LCLS are usually slightly higher than expected for the European XFEL. Note, however, that all values stated here for the European XFEL are based on simulations and may differ from experimental values, especially during the commissioning phase of the facility.

We now discuss the spectroscopic requirements of the two main methods to be applied at the SPB instrument, namely CXDI and nanocrystallography.

Coherent X-ray diffractive imaging (CXDI) In CXDI, the lens of a conventional (optical or electron) microscope is replaced by a numerical reconstruction scheme. As a consequence, there are usually no optical elements between the sample and the detector. The data that is recorded on a 2D detector, in the far field of the sample exit wave, is a diffraction pattern with no or little resemblance to the original object. To obtain an image of the sample (exit wave), the diffraction pattern is inverted numerically, which is achieved by iterative algorithms that apply known constraints both in real and Fourier space to the current iterate of the exit wave [74]. For this numerical inversion to be feasible, the diffraction pattern must be sampled in each coordinate direction on a fine enough pixel grid, so that—from an information

theoretical perspective–all information contained in the continuous diffraction pattern is contained in the discrete measurement on a pixellated detector.

According to the Shannon theorem, one requires at least two sampling points per speckle in the diffraction pattern, which eventually leads to the following relation between the linear extension N (number of pixels) of the detector in one coordinate direction and the number of (full-period) resolution elements N_{res} [57]:

$$\frac{N}{N_{\mathrm{res}}} = 2\sigma. \tag{7.1}$$

Here, σ is the linear sampling ratio in the corresponding coordinate direction with $\sigma = 2$ (two samples per speckle) as the minimum required sampling ratio. σ increases for increasing sample–detector distance and thus decreasing solid angle covered by the detector. For practical applications, usually $\sigma \geq 4$ is required.

Furthermore, let D denote the largest linear extension of the sample in a direction perpendicular to the beam and let us assume without loss of generality that the sample is oriented in the beam so that its largest linear extension lies in the plane perpendicular to the beam. The half-period resolution, i.e. the width of a pixel in real space, is then given by [1]

$$\Delta r = \frac{D}{2N_{\mathrm{res}}}. \tag{7.2}$$

For an assessment of the required specifications of the incoming X-ray beam, it is important to note that the wave field's bandwidth sets a lower bound to the size of a resolution element Δr. In other words, conventional CXDI (without taking the finite bandwidth of the wave field into account) can tolerate only a certain amount of polychromaticity for a successful reconstruction. For larger bandwidths/smaller resolutions, speckles of different sizes overlap. The minimum (best) resolution achievable for a certain bandwidth BW and sample size D is related to the interaction of rays originating from opposite edges of the sample in the plane perpendicular to the beam: if the path difference between those rays becomes smaller than the maximum path difference due to BW, the diffraction pattern deviates from an ideal (monochromatic) diffraction pattern. This argument leads to the relation [1]

$$\Delta r = \frac{D}{2} BW \tag{7.3}$$

for the minimum achievable resolution. Combining this with Equation 7.2 leads to the simple relation

$$BW = \frac{1}{N_{\mathrm{res}}} \tag{7.4}$$

for the maximum allowable bandwidth, given a certain number of resolution elements in a coherent diffraction experiment. N_{res} in turn depends on the size of the sample and the experimental sampling ratio, leading to

$$BW = \frac{2\sigma}{N}. \tag{7.5}$$

The main imaging detector that is foreseen for the SPB beamline is a 1 Mpx AGIPD device, i.e. the number of pixels in each coordinate direction is roughly given by $N = 1000$. With $\sigma = 4$, which will only be used for large particles such as viruses or cells, this gives $N_{\mathrm{res}} = 125$ resolution elements within the object and a maximum tolerable bandwidth of BW = 0.8%. Note that this is higher than any value that is expected for the SPB beamline.

Having established a relatively loose restriction of CXDI on the bandwidth of the incoming radiation at the SPB beamline, we now turn to the required repeatability of the mean photon wavelength and the needed accuracy in measuring it. Note that in plane-wave CDI—given the experimental illumination is ideal enough that it does not have to be taken into account—the wavelength of the incoming radiation never enters the analysis explicitly. On the contrary, the reconstruction of the object transmission function or projected electron density distribution is obtained by a successive operation of discrete Fourier transforms (which do not require any geometrical arguments) and algebraic operations on the real and Fourier space amplitude. Even though the important real-space support constraint—defined by the size of the object—is needed, this can be deduced on a relative scale with respect to the field of view from the autocorrelation of the object. Of course, as in any microscopy method, one needs to set a scale to the final images obtained. But, in the given situation, it is only the accuracy of this scale that is affected by the experimental uncertainty in the mean wavelength. The analysis process is not affected by an inaccurately known centre wavelength. The repeatability of $\bar{\lambda}$ becomes important when many measurements on equivalent objects are combined, such as in 3D CDI of randomly oriented reproducible particles [54]. If, however, the fluctuating mean wavelength is known to an accuracy better than the bandwidth, the obtainable resolution is not affected substantially. For a more precise estimate, let $\delta(s)$ denote the relative uncertainty in quantity s and $\sigma(s)$ its absolute uncertainty. The relative uncertainty in the largest relevant sample length scale, its diameter D, is given as

$$\delta(D) = \sqrt{\delta(\bar{\lambda})^2 + \delta(z)^2} \tag{7.6}$$

as can be verified though applying laws of Gaussian error propagation on the

real-space pixel size $\Delta x = \bar{\lambda} z/(N\Delta X)$. For a linear sampling ratio of 4, one can have at most 250 half-period resolution elements in the sample in each coordinate direction. Consequently, one requires at most

$$\delta(D) \geq \delta(\bar{\lambda}) \geq 1/250 = 0.4\% \tag{7.7}$$

accuracy in the knowledge of the mean wavelength. This, however, is essentially (up to a factor of 2, which depends on the definition of a resolution element) the same limit as given for the allowable bandwidth. In other words, the required accuracy of the measured mean wavelength $\bar{\lambda}$ for each shot is at least half the required maximum bandwidth. The repeatability of $\bar{\lambda}$ can be worse if it is known to the accuracy stated above.

Summarizing, the maximum tolerable bandwidth of BW = 0.8% for CXDI experiments at the SPB beamline is higher than any value expected under realistic conditions. Even if a 4 (2×2) Mpx detector becomes available, this value reduces to BW = 0.4% for a practical sampling ratio of 4. If the observed bandwidths at the European XFEL will be higher by a factor of 2 than the expected values in an extreme scenario, one only barely reaches the limiting bandwidth of BW = 0.4% for a 4 Mpx detector. Such a high bandwidth, however, is mostly only expected in the low-charge/short-pulse mode of the European XFEL. This mode is probably only required for the ultrahigh resolution needed for single biomolecules. Due to their smaller size, these, however, usually have larger sampling ratios for practical experimental geometries. This relaxes again the requirements on the bandwidth.

Nanocrystallography (NX) We now turn to the second main method to be applied at the SPB instrument, nanocrystallography (NX) [18, 11, 76]. Having been introduced and applied very successfully in recent years, NX is still a very new technique. It deviates substantially from conventional crystallography not only in the experimental procedure (thousands of crystals vs. few crystals, differing sample delivery techniques, etc.), but also in the analysis of the obtained diffraction patterns (unknown vs. known crystal orientation, differing treatment of partial reflections, etc.).

Therefore, the optimal requirements of NX, especially regarding the bandwidth and an accurate knowledge of the wavelength spectrum, are not entirely known at present and have yet to be fully established [107].

Bragg spots in crystallography are never ideal point-like objects, but fill a volume of finite size in reciprocal space. This is predominantly caused by sample effects such as mosaicity and finite sample size. The latter is easily seen to be important for NX

as the crystals vary in size from $D \approx 200$ nm and $D \approx 2$ µm [18], much smaller than the size of typical crystals studied at synchrotrons. As a consequence, crystal size is a major source of Bragg peak broadening in NX, caused by the large extent of the crystal shape transform.

Conversely, the crystal diffraction measurement involves probing reciprocal space in a very small volume, i.e. the shell of the Ewald sphere, whose thickness depends on the bandwidth and angular divergence of the incoming radiation. As a result, the "sensitive" volume of the measurement may be too small to fully cover a Bragg spot that is enlarged by the crystal shape transform and mosaicity. Therefore, the structure factor usually cannot directly be deduced from the measured intensity of a Bragg spot, but can only be inferred after a correction for the aforementioned effects is applied during the combination of the measured thousands of diffraction patterns with random crystal orientations [48, 18].

This correction is more difficult in NX compared to conventional crystallography, as e.g. for very small crystals, the shape transform extends over the whole space between Bragg peaks and leads to side maxima, which are prone to be misinterpreted as reflections by automatic indexing schemes [48, 18].

To assess the probability of partial reflection measurement, consider e.g. the first successful NX experiment [18, 48]. Here, a mean wavelength $\bar{\lambda} = 0.69$ nm with a bandwidth of 0.1% was used. This leads to a finite thickness of the Ewald sphere on the order of

$$|\Delta\nu| = \left(\frac{1}{\lambda_1} - \frac{1}{\lambda_2}\right) \approx \frac{\Delta\lambda}{\bar{\lambda}^2} = \frac{BW}{\bar{\lambda}} \approx 1.45\ \mu\text{m}^{-1}. \tag{7.8}$$

Here, λ_1 and λ_2 denote the lower and upper wavelength limit of the beam. The speckle size of a reflection, due to the size of crystals used between $D \approx 200$ nm and $D \approx 2$ µm [18], varies between $1/D \approx 0.5\ \mu\text{m}^{-1}$ and $1/D \approx 5\ \mu\text{m}^{-1}$. As a consequence, it is very likely that reflections are only partially recorded. It could thus even be desirable to have a wider bandwidth, so that a full reflection is recorded with a single shot. On the other hand, a precise knowledge of the actual (smaller) bandwidth and the spectrum could potentially help to make the analysis process more precise [107].

In conclusion, a bandwidth on the order of 0.1% is compatible with NX as demonstrated in the initial (relatively low-resolution) experiment. However, a smaller bandwidth and therefore a more accurate measurement of it may be useful for non-conventional NX variants.

The mean wavelength $\bar{\lambda}$ is an essential quantity to crystallographic analysis as it

determines the radius of the Ewald's sphere that is used to sweep diffraction space. Therefore, it should be measured with an accuracy to at least 10% of the bandwidth. It is possible to extract the mean photon wavelength from a measurement of the energy loss in the electron bunch in the undulator; however, it is very desirable to have an independent measure based solely on the photon beam [107]. This could be used as a way to calibrate the electron beam measurements, which could then be used for the shot-to-shot characterization of $\bar{\lambda}$.

Note that the measurement of the bandwidth also allows for an estimate of the pulse length, which can be better determined if the full spectrum is recorded [45].

7.1.3.5 Focal wavefront

For coherent imaging applications, the focal wavefront, i.e. the distribution of the wave field's amplitude and phase in the focal plane, can affect the collected diffraction patterns in various ways.

In the most ideal case, i.e. for perfect optics, the focal wavefront that is produced by the micrometre-scale—or the 100 nm–scale—KB mirrors can be well approximated by a Gaussian intensity distribution with a uniform phase, as long as only the central maximum in the focus is concerned. Nevertheless, due to the rectangular entrance pupil of the mirrors, which is either defined by their geometrical acceptance area or by beam-defining slits, the focal intensity distribution is in fact better approximated by a 2D sinc function. Its side lobes are areas with high intensity and uniform phase, distributed in the horizontal and vertical direction, and separated by boundaries of minimum intensity and highest phase gradients. If, in addition, the entrance pupil of the optics is not illuminated sufficiently uniformly in amplitude and phase, the focal wavefront can even strongly deviate from that of a rectangular entrance aperture.

As long as the particle under study is small enough with respect to the FWHM size of the focus, and as long as it is injected precisely enough so that it is only subject to a linear phase gradient and uniform intensity, the only effect on the collected diffraction pattern is a translation of its centre into the direction of the phase gradient and a decrease in the overall scattered intensity. Both effects, however, influence the analysis of diffraction data and need to be accounted for. In the case of strongly scattering particles or crystals, there is no difficulty in finding the centre of the diffraction pattern, e.g. by analysing its intensity distribution. Nevertheless, for weakly scattering particles, this task becomes nearly impossible from analysing the diffraction pattern alone (without knowledge of its central part). Therefore, in this case, any further independent information on the focal wavefront is of high value.

It is noted though that, fortunately, the locations of the highest phase gradient in the focal plane coincide with the lines of lowest intensity, so that the effect on the diffraction pattern is self-terminating to some extent, especially if it is combined with a hit-finding mechanism that reliably identifies a “strong hit” of the particle within the central maximum of the beam, e.g. by thresholding a measured fluorescence signal close to the interaction region.

If the size of the particle approaches the FWHM size of the focus, there is a significant probability that the wave field covering the particle is both non-uniform and non-linear in phase and amplitude, even in the case of a central hit. In such a case, a reliable reconstruction of the particle’s electron density without independent knowledge of the focal wavefront is not possible.

Furthermore, the contributions of the empty beam to the diffraction pattern on the detector have to be considered, and are independent of the precision of the injection process. Even for an ideal optical system, the entrance pupil of the focusing optics leads to scattering in the far field and thus to a change of the native sample diffraction pattern. For rectangular entrance pupils, however, the empty beam scattering is concentrated in a highly non-isotropic way into streaks in the horizontal and vertical directions that potentially extend to very high diffraction angles.[4] This allows for good separation of the sample scattering from the optics scattering. Note that this is not true for circular entrance pupils. To suppress empty beam scattering, “guard slits” or apertures can be used in between the optics and the sample.

In addition, a real optical system will always suffer from effects of aberrations on the focal wavefront due to imperfect geometrical finishing. One can gain some knowledge on the expected magnitude of aberrations from a few figures of merit that are derived from height fluctuation statistics of, in the case of SPB, the mirror (for more details, see Chapter 6, “X-ray optics layout”). Nevertheless, an accurate model of the focal wavefront and its aberrations can be obtained only from a complete knowledge of the final optics’ height deviations [47] as determined from a precise *in situ* measurement. For considerable figure errors (more than 1 nm r.m.s.) in the spatial wavelength range from 1 mm to 1 m, i.e. the mirror length, one can expect considerable effects on the system’s geometrical imaging properties, especially the focal intensity, size, and shape [47, 85].

Monitoring the wavefront in the focal plane is thus not a necessary condition for all experiments, but it is very beneficial and possibly mandatory for many of them.

[4]Therefore, they can usually not be measured on a detector that monitors the small-angle signal of the FEL beam after passing the central hole of the main detector.

In summary, the arguments for wavefront monitoring are as follows:

- **Wavefront aberrations**
  Knowledge of the wavefront in one lateral plane gives access to the knowledge of the wavefront in any plane along the optical axis by numerical forward and backward propagation. Therefore, wavefront monitoring can also be used to find the location of the focus during alignment.[5] In addition, feedback on wavefront aberrations (even without full reconstruction) is very helpful to optimize the alignment of the beamline focusing optics, slits, etc.

- **Focal wavefront**
  Knowledge of the focal wavefront allows the precise determination of the quality of the optical system as well as the nature of beam fluctuations (i.e. their amplitude and phase). In particular, the lateral and longitudinal source point fluctuations can be determined [81].

- **Large particles**
  For large particles that require analysis of single 2D diffraction patterns, the knowledge of the wavefront can be essential for a successful reconstruction of the sample electron density (see e.g. the literature on Fresnel CXDI as referenced in [66]).

- **Small particles**
  For small particles that produce average scattering intensities of much less than a single photon per pixel on the detector, a precise control of the wavefront is an important aid to the analysis process, which can depend on the interpretation of many thousands of diffraction patterns.

- **Real-time wavefront analysis**
  To access the necessity of a real-time wavefront analysis, one has to distinguish between static aberrations from an ideal wavefront and dynamic effects. Static aberrations can be relatively well-predicted after they have been measured once. These include those due to the mirrors' figure errors and the geometry of the beam conditioning system (entrance pupil, guard slits, etc.). Dynamic aberrations from an ideal wavefront are caused by inevitable FEL source point and beam positioning fluctuations [81], and are strongly depend on the final practical stability of the FEL beam.

The wavefront should ideally be monitored in a non-destructive way, so that it can be

[5] This, however, can also be found without complete determination of the wavefront, e.g. by a single-shot Ronchi test [65].

used to aid the analysis of the sample scattering data of the same shot. Ideally, the monitoring should be performed at the full pulse repetition rate.

7.1.3.6 Timing

Pump–probe experiments to be performed at the SPB instrument will require in some cases a very relaxed timing system, from picoseconds to milliseconds, while in other cases, they will aim for the best time-of-arrival resolution possible, on the order of femtoseconds. This latter goal is much more challenging, and a few conceptual approaches that may achieve this are outlined in Section 7.2.6, “Timing diagnostics”.

7.2 Diagnostic devices

The FEL beam parameters listed in Table 7.2 will be monitored by different devices that are placed either in the experiment (and/or optics) hutch or into the tunnel. The European XFEL X-Ray Photon Diagnostics group (WP74) conceives, installs, and commissions all diagnostic devices that go into the photon transport tunnel, i.e. those that are not installed directly in the experiment hall. Diagnostic devices in the SPB optics and experiment hutch lay within the responsibility of the SPB group, but are specified, chosen, developed, and/or acquired in close collaboration with the X-Ray Optics and Beam Transport group (WP73), WP74, and the other scientific instruments at European XFEL.

In the following, we give an overview of the planned and optional diagnostic devices within the optics and the experiment hutch as well as, partly, within the photon transport tunnel. The ordering largely follows the ordering in Section 7.1.3, “Detailed diagnostic requirements”.

7.2.1 Pulse energy

Many options are available to measure the total energy of a pulse. Most of them give an indirect result that needs to be calibrated in order to obtain an absolute estimate of the energy in a single pulse. However, their statistical error can be relatively small.

For a better overview and easier comparison, the available options are listed in Table 7.5 on the next page.

Table 7.5: Most important options for measurement of the full pulse energy with some specifications

X-ray gas monitor detector (XGMD)	Drift chamber based on low-pressure rare-gas ionization [98, 46]; two devices upstream of attenuators and offset mirrors in photon tunnel, two 1D devices downstream at tunnel exit, in perpendicular orientation; non-destructive, highly transmitting; 4.5 MHz measurement rate; measured accuracy better than 7% for ≈ 4–14 keV X-rays and pulse energies of ≈ 30–100 µJ; better accuracy expected for maximum pulse energy at European XFEL; provided by DESY.
Gas-based X-ray beam position monitor (XBPM)	Secondary pulse energy measurement; expected accuracy of 0.5 times the XGMD accuracy; for other specifications, see Section 7.2.2, "Beam centroid position".
Diamond backscattering monitor	Secondary pulse energy measurement using silicon PIN diodes[a] for X-rays backscattered from a diamond window [67, 99, 46]; measured accuracy[b] (at 10 Hz repetition rate) better than 7% [46] for pulse energies of ∼30–100 µJ and photon energies of ∼ 4–17 keV. As signal processing involves fitting routines [51], application currently only realized for 60 Hz operation. For other specifications, see Section 7.2.2, "Beam centroid position".
Others	Just like the gas-based XBPM, other devices that are primarily used for the measurement of the beam centroid position or the 2D intensity profile can also be used to give a relative measure of the total pulse energy, with varying levels of accuracy. Most accurate "parasitic" pulse energy measurements can be expected from the gas-based XBPM (see above) and diamond screens, used by measuring either backscattered photons or the charge separation signal within the screen (see below). Finally, another option for (relative) pulse intensity measurements is fluorescence imaging screens (other than diamond).

[a] Positive-intrinsic-negative diodes
[b] Note that the measured quantity here is the amount of separated charges that are produced when the backscattered X-rays hit the diode material. The relative accuracy here is that of the measured µC/J as calibrated with an independent pulse energy measurement [46].

7.2.2 Beam centroid position

Many devices that can be used for pulse energy measurements are primarily designed as beam position monitors. A detailed list with the most important specifications and references is given in Table 7.6. Those devices that have been explicitly mentioned in Table 7.5 on the previous page are explained in more detail in Table 7.6.

Table 7.6: Most important options for measurement of the beam centroid position with some specifications. BPMs are foreseen to be added to each 2D imaging screen throughout the beamline.

Gas-based X-ray beam position monitor (XBPM)	Drift chamber with split electrodes based on low-pressure rare-gas ionization for 1D beam centroid measurement [98]; two devices (x/y) upstream of attenuators and offset mirrors in photon tunnel, two devices (x/y) downstream at tunnel exit for two independent 2D centroid and a combined directional measurement; 4.5 MHz measurement rate; expected accuracy ca. 10 µm within a measurement range of $\pm$1 mm; provided by DESY.
Diamond backscattering monitor	Two pairs of silicon PIN diodes[a] in x- and y-direction for direct detection of backscattered X-rays from nanocrystalline CVD diamond film [99, 46]; measured accuracy (r.m.s.) of $\leq$ 7 µm in a synchrotron beam with 100 µm diameter, at photon energies of 8.27 keV and 12.40 keV and a photon flux of $\sim 10^{10}$–10^{11} s^{-1} [99]. Maximum rate depending on signal processing, 4.5 MHz probably possible; possible development/specification/tendering in collaboration with WP75 and WP76.
Diamond drift detector	Two pairs of electrodes for detection of electron–hole pairs in a single-crystal CVD diamond; field of view ca. $\gtrsim 3 \times 3$ mm^2; accuracy under investigation; planned frame rate of 4.5 MHz; in-house development by WP74, first positive prototype test at the Elettra synchrotron (end of 2012).

[a] Positive-intrinsic-negative diodes

7.2.3 2D intensity profile

Several 2D intensity imaging devices will be installed throughout the beamline (see Figures 7.1 and 7.2) especially for optics alignment purposes. Except for the last device directly upstream of the beam dump, which is foreseen as a 2D profile monitor capable of handling at least part of a full pulse train, the screens will be usable only at a 10 Hz frame rate—which is sufficient for alignment purposes. All screens are presently designed as pop-in devices with a horizontal motorized translation. The final specification, design, and procurement of the diagnostic screens will be carried out in close collaboration with the X-Ray Photon Diagnostics group (WP74).

All diagnostic imaging devices will be based on detection of a visible-light fluorescence signal from scintillation materials. At the beam stop position, this material will be single-crystalline or polycrystalline CVD diamond [68], due to considerations of radiation damage at this position. The remaining (standard) devices will be equipped with cerium-doped yttrium aluminium garnet (Ce:YAG) single-crystal screens as the scintillating material. Due to the high-Z elements contained in Ce:YAG and its much lower heat conductivity, it is not as radiation-hard as diamond.

With the exception of the diamond screen at the beam stop position, each imager position will be equipped with both partially transmissive and beam-blocking diagnostic screens. The obvious advantage of a transmissive device would be the possibility to obtain a real-time feedback on beam direction during optics alignment by using two screens at the same time. Beam blocking devices allow the experimenter to be concerned only with optics and devices upstream of that screen, easing alignment of the instrument.

For a non-transmissive design, the thickness of the Cd:YAG screens will be in the range of 50–75 µm. Note here that the achievable resolution is reduced for increasing scintillator thickness, even though the light yield increases. The latter, however, is not a major concern with the strong FEL radiation.

For the transmissive design, the Ce:YAG screens need to be equipped with an optical-grade surface for minimal impact on the X-ray wavefront. To minimize absorption and maximize resolution, the thickness can in principle be reduced to around 5 µm [50]. As with the non-transmissive screens, the reduced light yield of the thin scintillation material should be no major problem given the high intensity of the European XFEL beam [109]. For the transmissive diamond screen at the beam stop position, a thickness on the order of 20 µm or thinner should be chosen [68], especially in view of the low photon energy end of the SPB instrument, to minimize absorption and thus potential damage of the screen material.

For the non-transmissive design, the mirror that directs the fluorescence photons onto a visible-light camera can be an optical-grade standard mirror mounted at a 45° incidence angle [68].

For the transmissive design, the mirror needs to be at least semi-transmissive for X-rays, so that here a thin foil of X-ray transparent material (silicon nitride, silicon, etc.) with a thin (~ 50 nm) metal coating could be used as mirror material [68]. As an optical mirror would be destroyed in a full pulse train, the diamond imaging screen for high-load applications needs to be itself mounted at a 45° incidence angle. An additional option to decouple the optical fluorescence signal from the X-ray beam is given by a drilled optical mirror with a central hole to allow passage of the central beam.

As outlined in Section 7.1.3.3, "2D intensity profile", the required field of view for the first four upstream screens is 15×15 µm^2, 35×35 µm^2 for the fifth, and 45×45 µm^2 for the fast profile monitor at the beam stop position.

The lower limit for the required number of pixels in each coordinate direction for each screen is determined by the ratio of the required field of view side length and the required linear resolution as given in Table 7.4. For the six imaging screens required for the SPB instrument, these ratios are given as 88, 100, 250, 750, 3500, and 642, from upstream to downstream. As a consequence, for the first four screens, fixed magnification optics with a camera of about 1 Mpx are sufficient. As these screens will be primarily used for alignment, a fixed magnification is preferable to a zoom optics, as a fixed magnification removes one source of possible operational errors. For the second last case, a 4 Mpx camera should be sufficient. For the final fast imaging screen, a 1 Mpx camera would be ideal.

The cameras for the YAG screens should be low-noise, high dynamic range devices with the capability to run at a 10 Hz frame rate. The last camera should have a dead time as small as possible, so that the number of pixels might be reduced, e.g. by binning, in order to allow for shortest inter-frame separations. It is noted, however, that this requirement might be relaxed, depending on the actual beam fluctuations and their impact on the experiment at hand.

A preliminary design of a 2D screen device is shown in Figure 7.3 on the next page.

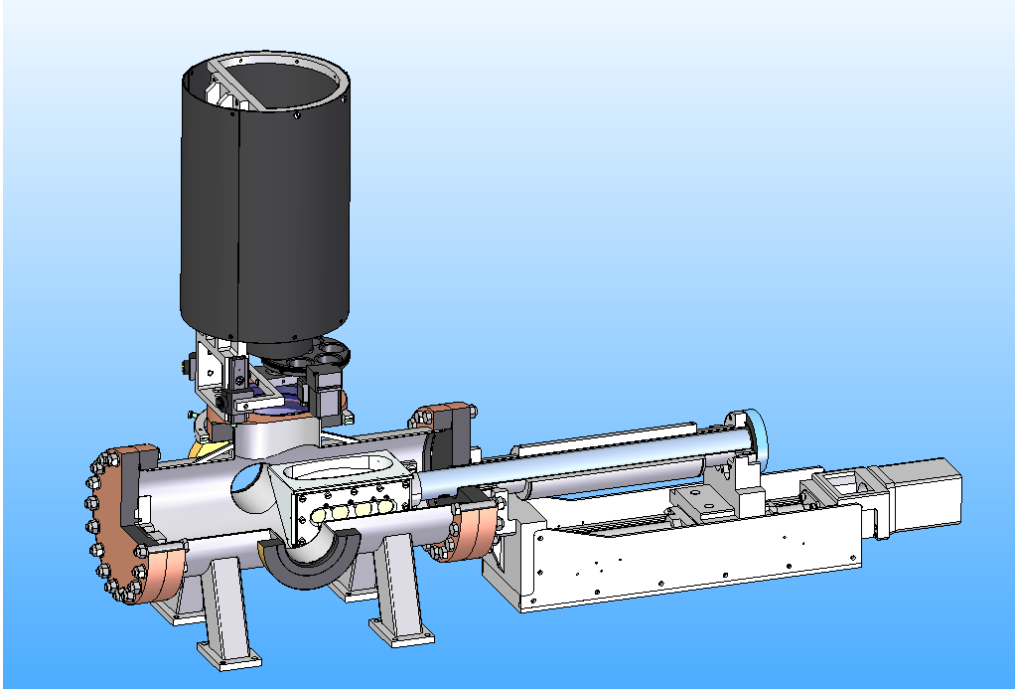

Figure 7.3: Preliminary technical design of a 2D imaging diagnostic device for the SPB instrument. Four alternative transmissive screens can be used in this setup. Figure courtesy of M. Planas, W. Freund, and C. Ozkan (WP74).

7.2.4 Mean wavelength, bandwidth, and wavelength spectrum

We noted earlier in this chapter that a full spectral measurement is not strictly necessary for the applications planned at the SPB instrument. Nevertheless, such knowledge can be beneficial for beam characterization purposes, calibration purposes, or just evaluating that the correct radiation is being delivered from the FEL. We consider two ways—one destructive and one transmissive—to measure this information upstream of the experiment.

In order to measure spectroscopic quantities such as the mean wavelength and the bandwidth, or even the full wavelength spectrum of the beam, several options exist that depend on technology, proof-of-principle demonstrations of which have just recently been performed at FELs [15, 45, 113, 110]. Therefore, a routine operation of these devices will still require some development efforts.

Currently, two different analysis principles can be distinguished, namely spectral measurements based either on photoemission signals from a noble gas or on diffractive optics. The disadvantage of the latter is that it will always be more

disturbing on the wavefront than a gas target and that all diffractive devices are chromatic.

Both of these methods are accommodated by diagnostic devices common to the SASE1 beamline and provided by the X-Ray Photon Diagnostics group (WP74). These devices are outlined in some detail in Appendix E, “SASE1 beamline spectrometers”.

7.2.5 Wavefront

As explained above, the specifications for a wavefront monitoring device strongly depend on the magnitude of aberrations that will in practice be observed in the SPB optical system and especially on their shot-to-shot stability. A mere fluctuation of the overall intensity distribution in the focal plane with negligible changes in the phase distribution, for example, would only require a monitoring of the overall fluorescence signal from the sample in order to correct the diffraction pattern for varying intensities incident on the sample.

Several options for wavefront monitoring of FEL beams are available. Like spectroscopic monitoring, however, they are still at relatively early stages of development. Three major techniques can be distinguished, namely interferometric wavefront monitoring using a Talbot grating [81, 80], Hartman-Shack–based wavefront monitoring [30], and coherent imaging–based wavefront reconstruction [75, 69].

In the hard X-ray range relevant for the SPB instrument, only the Talbot method has been demonstrated so far at an FEL source, even though synchrotron experiments have shown that coherent imaging methods for wavefront reconstruction that are compatible with single-shot imaging can also be applied in the hard X-ray range [69].

Methods using a grating exhibit the disadvantage that they have an impact on the wavefront by design. For example, insertion of a Talbot grating into the beam path [81] causes strong wavefront and intensity modulations at integer multiples of Talbot distances on the optical axis. Such disadvantages can be overcome by installing the wavefront monitoring device downstream of the sample and 2D detector.

As wavefront monitoring by coherent imaging applications should in principle be possible by inserting the pop-in screens that are already foreseen at the SPB instrument—in particular the fast imaging diamond screen to be installed at the beam stop location—coherent imaging is planned to be the baseline option for shot-to-shot wavefront reconstruction at the SPB instrument. A major drawback here could be the

limited dynamic range of the cameras that are used in the imaging devices. Unlike interferometric imaging, which has only modest requirements to the detector dynamic range, CDI relies on measuring the full beam profile at certain positions on the optical axis. On the other hand, grating-based methods are chromatic and require relatively expensive additional components in the beam path. As indicated in the beginning of this section, a decision for a specific technique will also depend on the magnitude and the stability of aberrations at the SPB instrument, which can eventually only be determined by *in situ* measurements during the commissioning phase.

7.2.6 Timing diagnostics

A reliable, simple, and highly time-resolving time-of-arrival monitor is an essential component for being able to interpret ultrafast, time-resolved experiments. Time resolutions of as good as 10–15 fs has been demonstrated at LCLS using a spectral encoding method [9] or a combination of spectral and spatial encoding methods [37].

7.2.6.1 Fast time-of-arrival diagnostics

Spatial encoding A spatial, or cross-correlation, tool consists of a material that changes in X-ray transmission or reflection as a function of illumination with the optical pulse. By illuminating such a material with an optical pulse incident at an angle other than the normal, the relative time of arrival of the optical pulse is encoded into a spatial variation in reflection or transmission of that material [56, 8, 37]. This spatial variation can then be correlated to a relative time of arrival of the optical and X-ray pulse.

Spectral encoding A spectral encoding method consists of delivering a broadband (continuum) pulse of optical radiation chirped such that different wavelengths arrive at a predefined plane (material) as a function of time. The interaction of the X-ray FEL pulse with the material (e.g. a silicon nitride membrane) changes the refractive index of the material. A subsequent examination of the optical spectrum transmitted through the material, compared with the continuum's unperturbed spectrum, allows one to understand which wavelengths arrived before and which after the X-ray pulse. As these wavelengths are mapped to arrival time through the chirp, a relative arrival time between X-ray and optical pulse can be deduced [9, 37].

Spatial and spectral combined device For timing, one may consider the use of a combined device with both spatial and spectral encoding, such as that demonstrated in [37]. This gives the benefit of the simpler analysis of spatial encoding—where a position is directly mapped to a relative time of arrival—as well as access to higher-resolution timing information from the more involved analysis of spectral encoding. One of the key issues at the European XFEL is to identify a material for the spatial and spectral encoding that is amenable to the 4.5 MHz intra-bunch repetition rate. It is not clear if silicon nitride or various crystalline bulk materials, such as sapphire, have lifetimes short enough to permit their successful use at the European XFEL. One suggestion is to use a constantly refreshed liquid as the material, thereby avoiding the need to consider the lifetime of the material [14]. Another possible route is THz streaking, which was demonstrated at longer-wavelength FELs [34], and which in principle should allow even full temporal diagnostics including not only time of arrival, but also pulse duration and temporal pulse substructure; however, the applicability to hard X-rays still needs to be demonstrated.

7.2.6.2 Slow time-of-arrival diagnostics

As some of the biological science in particular will be interested in exploring slower time scales, i.e. anything from many picoseconds to milliseconds, a slower time diagnostics that does not rely on overlapping the optical and X-ray beams is necessary. Fortunately, at these longer timescales, fast, commercially available photodiodes can simply be inserted in the timing diagnostics area and read out with a fast digitizer, allowing for the simple and accurate timing of these pump–probe experiments. It is envisaged that much of the envisioned pump–probe nanocrystallography could be performed using this much simpler system.

7.2.7 Multipurpose downstream diagnostics

Upstream of the beam dump, a section about 1 m long is foreseen along the optical axis where optional beam diagnostics—such as a wavefront monitor, a spectrometer, and a total intensity monitor—could be installed. This diagnostic section was formerly know as the “intelligent beam stop”, though we changed the nomenclature to avoid confusion with the beam dump (sometimes known as the “beam stop”), which is the final resting place of the beam. The diagnostic section will comprise the aforementioned three devices mounted on a horizontal translation stage to move each of these diagnostic components in and out of the beam as required.

8 Sample chamber

Chapter authors: N. Reimers[1], A. Aquila[2], G. Borchers[2], A.P. Mancuso[2]

The sample chamber will surround the common focal plane of both the micrometre-scale and 100 nm–scale optics. To maintain a reasonable degree of flexibility for various experimental configurations, there will be one relatively large vacuum chamber for the sample environment.

8.1 Requirements and overview

To support the photon–matter interaction region, the sample chamber requires a vacuum environment and the ability to control the sample position—whether the sample is injected or fixed. The sample chamber will contain a four-axis sample stage, or the liquid-jet setup, and three aperture stages upstream of the interaction region for final beam conditioning. It requires enough space to include an on-axis microscope and a fluorescence detector. There is also the need to include a differential pump upstream of the chamber. As the sample environment also allows sample delivery with particle injectors (e.g. aerosol streams), the chamber will feature a DN250 ConFlat (CF) flange on top of the chamber. The chamber will be equipped with an electron time-of-flight (ToF) spectrometer, in-coupling for the pump laser, and potentially a mass spectrometer. Several other ports for windows, feed-throughs, and lasers will be provided. Three so-called “cleanup” apertures will be mounted inside the chamber.

A breadboard that allows a quick change of the different experimental setups will be set up on the internal base of the chamber.

The interaction region must be located as close as possible to the downstream side of the chamber, as the primary detector will interface here and the sample–detector distance must be minimized for certain samples—in particular for nanocrystals.

The chamber itself requires movement by a couple of centimetres with two degrees of freedom (up/down and left/right), with an accuracy in the micrometre range, to account for the different beam pointings of the various optical configurations. Whether

[1]Central Instrumentation Engineering (CIE) group, European XFEL GmbH, Albert-Einstein-Ring 19, 22767 Hamburg, Germany
[2]Scientific Instrument SPB group (WP84), European XFEL GmbH, Albert-Einstein-Ring 19, 22767 Hamburg, Germany

vertical movement of the chamber is required will only be clear after the mechanical integration of the upstream detector is finalized. At the time of this writing, work is ongoing in collaboration with the AGIPD consortium.

8.1.1 Vacuum requirements

The pressure inside the chamber will be on the order of 10^{-6} mbar to 10^{-3} mbar. The chamber will be pumped down with one large vacuum pump, connected to the bottom. There will be an additional pumping port for the catcher of the liquid-jet setup. When the liquid jet is used for sample delivery, it is necessary to pump large volumes of water vapour out of the chamber. More information about the vacuum requirements can be found in Appendix A, "Vacuum concept and design".

8.1.2 Vibrational requirements

Given a best possible beam diameter of 100 nm and sample sizes of a few hundred nanometres, the sample chamber should be as stable as possible. Movements over 1 µm are not acceptable; indeed, vibrations should be limited to ideally much less than the focal spot sizes. To isolate the chamber from ground vibrations, it will be mounted on one large granite block. More information about the vibrational requirements can be found in Appendix B, "Vibrational, thermal, and mechanical considerations".

8.1.3 Geometrical requirements

The sample chamber has to be long enough to carry the fixed sample stage stack or the liquid-jet setup, an on-axis microscope, and stages for three cleanup apertures. A length of 1 m is sufficient for this requirement. For the mounting of the aerosol stream, a DN250 CF flange is required directly above the interaction region. The interaction region itself should be as close as possible to the downstream region of the sample chamber, to get a small distance to the detector. The mechanical integration of the detector is still in progress. At the moment, a DN500 flange is required at the downstream side for the integration. Several other ports—with sizes between DN63 and DN250—are necessary for laser in-coupling, microscopes, windows, ToFs, and a mass spectrometer.

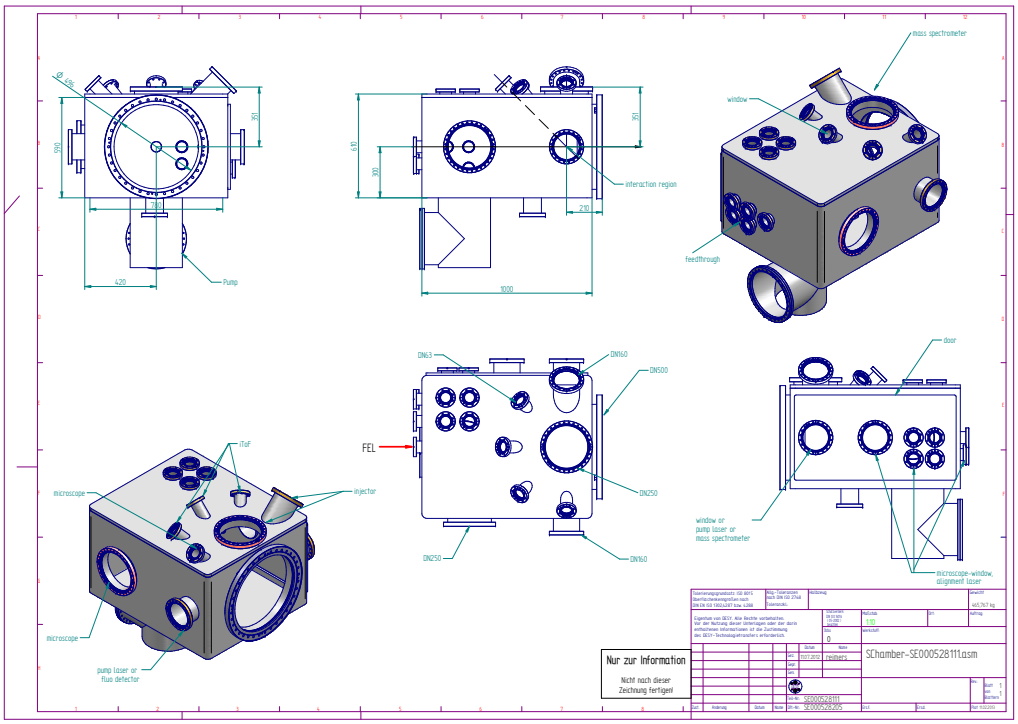

Figure 8.1: Conceptual drawing of the sample chamber. The DN500 flange on the downstream side is essential for the mechanical integration of the detector. On both sides of the chamber are large flanges for laser in-coupling, microscopes, or cameras. All ports on top of the downstream side of the chamber point to the interaction region. These will be used for sample delivery, microscopes, or ToFs. The pumping system on the bottom requires one large port for the general pump and a DN100 flange for a catcher pump, which will remove liquids and other sample deposits from the chamber. Several DN63 flanges on the side, top, and back of the chamber can accommodate feed-throughs.

8.1.4 Differential pumping

A critical part of the instrumentation will be the separation of the 100 nm–scale KB chamber with 10^{-9} mbar pressure from the sample chamber with a worst-case condition of 10^{-3} mbar. For this purpose, a differential pump was designed and will be tested in the second half of 2013 in cooperation with the X-Ray Optics and Beam Transport group (WP73).

The basic design of the differential pump upstream of the sample chamber is shown in Figure A.2 on page 168. A more detailed description can be found in Appendix A, “Vacuum concept and design”.

8.2 Mechanical design

To support various experimental configurations, the SPB instrument will be equipped with one large vacuum chamber. A cubic design of the chamber was chosen to achieve good access to the interaction region for experiment setup and maintenance. To avoid flexing of the cubic chamber, the outer structure will be reinforced with braces. The chamber will contain a removable breadboard, which can carry sample stages and diagnostic equipment. This makes it possible to prepare the setup outside of the chamber. To allow isolation from the rest of the instrument, e.g. for sample or nozzle changing, the chamber will be equipped with gate valves on the upstream and downstream side.

The integration of the detector on the upstream side of the sample chamber requires a DN500 flange. Further mechanical requirements for a successful integration are still under discussion.

A DN250 CF flange directly above the interaction region allows the mounting of different sample injection devices, such as an aerosol jet at 90° to the FEL beam. There will be several ports at 90° and 45° to the beam for diagnostic devices, cameras, and microscopes.

8.2.1 Sample delivery setups—downstream region

The following figures show setups with three different sample delivery systems as described in Chapter 10, “Sample delivery techniques”.

Figure 8.2 on the next page shows the sample chamber with the liquid-jet setup described in Chapter 10, “Sample delivery techniques”. The liquid jet is a design of Microliquids GmbH. The on-axis-microscope upstream of the jet was developed at CFEL.

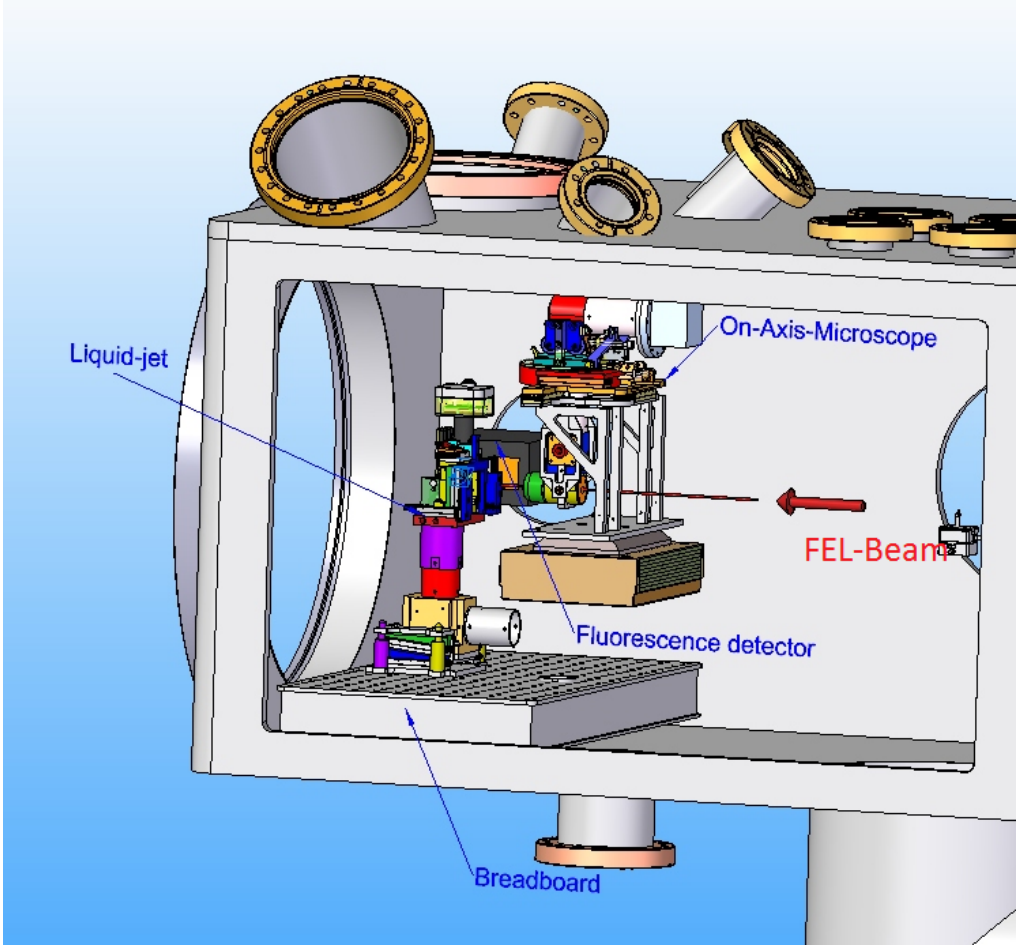

Figure 8.2: Setup with liquid jet. On-axis microscope developed by H. Fleckenstein (CFEL).

In Figure 8.3 on the following page, the aerosol injector of Uppsala University is mounted on the sample chamber at 90° to the FEL beam.

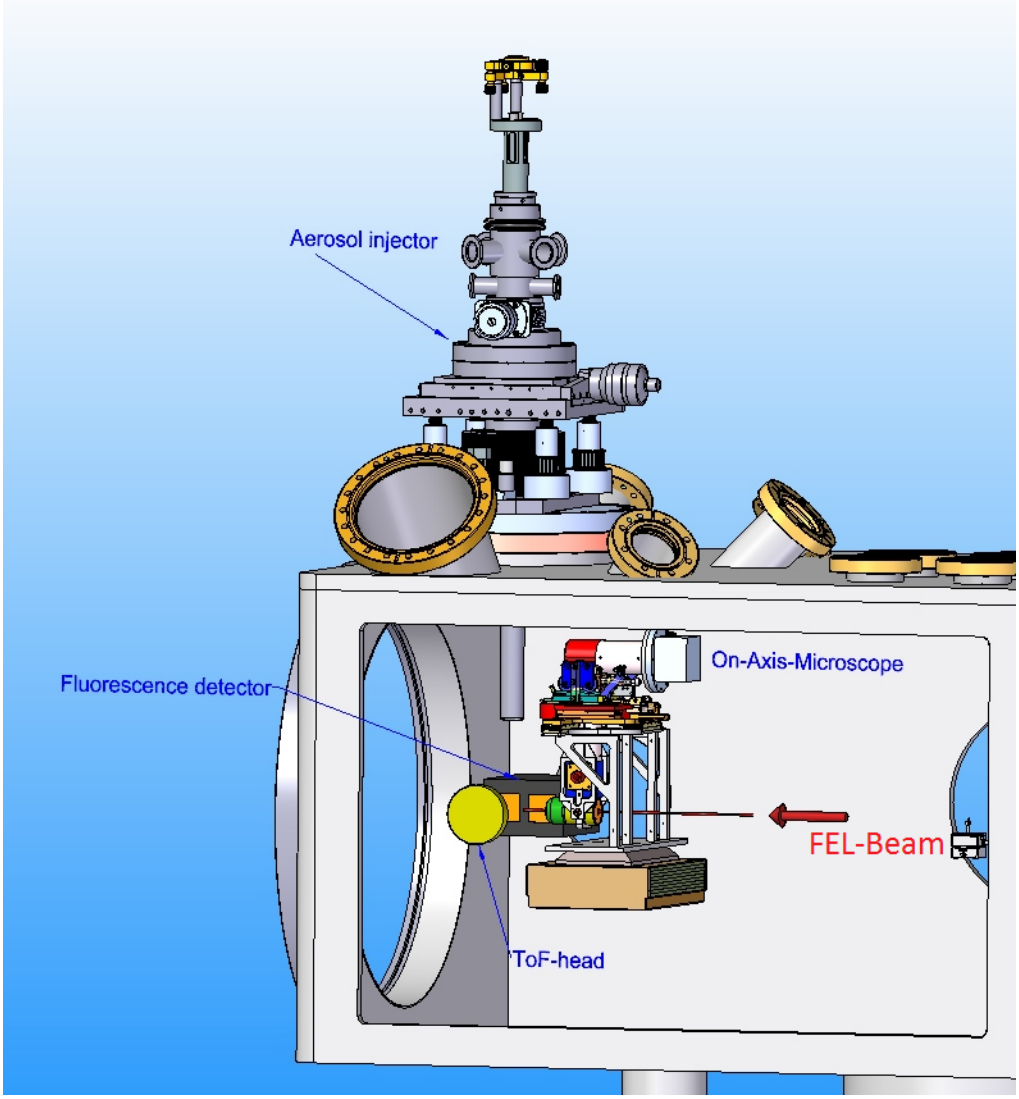

Figure 8.3: Sample chamber with aerosol injector. On-axis microscope developed by H. Fleckenstein (CFEL). Aerosol injector developed by Uppsala University.

A possible stage stack for fixed samples is shown in Figure 8.4 on the next page. In this example, two Smaract SLC2475 positioners are mounted on an elevation stage from Huber (Model 5103.A10). For fine alignment of the fixed samples, piezoelectric positioners with sub-nanometre resolution can be mounted on top of the stage stack.

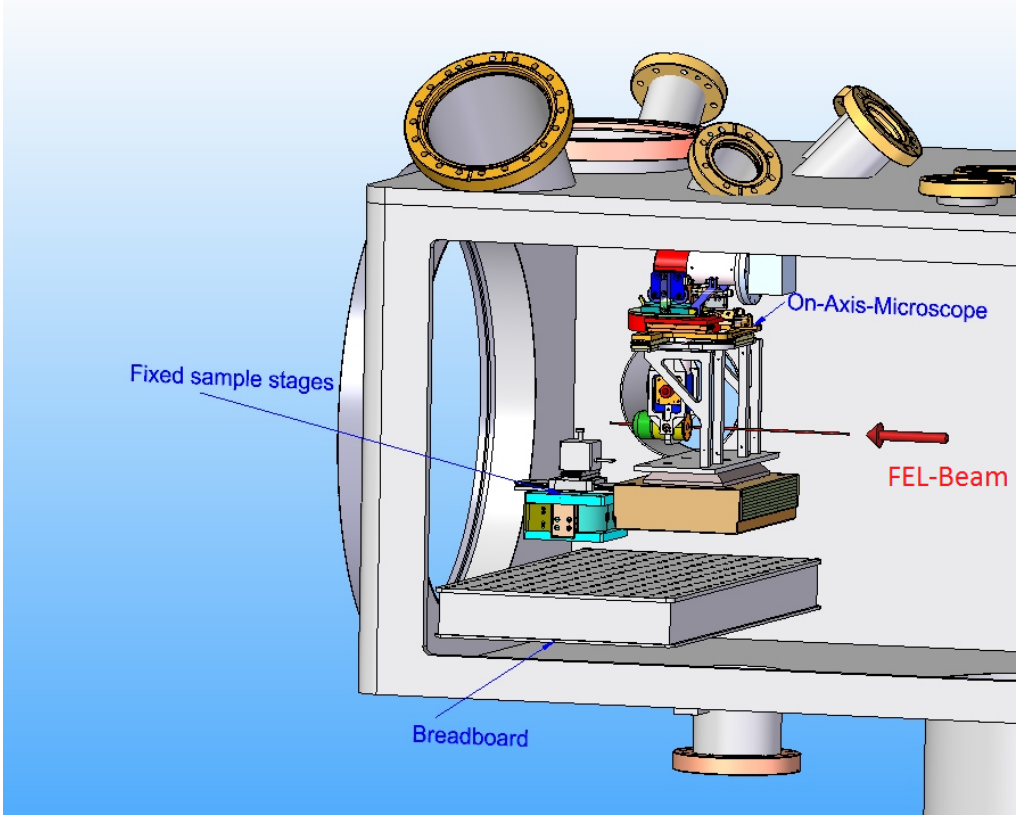

Figure 8.4: Fixed sample stages shown in the sample chamber. A removable breadboard allows for interchanging of the different sample environments. On-axis microscope developed by H. Fleckenstein (CFEL).

8.2.2 Upstream region

The upstream region of the chamber will be used for the laser in-coupling devices and the cleanup apertures. A removable breadboard will serve as a base structure for all parts mounted in this region.

The laser is coupled into the chamber through a window flange at 90° to the FEL beam. Different window materials will be available to minimize dispersion of the uncoupled laser, i.e. preserve the femtosecond nature of the optical laser pulse. An in-vacuum parabolic mirror will be the final laser mirror to focus and couple the laser on axis with the FEL, via a drilled hole to allow the FEL to propagate coaxially. The mirror is held by a vacuum-compatible, piezo-driven mirror mount. Additional motion control is provided by an xyz stage, which supports the mirror mount. The mirror has an axial hole to let the FEL beam through.

Three cleanup apertures for the beam can also be located in the upstream region of the sample chamber. The apertures are silicon frames with cutouts of $\approx$ 1 cm width. For motion control, the frames will be mounted on vacuum-compatible xyz stages with a travel range between 5 mm and 10 mm.

9 Detector integration

Chapter authors: K. Giewekemeyer[1], A.P. Mancuso[1], J. Sztuk-Dambietz[2], M. Turcato[2], A. Koch[2], M. Kuster[2]

The purpose of this chapter is to give an overview of the scientific requirements for 2D detectors at the SPB instrument and the resulting ramifications for the ongoing development and installation of the detectors. These devices are the Adaptive Gain Integrating Pixel Detector (AGIPD), which will be installed at the SPB instrument as its main detector at the start of its operation, and alternative devices, in particular the Depleted P-Channel Field Effect Transistor (DEPFET) Sensor with Signal Compression (DSSC) to be delivered to European XFEL (XFEL.EU) about a year and a half after initial operations have commenced. All relevant technical specifications of these detectors, as far as they are presently known, will be given in subsequent sections. For a recent overview on the status of XFEL.EU- related detector projects, see also [49].

9.1 General detection considerations

9.1.1 Science cases at the SPB instrument and their requirements for 2D detectors

The main scientific cases currently envisioned at the SPB instrument are crystallography of biological nanocrystals (NX), coherent diffractive imaging (CDI) of reproducible particles, and coherent diffractive imaging of non-reproducible particles (see Section 1.3, “Science case summary”). An overview of the requirements relevant for 2D detectors is given in Table 9.1 on the following page. For nanocrystallography, the requirements are less diverse and, to some extent, technically less demanding than for imaging experiments. The NX requirements are largely met by the baseline design parameters of the AGIPD detector (see Section 9.2, “AGIPD detector”). For imaging, the detection requirements are more demanding (dynamic range, missing data regions, etc.) and less well-defined, partly due to the less mature scientific application of coherent imaging at FELs and partly due to the more diverse group of samples to be studied.

[1]Scientific Instrument SPB group (WP84), European XFEL GmbH, Albert-Einstein-Ring 19, 22767 Hamburg, Germany
[2]Detector Development group (WP75), European XFEL GmbH, Albert-Einstein-Ring 19, 22767 Hamburg, Germany

Table 9.1: Sample parameters for typical science cases for applications in biology. Note that applications in material science are also expected. Here, however, one can usually expect much stronger scattering signals due to the heavier elements typical for material science samples. This increases the demand for high dynamic range.

	Reproducible single particles (SPR)	**Nano-crystallography (NX)**	**Non-reproducible single particles (SPnR)**
Typical samples from biological sciences	Macromolecules, viruses	Protein nanocrystals	Viruses, organelles, bacteria, small eukaryotes
Photon energy	ca. 3–6 keV	ca. 8–16 keV	ca. 3–6 keV
Sample size	ca. 10 nm – 500 nm	ca. 100 nm – 2 µm	ca. 100 nm – 3 µm
Images per dataset	On the order of 100 000 – 1 000 000 and more	On the order of 10 000	1
Dimensionality of reconstruction	3	3	2
Single photon sensitivity	Critical	No	Beneficial, but not critical
Dominant signal levels in one measured pattern/pixel	0–10 photons	ca. 10^2–10^4 photons and more	0–10^8 photons and more
Sampling / Number of pixels	Detector linear extent (pixels) ≅ 4 × number of resolution elements required (allows for adequate sampling of speckles); higher sampling favored	Detector linear extent (pixels) ≅ 10 × number of resolution elements required (i.e. ~ 10 pixels between Bragg peaks)	Detector linear extent (pixels) ≅ 4 × number of resolution elements required (allows for adequate sampling of speckles)
Sensitivity to missing data regions	Sensitive, low q-information critical, many images benefitial	Not sensitive, low-q information not needed	Very sensitive, can prohibit unique reconstruction

Nevertheless, due to the relatively high scattering power of nanocrystals and the recent rapid development of NX as a method [11], the required resolution, and thus the required detection angle to be covered by the detector, will be considerably higher in crystallography than in, at least initial, imaging experiments. As a consequence, the sample–detector distance will need to be minimized to be below 13 cm for certain crystallography experiments (see Section 9.1.3, “NX: Optimizing the geometrically limited resolution”), which represents a considerable technical challenge in a vacuum environment, especially for a detector with the four independently movable detection quadrants that are necessary and foreseen for use at the SPB instrument.

Note that materials science samples have not been explicitly discussed above. They have requirements similar to the larger non-reproducible biological particles (see Table 9.1). Compared to biological single particles, they usually have a much higher scattering power and thus require an even higher dynamic range if they are to be imaged in conventional CDI mode.

9.1.2 CDI: Minimization of missing data regions and the demand for high dynamic range

This section gives some details on the detector requirements and implications of CDI at the SPB instrument. The results of some basic simulations of CDI experiments are described, leading to specifications of detector layouts and geometries (i.e. sample–detector distances, number of detection planes, central hole size, etc.) that are compatible with the requirements given by the scientific cases. For further details on this subject, we refer to [32].

One of the key potentials of CDI lies in its ability to provide *quantitative* image contrast, so that each reconstructed real-space pixel can be associated with its sample electron density [66]. This imaging modality, however, is possible only if certain requirements for the detection geometry are met. As a necessary condition, the diffraction pattern needs to be sampled on a fine enough grid to record its full information content. In addition, the high-intensity scattering contributions close to the centre of the diffraction pattern need to be measured as completely as possible. In other words, any missing information due to, e.g. a beam stop that blocks the strong central beam, can distort or prevent a (quantitative) reconstruction [97]. The intensity in the direct FEL beam, however, is fatal for any pixel detector that will be used at the SPB instrument. Therefore, a central hole for the passage of the non-scattered, direct beam must be integrated into the detector design. At the same time, such a hole leads to missing information close to the centre of the diffraction pattern. Additional "blind regions" are introduced by the modular design of currently used and developed FEL detectors, which include non-sensitive stripes in between detector modules. The effect of such missing information on CDI reconstructions are inevitable ambiguities in the reconstructed real-space image [84], allowing only for a dark-field image contrast [59] for which the "image contrast can have a complicated relationship to the object structure" [59]. In other words, if certain parts in the diffraction pattern are missing, a quantitative reconstruction in which the image contrast is proportional to the object electron density is no longer possible.

Another demanding requirement in FEL CDI, particularly of larger samples, such as viruses or cells, is the high intensity range of diffraction patterns, which show an empirical power law decay in radial outward direction from the centre with an exponent between about -3 and -4 [44]. As a consequence, detectors with a dynamic range of seven orders of magnitude or more are required to cover the full dynamic range of the diffraction pattern for strongly scattering samples. This requirement, however, exceeds the maximum dynamic range of even the newest integrating detectors suitable for FEL applications by several orders of magnitude (see e.g. Section 9.2, "AGIPD detector").

It is shown in [32] that both aforementioned problems, i.e. missing data regions and the high intensity range of certain diffraction patterns, can be mitigated by utilizing two detectors: one device close to the sample with a relatively large active area and a central hole ($\varnothing \lesssim 2.5$ cm) to measure the high-resolution diffraction data, and one smaller, rear device at about twice the distance from the sample or more to measure the small-angle diffraction. This device also needs a central gap or hole to allow for the passage of the direct beam, which is eventually blocked by a beam dump at the end of the experiment hutch.

When such a transition to two detection planes is necessary, has been studied in detailed simulations [32]. The problem of the optimum detector layout for both the AGIPD and the DSSC detector is also considered in Reference [32].

9.1.3 NX: Optimizing the geometrically limited resolution

The resolution in crystallography (and in CDI) is geometrically (and thus independently of the sample) limited by the numerical aperture covered by the detector at a certain distance to the sample. The resolution is said to be geometrically limited if scattering from the sample extends beyond the detector area. If the sample (e.g. a single biological macromolecule) scatters only very weakly; the resolution, however, is signal-limited when considering only a single diffraction pattern. In such a case, even with the very high incident intensity of a modern FEL source, the average expected photon signal is much smaller than 1 ph/px (see Table 9.1 on page 116). In a crystal, in contrast to biological single particles, the signal is strongly enhanced by the large number of unit cells even in a nanocrystal. Here, the geometrically limited crystallographic (i.e. full-period) resolution of the SPB instrument becomes important. It is given as

$$\Delta x = \frac{\lambda}{2\sin\left(\frac{2\theta}{2}\right)} \tag{9.1}$$

where λ denotes the wavelength and 2θ the diffraction angle with respect to the optical axis. Consequently, the required minimum sample–detector distance z for a given resolution is given as

$$z = \frac{D}{2\tan\left(2\arcsin\left(\frac{\lambda}{2\Delta x}\right)\right)}. \tag{9.2}$$

Here, D denotes the horizontal (vertical) distance between outermost pixel columns (rows) on the detector. For the AGIPD detector, D is on the order of $(526 + 14 + 525) \times 0.2\text{ mm} + 2\text{ mm} = 215\text{ mm}$, assuming a hole width of 2 mm for the

passage of the central beam. Given the feasibility of 1.9 Å crystallographic resolution for NX [11], a resolution of at least 1.5–2 Å should be provided at the SPB instrument. With Equation 9.2, this leads to required minimum sample–detector distances of

$$z_{\text{min}} = 13.3\text{–}19.4 \text{ cm} \tag{9.3}$$

at a photon energy of 12.4 keV, and closer still for lower energies. For an overview of the necessary sample–detector distances and detection angles for the relevant photon energies at the SPB instrument, see Figure 9.1.

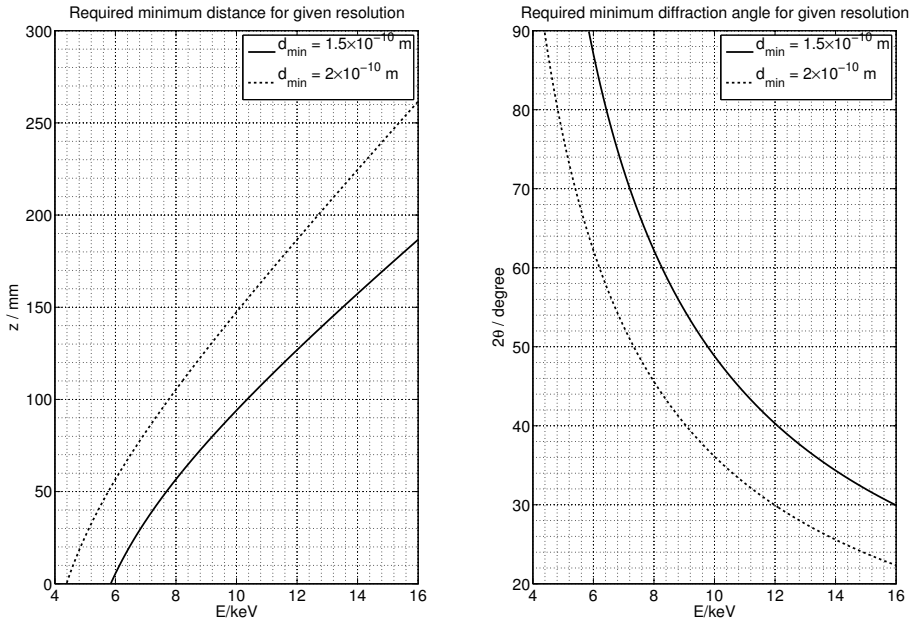

Figure 9.1: *Left:* Required minimum sample–detector distance for crystallographic, i.e. full-period, resolutions of 1.5 Å and 2 Å. *Right:* Required minimum diffraction angles corresponding to the sample–detector distances that are shown on the left.

9.1.4 Crystal parameters and resolution

Beyond the simple and compelling requirement to allow for the highest possible geometrically limited resolution, some additional parameters need to be considered for an optimum adjustment of the distance between the sample and the detector. As an example, a very small distance, and thus a very high resolution, cannot be exploited in crystallography if the number of pixels between Bragg peaks of neighbouring diffraction orders becomes too small for the peaks to be individually resolved.

We denote the ratio of the distance between two neighbouring diffraction orders to the detector pixel pitch the Bragg sampling ratio σ_B. For the same sample–detector distance, z, a crystal with a larger unit cell size, u, will lead to a smaller Bragg sampling. For a 1D crystal, the distance $r_\perp^{(n)}$ of the nth diffraction order to the optical axis is given as[1]:

$$r_\perp^{(n)} = z\sqrt{\frac{4u^4}{(2u^2 - n^2\lambda^2)^2} - 1}. \tag{9.4}$$

The Bragg sampling between diffraction orders $n-1$ and n is thus given as

$$\sigma_B^{(n)} = \frac{r_\perp^{(n)} - r_\perp^{(n-1)}}{\Delta X} \tag{9.5}$$

with ΔX denoting the detector pixel pitch. Solving Equation 9.5 for z allows to determine, for given diffraction order n, photon energy (or wavelength), Bragg sampling σ_B, and unit cell size u, the required sample–detector distance.

Clearly, σ_B is to be chosen as large as required, but as small as possible in order to maximize the geometrically limited resolution. A practical lower limit to the Bragg sampling value is given by $\sigma_B = 10$ [106]. Another parameter is the maximum diffraction order n that the detector area has to cover. For an average crystal, one might expect to see Bragg peaks to an order of $n \approx 50$. For highly ordered crystals, this number may increase to around 100, but not much further. In other words, beyond orders of around 100, and sometimes at much lower orders, the obtainable resolution is sample-limited.

In order to evaluate the practical consequences of Equations 9.4 and 9.5, we first fix the sample–detector distance to $z = 0.3$ m and calculate the Bragg sampling at the edge of the AGIPD detector for different unit cell sizes. The result is shown in Figure 9.2 on the next page. Evidently, the largest interval of unit cell sizes is accessible for lowest photon energies. This is due to an increasing σ_B, given a decreasing photon energy and a fixed unit cell size. At the same time, the resolution increases for increasing photon energies, and, if the Bragg sampling at $z = 0.1$ m decreases below a practically feasible value of $\sigma = 10$, one would have to increase z (not represented in this graph) and give up a fraction of the possible resolution.

[1] This equation follows from (a) the Bragg condition $n\lambda = 2\,u\,\sin(2\theta)$ with diffraction angle 2θ and the geometrical condition $\cos(2\theta) = z(z^2+r_\perp^2)^{1/2}$. The latter can be reformulated using the relation $\cos(2\theta) = 1 - 2\sin^2(\theta)$.

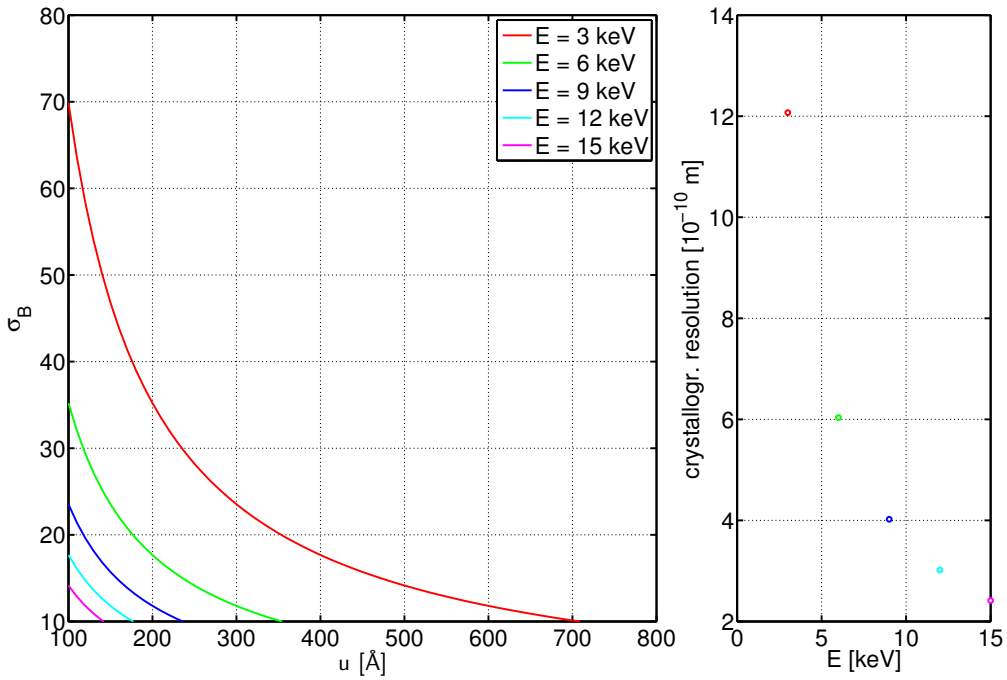

Figure 9.2: *Left:* Bragg sampling for the highest diffraction orders still visible on the detector at a detector distance of 0.3 m versus the unit cell size of the crystal. *Right:* Geometrically limited full-period resolution Δx versus the photon energy corresponding to the curves on the left side.

From the point of view of instrument design and operation, the required sample–detector distance z is very important. Therefore, it is plotted versus the photon energy in Figure 9.3 on the following page for a fixed Bragg sampling ratio of $\sigma_B = 10$ and fixed diffraction order $n = 50$, for crystal unit cell sizes between 100 and 800 Å. The red lines represent feasible parameter values for the AGIPD 1 Mpx geometry.

Evidently, the required sample–detector distance z increases for increasing photon energies as the detector region in Fourier space (for fixed z) decreases with increasing photon energy. For a fixed photon energy and increasing unit cell size, the detector distance has to be increased as well to keep the Bragg sampling constant. Thus, for small unit cells, it is generally possible to measure to higher resolution at a given Bragg sampling ratio than for larger unit cells. For very low photon energies and small unit cell sizes, however, the detector cannot be brought close enough to the sample to make all diffraction orders visible, merely because of geometrical constraints. In such a case, one has to increase the photon energy.

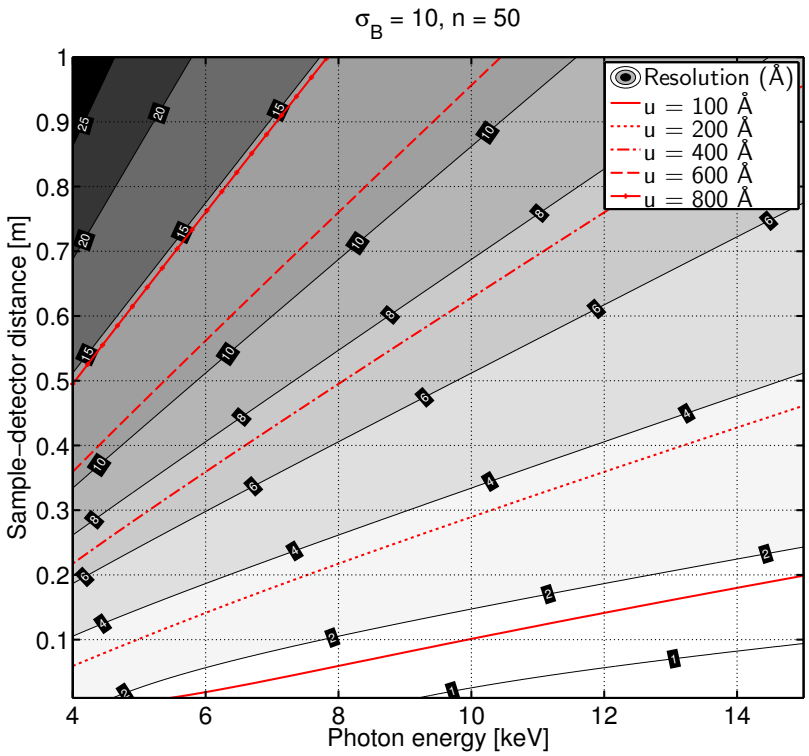

Figure 9.3: Required sample–detector distance versus photon energy for a given Bragg sampling $\sigma_B = 10$ between diffraction orders 50 and 51. The required distances are indicated by the red lines, for unit cell sizes between $u = 100$ Å and $u = 800$ Å. The underlying contour plot indicates the geometrically limited resolution for all combinations of photon energy and detector distance.

Concerning the geometrically limited resolution, Figure 9.3 reveals another interesting fact: for unit cell sizes above 400 Å, it is impossible to achieve resolutions better than 6 Å, independent of photon energy and detector distance. This is due to the required Bragg sampling of $\sigma_B = 10$ and the relatively large AGIPD pixels of dimensions 200×200 µm^2. These are, however, designed to cope with the 4.5 MHz repetition rate of the European XFEL.

Requiring now slightly higher maximum diffraction orders to be seen, namely up to $n = 55$, it becomes evident that some parameter combinations become geometrically inaccessible, especially for very large unit cells, i.e. above a diameter of 400 Å (see Figure 9.4 on the facing page).

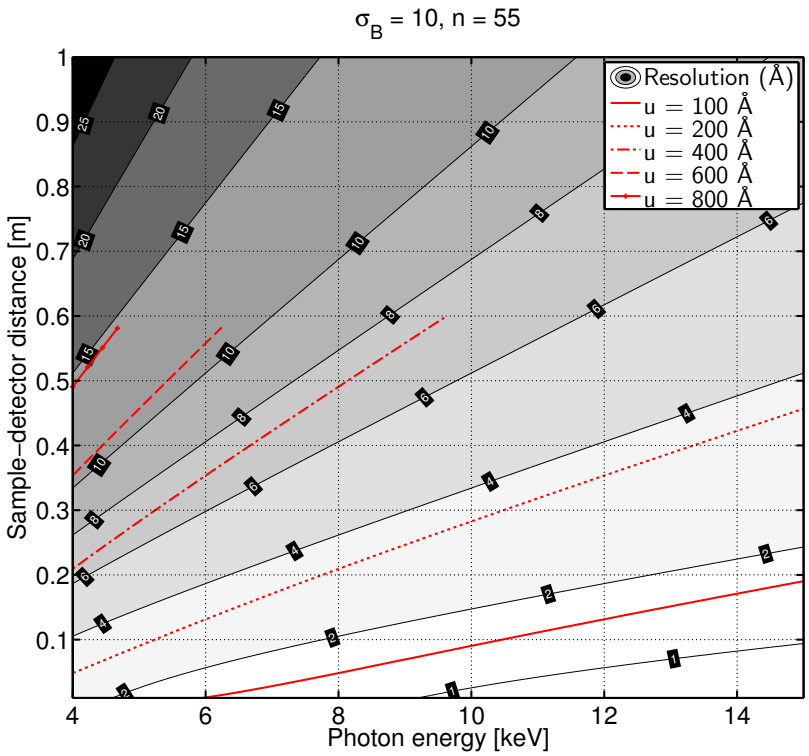

Figure 9.4: Similar to Figure 9.3 on the facing page, except the higher diffraction order of $n = 55$. The partially drawn lines indicate where the 55th diffraction order is no longer covered by the AGIPD 1 Mpx system at the detector distance required for a Bragg sampling of $\sigma_B = 10$.

Generally, the resolution can either be limited by the size of the detector (geometrical resolution limit), the pixel size, i.e. the requirement for a certain Bragg sampling ratio (depends on the unit cell size), the photon energy, and/or the highest order to which diffraction is observed. It is thus not always advisable to place the detector as close to the sample as possible, as one might initially expect. In certain cases, however, e.g. for objects with a very small unit cell size, a small sample–detector distance is indeed required.

Finally, we shortly discuss the impact of the finite crystal size in NX experiments on the measurement process. In fact, nanocrystals are so small that the Fourier transform of the crystal outline, the “crystal shape transform”, obtains a finite extension that may cover several pixels on the detector. On the one hand, measuring the shape transform of the crystal may aid the reconstruction of the unit cell electron density. On the other hand, the shape transform may significantly enlarge and/or distort the size of the Bragg peaks, which makes the evaluation of the Bragg peak intensity and position more difficult during crystallographic phasing. Without “coherent phasing”, one will thus mostly be interested in minimizing the effects of the crystal

shape transform. The number of coherent fringes from the shape transform between two Bragg spots is to a good approximation given by the ratio of the crystal size and its unit cell size. With a Bragg sampling σ_B between 5 and 10, a crystal has to have less than 10 unit cells for the coherent features to become considerably visible. As most nanocrystals have many more unit cells and as the shape transform is a fast decaying function, the effects due to the finite crystal size can be very small.

9.1.5 Preferred overall detector layout, including two detection planes

As discussed above, non-sensitive regions on the detector can have a considerable impact on the feasibility of coherent imaging experiments, especially if a real-space 2D image of the object is to be reconstructed from a single diffraction pattern alone. In this section, we present—using the example of the AGIPD detector (see Section 9.2, "AGIPD detector")—optimized detector layouts and experimental geometries to minimize missing data regions and maximize the intensity range of the recorded diffraction patterns. The conclusions are broadly the same for the DSSC detector, which will be available as an optional device at the SPB instrument, catering to the lowest photon energies available.

For the simulations that were carried out to obtain an optimum configuration of the AGIPD detector modules [32], a strong emphasis was put on an accurate description of the pixel (as well as module and quadrant) configuration in the detector plane. The photon–matter interaction physics was simplified using a continuum model of the sample within the paraxial projection approximation, which has no ramifications to the validity of the results here. The main goal was to find layouts and detection geometries (especially sample–detector distances) that fulfil necessary conditions for the feasibility of quantitative reconstructions to a resolution achievable for the given amount of scattering from the sample.

Two possible configurations of the conceptual layout (which is also referred to as the standard or "pile" layout) that was finally chosen both for technical and physical reasons are shown in Figure 9.5 on the next page.

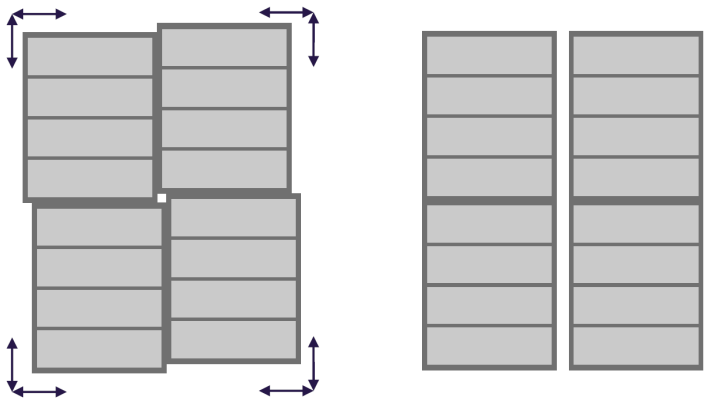

Figure 9.5: Schematic of the AGIPD detector layout. The detector comprises four independent quadrants of four modules each that can be moved independently within a range of several millimetres (for detailed specifications, see Table 9.3 on page 130). In particular, it will be possible to provide either a centre-symmetric hole layout (left) or, e.g. a mirror-symmetric gap layout (right). The light grey areas correspond to photon-sensitive areas, while the dark grey areas illustrate non-sensitive regions.

The main criterion for the feasibility of a quantitative reconstruction is to enable at least partial recording of the central speckle in the diffraction pattern. If this is not measured at all, a quantitative reconstruction becomes impossible [97]. As the speckle size on the detector is inversely proportional to the sample diameter[2], Nyquist (or better) sampling requires a minimum sample–detector distance for a given sample size. Thus, the sample–detector distance influences the feasibility of proper sampling (and thus, the reconstruction). In addition, it also has an effect on which parts of the central speckle can be measured without illumination of the sensor by the strong direct beam.

As an illustrative example, the simulated diffraction pattern from a 500 nm–sized idealized protein sphere (for details see [32]) is shown in Figure 9.6 on the following page. Note that here two detection planes have been simulated, so that the dynamic range is significantly increased and a partial measurement of the central speckle becomes possible. A photon energy of 5 keV was assumed here, which is a good compromise between possible resolution (better at higher energies) and scattering signal from the sample (better for lower energies).

[2]We always assume here samples that are sharply confined to a volume of finite diameter that is considerably smaller than the beam diameter. Otherwise, the sample transmission function at the exit plane behind the sample would be limited by the soft edge of the photon beam, which makes a reconstruction very difficult [96].

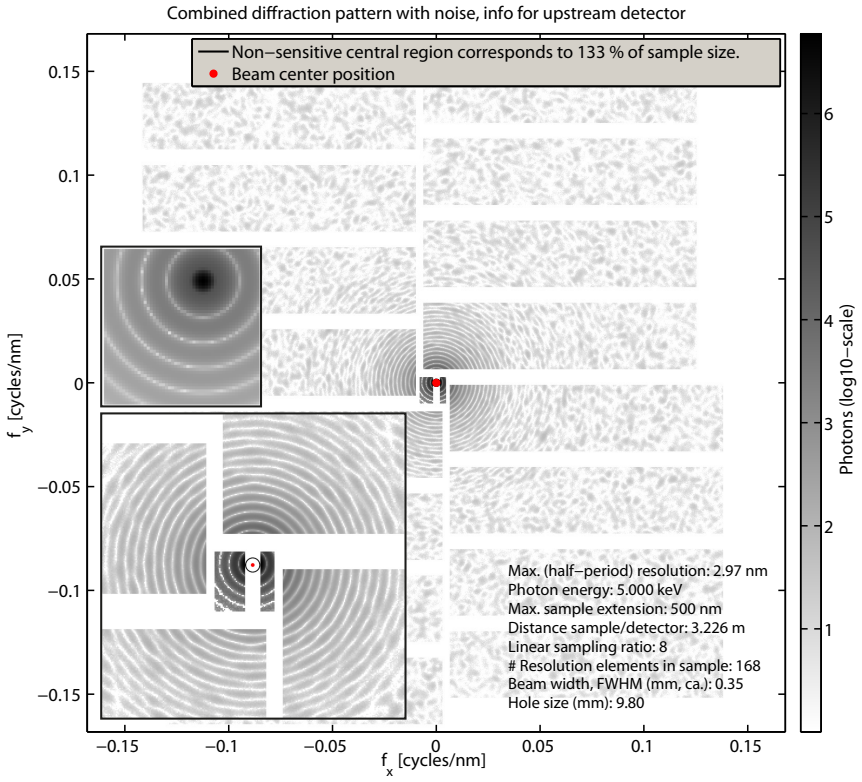

Figure 9.6: Simulated combined diffraction pattern from a 500 nm protein sphere, simultaneously measured with a front (large-angle) and a rear (low-angle) detector. The simulated photon energy is 5 keV. The inset on the lower left shows a magnified version of the small-angle region. As an additional inset, the central region of the ideal, non-noisy diffraction pattern is shown. In contrast to the other two images, this has no missing regions and no (photon) noise added to the expected diffraction signal. By comparing the two insets, it can be seen that the central speckle (the smallest area enclosed by a ring of zero intensity) is partially covered by sensitive detector regions.

The main general results and geometric parameters from the simulations are shown in Table 9.2 on the next page.

Table 9.2: Overview of the simulation results for different sample sizes

	Small particles (20 nm)		**Large particles (500 nm)**			**Huge particles (1500 nm)**	
Detection planes	1	1	1	2	2	2	2
Module layout	Pile	Windmill	Pile	Pile	Windmill	Pile	Windmill
Upstream sample–detector distance [m]	0.403	0.403	1.613	3.226	3.226	5.47	6.17
Sampling ratio	25	25	4	8	8	5	5
Geometrical half-period resolution [nm]	0.39	0.40	1.57	2.97	3.25	5.47	6.17
Number of half-period resolution elements within sample	51	50	319	168	153	274	243
Width of upstream hole [mm]	2.2	2.2	2.2	9.8	12.80	15.1	15.50
Downstream sample–detector distance [m]	n.a.	n.a.	n.a.	6.452	6.452	9.026	10.181
Width of downstream gap [mm]	n.a.	n.a.	n.a.	2.0	2.0	1.5	1.5
Beam width in focus, intensity FWHM [µm]	0.1	0.1	1.0	1.0	1.0	3.0	3.0
Unique reconstruction *prevented*?	With many patterns, no	With many patterns, no	Yes	Probably not	Probably not	Maybe	Maybe

In the following, we summarize and largely reiterate the most important simulation results as they are given in [32] for the AGIPD detector:

- **Detection planes**
  For small reproducible objects from which many diffraction patterns are collected for a single data set, one detection plane is sufficient. For larger ($\gtrsim$ 500 nm), (typically) non-reproducible particles, for which a reconstruction has to be obtained from a single diffraction pattern, two detection planes are required in order to obtain reconstructible data sets at resolutions that are possible from the expected number of scattered photons. Here, the upstream detector with an area of 16 modules covers most of the diffraction pattern, while the downstream detection plane only has to cover a small area that can usually be covered by two modules.

- **Upstream sample–detector distances**
  The required upstream sample–detector distance for coherent single-particle imaging of small particles ($\approx$ 20 nm diameter) is around 0.5 m at a photon energy of 5 keV (see Table 9.2). For medium-sized particles ($\approx$ 500 nm diameter), a

distance of around 3 m is required for sufficient sampling at the same photon energy, and an additional rear detector plane is required. For even larger particles, also measured at around 5 keV, upstream sample–detector distances of at least 5.5 m are required. This, however, necessitates the movement of the SFX apparatus on the rail to accommodate the upstream detector.

- **Upstream and downstream sample–detector distance ratio**
  Depending on the size of the sample and the photon energy, the required sample–detector distance varies by a factor of about 1.5 to 2.5 between the upstream and downstream detector. Generally, larger particle sizes and higher photon energies lead to an increase in the required upstream sample–detector distance. The factor between the up- and downstream sample–detector distance can be slightly decreased in this case, compared to the low-energy/small-particle case. In conclusion, a distance of several metres has to be foreseen between the two detection components.

- **Offsetting the upstream detector**
  To offset the upstream detector from a centre-symmetric position with respect to the beam[3], the whole detector needs to be movable in a plane perpendicular to the optical axis by a few centimetres. Such a translation could also be achieved by a synchronized translation of all four quadrants by the same vector.

- **Quadrant movement**
  The required accuracy of the quadrant movement in a plane perpendicular to the beam axis is on the order of 10 % of the pixel pitch, i.e. around 20 µm. Absolute positioning control of the quadrant movement is essential to allow for a reliable mapping of the physical detector grid onto a numerical analysis grid.

- **Pile layout**
  The “pile” layout provides the essential necessary conditions for the feasibility of quantitative reconstructions.

- **Hole width**
  It should be possible to vary the hole width between about 2 mm to at least 2.5 cm.

[3] The purpose here is to exploit Friedel symmetry in the analysis.

9.2 AGIPD detector

9.2.1 Properties and operating conditions

The Adaptive Gain Integrating Pixel Detector (AGIPD) [42] is one of the three fast 2D detector development projects approved by the European XFEL project team and currently under development. The development is performed in a collaboration between DESY, the University of Hamburg, the University of Bonn, and the Paul Scherrer Institute (PSI) in Switzerland. The AGIPD consists of a hybrid pixel array, with application-specific integrated circuits (ASICs) bump-bonded to a silicon sensor. The ASIC is designed in 8 metal layer 0.13 µm CMOS technology and uses dynamic gain switching to cover a large dynamic range. An analogue signal–processing pipeline is implemented for each individual pixel to store up to 352 frames recorded during the 0.6 ms long pulse train. The image frames are subsequently read out and digitized during the 99.4 ms interval between pulse trains. A veto signal can be processed within the pulse train for identification of frames to be stored. More precisely, the random access capability allows to reuse storage cells as soon as a veto signal is received. The expected performance is shown in Table 9.3 on the next page and the expected detector sensitivity in Figure 9.7.

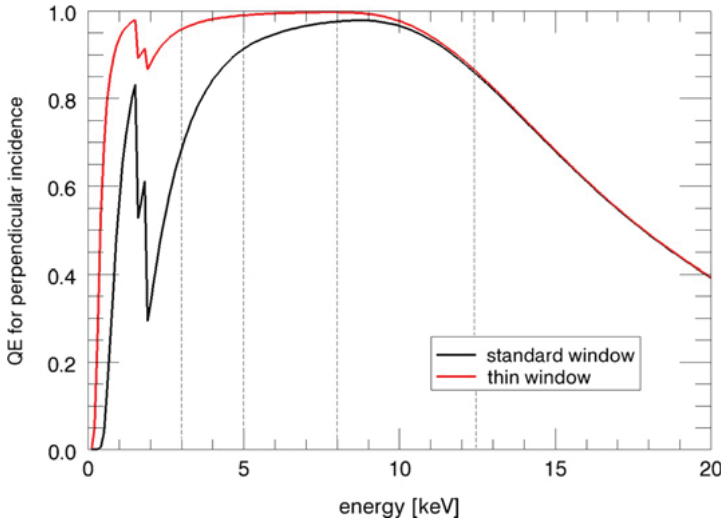

Figure 9.7: Quantum efficiency (QE) of the AGIPD sensor for two different detector entrance window designs. The standard window consists of 500 nm aluminium, while the thin one is five times thinner. Additional differences apply to the sensors. Figure from [7].

Table 9.3: Performance specifications of the AGIPD system

Primary energy range	3–13 keV, optimum at ~ 10 keV	Defined by the quantum efficiency and noise properties of the electronics and sensor; operation outside primary energy range possible, with reduced performance; single-photon sensitivity down to 6 keV
Dynamic range	0–34 Me^-	$> 10^4$ photons at 12.4 keV; 4×10^4 photons at 3 keV
Frame rate	4.5 MHz	
Noise	~ 350 e^- r.m.s.	Before irradiation, not considering radiation damage effects
Storage cells	352	Maximum number of stored frames per pulse train; random access design allows for reusage of storage cell within a pulse train, as soon as veto signal has been received
Sensor thickness	500 µm	Silicon sensor
Pixel size and shape	200 × 200 μm^2	Quadratic pixels, 400 × 200 μm^2 pixels between ASICs on the same module
Number of pixels (total)	1024 × 1024 (physical[a]), 1052 × 1024 (logical[b])	Double-sized pixels between ASICs are split into two logical pixels
Central beam hole	Variable	Max. hole size 27 × 27 mm^2 ; rectangular hole possible; up to 12.5 × 12.5 mm hole off centre; 2 mm slot option
Non-sensitive region between sensor modules	≈ 5.8/1.6 mm or 29/8 pixels (long side / short side)	Defined by space necessary for wire bonding, guard rings and mechanics

[a] I.e. detection units that may have a varying size
[b] Area units of size 200 × 200 μm^2

9.2.2 Integration of the AGIPD into the SPB instrument

Table 9.4 summarizes the operational parameters of the AGIPD system that are relevant for the mechanical integration and operation of the detector at the SPB instrument.

Table 9.4: Performance specifications of the AGIPD system

Detector weight without vacuum vessel	~ 170 kg	Mostly housing and motors, details to be defined
Vacuum vessel weight	TBD[a]	Under consideration
Detector dimensions	TBD	Under consideration
Detector front flange diameter	≥ 500 mm	Depending on integration at beamline; under consideration
Operation pressure	0.001–1 mbar / ambient	For vacuum above 1 mbar, potential of high-voltage breakdown
Sensor bias voltage	500 V, up to 900 V	—
Power consumption	< 28 kW	Detector electronics and cooling
Cooling	—	Julabo FPW91-SL cooling plant; silicon oil cooling liquid (at −40°C)

[a]To be determined

9.2.2.1 Mechanical design

The mechanical design of the AGIPD system comprises a concept for the independent movement of all four detector quadrants (see Figure 9.8 on the following page) as well as the overall housing and vacuum environment of the detector. The current status of the design (see Figure 9.9 on the next page) foresees a hybrid in- and out-of-vacuum system, with eight motors for movement of the quadrants being installed out of vacuum for easy maintenance and better heat dissipation. The module assemblies are mounted onto copper blocks, which are actively cooled using an external cooling plant. The central hole will be adjustable to a maximum diameter of 27×27 mm^2. A rectangular hole, gap modes, and a maximum decentering of the central hole by 12.5 mm relative to the photon beam axis will be possible (see Figure 9.10 on page 133).

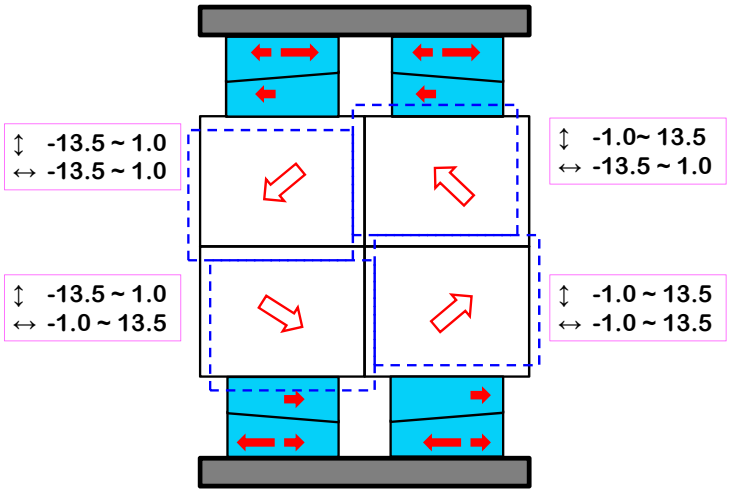

Figure 9.8: Concept for independent movement of all four detector quadrants. The motors are attached to ramped blocks that slide on each other to enable the “iris” opening and closing movement of the central hole. Also synchronous translations of all four quadrants are possible in the horizontal and vertical direction. All numbers in millimetres. Figure courtesy of the AGIPD consortium.

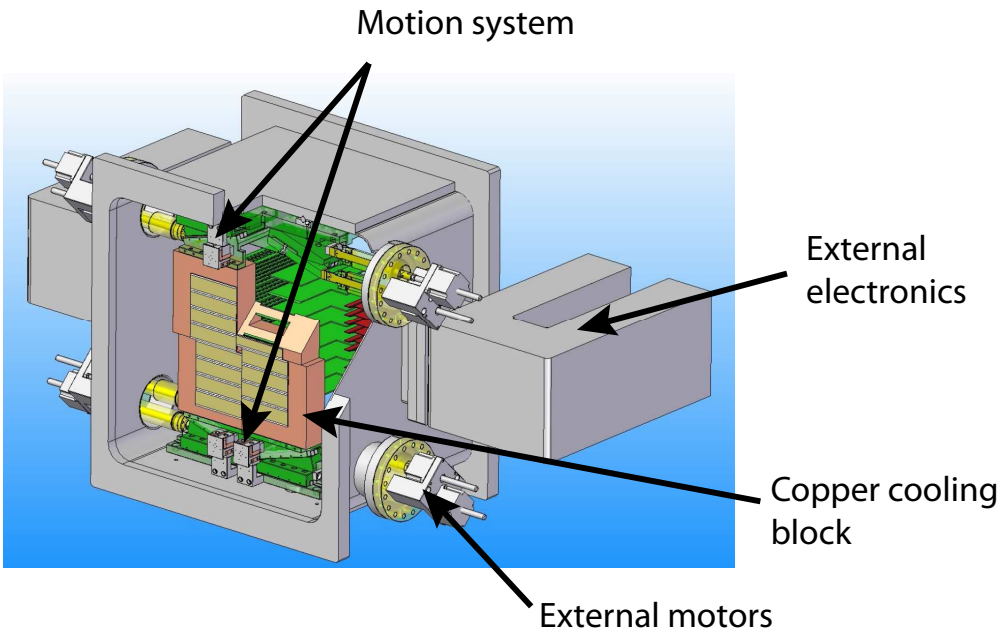

Figure 9.9: Overview on the preliminary technical design of the AGIPD (as of February 2013). Note that the motors for the translation of the detector quadrants are mounted outside of the vacuum of the detector chamber. The same is true for external readout electronics. Figure courtesy of the AGIPD consortium.

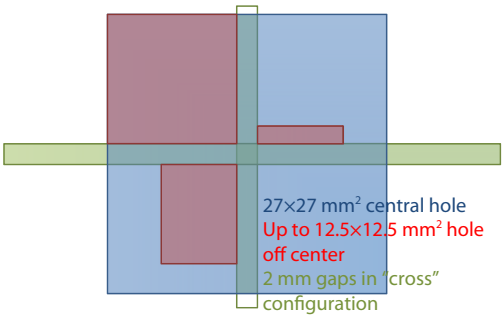

Figure 9.10: Examples of different possible geometrical configurations of the central hole area. The maximum size of the central hole is indicated in blue, and possible geometries of a rectangular central hole are shown in red, while the gaps between all detector quadrants in the "gap mode" are shown in green. Note that not only a cross shape, but also a single vertical or horizontal gap, is possible. Figure courtesy of the AGIPD consortium.

9.2.2.2 Longitudinal distance control

As discussed earlier, different sample sizes and requirements on resolution necessitate the option for a large range of possible sample–detector distances. For easy reference, Table 9.5 summarizes the requirements as given in the simulations presented in [32].

Table 9.5: Typical examples of geometrical parameters for experiments using the AGIPD detector

Application	Sample diameter [nm]	Sample-det. distance [m]	Linear sampling ratio	Photon energy [keV]
Crystallography	~ 500–1000	0.2–0.5	NA	12
CDI	20	0.4	25	5
CDI	500	3.2	8	5
CDI	1500	5.5	5	5

Movement of the front AGIPD device will be enabled by a common rail system that holds all instrument components downstream of the experiment chamber. This will allow continuous variation of the sample–detector distance from as small as possible to distances of several metres. For particles larger than 500 nm, it will be difficult to the reach the required distances, as this would require the movement of the SFX

apparatus downstream on the rail.

The detector chamber will be connected to the sample chamber via a bellow, so that, on the first few hundred millimetres, the sample–detector distance can be continuously adjusted. For larger distances, different flight tube segments will be inserted between the bellow and the detector chamber.

9.2.2.3 Downstream detector

A two-module rear detector version of the AGIPD will be installed on a rail system used in common with the larger front detector (see also Appendix B, “Vibrational, thermal, and mechanical considerations”), but about 6 to 10 m further downstream. The two modules will be movable so that the gap width in between the two modules can be adapted to the beam size. At present, the design for the rear detector is in the concept phase. Ideally, it could also be used as a versatile and portable device for fluorescence detection near the sample environment, and so on. To realize the large dynamic range required for strongly scattering large particles, an attenuator is often necessary upstream of the rear detector [32]. As this should cover the whole module area of both modules, and as it has to be translated synchronously with the detector modules themselves to avoid damage by the strong central beam, the attenuator should ideally be mechanically coupled with the rear detector modules. As attenuator material single-crystalline silicon could be used.

As a further option, the large 4 Mpx detector of the SFX instrument could be used as the rear detector when the SFX instrument is not in operation. The large size of the SFX detector can, however, not be exploited here, as only the small-angle contributions of the diffraction pattern pass through the central hole of the SPB front detector. The SFX detector is also not expected to arrive for “day one” of operation. The smaller downstream SPB detector may, in part, serve the SFX instrument until its own detector is delivered.

9.2.2.4 Open issues

There are some open issues that are currently under investigation by the AGIPD consortium and European XFEL:

- **Sample–detector distance**
  Minimization of the sample–detector distance; a combined effort is made by all concerned parties. The idea of the sensor head protruding

from the housing has been discussed. There is concern that this measure could reduce the overall mechanical system performance. A detailed cost–benefit evaluation has been initiated. Nevertheless, the detector is required to be positioned very close (circa 10 cm from the interaction region.

- **Veto signal**
  Nature of the veto signal to identify frames to be stored; detailed implementation of the vetoing process. More specifically, the veto signal generation has to be fast enough so that the storage cell can be freed and reused again before the pulse train ends.

- **Limiting contamination of the sensor area**
  Contamination of the sensor area by particle debris, solvent, etc.; it is planned to attach a removable transparent foil (e.g. mylar) inside the sample chamber in front of the sensor area. For the passage of the central beam, the foil will be equipped with a central hole. For experiments with long sample–detector distance and a requirement for small-angle signal recording, the foil can be removed. In addition, the challenge of installing a gate valve in between the sample chamber and the detector is considered.

- **Unified interfaces**
  Unified mechanical and DAQ interfaces for all detectors to be able to share them in between European XFEL instruments and to mount them to the calibration infrastructure.

- **Detector interlock protection system**
  Detector interlock protection system for instrument alignment and failure safety.

- ***In situ* calibration**
  Feasibility of *in situ* calibration.

- **Mechanics interfaces**
  Precise definition of mechanics interfaces and responsibilities.

- **Subcomponent interfaces**
  Interference between detector subcomponents in terms of thermal-, electrical-, and background-related issues.

9.3 DSSC detector

9.3.1 Properties and operating conditions

The Depleted P-Channel Field Effect Transistor (DEPFET) Sensor with Signal Compression (DSSC) is one of the three detector projects initiated for application at the European XFEL. It has been developed by an international consortium under the leadership of the Max Planck Institute for Extraterrestrial Physics / Max-Planck-Halbleiterlabor in Munich, Germany. A single quadrant is expected to be delivered in 2015, with the full system following in 2017. The detection principle is based on a pixellated hybrid silicon sensor where each pixel contains a field effect transistor as the main amplifier component [72]. For an optimized charge removal process from the centre region of the pixel, a hexagonal shape (side length 136 µm, pixel pitch (hor. × vert.) 204×236 µm^2) has been chosen. A dedicated design of the DEPFET sensor provides a non-linear amplification characteristic, which allows to measure single photons with high sensitivity in combination with a comparably high dynamic range. Within a pulse train provided by the FEL, 640 frames can be stored within the detector electronics before transport to the European XFEL data acquisition system during the inter-bunch gap of about 99 ms. A frame-to-frame selection of frames to be stored ("hits"), based on a veto signal, is possible.

In contrast to the AGIPD system, which is optimized for photon energies around 10 keV, the optimum energy range for the DSSC detector is substantially lower, namely 0.5–6 keV. Nevertheless, the detection efficiency of the 450 µm thick silicon sensor of the DSSC detector has a quantum efficiency above 90% over the whole energy range of 3–10 keV. The DSSC detector is planned to be used particularly for single-particle imaging experiments in the energy range of 3–6 keV where single-photon counting is expected to be required.

The main performance parameters of the DSSC detector are summarized in Table 9.6 on the next page.

Table 9.6: Performance specifications of the DSSC detector system (see also [72])

Primary energy range	0.5–6 keV	Defined by the quantum efficiency of the sensor and detector radiation hardness; operation outside primary energy range possible, with reduced performance. Due to radiation damage issues, operation above 6 keV should be avoided.
Dynamic range	Single photons up to 2.3×10^4 photons	At 3 keV; depending on frame rate and other settings; higher dynamic range possible without single-photon sensitivity
Frame rate	Up to 4.5 MHz	Max. dynamic range at 4.5 MHz: 8.3×10^3 at 3 keV and single-photon sensitivity
Min. noise	$\sim 100\ e^-$ r.m.s. at 3 keV	—
Storage cells	640	Maximum number of stored frames per pulse train
Sensor thickness	450 µm	Silicon sensor
Pixel size and shape	Hexagonal, side length 136 µm	—
Number of pixels	1024×1024	Arranged in 4 quadrants of 2×4 units of 128×512 pixels
Central beam hole	Variable	Independent movement of quadrants possible
Non-sensitive area between sensor modules	20×8 pixels	long side × short side
Non-sensitive area between quadrant modules	20×13 pixels	—

As the DSSC detector is not the primary detector at the SPB instrument and as it will only be available as a later option, the mechanical integration is still in the early stages of development. For the anticipated use case of the DSSC at the SPB instrument, i.e. single-particle imaging at the low photon energy range of 3–5 keV, it is foreseen to unmount the front AGIPD detector from its position in the SPB instrument and to replace it temporarily by the DSSC detector. Therefore, the mechanical housing of the DSSC detector should be compatible with the mechanical environment of the AGIPD detector.

Some parameters relevant for the operation of the DSSC detector are summarized in Table 9.7.

Table 9.7: Performance specifications of the DSSC detector system

Detector weight w/o vacuum vessel	~ 80 kg	Mostly housing and motors, details to be defined
Vacuum vessel weight	TBD[a]	
Detector dimensions	TBD	
Detector front flange diameter	TBD	
Operation pressure	$< 10^{-5}$ mbar	
Sensor bias voltage	150 V	
Power consumption	< 25 kW	Detector electronics and cooling; peak power consumption
Cooling power	~ 10 kW	

[a] To be determined.

9.4 Additional day-one options

As the DSSC detector will not be ready for use when the European XFEL starts user operation in 2016, additional options for 2D detection at lower photon energies for “day one” have been investigated. As a result, two additional 2D detector systems have been chosen as portable optional devices that can be used throughout the European XFEL facility: the FastCCD [22], developed by Lawrence Berkeley National Laboratory in Berkeley, USA, and the pnCCD [94], developed by Max-Planck-Halbleiterlabor in Munich, Germany.

Neither the FastCCD nor the pnCCD offer the high frame rate that is required to follow a 4.5 MHz pulse train of the European XFEL. As a consequence, they can only be used at a frame rate of 10 Hz at the European XFEL. Nevertheless, they offer a central advantage over the faster detectors, namely a smaller pixel size of $75 \times 75\ \mu m^2$ (pnCCD) and $30 \times 30\ \mu m^2$ (FastCCD). A pnCCD will be available as a single module of 256×256 pixels, with the acquisition of a 1 Mpx device currently being under consideration. The FastCCD will be equipped with a fixed-size central hole and offers 1 k $\times$ 1 k pixels (in frame storage mode, max. two frames per pulse train) or 2 k $\times$ 1 k pixels (in continuous mode, max. one frame per pulse train).

The main performance parameters of the two detectors are summarized in Table 9.8 on the next page.

Table 9.8: Main performance specifications of the pnCCD and FastCCD detector systems

	pnCCD	**FastCCD**
Technology	CCD	CCD
Pixel size	75×75 µm^2	30×30 µm^2
Detector size	1 k$\times$ 1 k	1 k $\times$ 2 k (continuous readout), 1k $\times$ 1k (frame storage readout)
Tiling, hole	Two halves with central gap	Monolithic, fixed hole
Quantum efficiency	$>$ 95% (0.3–13 keV)	$>$ 80% (0.3–6 keV)
Sensor thickness	450 µm	200 µm
Energy range	0.05–20 keV	0.25–6 keV
Dynamic range	10^3 ph at 12 keV	2.6×10^2 at 12.4 keV up to $> 1.1 \times 10^3$ at 2 keV
Noise	2e$^-$ r.m.s.	25e$^-$ r.m.s.
Frame rate	200 Hz	200 Hz (1k $\times$ 1k)

10 Sample delivery techniques

Chapter authors: N. Reimers[1], A.P. Mancuso[2], S. Bari[3], C. Uetrecht[3], J. Schulz[3]

To observe biological structure in a state most resembling the native state, one should ideally have the capability to work with hydrated, non-frozen biological samples. Two types of sample injectors presently in use at X-ray sources are liquid jets and gas phase streams. Both are able to produce highly collimated, high number-density, continuously flowing, hydrated sample streams. Both produce sample streams without confining walls or supports—no part of the injector reaches into the X-ray interaction region; as a result, the injector itself does not contribute to the background signal. Furthermore, pulsed sample sources are under development, which would allow the injection of sample at the 10 Hz pulse train rate, optimizing the use of what is typically very precious sample fluid.

10.1 Liquid jet

Liquid-jet systems can produce stable streams of particles in liquid suspension. Liquid jets with diameters below 1 µm have been developed at Arizona State University [23] and successfully used for nanocrystallography in many experiments by Henry Chapman's group from CFEL at the SLAC Linac Coherent Light Source (LCLS) and the DESY Free-Electron Laser in Hamburg (FLASH).

Handling of liquid jets in vacuum sets high demands on the pumping system. To avoid too high a gas load from the evaporating solvent, the length of the free jet in vacuum should be as short as possible. To avoid contamination of the detector (from sample and solvent dispersed in the sample chamber), a catcher system is required. This catcher is designed to accept the majority of the solvent and ideally all the suspended specimen therein. For catching the liquid jets, three different methods are in consideration. The liquid can be frozen out in a cold trap, it can be pumped away as a gas, or it can be recaptured in the liquid phase. The Sample Environment group (WP79) will perform tests to evaluate each of these methods in the near future.

WP79 is developing a versatile liquid-jet environment to be used within the SPB

[1]Central Instrumentation Engineering (CIE) group, European XFEL GmbH, Albert-Einstein-Ring 19, 22767 Hamburg, Germany
[2]Scientific Instrument SPB group (WP84), European XFEL GmbH, Albert-Einstein-Ring 19, 22767 Hamburg, Germany
[3]Sample Environment group (WP79), European XFEL GmbH, Albert-Einstein-Ring 19, 22767 Hamburg,Germany

sample chamber (see Figure 8.2). This setup will combine an adjustable nozzle holder and a liquid catcher for sample recovery. Both parts will be independently exchangeable to facilitate the adaption of the setup in response to future developments as well as to accommodate special requirements.

In its initial configuration, the liquid jet consists of a convergent quartz glass nozzle that is fixed in a custom-made polyether ether ketone (PEEK) holder and connected via a capillary tubing to a high-performance liquid-chromatography (HPLC) pump, which drives the liquid jet typically at 10–50 bar pressures, providing jet flow speeds up to 120 m/s.

The liquid-jet diameter can be chosen freely in a range from approximately 5 µm to 200 µm. The lateral jet stability is better than 1 µm at 1 mm distance from the nozzle exit. The maximum length of the uninterrupted cylindrical section of the liquid jet is 3 mm for 5 µm diameter jets. It increases rapidly with increasing jet diameters (reaching 20 mm length for 15 µm jets). Narrower jets have been made down to 2 µm diameter with this system. Lower jet diameters need more development for stable function. A broad range of solvents can be used for jet operation—even volatile and viscous solutions. Precautions should be taken with very corrosive materials.

The nozzle holder can also be equipped with gas-dynamic virtual nozzles that are capable of producing sub-micrometer thin jets [24]. In these nozzles, a helium stream further compresses a liquid jet after leaving a nozzle. The liquid beam can become much smaller, even smaller than the contained particles, with greatly reduced likelihood of clogging the nozzle compared to a conventional nozzle with a similar aperture-to-particle size ratio. The state-of-the-art gas-dynamic nozzles are presently difficult and labour-intensive to manufacture. New designs, e.g. using microfluidic devices for mass production of nozzles, are under consideration and could be readily integrated into our versatile setup.

The liquid-jet solution is returned through a narrow beam catcher aperture that improves the vacuum and allows for re-usage of the material. Heating of the catcher aperture helps to prevent ice formation and drives the condensing liquid to the cooled recycling vessel.

In a vacuum chamber with circa 1500 l/s turbomolecular pump capacity and using an additional, liquid nitrogen–filled, 2 litre volume hang-down cryotrap, a vacuum in the 10^{-5} to 10^{-6} mbar range is reached for these water microjets—well within the sample chamber's vacuum specifications (see Section 8.1.1, "Vacuum requirements").

Figure 10.1 on the facing page shows a sketch of a compact liquid-jet setup

(Microliquids GmbH) with a liquid microjet and the beam catcher unit. All movements of microjet and beam catcher are implemented by in-vacuum stepper motors. This solution allows the most compact design of the setup and allows the liquid-jet setup to be easily replaced with other sample environments, such as fixed targets or gas sources. Both the liquid delivery and recapture, as well as the electric connections for motors and diagnostics, will be fed through the flanges with flexible connections.

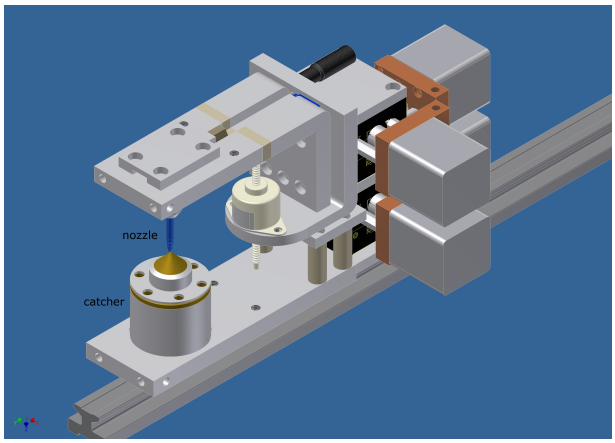

Figure 10.1: Scheme of the compact liquid-jet setup (Microliquids GmbH)

In close contact with WP79, the technical design of the injector will be further developed and optimized for use in the sample chamber at the SPB instrument. Construction, maintenance, and commissioning of the liquid-jet setup will be organized by WP79 in its own sample environment test vacuum chamber. The design will take requirements of flanges sizes and distances, as well as necessary space restrictions into account.

10.2 Aerosol stream

An aerosol sample injector allows the injection of droplets or dry particles from an aerosol into the vacuum chamber. This permits imaging of non-crystalline objects, such as single virus particles or biomolecules, with a considerably reduced background compared to liquid-jet injection. This is of great importance for most of the weakly scattering samples, as these are are expected to produce diffraction data where single-photon events in a detector pixel should be significant [33] and interpretable [55, 111, 71].

Aerosolized samples will be injected in the vacuum through an aerodynamic lens stack. An injector has been developed by Janos Hajdu's group at Uppsala University

(Figure 10.2 on the next page). The current prototype (Mark III) can focus particles of 3–3000 nm diameter into a spot of a few micrometres. During experiments at the AMO instrument of LCLS, a diameter of 15 µm has been measured.[1] The design of the injector aims for the best possible performance for particles in the range of 10–600 nm. The luminosity of this aerosol injector significantly exceeds that of other aerosol injectors, and matches the luminosity of currently available liquid-jet injectors (without the background signal from the excess liquid). Hit rates of 43% on mimivirus and 15% on RNA polymerase have been reached during experiments at LCLS.

As an in-kind contribution (IKC), the Uppsala group will deliver an aerodynamic lens stack optimized for use at the SPB instrument. The injector design includes a particle catcher and a fluorescence detector for quality control. The catcher efficiency should be such that there is no observable contamination from the injection on the camera or chamber interior after one week of normal injector operations. The present version of the catcher system allows injection to be performed with no detectable contamination. This will be independently verified by WP79 upon receipt of the injector.

Alignment of the injector with the FEL beam path can be performed with a laser beam that passes through the aerodynamic lens stack. It will be investigated if this capability can also be used to control the alignment of the sample particles during the injection process.

In close contact with WP79, the injector systems will be optimized for universal use at the SPB instrument and other instruments at the European XFEL that are interested in bio-imaging. The most important parameters to be optimized are the particle beam diameter, the sample throughput, and the hit rate.

[1] Andrew Aquila, personal communication.

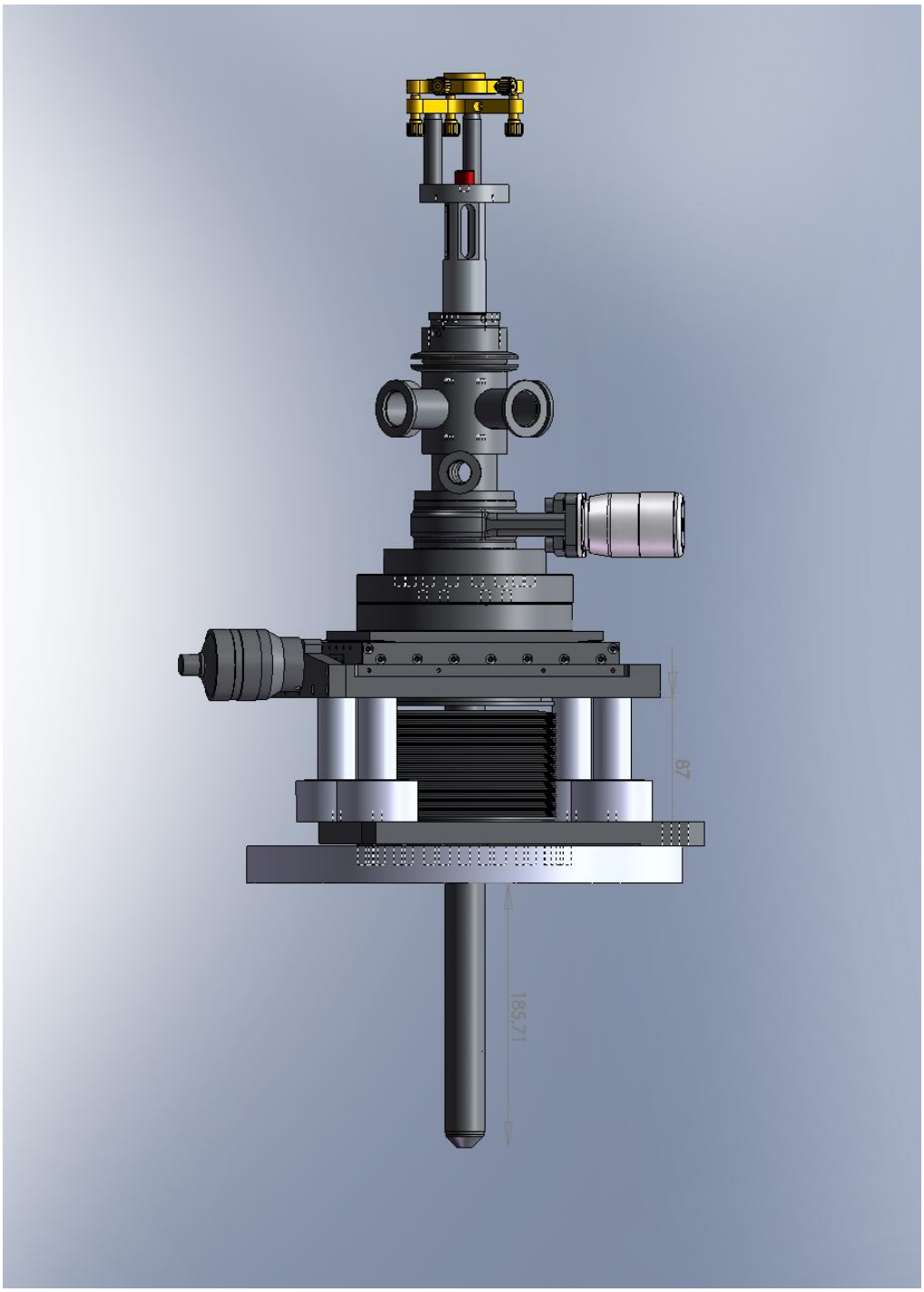

Figure 10.2: Scheme of the aerosol injector. Model courtesy of Uppsala University.

10.3 Ion injection

An additional way one may wish to deliver biosamples to the interaction region is through an ion injector. WP79 is investigating the possibility of implementing native mass spectrometry as a method to deliver biological samples to the beam of the SPB instrument. Quadrupole time-of-flight (Q-ToF) mass spectrometers adapted for transmission of high-mass ions have become available during the last decade [43]. In native mass spectrometry, these are used in conjunction with an electrospray source. This soft ionization technique enables the transfer of intact proteins and non-covalently bound protein complexes into the gas phase and subsequent structural analysis based on mass and shape of the ions [102]. Differential pumping stages allow the ions to transit from atmospheric pressure to the vacuum of the mass spectrometer, providing a low background for X-ray scattering. Studies have shown that most protein complexes retain their structure upon charging and transfer into the gas phase. The technique is very economic in sample consumption; flow rates can be as low as 10 nl/min with protein concentrations ranging from low µM to high nM. Therefore, this technique is ideally suited for scarce or difficult-to-obtain biosamples.

In the first mass analyser, a quadrupole, ions can be selected according to their mass-to-charge ratio, or the entire ensemble can be transmitted. This allows the selective analysis of transient species in reactions or the species of interest in a mixture. Detection of impurities from the production process can be avoided. After the quadrupole, the ions enter a collision cell. This cell can be changed to an ion trap to increase the ion density and function as an interaction region with the FEL beam. Either the interaction with the X-rays can take place in the trap, or the trap can be used to release a cloud of particles synchronously with the bunch trains of the European XFEL. Unused ions can be monitored in the final ToF mass analyser to verify their identity and the influx of particles from the electrospray source.

The technique is also suitable for samples other than proteins, such as nucleic acids, organic polymers, and many more. The analytes can range from a few 100 Daltons (Da) to several million Da, enabling studies on intact viruses [90, 95, 101] with virtually no upper mass limit.

As when using the aerodynamic lens, the sample is required to be in a volatile buffer, such as ammonium acetate. Buffer concentration and pH can be chosen to ensure stability of the protein or protein complex analyte. Even the addition of low amounts of salts (few mM) can be tolerated. This enables studies of conformational changes depending on small ligands or metal cations. Moreover, non-ionic detergents can be

used to study membrane proteins and their complexes [5].

The excess detergent can be stripped off by accelerating the ions in the trap. The optimal experimental conditions for a given sample can be identified before the X-ray beam is delivered. Using the implemented ToF mass analyser, the instrument can also work in stand-alone mode, providing information about sample composition, the stoichiometry and topology of protein complexes, binding affinities, etc. Therefore, this information enables an efficient use of the SPB instrument; how a sample has to be sprayed, and which species are of interest and should be looked at selectively, is known *a priori*. Ideally, users would analyse their samples on a second instrument in the user lab or their own lab well before an experimental run.

The detailed design of the mass spectrometer sample environment still has to be defined. It will likely be based on a Waters Q-ToF modified by MS Vision for high mass. Depending on the maximum tolerable gas pressure in the interaction region with the FEL beam, the collision cell can either be changed into a trap directly, or a smaller trap allowing lower pressures can be integrated afterwards. The trap design is crucial for implementation into the experiment chamber at the SPB instrument. The FEL beam exit pinhole can be gradually changed to larger angles for high-resolution X-ray scattering from biomolecules. In this way, the most suitable design of the trap can be identified to minimize shading on the detectors and maximize ion capacity/density and transmission efficiency. The trap will allow the ions to be squeezed in the longitudinal direction of the trap to increase the density even further and minimize the data acquisition time. Without squeezing, an acquisition time of 1 h 20 min has been estimated for 100 000 patterns with a 1 µm focus. Automated sample delivery systems are commercially available and can be implemented, which enables sample mixing and introduction with a set time delay to monitor reactions in a time-resolved fashion. The basic native mass spectrometer and subsequent modifications require external fund-raising to be realized.

10.4 Additional sample injection technology (optional)

An additional sample injection technology, known as controlled molecules (COMO), has been proposed under the User Consortium Expression of Interest programme [29] by a collaboration led by Jochen Küpper of CFEL, DESY, Hamburg. This injection technology [27, 28] would be able to deliver state-, size-, and isomer-selected samples of polar molecules and clusters. This addition would allow the preparation of “clean” samples for investigations of the quantum nature of larger and more complex molecular systems, as well as the imaging of such systems.

10.5 Motion control of fixed-target samples

In addition to sample injection methods, tools for holding and rapidly changing fixed-target samples are also required—for samples that are simply too rare to be streamed into the interaction region, for nanofabricated samples or certain material samples, and for essential beam-characterizing apertures, such as arrays of double slits [105].

10.5.1 Specifications of motion control in the sample chamber

The fixed-mounting system will have the capacity to include many small samples within the sample chamber simultaneously, to minimize the downtime associated with changing sample. The combination of many samples (which implies a large travel range) and small X-ray beams (less than 100 nm) places stringent requirements on the sample stages used to position the fixed samples in the beam. Suggested parameters would be in-vacuum stages that can travel up to 200 mm horizontally and 50 mm vertically, with reproducibility of position better than 10 nm.

Along the z-axis (the direction of the XFEL beam), the stage should be able to travel up to 200 mm with a resolution better than 10 nm. The stage should be able to take a load of approximately 300 g plus the weight of the x-stage. For the x-axis orthogonal to the beam, the same requirements apply for the resolution. The travel range of this stage should be 50 mm and the expected maximum load 300 g. The elevation stage for the y-axis needs to be of relatively small dimensions, as the space in the chamber is limited. It should be able to carry the other stages and the sample setup with a travel range of a least 12 mm. The resolution should be better than 10 nm. If angular control is required for certain experiments, a rotation stage can be added to the stage stack.

10.5.2 Motors for sample control meeting the specifications

Linear stages that meet our requirements for the z- and x-axis could be provided by SmarAct (model SLL-C42 or SLC2475) or by PI miCos (model PPS-28) as piezo-driven stages. An option with a stepper motor would be the model UPM-160 by PI miCos.

Possible solutions for the y-axis (lift) would be a vertical setup of the above-mentioned

SmarAct stages or the 5103.A10 model by Huber. More detailed informations about these stages are given in Tables 10.1, 10.2, and 10.3.

Table 10.1: Parameters for the linear positioner SLC2475 by SmarAct

Parameter	Value (range)	Unit
Load	120	N
Travel range	ca. 49	mm
Resolution of sensor (nanosensor)	1	nm
Repeatability	75	nm

Table 10.2: Parameters for the linear stage UPM-160 by PI miCos

Parameter	Value (range)	Unit
Load	350	N
Travel range	ca. 55–205	mm
Resolution	1	nm
Repeatability	35	nm

Table 10.3: Parameters for the elevation stage 5103.A10 by Huber

Parameter	Value (range)	Unit
Load	300	N
Travel range	15	mm
Accuracy	100	nm
Repeatability	100	nm
Resolution (depending on encoder system)	1	nm

An example of a three-axis stack that meets these requirements is shown in Figure 8.4 on page 113.

11 Optical laser for pump–probe experiments

Chapter authors: A.P. Mancuso[1], A. Aquila[1], G. Palmer[2], M. Lederer[2]

11.1 Optical pump requirements

The availability of ultrabright, ultrashort pulses of X-rays gives rise to the possibility of investigating the behaviour of samples on the femtosecond timescale. In particular, pump–probe experiments are possible, where the sample is perturbed, or "pumped", with a source of radiation, and the resulting state, some time delay later, is measured, or "probed", with an often different source of radiation. In particular, an optical laser pump and an FEL probe are a powerful way to observe temporal changes in the structure of a sample triggered by the optical laser and observed with the tools of single particle imaging.

To enable these experiments, an optical laser—with pulse durations comparable to that of the FEL and sufficient pulse energy to excite the expected suite of samples—is required. Ideally, this laser will also operate at the 4.5 MHz intra-train repetition rate of the European XFEL.

The use cases of optical pump radiation are here divided into two distinct cases. Case A considers the very shortest pulses possible of 15–30 fs at a selection of wavelengths. Case B considers much longer pulses, appropriate for probing many biological systems at picosecond and longer timescales, across an almost continuous spectrum of wavelengths, from the infrared to the ultraviolet. These two cases cover the distinct science cases discussed in Section 1.3, "Science case summary", and use two different laser-conditioning technologies, as described below. Both systems are amenable to later upgrade.

11.2 Central pump–probe lasers

The European XFEL will emit high repetition rate pulse bursts at 10 Hz burst rate and X-ray pulse widths down to 15 fs or even below. Off-the-shelf laser technology

[1]Scientific Instrument SPB group (WP84), European XFEL GmbH, Albert-Einstein-Ring 19, 22767 Hamburg, Germany
[2]Optical Laser group (WP78), European XFEL GmbH, Albert-Einstein-Ring 19, 22767 Hamburg, Germany

to match both the required pulse parameters and the timing structure (pulse width and repetition rate), as well as deliver substantial pulse energy, is not available. Hence, at the beginning of 2011, the Optical Lasers group (WP78) of European XFEL embarked on a laser development programme aiming to fill that gap. Based on non-collinear optical parametric amplification (NOPA) [17], a first demonstration, operating continuously at up to 100 kHz, was shown at DESY in collaboration with the University of Jena and Helmholtz Institute Jena. In 2009, this system delivered in excess of 60 μJ, sub-10 fs pulses at 800 nm [79]. The development aims to scale the pulse energy and repetition rate to the mJ and MHz levels, respectively, with a timing structure matching that of the European XFEL (10 Hz train operation, up to 4.5 MHz intra-train) [52]. Due to similar laser requirements for other FELs at DESY (FLASH II), the European XFEL and DESY laser groups have formed a collaboration to address these requirements. For the start of operation of the European XFEL in 2015, it is envisaged that WP78 will provide 800 nm burst mode lasers with pulse durations of around 15 fs and pulse energies of 0.1–0.2 mJ at 4.5 MHz intra-train repetition rate. Furthermore, the system should also be capable of several mJ pulse energy at 100 kHz with a configuration change.

WP78 will provide two optical laser beams in two separate transport vacuum pipes from the central optical pump laser laboratory in the SASE1 area to the SPB/SFX laser conditioning laboratory. The properties of the so-called “PP laser” and “MAL laser” are described in Figure 11.1 on the next page and Figure 11.2 on the facing page, respectively. It is these beams that will be conditioned in the SPB/SFX laser laboratory for final delivery to the SPB and SFX interaction areas.

Synchronization between XFEL and laser pulses, as well as the lowest possible timing jitter and drift of the laser, are basic requirements for time-resolved, pump–probe experiments, including the time-resolved imaging of single particles and biomolecules as well as studies of laser-oriented molecules. The laser is to be synchronized to the XFEL timing distribution system (WP18), which has a prospective timing jitter of around 10 fs (r.m.s.) with respect to the XFEL machine clock. The laser is expected to add little to the pulse-to-pulse jitter and should therefore have the best possible synchronization with the FEL pulses. We budget on the order of 20 fs as the total jitter. There will, however, be slow drift requiring compensation within the laser and possibly also reaching as far as the experiment chamber if drifts due to the beam delivery system are too severe. Ultimately, however, the synchronicity will, of course, also depend on and be determined by the timing jitter and drift of the XFEL with respect to the machine clock.

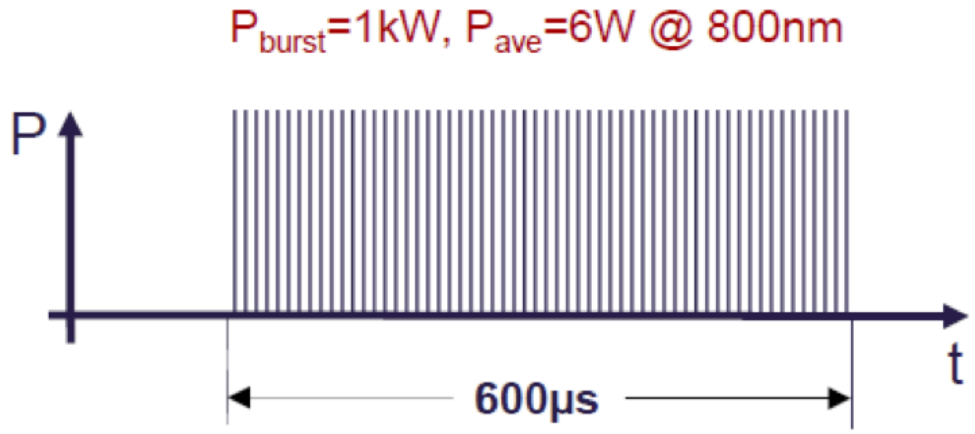

Figure 11.1: High repetition rate operation (PP mode):

- 10 Hz burst, 0.6% duty cycle
- 15–30, 50, 100 fs (in discrete steps)
- 1–4.5 MHz intra-burst, “pulse on demand”
- 1–0.2 mJ per pulse, ca. 800 nm

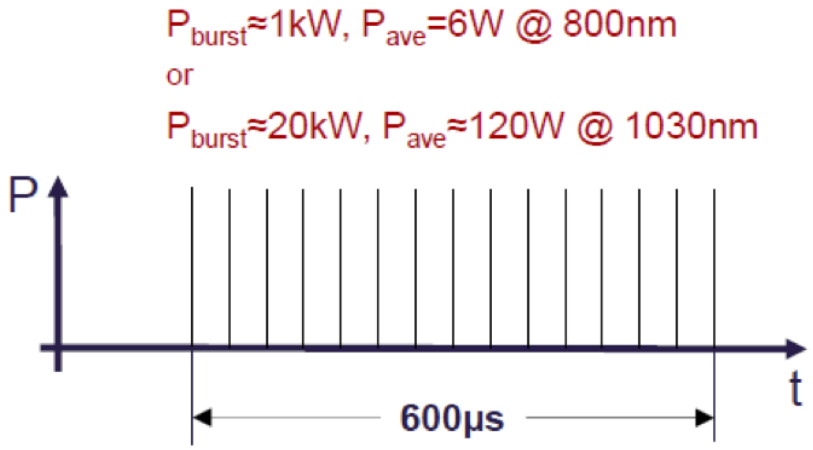

Figure 11.2: Low repetition rate operation (MAL mode):

- 10 Hz, 0.6% duty cycle
- 200 kHz intra-burst, “pulse on demand”
- sub-20 fs, > 3 mJ per pulse, 800 nm (or ps or ns, ≈ 0.1 J per pulse, 1030 nm)

11.3 Laser conditioning and delivery to the SPB and SFX interaction areas

To fulfil specific user requirements, SPB will need to change pulse properties in some cases. A general optical layout has been conceived that will give profound flexibility with respect to these demands.

The typical laser requirements can be divided into two cases:

- **Case A: Very short pulses**
  Very short pulses (from 15–30 fs to 100 fs, in steps of 5 fs) at 800 nm with the option to generate the second harmonic (SHG: 400 nm) and the third harmonic (THG: 266 nm) to allow for a shorter wavelength range. Here, jitter and management of the temporal overlap with the X-rays will be mandatory to achieve adequate time resolution for experiments. This case implies a thorough dispersion and non-linearity concept to provide the shortest pulse duration at the sample inside the chamber.

- **Case B: Long pulses**
  Long pulses in the range of 800 fs (compressed) or 500 ps (uncompressed) with the highest possible pulse energies up to 100 mJ (200 kHz). The fundamental wavelength of the PP laser amplifier of 1030 nm therefore delivers the highest energies. Similar to the previous case, optional SHG and THG will be applicable. Additionally, spectral tunability from approximately 200 nm – 20 µm will be realized by utilizing optical parametric amplifiers, such as ORPHEUS or TOPAS by Light Conversion Ltd. Because these Case B users will investigate processes much longer in duration than the few-fs regime, no overlap technique is designated, and timing is expected to be performed using a suitable photodiode. A delay line will be installed for pump–probe scanning.

The following section gives an overview and details about the current status. Distinct parts and components are undergoing evaluation in close collaboration with WP78 and may be subject to change. Figure 11.3 on the next page illustrates the most recent layout.

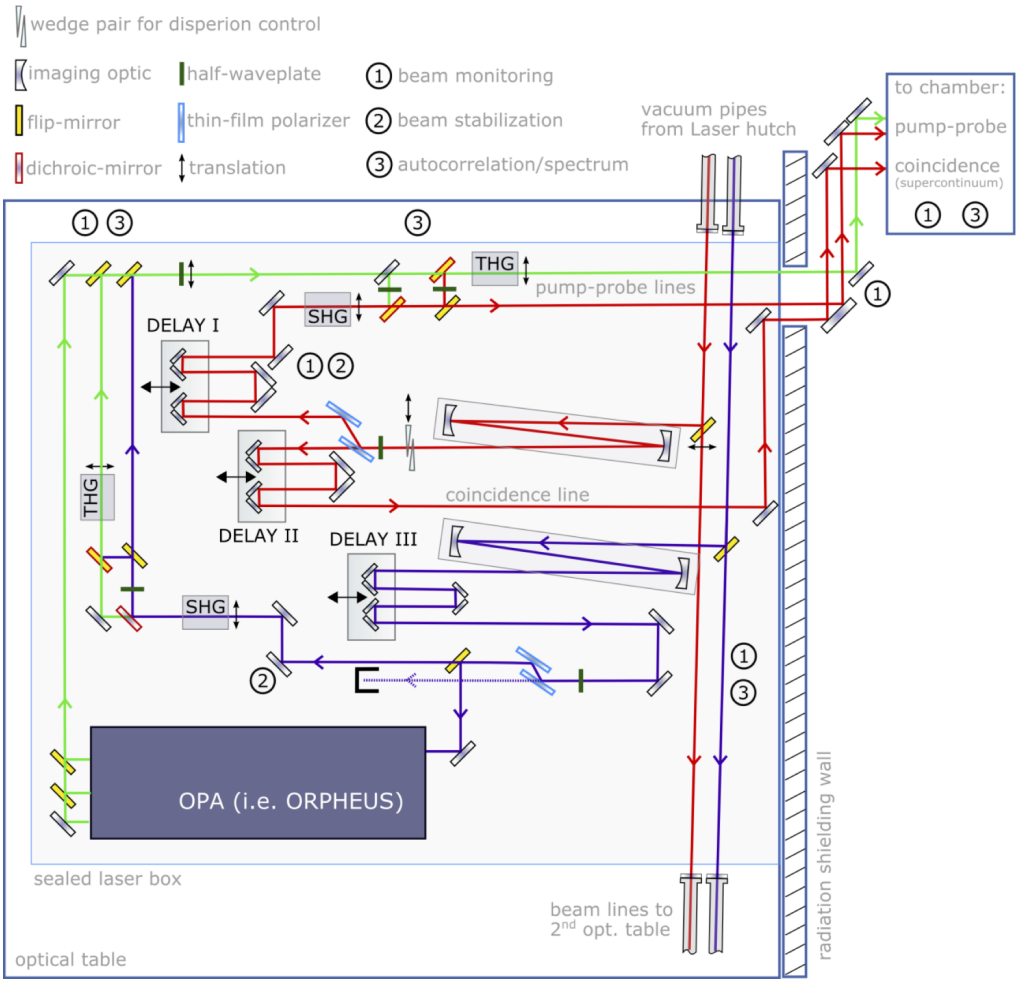

Figure 11.3: Schematic drawing of optical laser setup in SPB laser hutch

11.3.1 Frequency conversion and compression for SPB and SFX

In Case A, the beam will be picked up from either entrance beamline with a displaceable mirror. After relay imaging, it will be divided into a temporal-overlap arm and a pump–probe arm. The attenuator ($\lambda/2$ waveplate and thin-film polarizers) permits a continuously tunable energy splitting. However, it is currently subject to evaluation, as polarizers may introduce too much chirp (pulse broadening). In that case, reflective optics can be used instead. Delay Line I is responsible for pump–probe scanning, whereas Delay Line II is a manual translation unit to compensate any coarse path differences between pump–probe and coincidence beam. Displaceable SHG and THG units offer frequency conversion, and waveplates ($\lambda/2$, $\lambda/4$) serve as polarization control for the actual experiment but also for THG (i.e. type I–critical phase matching in beta barium borate (BBO)). All reflective mirrors must be equipped with very low dispersion coatings for the respective wavelength operation

regime. In the current design, the 15 fs long pulse will enter the SPB laser hutch negatively chirped to 300 fs pulse duration. Its dispersion is conjugated to fused silica. When propagating through fused silica components with pre-determined length, it will finally be compressed by the vacuum chamber window to the 15 fs bandwidth limit. The fused silica “budget” will be on the order of 30–40 mm length. A pair of fused silica wedges will make fine-tuning possible. The drawing does not include any fused silica imaging optics close to the chamber (i.e. for focusing).

The Case B setup has much lower constraints on dispersion. On the other hand, mirrors need to supply sufficient damage thresholds. Adding to this the variety of different wavelengths, calls for flexible mirror solutions. It means that some mirrors and the chamber window should be accessible and easy to exchange, respectively. In the figure, the purple line represents the optical path. In principle, the long-pulse beamline resembles the previous one (relay imaging unit, pump–probe delay line, attenuator, SHG, THG, and polarization control), although it foresees an optional optical parametric amplifier to realize tunability over a very broad spectral range (desirable: 200 nm – 20 µm). Commercial devices are currently being evaluated and selected.

In Figure 11.3 on the preceding page, numbers stand for monitoring and control locations where pulse properties should be analysed and corrected, if appropriate. Some of these observation points are locally flexible, whereas others may need to be fixed (i.e. beam stabilization in the red line after delay lines). The assembly will be mounted on an optical table that is mechanically damped and possibly passively stabilized against thermal drifting. A sealed box will shield the setup from any potential external perturbations, and the entire table(s) will be enclosed within a dedicated laser conditioning room. The vacuum delivery pipes will not hold any mirror mounts (purely transmitting) and will be decoupled from the optical configuration to ensure maximum stability. The design is regarded as the initial system, and further extensions may be added at a later stage. Possible changes could include simultaneous operation of different pulses (length, wavelength, spectra, beam size, etc.).

Pending input from the SFX user consortium, an identical laser setup could be duplicated in the same SPB/SFX laser hutch near the SFX interaction region for use at the SFX interaction region. Alternatively, the SFX user consortium may define a different pump laser apparatus within this laser room that utilizes one or both of the central pump laser beams. For an overview of the laser room locations, see Figure 11.4 on the next page.

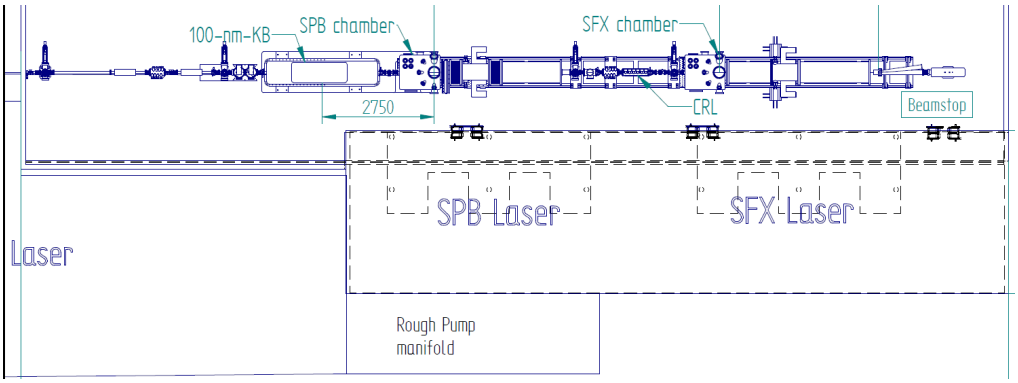

Figure 11.4: Overview of the central laser hutch, SPB experiment hutch, and SPB laser hutch. The close proximity of the SPB and SFX laser tables to the respective interaction regions minimize jitter and drift.

11.3.2 Supercontinuum and timing

Fast timing between the conditioned optical pump pulse and the subsequent X-ray probe pulse, as described in Chapter 7, “Instrument diagnostics”, is in most cases expected to require a source of continuum radiation. This may also be supplied from the central lasers via the instrument laser room. Continuum radiation can be generated from a variety of bulk materials [12] by driving them with a pump laser. Alternatively, gases may also be used—though the drive energies required are higher. The required pump laser characteristics are satisfied by the central optical lasers provided by WP78 [13, 77], and, with some restrictions, a bulk material continuum generation can be performed at repetition rates compatible with the 4.5 MHz repetition rate of the European XFEL [12].

Example bulk materials could include sapphire for the shortest pulse durations ($<$ 100 fs), while YAG could be more suitable for pulses longer than 100 fs [13, 77].

For timing, the delay between the optical and X-ray pulses may be measured using two complementary tools, which are described more fully in Section 7.2.6, “Timing diagnostics”.

12 Conclusions

12.1 General conclusions

This document presents the technical design of the Single Particles, Clusters, and Biomolecules (SPB) scientific instrument, including the incorporation of an additional user consortium–proposed interaction region for nanocrystallography. This 3–16 keV, forward-scattering, in-vacuum instrument will be incorporated with a variety of sample delivery methods, in particular (but not exclusively) suited to biological specimens. The use of mirror technology for focusing to the 100 nm–scale and the micrometre-scale spot sizes ensures a high transmission. Future upgrades identified may also provide a high-quality wavefront at these foci, which is beneficial for imaging experiments.

Additional infrastructure to support the instrument has been identified, and is in part also detailed in this document's appendices. User consortia proposals also attempt to address some of these concerns important to SPB science.

It is hoped that this careful, practical, ambitious-yet-achievable design paves the way to a future SPB instrument that performs world-leading imaging science and crystallography during operation of the European XFEL.

12.2 Key timelines

Figures 12.1, 12.2, and 12.3 are some highly simplified key time scales for the development and delivery of the SPB instrument. These are highly simplified as there is a clear deadline to expect beam at the end of 2015, thus constraining the timelines. The most important near- to mid-term timeline is that for the X-ray mirror acquisition, which is described in more detail due to its position on the project's critical path.

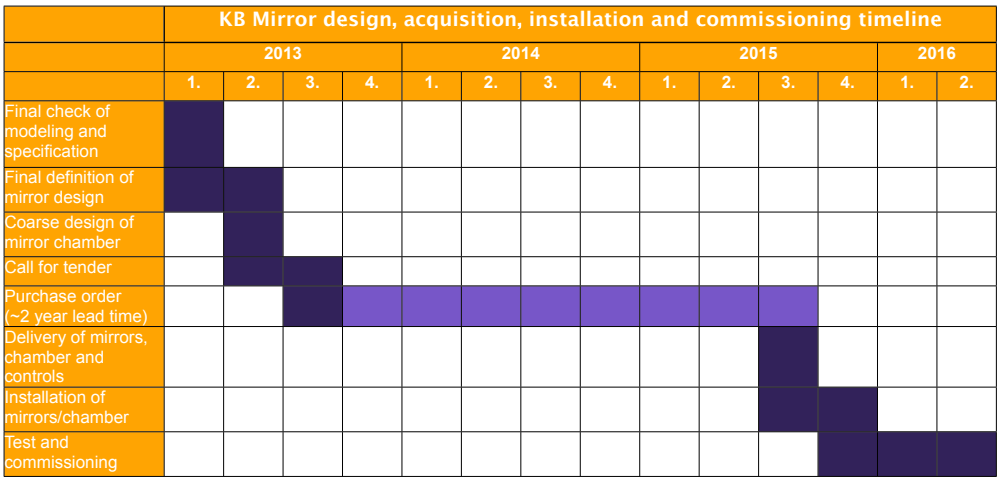

Figure 12.1: Timeline for the design, acquisition, installation, and commissioning of the KB mirrors

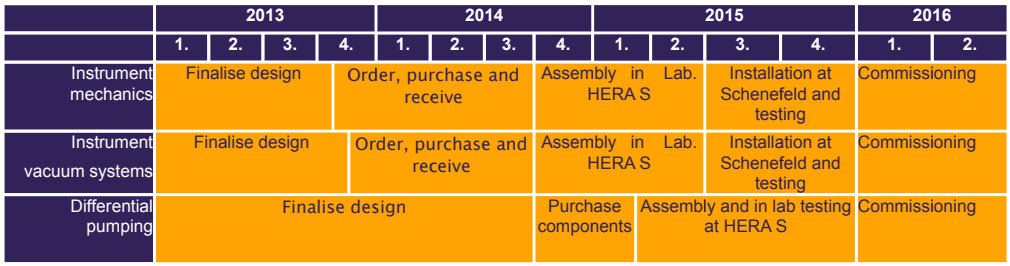

Figure 12.2: Simplified timeline for vacuum and mechanical components of the SPB instrument

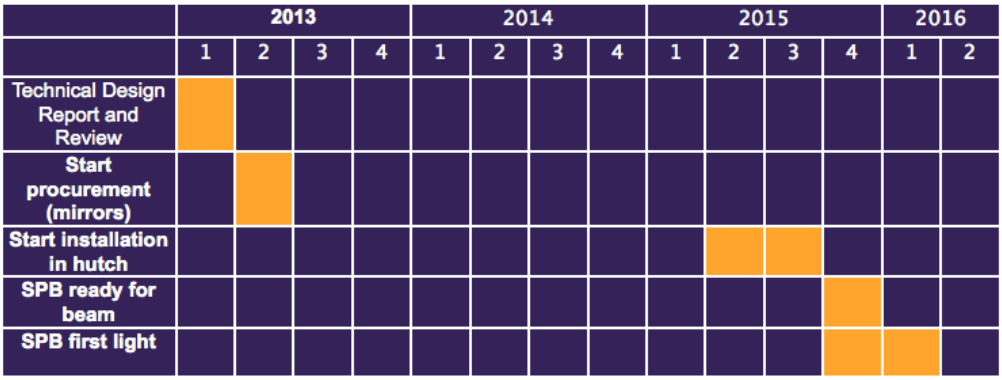

Figure 12.3: Simplified timeline for key SPB-relevant milestones

Part II

SUNDRY TOPICS

A Vacuum concept and design

Appendix authors: G. Borchers[1], A.P. Mancuso[1], A. Aquila[1]

A.1 Preface

To minimize background scattering and absorption due to air in the beam path, as well as to preserve the surfaces of the KB mirrors, the SPB instrument is designed as a fully in-vacuum instrument.

This appendix describes the vacuum requirements of the SPB instrument, including known sources of vacuum contamination, and the proposed pumping system, which will enable us to reach the target vacuum required to ensure optimal beam properties for the SPB beamline.

A.2 Pressure requirements

In the SPB instrument, wavefront preservation and total instrument transmission are particularly important. Therefore, good vacuum is required throughout the entire beam path. Many of the samples injected into the SPB sample chamber will be liquids or aerosolized gases, making this pressure goal difficult to reach.

The SPB vacuum system can be divided into three vacuum sections: upstream of the sample chamber, the sample chamber itself, and downstream of the sample chamber. The ideal pressure in all three sections would be 10^{-9} mbar. This is considered ultrahigh vacuum (UHV) and could be difficult to reach and maintain, but should be feasible in the optics section. The upstream and downstream vacuum systems will be designed to meet a 10^{-9} mbar standard. However, as stated above, the sample chamber pressure is assumed to rise to around 10^{-5} or 10^{-4} mbar—or even poorer—during operation. Note that the pressure in all three of these sections must be stable and be maintained during an experiment. Also, differential pumping methods will be required, as there can be only minimal interferences in the throughput of the beam, and windows may not be feasible when using the full pulse train.

[1]Scientific Instrument SPB group (WP84), European XFEL GmbH, Albert-Einstein-Ring 19, 22767 Hamburg, Germany

A.2.1 Vacuum contamination

A.2.1.1 Sample injection

In the SPB sample chamber, users plan to illuminate biological samples with the European XFEL beam. One of the best ways to do this is using a stream of liquid running perpendicular to the beam. In a gas-focused liquid jet, the fluid is also surrounded by a shroud of helium. These contaminants significantly affect the achievable vacuum pressure. However, these issues have been addressed in practice in experiments at FLASH and at the CXI instrument of LCLS, and we are confident that using similar technologies (sample catchers, heavy-duty pumping, and so on) will mitigate this source of residual gas.

A.2.1.2 Other leaks

In addition to the known gases and liquids being injected into the sample chamber, normal leaks through valves, connections, and feed-throughs must be expected and accounted for. Also, different materials and coatings pose a threat due to outgassing. These leaks are difficult to calculate accurately, but have been taken into consideration in the analysis and planning of the SPB vacuum system.

A.3 Proposed pumping system

In the experiment hutch, there will be much activity from experiment chamber access, adjusting equipment, and swapping instrumentation (such as adding or removing a spool piece in front of the detector). To achieve and maintain the required pressures, multiple turbomolecular (“turbo”) pumps will be installed along the beamline. There will also be ion pumps and differential pump sections used to separate critical sections, such as the optics. To ensure the initial pumping of the chambers from atmosphere and maintain backing pressure for the turbo pumps, roughing pumps will be required. These roughing pumps will be installed outside of the hutch to reduce noise and vibrations. They will also be fitted with a manifold to allow specific sections to be vented for maintenance, while adjacent sections can maintain vacuum. For more information, see Section A.3.2, “Roughing pumps outside experiment hutch”.

In the sample chamber, a turbo pump with a pumping speed of at least 2000 L/s will be installed. Preferably, a magnetic-bearing pump will be used to minimize vibrations. In addition, a “catch pump” will be attached to the injector shroud to facilitate the removal of the liquids and gases being injected into the chamber.

The differential pump located between the sample chamber and the KB chamber is a critical component. It has been designed to sufficiently separate the different vacuum pressures and will be tested later in 2013. For more information, see Section A.3.1, “Differential pump between 100 nm–scale KB and sample chamber”.

The detector on the downstream side of the sample chamber cannot be exposed to a pressure of 10^{-3} mbar while it is active, as this could lead to shorting. Therefore, other methods of collecting the particles in the sample chamber are being investigated, for example, cryo pumps and cryo sinks.

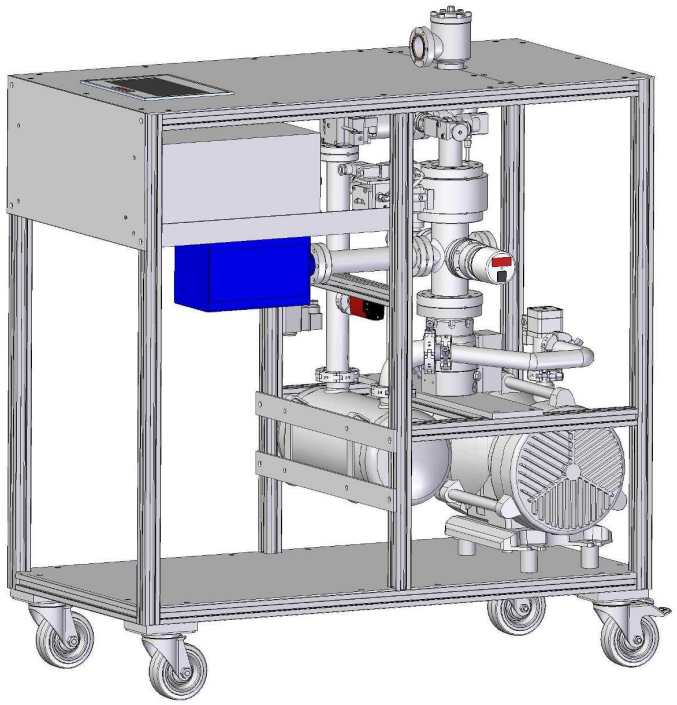

Figure A.1: Pump cart that will be used to pump down sections of the optics hutch. The pump cart includes a roughing pump and a turbo pump, and is designed to pump to pressures adequate for ion pumps. Figure courtesy of WP73.

In the optics hutch, the initial pump-down will be carried out by mobile oil-free pump station carts (Figure A.1). These carts consist of an 80 L/s turbo pump and a 10 m^3/h scroll pump, and have been designed by the X-Ray Optics and Beam Transport group (WP73). The scroll pump is capable of pumping down to 10^{-2} mbar. At that point, the turbo pump will start and pump down to a pressure level where the ion pumps in turn can be switched on. The ion pumps have a low pumping speed but negligible vibrations; they are very stable and good for sustaining ultrahigh vacuum. They will be installed along the optics hutch and flight tube to maintain 10^{-8} or 10^{-9} mbar.

Operation and control of the rough pumping process is done manually, and the exhaust is vented into the hutch. For more information on the pump cart, refer to *Technical Design Report: X-Ray Optics and Beam Transport* [87].

A.3.1 Differential pump separating 100 nm–scale KB and sample chamber

To separate the sample chamber from the 100 nm–scale KB chamber, a differential pump will be used. This differential pump has been custom designed to fit in the allocated space and provide the proper amount of vacuum and particle separation. The ideal vacuum pressure of the 100 nm–scale KB chamber is 10^{-9} mbar, while the worst-case operating conditions of the sample chamber will be 10^{-4} mbar. The design consists of a DN63 flange size “T” that has two orifices on both flange ends. The high-vacuum side orifice has a pipe extrusion into the “T” section. Attached to the branched-off end of the “T” section is a turbo pump (Figure A.2).

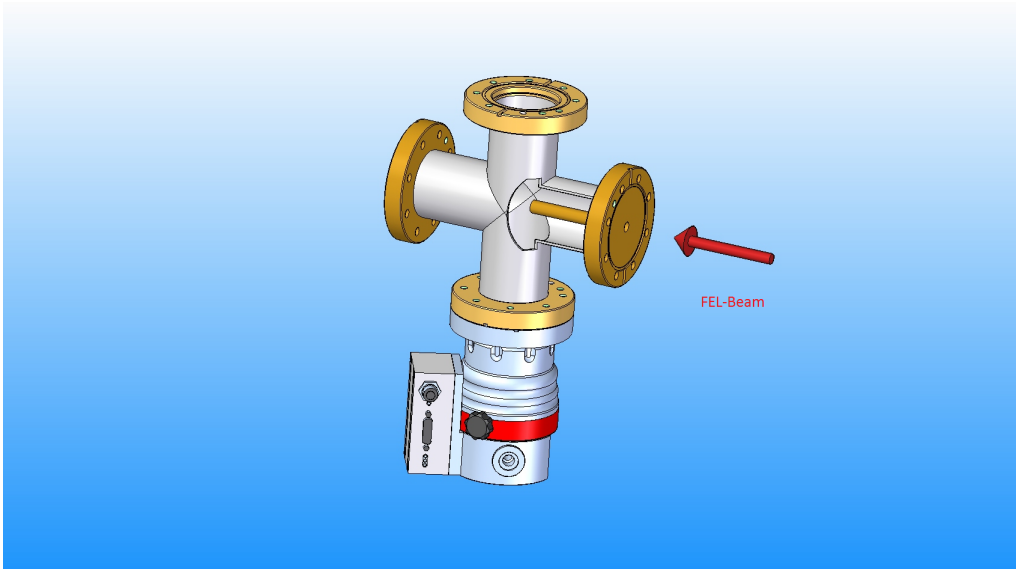

Figure A.2: The differential pump has been calculated and designed to separate the 10^{-4} and 10^{-9} mbar sections of the vacuum system. Note the 8 cm long tube on the UHV side of the chamber. Tests will be conducted later in 2013.

A simulation was conducted to analyse the differential pump design. Assuming a standard outgassing constant and a tube extending 8 cm into the “T” chamber, the design is plausible. The turbo pump needs to be rated to just over 200 L/s. This might require a flange reduction coupling to fit a DN100 Pfeiffer turbo pump onto the DN63

flange.

The required open aperture for this section of the beamline is 2 cm in order to allow all orientations and powers of the FEL beam to pass through. Calculations show that to achieve proper differential pumping pressures, the orifice must be less than 2 cm. This requires the entire differential pump to move with the FEL beam, depending on the mode of operation and the power level. The movement will have to be controlled with a system of motors that can be precision-operated from inside the control hutch. In addition, bellows must be installed on either side to allow sufficient movement and possibly damp vibrations from the pump. An orifice size of only 0.7 cm is required to allow the FEL beam to pass through with plenty of extra room, and the simulation above was done assuming a 0.7 cm orifice.

It is planned to build the differential pump and test it with worst-case scenario situations. Pending the results of the test, alterations to the design can be made that might improve the isolation of particles from the sample chamber to the KB chamber. Such improvements could include: increasing the turbo pump capacity, extending or reducing the length of the high-vacuum tube extrusion, and adding another section, including a third orifice.

Diagnostic devices, including position monitors, will be installed upstream and downstream of the differential pump. Using the position monitors, one can ensure that the differential pump is positioned correctly so that the beam will not illuminate any part of the chamber or aperture.

A.3.2 Installing roughing pumps outside of the experiment hutch

During operation, one roughing pump produces about 57 dB of noise. Besides creating an inhospitable work environment for staff and users, multiple pumps resonating at different frequencies pose a serious threat to the instruments in the hutch, which are extremely sensitive to vibrations. These considerations led to the idea to install the roughing pumps outside of the hutch. An analysis was conducted to prove that lengthening the pipe system by 6 m would not choke the pumps and would be feasible for the SPB experiment hutch. By increasing the pipe length, the volume also becomes greater. Adding volume to a system will always increase the amount of time it takes to pump to the desired vacuum. However, this can be mitigated by additional roughing pumps providing extra pumping power. In addition, a small roughing-pump cart will be used to rough out the SPB and SFX chambers after routine system ventilation. This is to prevent sudden pressure spikes in the backing lines between the other turbo pumps in the system and the roughing pumps.

B Vibrational, thermal, and mechanical considerations

B.1 Vibrations

Ideally, one would prefer to have no vibrations throughout any instrument involving sub-micrometre sizes. Our goal is to avoid amplification or resonances of vibrations across the beamline to meet the stability requirements for the SPB instrument, the most sensitive parts of which are the sample chamber and the KB optics.

Our analysis is based on vibrational data recorded by DESY in the future European XFEL experiment hall (http://vibration.desy.de).

B.1.1 Sample chamber

The sample chamber has to be as stable as possible; any movement larger than the larger spot diameter of approximately 1 µm would not be acceptable. To minimize effects of ground vibrations, the sample chamber will be mounted on a large granite block. This block will also support the 100 nm–scale KB chamber such that any ground motion will vibrate both the sample chamber and the 100 nm–scale optics in phase and at the same amplitude. There will be no roughing pumps in the area. Vibrations from any motors or machinery in the area must be suppressed using dampening techniques.

B.1.2 KB chambers

The KB chambers are the components most sensitive to any movement. Small vibrations of the internal mirrors will be compounded over longer distances (such as that between the optics and experiment hutches) and affect the location of the focal point. For the micrometre-scale KB optics, we have a four-bounce system, which minimizes many forms of angular motion. If the coupled mirror pairs vibrate or rotate as a unit, then the change in pointing or lateral position is negligible.

However, to maintain stability over the 20 m between the micrometre-scale KB system and the sample interaction point, the KB chambers will also be mounted on a block

of granite. Based on the data collected from the location of the future experiment hall, ground vibrations above 90 Hz are well-damped. The use of other dampening materials, such as rubber spacers or optical tables, are options under consideration to further suppress higher-frequency vibrations.

For the remainder of the scientific instrument, all available methods will be used to limit the amount of vibrations. The roughing pumps will be placed outside of the experiment hutch. Extensive use of bellows between components and the use of magnetic bearing turbo pumps will help minimize vibrations. Vibration effects from water-cooling lines will need to be investigated.

B.2 Thermal considerations

Thermal fluctuations can change the conditions of the SPB instruments, affecting such parameters as alignment, sensitive angles, and precise distances and calibrations, or causing undesirable drifts in the position of the X-ray focus. The optics and experiment hutches have been requested to be temperature-controlled to 0.1°C. In the optics hutch, instruments will be fairly stable and access will be limited, allowing the temperature to be maintained at a relatively constant value. The experiment hutch, on the contrary, will be accessed frequently for maintenance of the sample injection system and any other parts of the beamline. Therefore, additional measures are envisaged. Calculations have shown that a temperature difference as small as 0.1°C at the most sensitive instrument, the 100 nm–scale KB chamber, can have a negative impact on alignment. To compensate for this, a plastic or foam shroud has been proposed to encase the chamber and limit the air current around the surface. This is common practice where high temperature stability is required, and has been successfully demonstrated for the micrometre-scale KB systems at the CXI instrument of LCLS.

B.2.1 Expansion calculations

In our calculations, we analysed the maximum acceptable thermal gradient for the hutches. To estimate the drift motion caused by temperature fluctuations, we focused on the transverse drift caused by the horizontal or vertical motion of the mirror chamber with respect to the sample chamber. This analysis ignores bending of the KB mirrors or changes in their pointing.

To calculate the transverse drift, we made the approximation that the X-ray beam is propagating along the horizontal Z axis, and that the reflection angle from the KB

optics is small. Therefore, any temperature difference between the sample chamber and the optics chamber will translate to a 1:1 proportional transverse motion. If we assume that the KB mirror chambers are 1.5 m high and made of Type 304 stainless steel, we obtain the following transverse displacements:

ΔT °C	ΔL μm
1.0	25.4
0.2	5.1
0.1	2.5

To place these numbers in context, the expected sample injector particle spot cross section is of the order of 1–10 μm^2. It is clear that any temperature fluctuations larger than 0.2°C will have an impact on overlap and alignment of the X-ray beam with the sample injector. The thermal stability of the hutch needs to be maintained at better than 0.1°C during operation to ensure transverse thermal drifts do not impact alignment. As stated above, we plan to implement a thermal enclosure around the 100 nm–scale KB chamber to minimize thermal fluctuation and maintain temperature stability.

B.3 Rail system

As we operate two optical configurations produced by mirrors reflecting at different angles from different locations, there will be a shift of the beam angle between these configurations, which causes the optical path to point in different directions. Each time the KB configuration is changed, every device in the instrument must be realigned to the correct location. To mitigate this, we plan to install all of the instruments downstream of the focal point onto one line or rail. In this way, when the KB configuration is changed, the entire rail can be moved to coarsely align all of the components with the new optical path. This also has the added benefit of allowing movement of components in the longitudinal direction on the rail, facilitating detector shifts and movement of the SFX refocusing optics and sample chamber.

The rail system proposed must be 11 m long (Figure B.1 on the following page). This will present some bending and vibrational issues that must be mitigated. The idea to use a large granite air rail, which might reduce the amount of possible deflection and vibration, will also be evaluated. The upstream end of the rail system will move 2 cm in both vertical and horizontal directions, and the downstream end must move 10 cm in order to align the instruments with the different possible optical paths. The (upstream) detector will be the farthest upstream instrument mounted on the rail. It

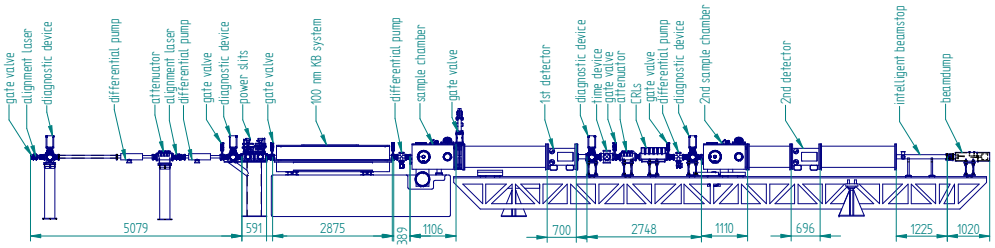

Figure B.1: Side view of the components in the SPB experiment hutch, illustrating the downstream rail and the components it supports

needs to be able to move from directly adjacent to the sample chamber, which is not on the rail, to approximately 6 m downstream. To enable such a system, quickly removable spool pieces will be used to change the length of the required vacuum hardware, and bellows will be installed for fine tuning and required motions during operation. Bellows will be used upstream and downstream of all movable instruments to minimize vacuum forces, and the Z position will be read using an encoder on the rail. Bearings on the rail will be designed to enable components to be lifted straight up and off the rail, or to be set straight down using a crane, eliminating the need to slide the bearings off either end. In this way, diagnostic devices and other instrumentation can be added or moved anywhere along the rail, as needed. As high vacuum is required for all components, flight tube spool sections can be moved or swapped to different locations. This allows for flexibility in the configuration as the Adaptive Gain Integrating Pixel Detector (AGIPD), the timing diagnostics, the SFX compound refractive lens (CRL) chamber, the SFX experiment chamber, the SFX AGIPD, the beam diagnostics, and the beam dump must all be positioned on the rail and may readily be adjusted.

C Additional optical considerations

C.1 Additional optics designs

In addition to the standard KB optics and a four-bounce KB system, both described in the main optics text, we investigated three additional options, which were subsequently eliminated due to lack of feasibility and preference for the four-bounce system.

C.1.1 Single traditional KB optic and single sagittally curved focusing optic

One way to mitigate the large spatial offset of the traditional KB design is to introduce a mirror with sagittal curvature [91] as one of the pair (Figure C.1 on the next page), which results in a reduced offset in at least one dimension by having the reflected and the focused beam propagate in parallel with the through beam (offset of approx. 2 cm or slightly double the 4σ beam size compared to 30 cm for the traditional KB case in the focal plane). The mirror would also require two sagittal stripes, each with a clear aperture of 2.5 mm in diameter. This aperture may appear smaller than the expected 4σ values would dictate. This is mitigated by including a slight pre-focusing bend at the horizontal offset mirrors (HOMs), leading to a smaller horizontal beam size at the entrance to the focusing optics. For a description of the HOMs, see Section 6.2, "Horizontal offset mirrors".

The chief design challenge here is the sagittally curved optics itself, which requires a very short radius of curvature—about 20 cm for the 4 mrad case. This is a challenge for the metrology required to determine if the optics meets height error specifications.

The chief benefit is the simplified X-ray path and working points. When this pair of optics is retracted or removed, a small (few mm) vertical shift is all that is required for realignment of the unreflected, direct beam.

Pros of this design:

- Vastly simplifies X-ray transport
- Simplifies motion of components and working points
- Maintains a high-efficiency two-optic system

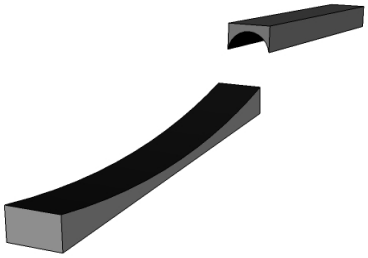

Figure C.1: Pictorial view of sagittally curved optics and standard KB optics

Cons of this design:

- New design comes with many fabrication risks: currently no sagittal optics of this length, nor with the required two coatings, have been fabricated to the required slope error and finish. So far, such slope error and finish requirements have been met for only 450 mm traditional KB substrates.
- No metrology has been developed so far that would be capable of measuring the sagittally curved optics. Such a metrology would need to be perfected prior to optical fabrication.
- Aberrations in slope and figure error could lead to larger focal spot size.
- Aberrations could also produce a worse wavefront.
- Alignment complications could occur as the sagittal mirror is sensitive to rotations.
- If one of the coatings is damaged or deteriorates, potentially a new optics is needed.

C.1.2 Traditional KB optics followed by plane steering mirror oriented at 45°

To achieve the same goal as in a four-bounce KB system while minimizing the number of optical elements used, one can also conceive of using a single 45°-angled plane mirror to steer the beam back onto its original optical axis (Figure C.2). This has the added complication of needing to characterize this plane mirror at a 45° (or non-rectilinear) angle. As the mirror is mounted neither vertically nor horizontally, no metrology currently exists to measure flatness. Also, there are concerns over the sag of such a mirror as the forces are not at right angles to the surface. In addition, the angle of such a mirror would be a factor of $\sqrt{2}$ larger for the same length because of the 45° nature of the reflection (need to compensate both vertically and horizontally). This adds concern as it brings the angle of the optics closer to the damage thresholds.

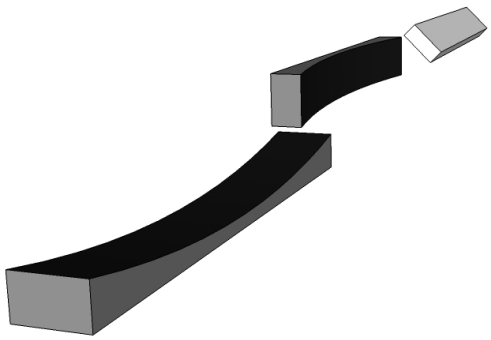

Figure C.2: Pictorial view of a three-bounce system using standard KB optics for two of the mirrors

Pros of this design:

- Simplifies X-ray transport.
- Simplifies motion of components and working points.
- Three-optic system is an improvement compared with four-optic system.
- If optics deteriorates or is damaged, a small lateral translation can restore performance.

Cons of this design:

- Absolute system efficiency is reduced by 10%—potentially more due to the higher working angles.
- There is currently no metrology implemented to measure the gravitational and mounting sag of a 45° mirror.
- Due to the angle limitations of reflectivity, a single mirror would not be able to kick the beam parallel to the direct beam, meaning an angular offset would still exist.
- Additional optics causes additional wavefront distortion, but possibly less than in the chosen mirror setup.
- Additional wavefront distortions will increase focal spot size.
- Alignment complications could occur as there are now three mirrors.
- Additional optics adds expense, though less than a four-bounce system.
- Length of the optics chamber will need to be longer to accommodate the additional optics, but less than for the four-bounce system.
- Mechanical design of KB chamber and mounts will be slightly more complicated.

C.1.3 Traditional KB for the micrometre-scale focus and the same beam transport for the 100 nm–scale focus

Another possible method is to use the traditional KB system for the micrometre-scale focus. The difference arises when switching from the micrometre-scale KB to the 100 nm–scale KB optics. In this case, we insert long flats into the optics positions of the micrometre-scale KB chamber. This plane-reflected beam in then delivered to the 100 nm–scale focusing optics. The pointing of the beam means that there never is an unreflected beam in the SPB hutch and that we will always deflect off the focusing or plane mirrors in the SPB optics hutch. A sketch of this design is shown in figure Figure C.3 on the next page.

Pros of this design:

- Limited working point distance (10 cm of motion instead of 30 cm) to cover theta angles between 3 and 4.5 mrad
- Less radiation shielding required for SPB experiment hutch
- Fewer optics to fabricate
- High efficiency for the micrometre-scale focus

Cons of this design:

- No possibility to use the unreflected, direct beam
- Wider micrometre-scale KB optics with a more complex shape (two curves and a flat section, with four coatings)
- More complex alignment for 100 nm–scale KB optics
- Additional wavefront distortions for 100 nm–scale KB optics
- 20% reduction in efficiency for 100 nm–scale focus

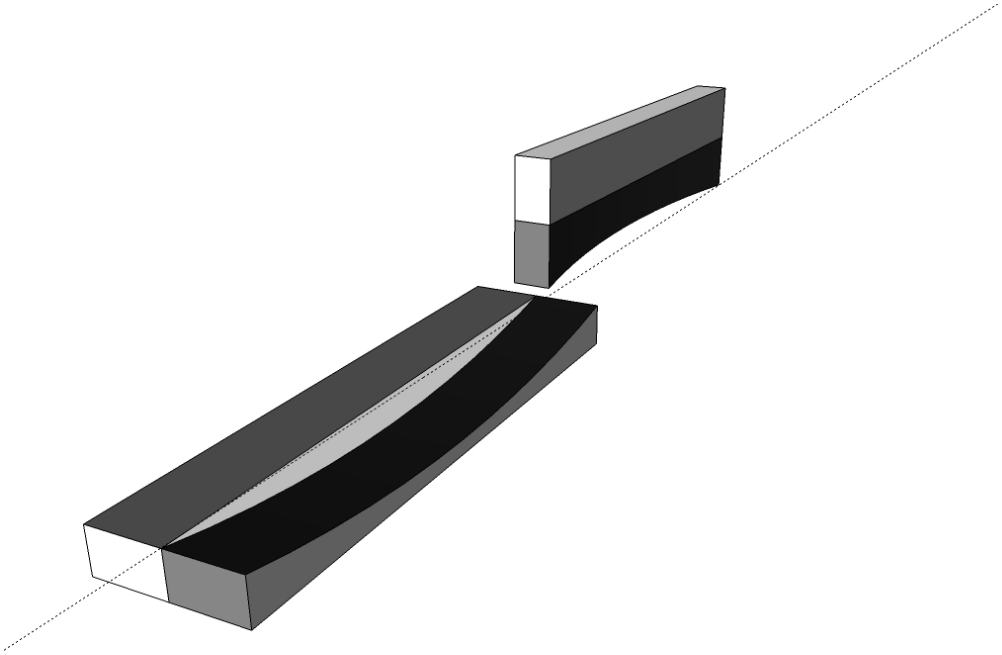

Figure C.3: Pictorial view of the upstream optics if a four-bounce 100 nm–scale KB system were to be used

While the four-bounce micrometre-scale scale and four-bounce 100 nm–scale systems are similar, the choice between them becomes a question of which focal spot requires the higher efficiency and a better wavefront: the micrometre-scale focus or the 100 nm–scale focus. As the 100 nm–scale focus spot will be used for imaging experiments that are photon-starved, while the larger micrometre-scale focus will be used for nanocrystals and large non-reproducible objects with stronger scattering, our preference is towards the four-bounce micrometre-scale focus over the four-bounce 100 nm–scale focus to preserve the 100 nm–scale focus spot. While the flats could be adaptive, this could produce a better 100 nm–scale focus. However, we believe there are more experiments for the micrometre-scale adaptive focus.

C.2 CVD diamond windows

We have conducted both damage simulations and thermal analysis simulations on the possibility of placing a CVD diamond window between the 100 nm–scale focus and the sample chamber. Based on the ray-tracing tool we developed, we estimate that, 40 mm past the vertical KB mirror, the horizontal beam size will be 930 µm FWHM at 8 keV and 570 µm at 15 keV due to the different divergence angles. For comparison, the micrometre-scale focus beam size is 100 µm and 50 µm for 8 keV and 15 keV, respectively, at this location.

For the damage simulation, we took a 1 µJ pulse, adjusted the FWHM beam size, and calculated the dose in the top nm^3at the centre of a Gaussian pulse. The dose was calculated per atom, assuming a bulk density of the diamond film. Even though the front surface suffers the highest dose as the material is optically thin, the results are nearly independent of voxel size. The results show that a single pulse with 50 µm FWHM will be an order of magnitude away from destroying the thin film (Figure C.4 on the facing page). It is worth mentioning that European XFEL also tested damage threshold limits for CVD diamond at SACLA[1].

However, thermal loads are also an issue, as diamond graphitizes between 800 and 1000°C. Even though diamond has a high thermal heat conductivity, we first estimated the thermal load assuming no heat transfer. To calculate the heat load, we assumed a 1 mJ pulse energy and a 500 µm FWHM pulse width and calculated the thermal rise for a single pulse for the centre of the film (Figure C.5 on page 182). The results show that the CVD diamond heats up by only 1°C per pulse at the centre of the pulse for photon energies above 10 keV. Therefore, even in a worse case at this location just 40 mm after the end of the 100 nm–scale KB system, we can sustain 300 pulses at nearly full pulse energy, and possibly a full pulse train under certain conditions if

[1] C. Ozkan, et al., in progress.

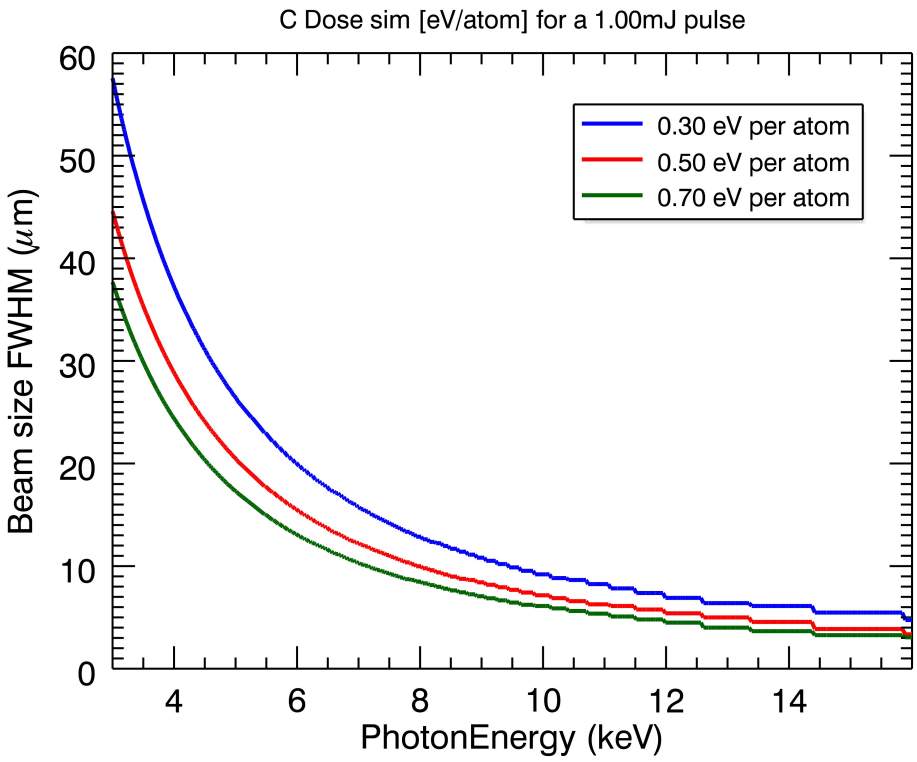

Figure C.4: Approximate damage threshold for CVD diamond

thermal conduction and water cooling are taken into consideration. A more detailed calculation assuming heat transfer is therefore needed to determine the maximum number of sustainable pulses. However, it is clear that a CVD diamond window can sustain Mode 2 of operation as described in *Technical Design Report: X-Ray Optics and Beam Transport* [87].

C.3 Wavefront simulations

It is difficult to conduct simulations on our four-bounce KB optics. The Marechal criterion would suggest we multiply the slope errors by $\sqrt{2}$ to obtain the proper scaling in the height errors. However, this is a statistical argument, with uncorrelated height errors in each optics. While this is most likely true, optics sag or other systematic errors may make the height or slope errors correlate between optics. Therefore, a worst-case scenario would be to multiply the height errors required to produce 50 nrad slope errors by a factor of two. Figure C.6 on page 183 and Figure C.7 on page 184 correspond to Figure 6.16 on page 71 and Figure 6.17 on page 72, respectively.

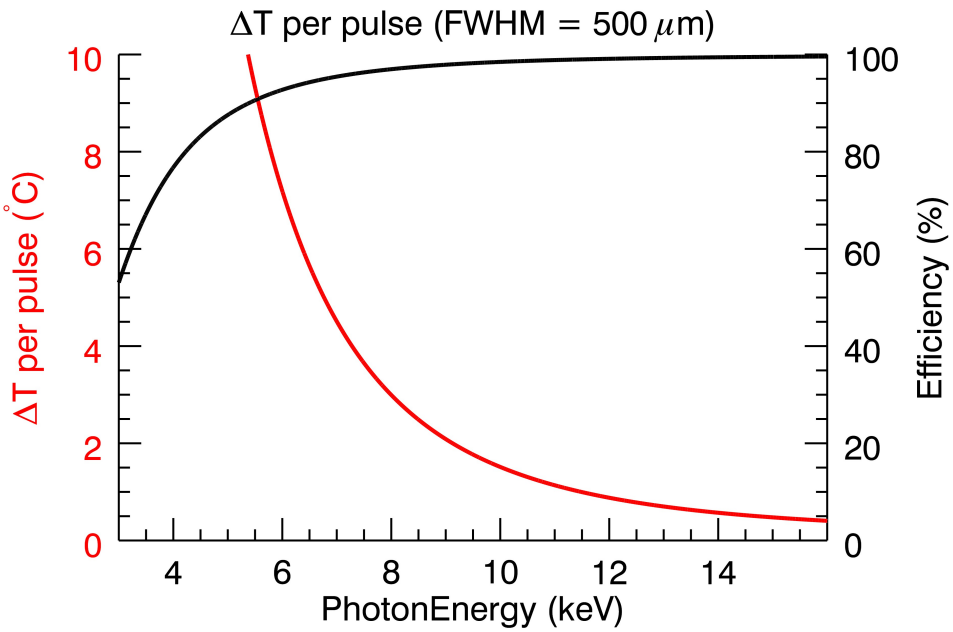

Figure C.5: Transmission efficiency and expected thermal rise per pulse for a 20 µm thin CVD diamond film. This simulation ignores heat transfer and water cooling. Both effects will increase the maximum number of pulses per train.

C.4 Protection systems

As the SPB optics can be moved, it is vital that we consider radiation safety for the protection of people working with the instrument, as well as from an equipment protection standpoint.

From the personal protection point of view, we need to consider the SPB optics hutch, the FXE instrument hutch, where we have a flight tube, and the SPB instrument hutch. From the SPB optics hutch point of view, the radiation safety shutter will prevent any radiation from entering the hutch while the door is open. For the FXE instrument, the micrometre-scale KB system could potentially steer the beam into the beampipe. To mitigate this, we propose to use a collimator with a beam loss monitor installed in the optics hutch for radiation protection. (For more details, see Appendix D, “Beam conditioning components”). Additionally, a lead-shielded beam pipe can be installed,

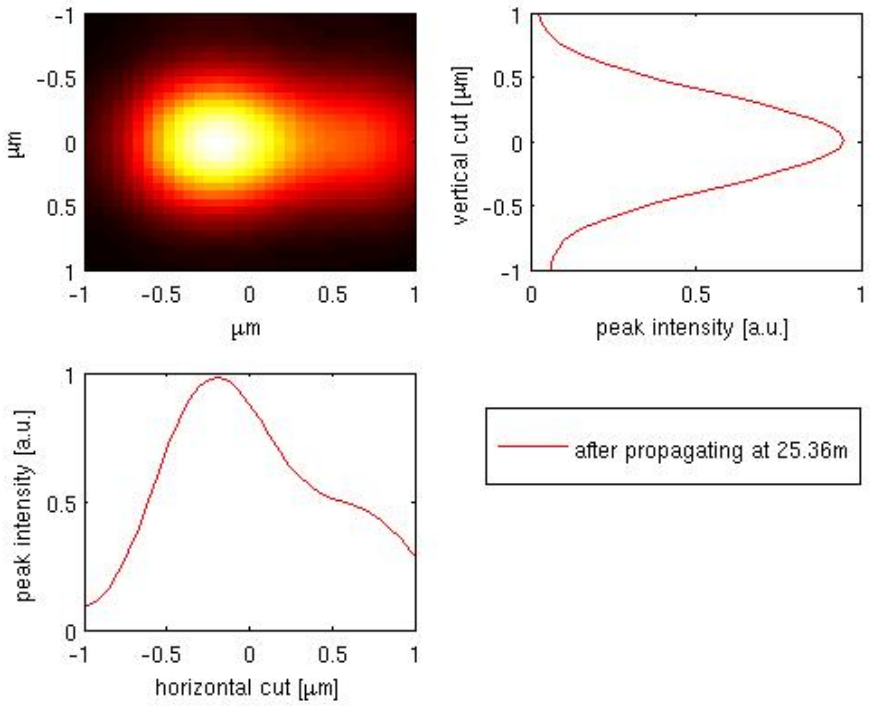

Figure C.6: Intensity profile from a wave propagation for the micrometre-scale focus using an approximate, worst-case, height error profile with twice the height errors as shown in Figure 6.16 on page 71. The optics correspond to the same 12 keV photon energy, a clear transverse aperture of 3.8 mm, and a divergence of 2.19 µrad FWHM.

which will be coordinated with the radiation safety group. As the SPB beam shutter in the optics hutch, or the shutter in the tunnel, will prevent radiation from entering the hutch, we will be following the personal protection guidelines and implementation set out in *Technical Design Report: X-Ray Optics and Beam Transport* [87].

Equipment protection is another challenge. With two KB systems and six optics, it is critical not to damage any of the detectors or any other piece of equipment by steering the X-ray beam onto it or by inserting a screen or aperture into the beam and destroying it. To ensure this, we will only align in Operation Mode 1 (single low bunch charge pulse at 10 Hz). To go to Mode 3 or 4 (many-pulse operation at high bunch charge), we must ensure that the instrument is already well-aligned. Operation will require interlocks that close the SPB shutter or switches to Mode 1 if a screen or other device is inserted into the beam path. Also, as the detector rail (described in Section B.3, “Rail system”) will require a different alignment for different KB settings, we expect to manually and mechanically secure the rail with bolts that lock its position

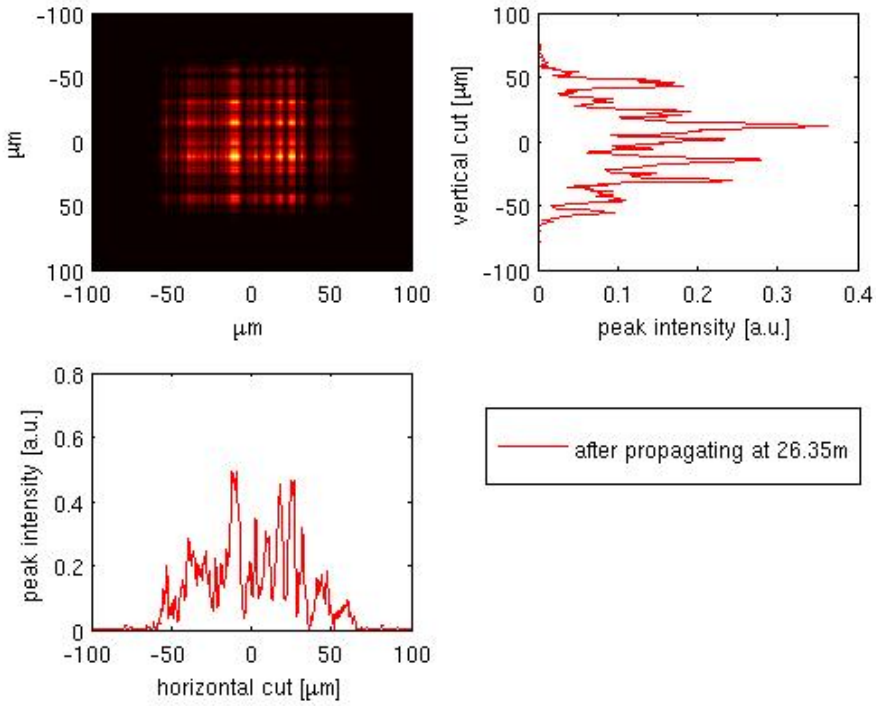

Figure C.7: Same intensity profile and parameters from a wave propagation for the micrometre-scale focus as shown in Figure C.6 on the previous page, propagated 1 m out of focus into the far field

once aligned. These bolts will activate binary-condition switches that will inform to the machine protection system that it is safe to go into Mode 3 or 4. Controls for the KB optics must also be disabled to enter Mode 3 or 4 in order to prevent drifts of the KB optics while the FEL is operating at full power and maximum repetition rate.

C.5 Ray tracing

As our KB optics are elliptically polished, they are subject to aberrations and defocus if the source point is moved. To compensate and move the focus back into the required Z position, often a slight tip or tilt of the KB system is implemented. We investigated the effects of source point motion on our KB design to anticipate the necessary correction. Ray tracing was conducted to model the FWHM focal spot size of the 100 nm–scale KB design for various degrees of horizontal mirror tilt angle from nominal and source point Z position relative to the expected position. While this procedure causes slight aberrations from a perfect focus, these were ignored and a 2D Gaussian curve was fitted for every simulation. Each simulation used 20 000 random rays. The results of the 2D Gaussian fit is shown is Figure C.8 on the following page. The divergence corresponded to the expected divergence of 2.96 µrad at 8 keV and a FWHM source size of 40 µrad. The results show that small changes in mirror position can compensate for drifts in the source point. This technique can also compensate for astigmatism.

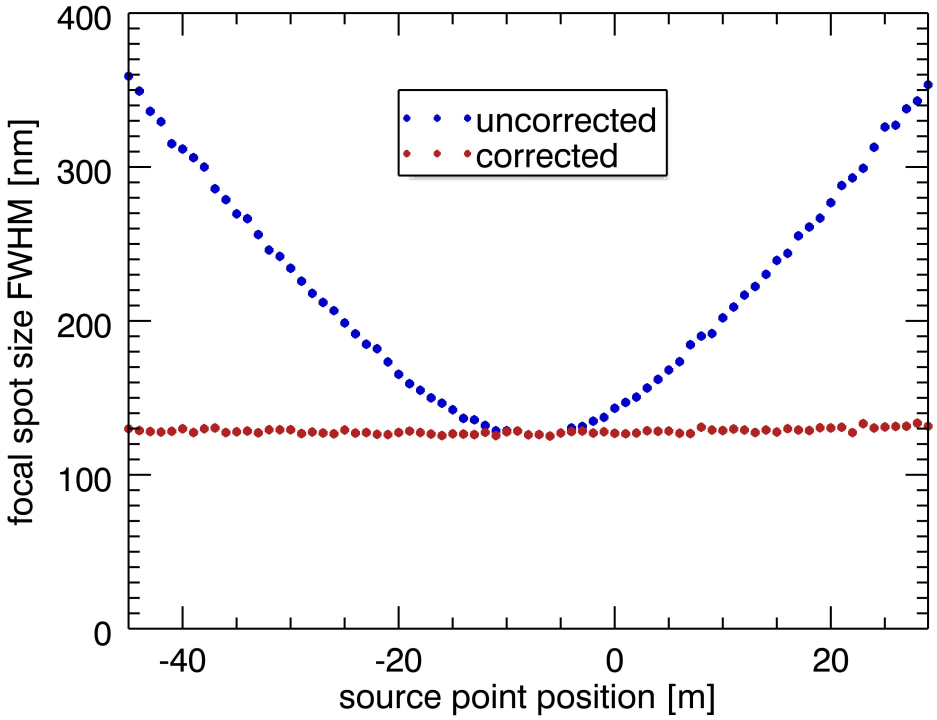

Figure C.8: Results of 1500 ray tracing simulations. The source point was simulated every 1 m, and the horizontal KB mirror was scanned between ±100 nrad in 50 nrad steps. The uncorrected and corrected spot sizes are shown.

D Beam conditioning components

Appendix authors: G. Borchers[1], A. Aquila[1], K. Giewekemeyer[1], A.P. Mancuso[1]

D.1 Introduction

A variety of devices need to be installed in the SPB instrument to “condition” the FEL beam for practical use. This appendix explains the requirements for each element and its purpose in the SPB instrument. Explicitly excluded are the KB focusing optics, which are described extensively in Chapter 6, “X-ray optics layout”.

D.2 Power slits

Power slits are essentially adjustable-sized beam apertures that can take the full power of the FEL beam tails. Their function is to aperture the FEL beam before it interacts with the KB optics. As there are two SPB KB foci, two sets of power slits will be needed: one near the beginning of the optics hutch (upstream of the micrometre-scale optics) and one near the beginning of the experiment hutch (just upstream of the 100 nm–scale optics).

The power slits will most likely consist of two horizontal and two vertical boron carbide (B_4C) and tungsten blades. Tungsten can remove any remaining third harmonic from the beam. However, it is incapable of withstanding the fundamental FEL beam. Water-cooled B_4C blocks need to be installed adjacent to the tungsten to maintain a temperature of 20°. The B_4C needs to be carefully mounted to prevent cracking or any movement over time.

The SPB power slit requirements are:

- Power slits must be capable of operating in the direct FEL beam for a limited time.
- Mounting of tungsten on B_4C blades must be water-cooled to maintain 20°.
- Resolution of motor movement must be 2 µm or better.
- Temperature will be monitored using thermocouples.

[1]Scientific Instrument SPB group (WP84), European XFEL GmbH, Albert-Einstein-Ring 19, 22767 Hamburg, Germany

- Length must be equal to or under 400 mm in the beam direction.
- Slits must be able to close completely and open to a 20 x 20 mmhole, remotely controlled with a motor precision of 2 µm or better.

Based on the experience of the X-Ray Optics and Beam Transport group (WP73), the power slits should be readily available from a vendor who can meet these specifications.

D.3 Attenuators

The SPB attenuators are critical components for alignment purposes and experiments where a reduced intensity is required. The attenuators also serve as equipment protection devices, as they will be used while the direct beam is directed at critical instruments, such as the KB optics and the detectors, during alignment.

Therefore, strict requirements have been set for the attenuators:

- Enough attenuation capability to block the beam; 10^{-12} transmission (i.e., 12 decades of attenuation capability with Si and CVD diamond options)
- Three attenuations per decade with Si and CVD diamond options (i.e., a factor of approximately 3 between attenuator settings)
- At least one spare duplicate of each attenuator screen in the device (for redundancy in case of screen failure or beam damage)
- Motor-driven to allow for multiple positions on each attenuator screen to be used
- Less than 400 mm length in the beam direction

The main set of attenuators will be located in the tunnel just before the optics hutch. This set will allow the users to attenuate the beam before it reaches any of the other instruments, including the sensitive KB optics. Another set of attenuators is to be located immediately upstream of the 100 nm–scale KB mirrors to allow attenuation for the 100 nm–scale spot with minimal wavefront effects. A third attenuator is to be installed before the SFX compound refractive lenses (CRLs) to provide independent intensity control at the SFX instrument.

For the same reasons as the slits, these elements will need to be water-cooled. The motors used to drive the screens in and out of the beamline must have a precision of 1 µm or better. If one location on the screen has been damaged by the FEL beam, we will be able to slightly adjust the position, temporarily preventing the replacement of an entire screen. This option can save users valuable beamtime in the event of

attenuator damage.

D.4 Apertures

Also referred to as cleanup apertures or post-optics slits, apertures are similar to the power slits with the exception of not being required to withstand the high peak power from the FEL beam. The cleanup apertures will be installed after the micrometre-scale KB chambers in the optics hutch of the SPB instrument, and are intended to be used to remove scatter from the beam profile downstream of the KB optics, in particular any diffraction produced by aperturing the beam upstream of the KBs as well as the partially reflected beams (that is, radiation that passes through the KB chamber and is reflected off one of the two mirrors, but not both).

Many companies are providing these slits, and an off-the-shelf model that fits our requirements will suffice. However, custom B_4C blades backed by tungsten may have to be added to a conventional slit design.

D.5 Collimator

The collimator in the SPB optics hutch is designed as a safety device in case the beam is accidentally directed away from the intended path. In this case, it will intercept the FEL beam, preventing any instruments or the beam pipe from being exposed to the intense beam. The collimator will be installed at the end of the optics hutch, specifically protecting the flight tube between the optics hutch and the experiment hutch. Requirements for the SPB collimator are:

- Must prevent the flight tube from being hit by the direct beam of the FEL
- Must be able to take a full-energy hit from the FEL for a short amount of time
- Must trip the machine protection system (MPS) and personnel protection system (PPS) if too much radiation is absorbed in the collimator (indicating misalignment)
- Must fit at the end of the optics hutch

Calculations of the geometry showed that, for the FEL beam being misaligned in its worst-case scenario, a monolithic collimator would need to be 3 m in length. The SPB optics hutch is already overfilled in the longitudinal direction, and there is no room for a 3 m long collimator. A solution being investigated is to break up the geometry into two washer-like pieces, and position these just after the micrometre-scale KB mirrors and at the most downstream position of the optics hutch, since the entrance and exit acceptance diameter and angles are the only critical factors of the design.

The thickness of the collimating material is important and will be investigated further. These studies will be coordinated with the radiation safety group.

We also plans to use a photoelectric current or X-ray diode to alarm the MPS if the—likely B_4C—collimator is illuminated. The photoelectric current is simple and can also determine how much of the FEL beam is hitting the B_4C, because the electrical output is directly related to the amount of energy hitting the collimator. Using a split anode, or multiple X-ray diodes, would also enable us to estimate the direction of the beam clipping.

D.6 Alignment lasers

Two alignment lasers will be used on the SPB beamline. They will serve to align the instruments in order to ensure that when the FEL beam is activated, the instrument is already coarsely aligned, saving valuable beamtime. The alignment lasers also provide the ability to pre-align many elements without the FEL beam, e.g. on machine days or when the neighbouring instrument is taking beam. The alignment lasers are off-the-shelf products, but must be altered to fit the instrument and vacuum requirements.

The requirements for the SPB alignment lasers are:

- Power of less than 5 mW
- Preferably Safety Class 2 to avoid having to use laser eye protection; however, Class 3a may be acceptable.
- Pop-in and pop-out capability
- Focusing collimator or lens
- Remotely controlled on/off
- Two axes of rotation on lower mirror, three axes on upper mirror (for accurate alignment)
- Pop-in polarized screens (for continuously varying attenuation)
- Include an iris to aperture the beam
- Single-mode (transverse electromagnetic mode,$TEM_{0,0}$) laser (for the possibility of visible wavefront measurements)

The plan is to design two identical alignment laser systems, each in-coupled with a DN63 cross. The laser will be mounted under the cross perpendicular to the FEL beam and parallel to the floor. A mirror will direct the beam up through a window flange and into the cross. The in-coupling optics will have two degrees of freedom,

pitch and roll, and be fixed in the vertical direction. An in-vacuum mirror on a linear feed-through will be installed on a motor at the top of the cross. It will have two axes of rotation to aim the laser directly down the flight tube, as well as lateral traveling capability for in and out motion. An out-of-vacuum collimating telescope will also be installed to allow the alignment lasers to be focused at multiple positions along the beamline, easing the alignment of components at different longitudinal distances.

D.7 Beam dump

The SPB beam stop will comprise several components, with the central device being the actual beam dump, which has to fully absorb and thus eliminate the FEL beam.

The European XFEL will deliver pulses in a pattern that consists of 10 pulse trains per second, with a maximum train duration of 600 µs. Each of these pulse trains will consist of at most 2700 pulses, which themselves are 1–100 fs long and will be repeated at a rate of 4.5 MHz (i.e. separated by ca. 220 ns). With an expected pulse energy between 1 and 4 mJ (for a maximum bunch charge of 1 nC) [83], this leads to a bunch power between about 4 and 18 kW. In practice, due to limitations on the electron beam dump, the maximum number of 1 nC pulses is limited to 1350 (within 300 µs) [88]. In contrast to the power during a pulse train, the *average* power of the European XFEL beam, due to the large gaps in between bunches, is at most of the order of 50 W, which can be absorbed by a simple water-cooling system.

The high power acting on the beam dump during a pulse train, however, is required to be absorbed within a lateral spot diameter between several 100 µm and several millimetres. The primary effect of the absorbed X-ray energy in the material is its conversion into heat, which can eventually lead to melting if the energy is not dissipated quickly enough. The penetration depth of the radiation, however, is usually so large and temperature gradients are so small that, within the time span of a single pulse train, the thermal load on any beam stop material can, at most, partially be transported away by passive or active cooling. One therefore has to ensure that, within a pulse train, the temperature of the beam stop material is kept well below the melting temperature T_m, and for some materials, such as diamond, even below a temperature where solid–solid phase transitions occur, which can be substantially lower than T_m.

As the whole beam path will be in vacuum, the beam stop material should ideally be a solid at ambient temperature. Such an ideal beam stop material has a high thermal conductivity, a large absorption length, as well as a high heat capacity and melting temperature [88]. B_4C has been identified as a very suitable material in terms of its

physical properties, with diamond having similar characteristics [88].

An analytical estimate of the maximum allowable number of pulses within a bunch train has been given in [88]. As the inter-pulse time is only 220 ns, in a first approximation, heat dissipation can be neglected (adiabatic limit). For low photon energies, where absorption lengths are shorter, heat dissipation plays a considerable role, however, and should thus also be included [88], here by using a simple 1D Gaussian heat diffusion model. Note that an inclination of the beam stop surface to grazing incidence angles is only beneficial if the thermal conduction is quick enough to dissipate the heat into the vicinity. At high energies, thermal conduction does not play a role, as absorption lengths are longer, and the increase in the beam footprint area does not lead to higher radiation tolerance compared to normal incidence.[1]

Similar calculations as presented in [88] have been reiterated here to evaluate the heat load on the beam stop at the SPB instrument. The beam size at the beam stop position has been calculated based on the lower limit of the beam size (worst-case scenario) in the tunnel, 900 m away from the source (see [88], p. 22) by application of geometrical optics. The most critical of all use cases in terms of heat load on the beam stop are “micrometre-scale focus without SFX” and especially “micrometre-scale focus with SFX” (Table 7.1), as in these cases the beam size at the beam stop is the smallest.

The calculated limiting total energy in a pulse train for which thermal melting starts to occur in the beam stop material (B_4C) are shown in Figure D.1 on the next page for the photon energy range of the SPB instrument, for the micrometre-scale focus with refocusing and without refocusing for SFX. The adiabatic limit agrees increasingly well with the thermal estimation for increasing photon energies. At low photon energies, heat dissipation considerably increases radiation tolerance. It is also at low photon energies that a transition from normal incidence to 4° improves radiation hardness the most.

[1] The volume into which the radiation is absorbed within the adiabatic limit is independent of the incidence angle.

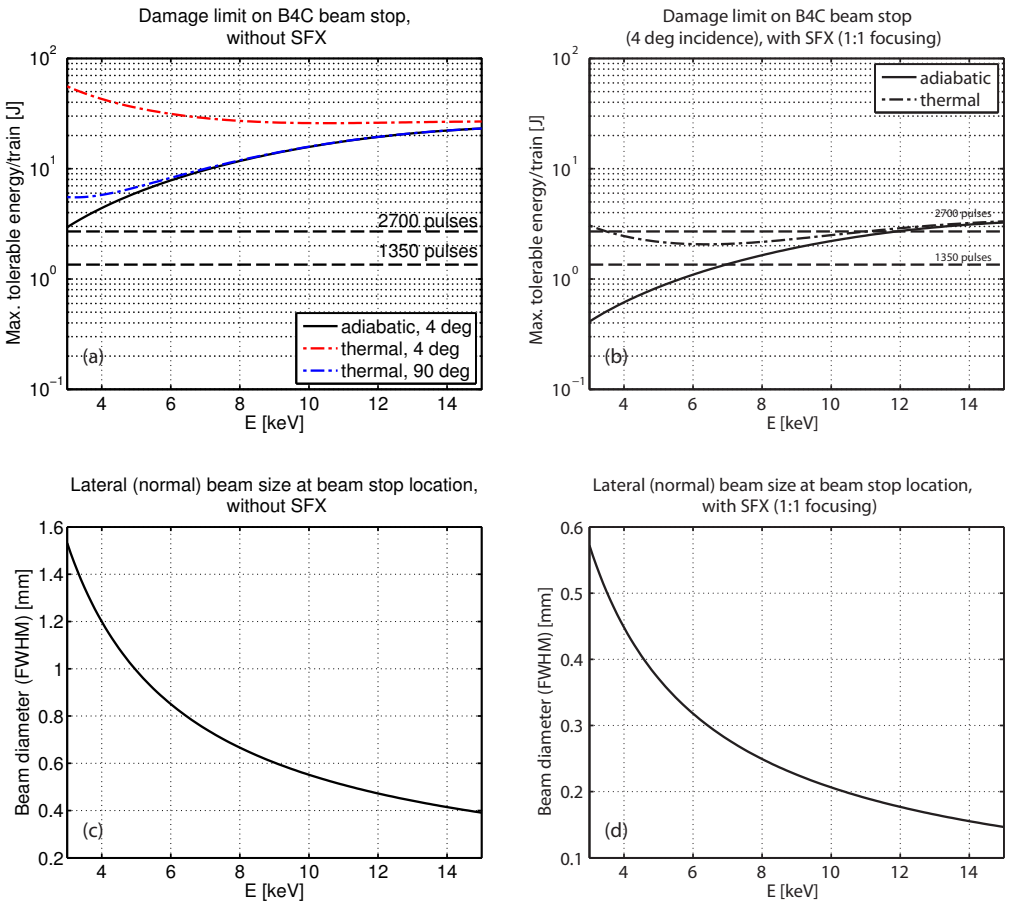

Figure D.1: Overview of the maximum tolerable energy per pulse train (melting limit) on the surface of the beam dump for the micrometre-scale focus, without (a, c) and with (b, d) refocusing for the SFX instrument. The energy is given in J. Assuming that one pulse has about 1 mJ, one can easily rescale the y-axis to the maximum number of pulses in a pulse train before melting occurs. The damage thresholds are shown in (a) and (b); the corresponding lateral beam sizes as FWHM (normal cross section) are given in (c) and (d), respectively. In addition to the damage thresholds per train for an incidence angle of 4°, which are shown in (a) and (b) for the adiabatic and the thermal case, the thermal case for normal incidence (90°) is shown in (a) as well. Note the horizontal lines in (a) and (b), which indicate a limit of 1350 and 2700 pulses, assuming 1 mJ in a pulse for all photon energies.

The horizontal lines in (a) and (b) indicate energy values in a pulse train corresponding to 1350 and 2700 pulses, respectively. They have been calculated assuming a pulse energy of 1 mJ (which can raise to about 4 mJ when saturated) and using the lower limit of expected beam sizes in the tunnel as given in [88]. Note that taking the upper-size limit would lead to an increase in heat load tolerance by about a factor of 4 [88].

Given that the critical angle of B_4C between photon energies of 3 keV and 15 keV is always below 1°, a grazing angle of $\alpha = 4°$ is a good compromise between technical feasibility and increase in radiation tolerance[2]. Without the SFX refocusing, the tolerable pulse train energy (from the thermal calculation) is substantially higher than the energy from 2700 1 mJ-pulses in a train. With a one-to-one refocusing option, however, the beam has much less longitudinal distance to expand via propagation, and the maximum tolerable pulse train energy is very similar to the energy from 2700 1 mJ–pulses in a train. Most critical are photon energies around 6 keV, where neither an increase in penetration depth (or volume) nor thermal conduction can lead to a higher pulse tolerance. The SFX refocusing option was assumed here to image the primary focus with a magnification of 1 onto the SFX focal plane.

Making the refocusing option compatible with the current beam stop concept, which is sufficient for the SPB instrument, thus requires defocusing to a larger spot on the beam stop and/or limiting the maximum number of pulses in a train when the SFX instrument is in operation.

Following the design of the front-end beam stops devised by WP73, a concept for the SPB beam stop at the end of the instrument's flight tube was developed (Figure D.2). With an inclination angle of $\alpha = 4°$, a length of $L_2 = 429$ mm would be sufficient to maintain a clear aperture of $a = 30$ mm. If the beam is centered on the beam stop area, this aperture could exceed all FWHM beam sizes of the use cases listed in Table 7.1 on page 84 by at least a factor of about 2.

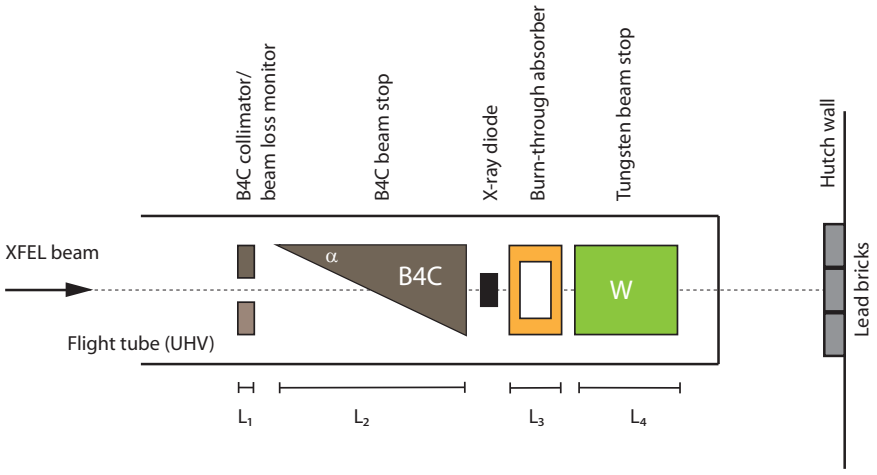

Figure D.2: Conceptual design of a beam stop for the SPB instrument. Note that all components are inside the vacuum of the flight tube.

[2]The reflectivity at 4° incidence angle and for a B_4C surface with an rms roughness of 2 nm is always below 10^{-12} [41]. As the B_4C beam stop surface will be of even higher roughness, the reflected radiation is of no concern at a 4° incidence angle.

With a magnification of $M = 1$ (one-to-one focusing), the refocusing option is not compatible with a full pulse train of 2700 pulses, assuming a 1 mJ pulse energy. As stated earlier, for refocusing one thus has to consider a magnifying geometry for the CRLs (magnification $M > 1$) and a reduced number of pulses per train.

The lateral movement of the beam for different use cases (by about 12 cm) requires a translation of the beam stop (i.e. the flight tube needs to be collinear with the optical axis). As a consequence, when the beam is not properly centred within the flight tube, the beamline may ever only be operated in a “system protection mode” (10 Hz bunch repetition rate, one pulse per bunch).

A safety collimator ($L_1 \lesssim 30$ mm) upstream of the B_4C absorber can be used to control the pointing of the beam. Ideally, this is designed as a beam loss monitor, either by detecting back-scattered X-rays as in the back-scattering monitor or by measuring the photocurrent with electrodes placed at different angular positions around the B_4C ring. Such a beam loss monitor might also be based on the design that will be developed by WP73 [87].

A burn-through absorber ($L_3 \approx 15$ mm) made of copper and filled with air will cause an instrument vacuum leak and thus a complete shutdown of the machine if the B_4C block and the copper are burned through by the beam.

An X-ray diode is planned in between the B_4C wedge and the copper block to trigger the SPB shutter to close if the B_4C wedge has been completely ablated by the beam. This serves as an additional equipment protection measure before the instrument is vented due to a hole in the burn-through copper absorber.

A block of tungsten ($L_4 \gtrsim 100$ mm) further downstream ensures complete extinction of the beam’s higher-energy components. Lead bricks at the back of the experiment hutch could be seen as an ultimate resort if the beam was ever directed through the back wall of the flight tube. This, however, would also cause the system to be vented and should trigger a shutdown of the machine.

Based on the experience of WP73, the entire beam dump system could be obtained from an external vendor.

E SASE1 beamline spectrometers

Appendix authors: K. Giewekemeyer[1], J. Buck[2], J. Grünert[2]

This appendix describes the gas-based spectrometer that will be installed in the SASE1 tunnel as a baseline instrument as well as diffraction-based spectrometers that are also planned to be installed in the SASE1 beamline.

E.1 Time-of-flight photoemission spectrometer

The X-Ray Photon Diagnostics group (WP74) is currently developing a photoemission time-of-flight (ToF) spectrometer for shot–shot spectral diagnostics of the European XFEL radiation for all SASE beamlines (Figure E.1 on the following page). The spectrometer is based on a mature design provided by the P04 group at the PETRA III synchrotron radiation facility at DESY. It comprises up to 16 independent flight tubes and detectors, arranged on a full circle in a plane perpendicular to the beam axis. It will be employed to observe the core-level photoemission signal from a pulsed rare-gas beam injected into the chamber, so the single-pulse spectrum of the SASE radiation can be assessed using the observed photoemission spectrum. The kinetic-energy resolution of $\Delta E/E < 10^{-3}$ of the spectrometer is well-confirmed experimentally for the low kinetic-energy range, whereas simulations predict that this resolution can also be achieved for a kinetic energy of several keV. With a reasonable choice of the observed core level, the full photon energy range of the European XFEL can be covered. Note that the actual photon energy resolution, due to the relation $E_{\mathrm{kin}} = h\nu - E_B$ (binding energy), will actually be better than the stated resolution for the kinetic energy.

Aside from detector efficiencies and flight tube geometry, this technique is limited by the available gas pressure, i.e. the number of detected photoelectrons per shot. For the expected performance of the SASE1 undulator [83], a peak gas pressure in the 10^{-3} mbar region (in the worst case) is found to provide sufficient signal strength in order to determine the centre wavelength and spectral FWHM within the specified boundaries of statistical uncertainty ($\sigma(\bar{\lambda}) = 0.1\%\,\mathrm{BW}$ and $\sigma(\mathrm{BW}) = 0.1\%\,\mathrm{BW}$). Hence,

[1]Scientific Instrument SPB group (WP84), European XFEL GmbH, Albert-Einstein-Ring 19, 22767 Hamburg, Germany
[2]X-Ray Photon Diagnostics group (WP74), European XFEL GmbH, Albert-Einstein-Ring 19, 22767 Hamburg, Germany

the absorption of the beam in the spectrometer chamber (length < 1 m) can be neglected, providing true non-invasiveness during user operation. The stated partial pressure of the rare gas is derived from the minimum requirement of $N = 100$ detected photoelectrons per shot and channel. Since the statistical uncertainty of the probed width and centre of the spectrum scales with $\sqrt{N}$, these measures are expected to be approximately one order of magnitude smaller than the energy resolution of the spectrometer. Better results can be achieved when combining the signal from several channels.

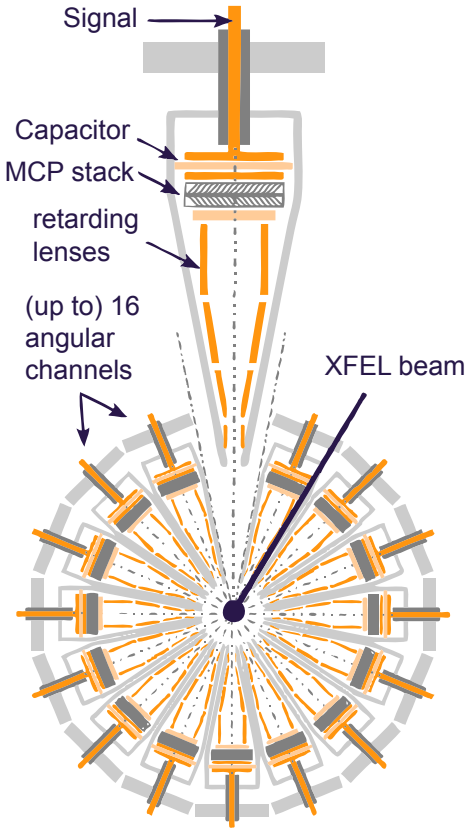

Figure E.1: Concept of the time-of-flight photoemission spectrometer to be used at the European XFEL (Figure courtesy of J. Buck, European XFEL)

The complete spectrometer station will make strong use of the Karabo control software framework (DAQ and Control Systems group, WP76). Features demanded here are database access, synchronization and timing, user interface, and automation. A user interface for the device is currently being discussed. Since the operation of the diagnostics station as a whole will be non-trivial, a high level of automation must be employed from the first minute to make details of operation widely transparent. Evaluation of the raw data will be designed such that it runs autonomously and

reduces the amount of redundant information as much as possible. The design foreseen will allow us to provide diagnostics data with a very low latency in the low microsecond range to the user, also featuring a potential use for veto applications. Advanced applications, such as on-chip data reduction using principal component analysis (PCA), are also deemed possible and have recently been proposed [15]. Interfaces are under design in a close collaboration between WP74 and WP76.

Further technical requirements of the spectrometer station have been discussed in detail in [16]. The station will include differential pumping units to satisfy the pressure requirements of adjacent beamline segments [88, 87]. Currently, a position a few metres downstream of the offset mirrors is foreseen. Recent discussions make a final positioning upstream of the offset mirrors, close to the other gas-based diagnostics devices (XBPM, XGMD), appear more likely. Further aspects of expected maintenance and operation issues can be found in [16].

E.2 Diffractive spectrometers

Spectroscopic analysis of FEL beams has recently been realized based on thin, bent crystal films [113] and on nano-fabricated diffraction gratings [45]. None of these methods are absolutely non-invasive. However, their impact on the wavefront is relatively small and they are more effective at hard X-ray energies than photoemission spectrometers. For applications where wavefront preservation is not critical, such as nanocrystallography, diffractive spectrometers are thus a viable option. Currently achieved spectroscopic resolutions are $\Delta E/E = 2.4 \times 10^{-5}$ at 8.3 keV using a bent crystal [113] and $\Delta E/E = 2 \times 10^{-4}$ at 6 keV using a nano-fabricated grating [45]. Both methods could be combined to reach even better resolution [45]. They are both only detector-limited in speed and can currently reach frame rates of up to 1 MHz [45]. It should be noted, however, that the lifetime of a transmission grating, even if it is made of diamond, might be limited if it is illuminated by full pulse trains of the European XFEL beam. Depending on the necessary maintenance rate, this could make such a device very expensive.

If the spectrometry can be performed in destructive mode, i.e. downstream of the sample interaction region, an alternative option is using a reflective focusing optics and a flat crystal in reflection geometry [110].

WP74 is currently investigating the installation of a hybrid device that is based on primary diffraction by a transmission grating and secondary diffraction by a bent crystal in the SASE1 tunnel area.

F Control and data acquisition

Appendix authors: A. P. Mancuso[1], N. Coppola[2], C. Youngman[2]

F.1 Overview

The SPB instrument will benefit from a centralized effort to perform the experiment control and data acquisition (DAQ) using the software, firmware, and hardware system being developed by the DAQ and Control Systems group (WP76) at European XFEL.

WP76 aims to provide experiment designers and instrument scientists with solutions ensuring that:

- Operating tasks are performed intuitively, efficiently, and safely (including allowing only authorized users to operate critical components
- Integration or reconfiguration of hardware and software is simple to accomplish
- Data recorded is of high quality and can be analysed efficiently

This last point is of particular importance to the SPB instrument, with high data rates expected as well as demanding analysis techniques to interpret this data. The user consortium proposal “DataXpress” aims to address some of these concerns that are directly related to the SPB instrument.

This appendix describes the requirements of the SPB instrument as well as the facility-wide software, hardware, and DAQ solutions.

F.2 Requirements

F.2.1 Control

The SPB instrument requires the control of more than 260 axes of motion (listed in Table F.1 on page 203), which range from very high-load, coarse-motion axes to very precise, nanoscale motions within the sample chamber vacuum.

[1]Scientific Instrument SPB group (WP84), European XFEL GmbH, Albert-Einstein-Ring 19, 22767 Hamburg, Germany
[2]DAQ and Control Systems group (WP76), European XFEL GmbH, Albert-Einstein-Ring 19, 22767 Hamburg, Germany

Table F.1: Axes of motion required by the SPB instrument

Device	Number of motors
Attenuator	4
Alignment laser	10
Gate valve	1
Power slits	4
Diagnostics	3
Horizontal micrometre-scale KB chamber	14
Vertical micrometre-scale KB chamber	14
Cleanup apertures	4
Diagnostics	3
Collimator	0
Beam stop	1
Gate valve	1
Gate valve	1
Alignment laser	10
Power slits	4
Diagnostics	3
Gate valve	1
100 nm–scale KB	15
Diamond window	1
Differential pump	4
Gate valve	1
Sample chamber: 3 cleanup apertures	9
Sample chamber: in-coupling laser mirror	5
Sample chamber: 3 cleanup apertures	9
Sample chamber: injector motion	5
Sample chamber: pressure regulators	2
Sample chamber: out-coupling laser mirror	5
Sample chamber: on-axis viewing camera	6

Table F.1: Axes of motion required by the SPB instrument

Device	Number of motors
Sample chamber: off-axis viewing camera	4
Sample chamber: future upgrades	10
Sample chamber: off-axis viewing camera	4
Sample chamber: chamber	2
Gate valve	1
Rail	6
Diagnostics	3
Time arrival device	4
Gate valve	1
SFX: Attenuator	4
SFX: CRLs	30
SFX: CRL chamber	5
SFX: Gate valve	1
SFX: Differential pump	4
SFX: Diagnostics	3
SFX: Cleanup aperture	3
SFX: Injector motion	5
SFX: Pressure regulators	2
SFX: Sample chamber	5
SFX: Gate valve	1
SFX: AGIPD	11
Downstream AGIPD	6
Intelligent beam stop	10
Beam dump	2
Total	**263**

F.2.2 Data acquisition

The SPB instrument is a photon and detector frame–hungry instrument. More frames of (quality) data usually mean a higher degree of success of interpreting that data. The data acquisition system is required to collect data from at least one 1 Mpx Adaptive Gain Integrating Pixel Detector (AGIPD) and its smaller downstream partner simultaneously. Following the installation of the SFX 4 Mpxl AGIPD detector, a total of 5 Mpx of AGIPD detectors will need to be accommodated simultaneously .

F.2.3 Data management

The AGIPD detector ASIC and front-end electronics (FEE) systems are capable of acquiring 350 frames per pulse train. The 1 k x 1 k detector's 2 MB frame size results in 700 MB/train, which are transferred by the train builder to PC layer blades using 10 Gbps links. This bandwidth can be written to disk, but use of a veto trigger system implemented in the FEE, use of simple FPGA-based algorithms in the train builder, and processing on the PC layer blades should reduce the data volume appreciably by rejecting events. The aim is to implement the reduction factors seen during analysis of LCLS data as early as possible in the readout chain to reduce the volume of the final data set.

F.3 Software control

The logical view of the control architecture is shown in Figure F.1. All hardware (pumps, motors, valves, DAQ systems, etc.) and software (data quality monitoring, data rejection and analysis algorithms, etc.) entities are controlled and configured via specific software clients called devices, displayed as white circles inside grey boxes. The latter represent device server applications responsible for running devices. Device servers and devices are controlled by controller applications like the graphical user interface (GUI), Python script terminal, and so on, and are typically started by an operator.

Technically, a device is a logical unit that can be regarded as a small application performing a specific task (e.g. driving a camera or motor), which can be configured and controlled by setting device property values (e.g. camera image format or motor end position) or requesting a device action with a command (e.g. acquire image or move motor). It is implemented as a class that, finally, inherits the device base class and is compiled into a shared library. The device server is a generic executable that is able to run or instantiate one or more devices. It is implemented as a class equipped

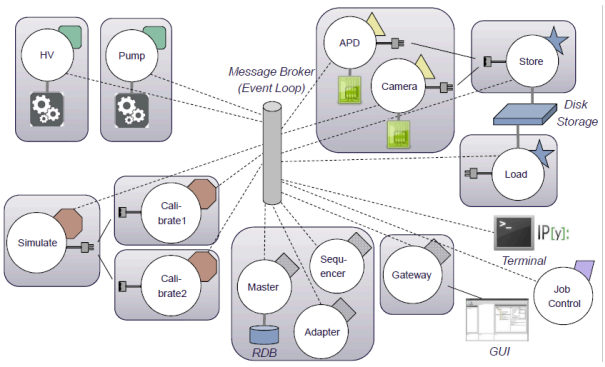

Figure F.1: Software control system architecture

with functions for parsing configurations, loading device-shared libraries at runtime, and constructing and destroying device instances.

Three ingredients (communication, configuration, and flow control) must be added to the device server and device view to enable additional functionality needed to provide a useable control system.

Controllers exchange control information (property values and commands) with devices and device servers to perform control operations, and devices exchange control information and data with other devices. Control information is usually small-size and transmitted at a repetition rate of 10 Hz, whereas data is often large and continuously transmitted during scans. The different transport requirements are satisfied by using broker-based N x N and point-to-point network channels for control information and data, respectively—mixing control and data is avoided. Broker transport is currently performed by a message-oriented middleware (MOM) based on the OpenMQ implementation of the Java Messaging System (JMS) specification. Point-to-point transport is implemented using the boost::asio library. The communications application-programming interface (API) is used to build XML or binary-content messages, address and inject them into the transport layer, and decode them on reception. By design, the software interface separates the communications API and underlying transport layer, allowing different transport layer implementations to be used without changes to application code. Messages are always delivered asynchronous to callback functions using a network signal–slot observer notification design pattern, but the communications API also implements blocking direct call (RPC-like) and request–reply functions. Note that an additional transport category exists where intelligent DAQ front-end systems establish point-to-point or multicast channels directly without passing the data through their control device, but that the channel properties are still configured by control information sent to the device controlling the hardware.

Configuration of applications at startup and reconfiguration during running are clearly required features of control system applications. This is implemented by the configuration API by requiring configuration information (command line, file, or message-based) to be XML formatted and enforcing the programmatic definition of configuration parameter attributes (name, description, units, read-only, type, default value, etc.) in the application class. The latter allows runtime generation of an XSD schema precisely describing expected configuration information, thus allowing validation before setting parameter values in the application. A powerful feature of the API is that the schema definition can be generated statically from the class without instantiation, thus allowing controller applications to display and manipulate device and device server properties.

Sequencing actions and synchronizing behaviour are required to satisfy conditional requirements, like “an experiment should start only if all participating devices signal that they are ready”, or “an output voltage should be set only if the power supply is on”. The required functionality is called “flow control” and is implemented by the finite state machine (FSM) API using the boost::fsm library. Devices requiring FSM functionality must define the set of states (ready, running, etc.) in which they exist and, for all transitions, a transition-driving event (reconfigure, compute, etc.), a Boolean guard callback that flags whether a transition can be started, and a callback that is called when a transition is started. The FSM API is fully integrated with the communications API, and the event is simply the name of callback fired by an incoming message. The FSM implementation allows large and complex control systems to be broken down into smaller parts, each with its own device and FSM, allowing composite systems to be easily build.

As noted, the above-mentioned concepts and their implementations provide the necessary framework to build a control system. Additional higher-level services are needed behind the scenes, including persistent databases (configuration, monitoring, access control), event logging, alarm notification, role-based access control (RBAC), experiment configuration tools, deployment system for device servers and device plugins (device control), interfacing of external control systems (DOOCS e-machine, undulator global control, TINE, etc.), composite device API, etc.

The control system software provides the experiment operator with the necessary tools to select and configure equipment to be used and to acquire data. Once acquired, the data and metadata pass into the data management and scientific computing (see Appendix G, “Scientific software in the European XFEL framework Karabo”) systems, whose tools allow data location and further processing.

F.3.1 Experiment operator view of the control system

The experiment operator's view of the experiment consists of graphical controllers or viewer tools.

The most significant of these are:

- Global experiment controller—configure, start, and stop experiment data taking (sometimes colloquially known as "the DAQ")
- Data quality viewer—monitor experiment performance using standard detector algorithms, and experiment performance using analysis algorithms
- Physical layer data processing and storage viewer—monitor data processing, used and available storage capacity, etc.
- Beam/hutch interlock controller—experiment hutch access beam shutter interlock
- Accelerator, beamline, and diagnostic viewer—graphical viewer of overall and component-specific status
- Alarm and error notification controller—persistent monitoring of notification states
- eLog—electronic logbook web application
- Webcam viewer—in-hutch and in-chamber monitoring

Prototype generic GUI and Python script controllers are available as part of the Karabo software framework (the European XFEL's own software framework). The generic GUI being developed will eventually provide the entire solution with the exception of beam interlock controller (provided by the safety group) and web applications. Script controllers, either imbedded in the GUI or stand-alone, provide scan and low-level user request support.

F.4 Hardware control

F.4.1 Vacuum hardware requirements

The vacuum chambers of the SPB instrument (including the anticipated SFX consortium contribution) are pumped by approximately ten turbomolecular pumps, seven ion pumps and two primary pumps, with a total maximum power consumption of approximately 25 kW. Vacuum is monitored by three classes of vacuum gauges (hot cathodes, cold cathodes, and Pirani gauges). Redundancy for critical vacuum measurements is foreseen. Both vacuum pumps and gauges are controlled via serial ports, RS232/RS422/RS485, with an open protocol, compatible with the control system solutions. Where possible, faster and easier-to-handle digital or analogue signals will be used.

Interlock system for safe operation of shutters and pumps must be completely configurable via software within this frame. This is guaranteed by the programmable logic controller (PLC) firmware being developed.

F.4.2 Motion control requirements

The SPB instrument anticipates a minimum of 260 axes of motion control across the instrument, ranging from centimetres of coarse motion for large components, such as detectors, down to very fine control of samples to positions of better than 100 nm. Much of this motion control will need to occur inside the instrument's vacuum, and additional geometric constraints may lead to long (30 m) cable lengths in certain cases. A list of devices and anticipated motors is shown in Table F.1.

F.4.3 Hardware control via Beckhoff PLCs

Beckhoff PLC and equipment connection terminals connected via Ethernet for control automation technology (EtherCAT) fieldbus are used to control the beamline and experiment vacuum (pumps, valves, gauges, etc.), positioning (stepping and servo motors, actuators, etc.) and associated monitoring (temperature, pressure gauges, currents, etc.) equipment. Beckhoff and similar (Siemens SPS, Wrago, etc.) commercial rail-based control systems offer considerable advantages when implementing large control systems. These include flexible inter-rail topology choices (loop, star, branch, etc.), real-time execution of control firmware executing condition evaluation, built-in redundancy allowing fault-tolerant operation, large and increasing number of equipment interface terminals for connecting to fieldbus (profibus, CANbus, RS242, RS485, etc.) and direct measurement terminals (digital IO, analogue IO, ADC, DAC, etc.), and integrated design environment for firmware development. In addition, they are inexpensive per channel.

F.4.4 Hardware control via Ethernet

Equipment with an Ethernet connection is controlled from networked host machines and not via Beckhoff terminals. Such equipment includes custom DAQ developments (digitizers, fast ADCs, 2D detectors, crate CPUs, etc.) and commercial equipment (commercial cameras, power supplies, etc.). Beckhoff systems are not used because data payloads associated with EtherCAT usage and processing time per terminal are limited to guarantee real-time performance. The large data volumes (camera images, etc.) typically produced by Ethernet-controlled equipment are transmitted

via dedicated point-to-point channels. Equipment without an Ethernet fieldbus connection, which is not suitable to use with EtherCAT, must be interfaced to Ethernet via a networked host. Commercial cameras read out by firewire or camera link are examples of such systems, but they can usually be avoided by using GigE cameras.

Figure F.2 shows a schematic of how the control system for a screen camera, camera power, filter, and positioning stage is implemented. The Screen Camera 1 device server runs the four devices required. Axis, filter, and power devices are configure-and-control Beckhoff-connected equipment. There is a one-to-one relation between software device and firmware device, which communicate with each other through a single device, Beam 1, necessary to shape IO traffic with the Beckhoff PLC. The Camera 1 device is an example of composite device capable of controlling Screen Camera 1 devices as a single device.

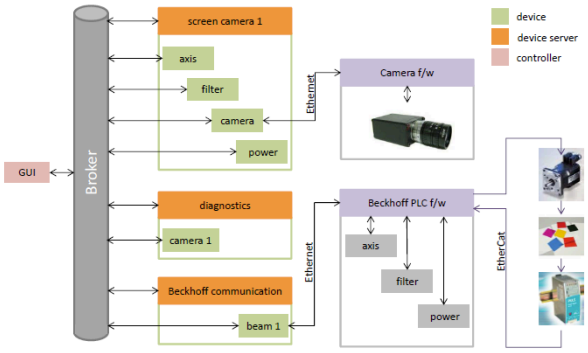

Figure F.2: Mixed Beckhoff and Ethernet control system of a diagnostic camera station

F.5 DAQ readout systems

The DAQ and data management architecture defined for use by WP76 is shown in Figure F.3. The front-end electronics (FEE) and front-end interface (FEI) layers are closely associated with the hardware and implement the firmware control and readout interface, respectively. The PC layer receives data sent by all participating FEIs and processes the data (monitoring, rejection, compression, and aggregation) before sending it to the data cache layer. After further processing at the data cache, only data from scans of high quality are transferred to the data archive and analysis layer, where offline processing is performed.

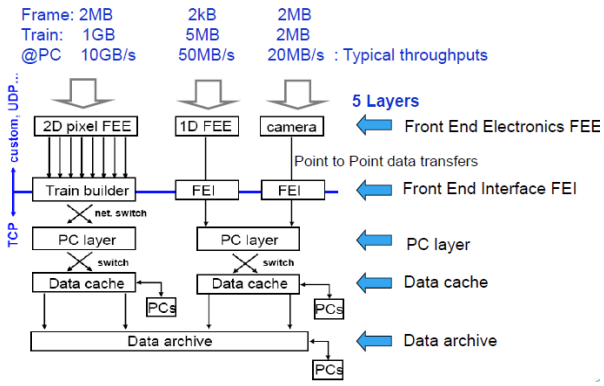

Figure F.3: European XFEL DAQ architecture

All FEEs are Ethernet-controlled and must implement the veto specification (2.5 and 3.125 Gbps SFP link and low-latency messaging protocol between FPGAs) for rejecting poor-quality data associated with pulses within a train.

All FEIs must stream data out to the PC layer using 10 GbE SFP+ links implementing UDP or TCP protocols. Data that is streamed out must contain pulse-ordered information from the acquisition of an entire train. For large-area cameras, this corresponds to images; for digitizers and fast ADCs, this must be time-ordered digitized sample values or properties calculated from them; and for commercial cameras, this corresponds to time-ordered images if more than one is exposed during a train period. Data is identified primarily through the unique train number distributed by the machine timing system and FEE-generated pulse numbers. Data streamed out by the FEI to the PC layer must implement the data-formatting requirements, which foresee additional information allowing the veto, generic FPGA firmware implementation, and data corruption to be checked for downstream.

The large-area camera (AGIPD, DSSC and LPD) FEEs and associated FEI (train builder) electronics being developed satisfy these requirements and are not described further.

F.6 dataXpress user consortium proposal

One aim of the dataXpress UC proposal is to mine and exploit existing X-ray FEL data to aid in developing suitable veto algorithms for the SPB instrument. This will, hopefully, lead to the identification of the aforementioned “high-quality” data sets and help address the data volume issue expected at European XFEL, and in particular at the SPB instrument.

G Scientific software in the European XFEL framework Karabo

Appendix authors: C. Yoon[1,2], A.P. Mancuso[1], B. Heisen[3]

G.1 Note

Large portions of this appendix are reproduced from ideas contained in the European XFEL Technical Note *Scientific Computing Framework at the European XFEL* [40], which should be referred to for a more complete discussion of scientific computing at the European XFEL. Here, we present a discussion of scientific computing focused on the SPB case, but containing many of the ideas common to the broader European XFEL policy.

G.2 Karabo as a platform for scientific software

The European XFEL is a large and complex machine. Efficient use of this infrastructure requires an interface that allows for experiment control, readout of all associated detectors and sensors, safe storage of all meaningful data, and immediate data analysis for quality monitoring and subsequent scientific processing. All these tasks must happen with the highest performance and in a most integrated way, as the European XFEL will produce more data per second than any other scientific instrument in the world. This ambitious goal can only be reached with a standardized, homogeneous software landscape that allows communication between distributed endpoints of any category (be it control, acquisition, data management or scientific computing). Such a software system, called “Karabo”, is currently being developed at European XFEL. The interested reader is referred to the presentation “Karabo: The European XFEL software framework” for details about all concepts that are beyond the scope of this appendix [39].

[1]Scientific Instrument SPB group (WP84), European XFEL GmbH, Albert-Einstein-Ring 19, 22767 Hamburg, Germany
[2]Center for Free-Electron Laser Science (CFEL), Deutsches Elektronen-Synchrotron (DESY), 22607 Hamburg, Germany
[3]DAQ and Control Systems group (WP76), European XFEL GmbH, Albert-Einstein-Ring 19, 22767 Hamburg, Germany

This appendix gives an overview of the scientific computing framework, which is part of Karabo. It is directly linked into the data management layer and capable of autonomously and immediately starting to process data once that data reaches the online storage layer. Data is processed in modules, which can be connected together to form a scientific analysis workflow (Figure G.1).

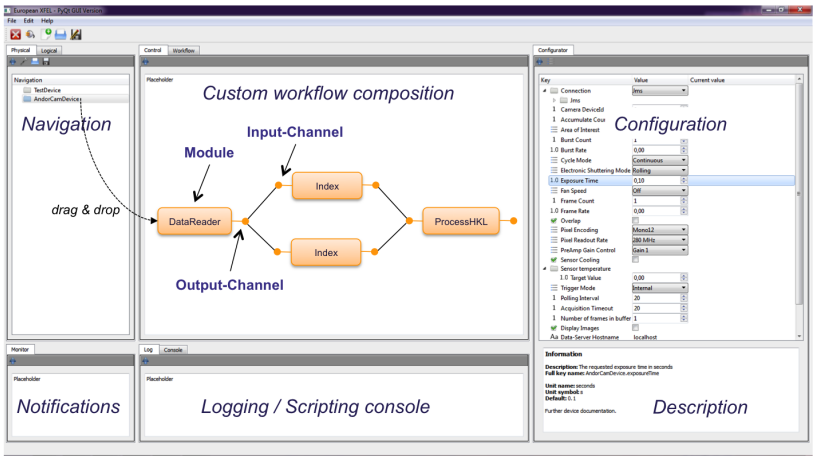

Figure G.1: Graphical user interface (GUI)–based creation and configuration of scientific workflows. Workflows can be composed by dragging and dropping desired modules from the navigation panel on the composition panel. Individual modules may be configured by clicking and utilizing the configuration panel for the currently selected module. Data flow within the workflow is configured by connecting compatible I/O channels.

Each module provides a compute function, which can be equipped with customized procedural code. Furthermore, each module provides a sophisticated way to (self-)describe its possible or expected configuration parameters. In other words, a standardized application-programming interface (API) is available that is analogous to the section(s) of code that typically describe and parse the possible command line arguments. Part of this configuration allows the description of expected input and output (I/O) channels. Input and output channels are specific to the underlying data structures holding the data. Only channels using the same underlying data structure may be connected between modules. The framework will provide highly optimized data structures for common tasks (such as image processing or meta-data handling). Foreign data structures can easily be “registered” to the system and are readily exchangeable between modules. In the most basic case, binary streams may be used, allowing shipping of files (of any type) between modules.

Modules can be written in either C/C++ or the Python programming language. Java may be available at a later stage. The use of Karabo data structures within the compute function is encouraged though not required. In a minimal case (Level 1), system calls to existing binary scientific applications can be issued and the

produced files be transferred to the next connected module(s). In a more involved case (Level 2), existing source code is placed into the compute function and slightly adapted to use Karabo data structures for I/O and to fetch the startup parameters from the Karabo configuration system. This allows for a more flexible re-usage of such modules in other workflows (as the I/O channels are standardized and not file format specific). If circumstances allow, algorithms may be rewritten or newly developed (Level 3) to exploit the full capability of the framework, such as GPU-enhanced computations. A standardized wiki page is associated to each module, which holds documentation, authorship(s), references, institution logos of contributors, and so on. This wiki page will be editable in a regular browser or directly within the multipurpose Karabo GUI system, which—most importantly—allows detailed workflow control.

Workflows may be assembled and edited by means of dragging and dropping modules and their connections. Workflows can be stored and shared (following the general rules of data privacy and security), executed, paused and stepped. Workflow execution will be visualized and data may be inspected at execution time (with limited frequency and resolution). Notifications about finished runs or errors will be visible in the GUI and be forwarded, e.g. via email. Final results of workflow runs will be reintegrated into the data management layer for seamless and user-aware access. The workflow allows for pipelined operation on chunks of data and automatic parallelization on a per-module level (either as CPU threads or in the form of distributed computing, depending where modules run relative to each other). Non-pipeline scenarios can be realized by specifying the minimum needed amount of input data as a configuration property of any module. Data will be locally accumulated and the compute function only triggered upon completed accumulation. The I/O and the processing system are decoupled from each other (asynchronous I/O) such that data can be transferred whilst modules are processing. The workflow system provides in-built protection systems for memory overruns. By default, the processing speed will automatically be adjusted to the I/O capabilities. The data transfer model follows an event-driven poll architecture, allowing maximum per-module performance even on heterogeneous hardware. From a technology point of view, workflows are realized by two different communication patterns, a message broker based publish–subscribe pattern (allowing N x N module control communication and distributed meta-data management) and a highly optimized point-to-point communication pattern (for fast I/O transfer between connected modules). Communication in general is cross-network, cross-language (initially C/C++ and Python), and cross-platform (initially Linux and MacOSX, later Windows7) capable. Besides the graphical system, a command line/scripting interface (based on Python/iPython) is available for workflow control.

The described system is intended to provide scientists with a user-friendly system that

allows them to (at least in part) process their collected data using in-house hardware and community-driven, sharable software resources in the form of pluggable modules or pre-defined workflows.

G.3 CrystFEL—scientific software for nanocrystallographic analysis

Structure recovery from crystalline samples is different from single-particle reconstruction. Unlike the continuous diffraction patterns from single particles, coherent diffraction from nanocrystals produce Bragg peaks that can be used to recover the orientation of the crystal.

CrystFEL [108] is a suite of programs specially designed to process data from the SFX instrument, that is, recover the crystal orientation by indexing Bragg peaks and merge *hkl* indices into 3D diffraction volumes. It also has programs for producing virtual powder plots, visualization, and simulation tools. CrystFEL can automate processes that are too large for manual analysis, and computational requirements scale linearly with the number of patterns, which is ideal for the very high repetition rate at the European XFEL.

European XFEL users will have access to CrystFEL through Karabo. CrystFEL's shared library will be packaged in Karabo's external library. We have already demonstrated Level 2 integration of the software, and are preparing for a Level 3 integration. This entails identifying embarrassingly parallel components of the programs and parallelizing these components across multiple workflow modules. The customized implementation of CrystFEL at the SPB instrument will enable the fast data analysis required by the immense data acquisition. The users will also have access to the Karabo GUI to graphically create dynamical system models and executing CrystFEL jobs.

G.4 Start-to-end (S2E) simulation project at European XFEL

"S2E simulation" refers to modeling single-particle experiments from start to end. One of the goals is to provide upper and lower parameter boundaries for proposed experiments at the SPB instrument, such as the number of photons per pulse, number of hits required, expected photons at the detector, etc.

This propagation model has five major components chained together. First, FEL

photon properties are modeled by taking into account the undulator and experiment setup. Then the photons are propagated through the focusing optics that generates the beam. Next, radiation damage is modeled based on photon–matter interaction with the beam and the sample particle. The diffracted photons are then propagated to the detector where the characteristic noise of the detector is added. The resulting diffraction patterns are then reconstructed using algorithms such as Expansion-Maximization-Compression (EMC).

Table G.1: Collaborators in start-to-end simulations for the SPB instrument

Name	Organization	Role
Chunhong Yoon	European XFEL CFEL	Practical implementation File structure, file conversion Orientation algorithms Image reconstruction
Liubov Samoylova	European XFEL	X-ray optics, propagation code
Alexey Buzmakov	European XFEL	X-ray optics, propagation code
Oleg Chubar	BNL	SRWLib Propagation code
Beata Ziaja	CFEL	Photon–matter interaction simulation
Zoltan Jurek	CFEL	Photon–matter interaction simulation
Markus Kuster	European XFEL	Detector effects
Julian Becker	DESY	Detector effects
Heinz Graafsma	DESY	Detector effects
Mikhail Yurkov	DESY	Source photon field simulations
Evgeny Schneidmiller	DESY	Source photon field simulations
Krzysztof Wrona	European XFEL	Scientific computing, image reconstruction
Burkhard Heisen	European XFEL	Scientific computing, image reconstruction
Duane Loh	SLAC	Orientation algorithms, image reconstruction
Andrew Aquila	European XFEL	X-ray optics, image reconstruction
Klaus Giewekemeyer	European XFEL	Scientific computing Detector geometry Image reconstruction
Adrian Mancuso	European XFEL	Coordinator, image reconstruction
Thomas Tschentscher	European XFEL	Scientific Director, European XFEL Responsible for optics and SPB

Table G.1 on the previous page lists the collaborators involved in the S2E project, who are predominantly from the Hamburg area—with some notable exceptions.

Progress in accurately modeling experiments using the S2E program helps to improve the design of the SPB instrument, and the program can ultimately serve a more broad use. Some of its modules have already been used to optimize the instrument design, and work is continuing to further this project.

H Additional SPB-relevant spaces

This appendix outlines additional spaces that are relevant for the SPB instrument.

H.1 Biological sample characterization lab

The SPB instrument is to include a small biological Class 1 facility, which will serve for characterization, temporary storage, and loading of samples. The goal is to facilitate the final preparation and possible characterization steps for the samples just before they are injected. The lab will be located just above the experiment hutch on the ground floor. An elevator will connect it to the experiment floor, facilitating the delivery of samples.

It is expected that users will have already prepared their samples prior to arriving at the European XFEL. This step may have been conducted at user home institutions or at the XBI consortium facility described below. Users who bring samples from offsite will require temporary storage in refrigerated, frozen, or dry environments. After the users have arrived, workflow in the lab will be centred around final checks of sample quality (such as microscopy), flowing a small batch of sample through a test injector (to check for clogging or icing in case of liquid injection), and loading samples into an appropriate sample delivery apparatus. The lab is also expected to be used to implement iterative, user-typical processes during beamtime. This often involves screening different growth methods and adapting buffer conditions (i.e. a sample might need to be concentrated or diluted, it might need a change of pH in the buffer, or it might need to be held at very specific temperature or under particular lighting conditions). The SPB biological sample characterization lab will have an area of approximately 7.9 m by 6.2 m to facilitate both SPB and SFX experiments.

In addition to the SPB characterization lab, the much more extensive XBI consortium biology laboratory will provide a more comprehensive biological workspace for users, with the XBI consortium proposing to provide more tools for sample growth and characterization (see below).

H.2 Preparation area

Based on experience at the CXI instrument at LCLS, it is often desirable to have a biological preparation area that is located next to the experiment and can also be accessed while the experiment is running. This area is useful for loading samples into injectors, mounting silicon nitrate wafers, cleaning injector catchers and other injector parts, and running or loading liquid and gas systems for the injector, such as high-performance liquid chromatography. This allows for fast sample changing without hutch access, and the samples do not have to leave a clean, biological Safety Level 1 environment.

The preparation area will be approximately 6 m by 4 m and have counter workspaces as well as a small sample elevator to the biological characterization lab. There will also be two doors, one accessing the walkway outside of the SPB area and the other providing direct access to the experiment hutch. While there will also be a door from the SPB control room into the hutch, it is envisioned that the preparation area door will be the primary access point to the experiment hutch. The door from the SPB control room will serve mostly as an access point during commissioning. This arrangement is to limit access to the apparatus and to maintain cleanliness and temperature stability.

Importantly, SFX and SPB users will need to share the preparation area when both experiments are running simultaneously. As with the control rooms, access to the characterization lab and the preparation area will be granted to user groups for the duration of their beamtime. For an overview of these spaces, see Figure H.1 on the facing page and Figure H.2 on page 222.

H.3 Sample lift

To assist and expedite sample delivery to the experiment area, we plan to install a small sample lift that connects the biological characterization lab on the ground floor to the preparation space underneath it on the experiment floor. This has many advantages for the SPB and SFX instruments. The sample lift ensures there is less of a chance to drop, shake, or disturb the samples by needing to carry them from the characterization room to the experiment floor. This is quite critical for samples that have been centrifuged or are rare and valuable. Another advantage is improved efficiency and time saving compared to having to walk or take the human elevator 20 m up to the ground floor. As the hourly cost of running the instrument is high, there is a potential for significant savings and improving the throughput and efficiency of the instrument. Time saving also means that recently characterized samples

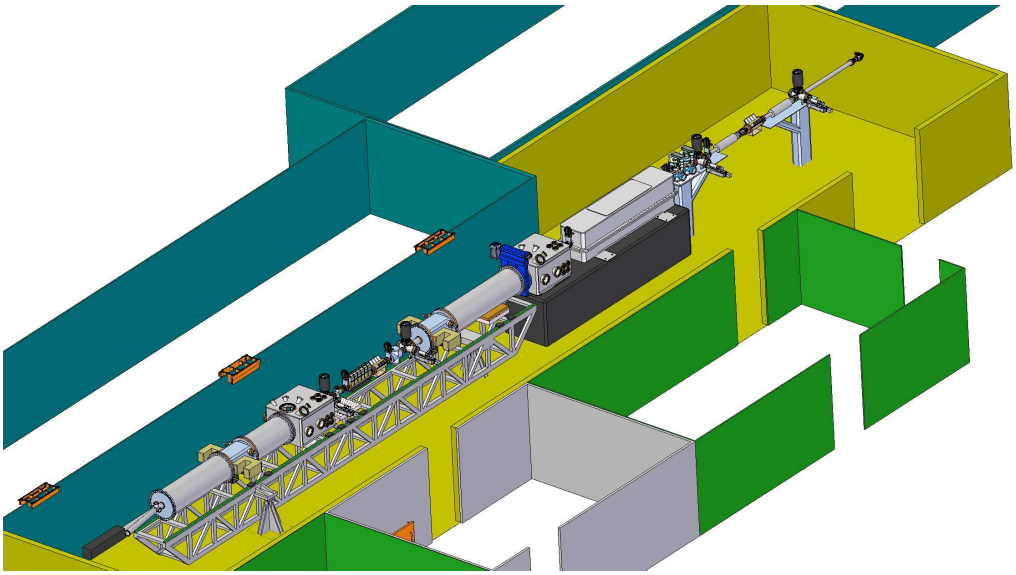

Figure H.1: Overview of the experiment hall level spaces, including experiment hutch (yellow), preparation area (grey), laser room (blue-green), and SPB and SFX control rooms (bright green)

are delivered in a timely way to the X-ray instrumentation. These efficiencies are especially important when screening differently prepared batches of sample where the quantity of the batch is limited. Lastly, there is a big improvement in the workflow, as it requires fewer characterization tools in the preparation area and fewer people in the limited space of the preparation area, which is of particular importance when the SPB and SFX instruments are running in parallel.

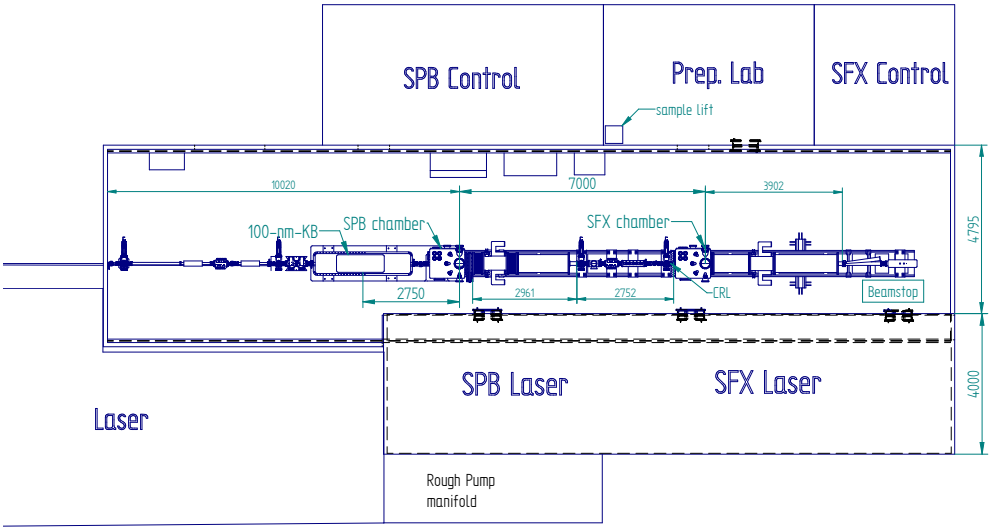

Figure H.2: Top view, looking down, of the experiment hall, including the experiment hutch with key components, preparation area, laser room, and SPB and SFX control rooms

H.4 Control rooms

There will be two control rooms in the SPB and SFX area, one for each instrument. As there is a significant possibility that the SPB and SFX instruments will be running simultaneously, but with different samples and most likely with different experimental teams, these are separate control rooms. The most technically challenging experiments are expected to be performed at the SPB instrument, in some cases requiring the 100 nm–scale spot. As the SFX instrument will be used for crystal screening and more routine nanocrystallography experiments, it is expected that fewer SFX users will be present at any given time, who will hence require less space. The SPB instrument will have a door to the experiment hutch while SFX will not. However, as stated earlier, the SPB control-room-to-hutch door will be mostly used during commissioning and setup, and the primary access point for both SPB and SFX is via the preparation area when the instrument is in operation.

The SPB control room will be approximately 8 m by 4 m, the SFX control room 4 m by 4 m.

H.5 Rack room on roof

Because of thermal drift concerns and space limitations, the control and data racks for both SPB and SFX are not located in the experiment hutch. As floor space is at a premium in the experiment hall, and there are cable-length issues for many beamline components, the decision was made to place the racks on the roof of the hutch in their own special room. Including Beckhoff and control racks, the AGPID detector electronics, and cooling racks, we estimate that 16 racks are required for SPB, plus 2 for the SPB optics hutch. We also estimate that the rack room will consume approximately 140 kW of power. Table H.1 is an estimate of the number of racks.

Table H.1: Number of control and data racks required for SPB and SFX

	SPB	SFX
Beckhoff & controls	2	1
E-racks	5	4
AGPID cooling (1 per megapixel)	1	4

H.6 XBI consortium biology laboratory

The XBI consortium plans to provide a much more extensive biological laboratory than the SPB biological sample characterization lab described above. More than 460 m^2 is planned for sample manufacture, characterization, and quality control. Crystal growth facilities are foreseen, as are cell culture laboratories, sample storage, and more. The laboratory is proposed to be available to bioscience users of the European XFEL. Users who make use of the XBI infrastructure and also have beamtime at the SPB instrument will also have access to the SPB characterization lab and preparation area during that beamtime.

I Bibliography

[1] B. Abbey, L. W. Whitehead, H. M. Quiney, et al.: “Lensless imaging using broadband X-ray sources”, Nat Photon **5**, 420–424 (2011) doi:10.1038/nphoton.2011.125

[2] R. Akre, H. Loos, J. Krzywinski, et al.: “FEL Beam Stability in the LCLS*”, Proceedings of the 2011 Particle Accelerator Conference, New York, 2423–2425 (2011)

[3] J. Amann, W. Berg, V. Blank, et al.: “Demonstration of self-seeding in a hard-X-ray free-electron laser”, Nature Photonics (2012) doi:10.1038/nphoton.2012.180

[4] A. A. Aquila, M. S. M. Hunter, R. B. R. Doak, et al.: “Time-resolved protein nanocrystallography using an X-ray free-electron laser.”, Optics Express **20**, 2706–2716 (2012)

[5] N. P. Barrera, N Di Bartolo, P. J. Booth, et al.: “Micelles Protect Membrane Complexes from Solution to Vacuum”, Science (New York, NY) **321**, 243–246 (2008)

[6] A. Barty, C. Caleman, A. Aquila, et al.: “Self-terminating diffraction gates femtosecond X-ray nanocrystallography measurements”, Nature Photonics **6**, 35–40 (2012)

[7] J. Becker, D. Greiffenberg, U. Trunk, et al.: “The single photon sensitivity of the Adaptive Gain Integrating Pixel Detector”, Nuclear Instruments and Methods in Physics Research Section A: Accelerators, Spectrometers, Detectors and Associated Equipment **694**, 82–90 (2012) doi:10.1016/j.nima.2012.08.008

[8] M Beye, O Krupin, G Hays, et al.: “X-ray pulse preserving single-shot optical cross-correlation method for improved experimental temporal resolution”, Applied Physics Letters **100**, 121108–4 (2012)

[9] M. R. Bionta, H. T. Lemke, J. P. Cryan, et al.: “Spectral encoding of x-ray/optical relative delay”, Optics Express **19**, 21855–21865 (2011)

[10] S. Boutet, G. J Williams: “The Coherent X-ray Imaging (CXI) instrument at the Linac Coherent Light Source (LCLS)”, New Journal of Physics **12**, 035024 (2010)

[11] S. Boutet, L. Lomb, G. J. Williams, et al.: “High-Resolution Protein Structure Determination by Serial Femtosecond Crystallography.”, Science (New York, NY) (2012) doi:10.1126/science.1217737

[12] M Bradler, P Baum, E Riedle: “Femtosecond continuum generation in bulk laser host materials with sub-micro-Joule pump pulses”, Applied Physics B **97**, 561–574 (2009)

[13] M. Bradler, C. Homann, E. Riedle: “Investigation and optimization of continuum generation in crystals - white-light beyond sapphire”, CLEO/Europe and EQEC 2009 Conference Digest (2009), paper CF7_4 (2009)

[14] C. Bressler: *Personal Communication*, 2013

[15] J. Buck, J. Viefhaus, F. Scholz, et al.: “Time-of-flight photoemission spectroscopy from rare gases for non-invasive, pulse-to-pulse x-ray photon diagnostics at the European XFEL”, 85040U–85040U (2012) doi:10.1117/12.929805

[16] J. Buck: “Conceptual Design Report: Online Time-of-Flight Photoemission Spectrometer for X-Ray Photon Diagnostics” (2012) doi:10.3204/XFEL.EU/TR-2012-002

[17] G. Cerullo, S. R. o. S. I. De Silvestri: “Ultrafast optical parametric amplifiers”, Review of Scientific Instruments **74** ()

[18] H. N. Chapman, P. Fromme, A. Barty, et al.: “Femtosecond X-ray protein nanocrystallography.”, Nature **470**, 73–77 (2011)

[19] E. L. Church, P. Z. Takacs: “Specification of Glancing-Incidence and Normal-Incidence X-Ray Mirrors”, Optical engineering **34**, 353–360 (1995)

[20] E. L. Church: “Specification of glancing- and normal-incidence x-ray mirrors [also Erratum 34(11)3348(Nov1995)]”, Optical Engineering **34**, 353 (1995) doi:10.1117/12.196057

[21] S. T. Coleridge: *The Rime of the Ancient Mariner*, http://www.gutenberg.org/files/151/151-h/151-h.htm

[22] P. Denes, D. Doering, H. A. Padmore, et al.: “A fast, direct x-ray detection charge-coupled device”, Review of Scientific Instruments **80**, 083302–083302–5 (2009) doi:10.1063/1.3187222

[23] D DePonte, R Doak, M Hunter, et al.: “SEM imaging of liquid jets”, Micron **40**, 507–509 (2009)

[24] D. P. DePonte, U Weierstall, K Schmidt, et al.: “Gas dynamic virtual nozzle for generation of microscopic droplet streams”, Journal of Physics D: Applied Physics **41**, 195505 (2008)

[25] G. C. R. Ellis-Davies: “Caged compounds: photorelease technology for control of cellular chemistry and physiology”, Nature Methods **4**, 619–628 (2007)

[26] P. Emma, R. Akre, J. Arthur, et al.: “First lasing and operation of an ångstrom-wavelength free-electron laser”, Nature Photonics **4**, 641–647 (2010) doi:10.1038/nphoton.2010.176

[27] F. Filsinger, U. Erlekam, G. von Helden, et al.: “Selector for Structural Isomers of Neutral Molecules”, Physical Review Letters **100** (2008)

[28] F. Filsinger, J. Küpper, G. Meijer, et al.: “Pure Samples of Individual Conformers: The Separation of Stereoisomers of Complex Molecules Using Electric Fields”, Angewandte Chemie International Edition **48**, 6900–6902 (2009)

[29] *First Call for Expressions of Interest in the formation of User Consortia*, http://www.xfel.eu/organization/calls_for_expressions_of_interest/user_consortia/e113386/index_eng.html

[30] B. Flöter, P. Juranić, P. Großmann, et al.: “Beam parameters of FLASH beamline BL1 from Hartmann wavefront measurements”, Nuclear Instruments and Methods in Physics Research Section A: Accelerators, Spectrometers, Detectors and Associated Equipment **635**, S108–S112 (2011) doi:10.1016/j.nima.2010.10.016

[31] H. J. Freund, M Bäumer, J Libuda: “Metal Aggregates on Oxide Surfaces: Structure and Adsorption”, Crystal Research and Technology **33**, 977–1008 (1998)

[32] K. Giewekemeyer, M. Turcato, A. Mancuso: “Detector geometries for Coherent X-ray Diffractive Imaging at the SPB beamline”, European XFEL GmbH, Technical Report (2013) doi:10.3204/XFEL.EU/TR-2013-007

[33] H Graafsma: “Requirements for and development of 2 dimensional X-ray detectors for the European X-ray Free Electron Laser in Hamburg”, Journal Of Instrumentation **4**, P12011 (2009)

[34] I. Grguraš, A. R. Maier, C. Behrens, et al.: “Ultrafast X-ray pulse characterization at free-electron lasers”, Nature Photonics **6**, 852–857 (2012) doi:10.1038/nphoton.2012.276

[35] J. Grünert: “Conceptual Design Report: Framework for X-Ray Photon Diagnostics at the European XFEL” (2012) doi:10.3204/XFEL.EU/TR-2012-003

[36] J Gulden, S. Mariager, A. P. Mancuso, et al.: “Coherent X-ray nanodiffraction on single GaAs nanowires”, physica status solidi (a) (2011)

[37] M Harmand, R Coffee, M. R. Bionta, et al.: “Achieving few-femtosecond time-sorting at hard X-ray free-electron lasers”, Nature Photonics **7**, 215–218 (2013)

[38] C. Heintzen: “Plant and fungal photopigments”, Wiley Interdisciplinary Reviews: Membrane Transport and Signaling (2012)

[39] B. Heisen: *Karabo: The European XFEL software framework*, https://docs.xfel.eu/alfresco/d/a/workspace/SpacesStore/9b331f2f-fe2e-4ece-850d-96b486207f10/Karabo_Design_Concepts.pptx

[40] B. Heisen: “Scientific Computing Framework at the European XFEL” (2013)

[41] B. Henke, E. Gullikson, J. Davis: “X-Ray Interactions: Photoabsorption, Scattering, Transmission, and Reflection at E = 50-30,000 eV, Z = 1-92”, Atomic Data and Nuclear Data Tables **54**, 181–342 (1993) doi:10.1006/adnd.1993.1013

[42] B. Henrich, J. Becker, R. Dinapoli, et al.: “The adaptive gain integrating pixel detector AGIPD a detector for the European XFEL”, Nuclear Instruments and Methods in Physics Research Section A: Accelerators, Spectrometers,

Detectors and Associated Equipment **633, Supplement 1**, S11–S14 (2011) doi:10.1016/j.nima.2010.06.107

[43] R. H. H. van den Heuvel, E. van Duijn, H. Mazon, et al.: “Improving the Performance of a Quadrupole Time-of-Flight Instrument for Macromolecular Mass Spectrometry”, Analytical chemistry **78**, 7473–7483 (2006)

[44] X. Huang, H. Miao, J. Steinbrener, et al.: “Signal-to-noise and radiation exposure considerations in conventional and diffraction x-ray microscopy”, Optics Express **17**, 13541 (2009) doi:10.1364/OE.17.013541

[45] P. Karvinen, S. Rutishauser, A. Mozzanica, et al.: “Single-shot analysis of hard x-ray laser radiation using a noninvasive grating spectrometer”, Optics Letters **37**, 5073–5075 (2012) doi:10.1364/OL.37.005073

[46] M. Kato, T. Tanaka, T. Kurosawa, et al.: “Pulse energy measurement at the hard x-ray laser in Japan”, Applied Physics Letters **101**, 023503–023503–4 (2012) doi:10.1063/1.4733354

[47] C. M. Kewish, L. Assoufid, A. T. Macrander, et al.: “Wave-optical simulation of hard-x-ray nanofocusing by precisely figured elliptical mirrors”, Applied Optics **46**, 2010–2021 (2007) doi:10.1364/AO.46.002010

[48] R. A. Kirian, T. A. White, J. M. Holton, et al.: “Structure-factor analysis of femtosecond microdiffraction patterns from protein nanocrystals”, Acta Crystallographica Section A Foundations of Crystallography **67**, 131–140 (2011) doi:10.1107/S0108767310050981

[49] A. Koch, M. Kuster, J. Sztuk-Dambietz, et al.: “Detector Development for the European XFEL: Requirements and Status”, arXiv:1210.1750 (2012)

[50] A. Koch, C. Raven, P. Spanne, et al.: “X-ray imaging with submicrometer resolution employing transparent luminescent screens”, Journal of the Optical Society of America A **15**, 1940–1951 (1998) doi:10.1364/JOSAA.15.001940

[51] T. Kudo, K. Tono, M. Yabashi, et al.: “A photodiode amplifier system for pulse-by-pulse intensity measurement of an x-ray free electron laser”, Review of Scientific Instruments **83**, 043108–043108–6 (2012) doi:10.1063/1.3701713

[52] M. J. Lederer, M Pergament, M. Kellert, et al.: “Pump-probe laser development for the European X-ray Free-Electron Laser facility”, Proc. SPIE 8504, X-Ray Free-Electron Lasers: Beam Diagnostics, Beamline Instrumentation, and Applications (2012) doi:10.1117/12.928961

[53] H.-M. Lee, D. R. Larson, D. S. Lawrence: “Illuminating the chemistry of life: design, synthesis, and applications of “caged” and related photoresponsive compounds”, ACS chemical biology **4**, 409–427 (2009)

[54] N. D. Loh, M. J. Bogan, V. Elser, et al.: “Cryptotomography: Reconstructing 3D Fourier Intensities from Randomly Oriented Single-Shot Diffraction Patterns”, Physical Review Letters **104**, 225501 (2010) doi:10.1103/PhysRevLett.104.225501

[55] N.-T. D. Loh, V. Elser: “Reconstruction algorithm for single-particle diffraction imaging experiments”, Physical Review E **80**, 026705 (2009)

[56] T. Maltezopoulos, S. Cunovic, M. Wieland, et al.: “Single-shot timing measurement of extreme-ultraviolet free-electron laser pulses”, New Journal of Physics **10**, 033026 (2008)

[57] A. P. Mancuso: “Conceptual Design Report: Single Particles, Clusters and Biomolecules (SPB)” (2011) doi:10.3204/XFEL.EU/TR-2011-007

[58] A. P. Mancuso, H. N. Chapman: “International Workshop on Science with and Instrumentation for Ultrafast Coherent Diffraction Imaging of Single Particles, Clusters, and Biomolecules (SPB) at the European XFEL” (2011)

[59] A. Martin, N. Loh, C. Hampton, et al.: “Femtosecond dark-field imaging with an X-ray free electron laser”, Optics Express **20**, 13501–13512 (2012) doi:10.1364/OE.20.013501

[60] M Marvin Seibert, T. Ekeberg, F. R. N. C. Maia, et al.: “Single mimivirus particles intercepted and imaged with an X-ray laser”, Nature **470**, 78 (2011)

[61] H. Mimura, S. Handa, T. Kimura, et al.: “Breaking the 10-nm barrier in hard-X-ray focusing”, Nature Physics **6**, 122–125 (2009)

[62] H. Mimura, S. Handa, T. Kimura, et al.: “Breaking the 10 nm barrier in hard-X-ray focusing”, Nature Physics **6**, 122–125 (2010) doi:10.1038/nphys1457

[63] R. Neutze, K. Moffat: “Time-resolved structural studies at synchrotrons and X-ray free electron lasers: opportunities and challenges”, Current Opinion in Structural Biology **22**, 651–659 (2012)

[64] R. Neutze, R. Wouts, D. van der Spoel, et al.: “Potential for biomolecular imaging with femtosecond X-ray pulses”, Nature **406**, 752–757 (2000) doi:10.1038/35021099

[65] D. Nilsson, F. Uhlén, A. Holmberg, et al.: “Ronchi test for characterization of nanofocusing optics at a hard x-ray free-electron laser”, Optics Letters **37**, 5046 (2012) doi:10.1364/OL.37.005046

[66] K. A. Nugent: “Coherent methods in the X-ray sciences”, Advances in Physics **59**, 1–99 (2010) doi:10.1080/00018730903270926

[67] R. L. Owen, J. M. Holton, C. Schulze-Briese, et al.: “Determination of X-ray flux using silicon pin diodes”, Journal of Synchrotron Radiation **16**, 143–151 (2009) doi:10.1107/S0909049508040429

[68] C. Ozkan: “Conceptual Design Report: Imaging Stations for Invasive Photon Diagnostics” (2012) doi:10.3204/XFEL.EU/TR-2012-004

[69] D. M. Paganin: *Coherent x-ray optics*, Oxford series on synchrotron radiation (Oxford Univ. Press, Oxford, Reprinted 2006)

[70] M. A. Pfeifer, G. J. Williams, I. A. Vartanyants, et al.: “Three-dimensional mapping of a deformation field inside a nanocrystal”, Nature **442**, 63–66 (2006)

[71] H. T. Philipp, K. Ayyer, M. W. Tate, et al.: “Solving Structure with Sparse, Randomly-Oriented X-ray Data”, Optics Express **20**, 13129–13137 (2012)

[72] M. Porro, L. Andricek, S. Aschauer, et al.: “Development of the DEPFET Sensor With Signal Compression: A Large Format X-Ray Imager With Mega-Frame Readout Capability for the European XFEL”, IEEE Transactions on Nuclear Science **PP**, 1 (2012) doi:10.1109/TNS.2012.2217755

[73] H. M. Quiney, K. A. Nugent: “Biomolecular imaging and electronic damage using X-ray free-electron lasers”, Nat Phys **7**, 142–146 (2011) doi:10.1038/nphys1859

[74] H. Quiney: “Coherent diffractive imaging using short wavelength light sources”, Journal of Modern Optics **57**, 1109–1149 (2010) doi:10.1080/09500340.2010.495459

[75] H. Quiney, A. G. Peele, Z. Cai, et al.: “Diffractive imaging of highly focused X-ray fields”, Nature Physics **2**, 101–104 (2006)

[76] L. Redecke, K. Nass, D. P. DePonte, et al.: “Natively Inhibited Trypanosoma brucei Cathepsin B Structure Determined by Using an X-ray Laser”, Science **339**, 227–230 (2013) doi:10.1126/science.1229663

[77] M. B. E. Riedle: “Supercontinuum generation in laser host materials with pulse durations over the entire femtosecond regime”, CLEO/Europe and EQEC 2009 Conference Digest (2009), paper CF7_4 (2011)

[78] I. Robinson, I. A. Vartanyants, G. J. Williams, et al.: “Reconstruction of the Shapes of Gold Nanocrystals Using Coherent X-Ray Diffraction”, Physical Review Letters **87**, 195505 (2001)

[79] J Rothhardt, S Hädrich, E Seise, et al.: “High average and peak power few-cycle laser pulses delivered by fiber pumped OPCPA system”, Optics Express **18**, 12719 (2010)

[80] S. Rutishauser, A. Rack, T. Weitkamp, et al.: “Heat bump on a monochromator crystal measured with X-ray grating interferometry”, Journal of Synchrotron Radiation **20**, 300–305 (2013) doi:10.1107/S0909049513001817

[81] S. Rutishauser, L. Samoylova, J. Krzywinski, et al.: “Exploring the wavefront of hard X-ray free-electron laser radiation”, Nature Communications **3**, 947 (2012) doi:10.1038/ncomms1950

[82] L. Samoylova, Personal Communication, 2012

[83] E. A. Schneidmiller, M. V. Yurkov: “Photon beam properties at the European XFEL (December 2010 revision)” (2011)

[84] M. M. Seibert, T. Ekeberg, F. R. N. C. Maia, et al.: “Single mimivirus particles intercepted and imaged with an X-ray laser”, Nature **470**, 78–81 (2011) doi:10.1038/nature09748

[85] F. Siewert: “Slope Error and Surface Roughness”, in: *Modern Developments in X-Ray and Neutron Optics*, ed. by A. Erko, D. M. Idir, D. T. Krist, et al.,

Springer Series in optical science 137 (Springer Berlin Heidelberg 2008), pp. 175–179

[86] F. Siewert, J. Buchheim, S. Boutet, et al.: “Ultra-precise characterization of LCLS hard X-ray focusing mirrors by high resolution slope measuring deflectometry”, Opt. Express **20**, 4525–4536 (2012) doi:10.1364/OE.20.004525

[87] H. Sinn, M. Dommach, X. Dong, et al.: “Technical Design Report: X-Ray Optics and Beam Transport” (2012) doi:10.3204/XFEL.EU/TR-2012-006

[88] H. Sinn, J. Gaudin, L. Samoylova, et al.: “Conceptual Design Report: X-Ray Optics and Beam Transport” (2011) doi:10.3204/XFEL.EU/TR-2011-002

[89] SLAC National Accelerator Laboratory: *LCLS machine parameters {September} 2012*, 2012, https://slacportal.slac.stanford.edu/sites/lclscore_public/Pages/Default.aspx (visited on September 25, 2012)

[90] J. Snijder, R. J. Rose, D. Veesler, et al.: “Studying 18 MDa Virus Assemblies with Native Mass Spectrometry.”, Angewandte Chemie (International ed. in English) (2013) doi:10.1002/ange.201210197

[91] A Somogyi, C. M. Kewish, F Polack, et al.: “AIP Conference Proceedings”, The 10th International Conference on X-ray Microscopy, vol. 1365, 57–60 (AIP 2011)

[92] R. Soufli, A. L. Aquila, F. Salmassi, et al.: “Optical constants of magnetron-sputtered boron carbide thin films from photoabsorption data in the range 30 to 770 eV”, Applied Optics **47**, 4633–4639 (2008) doi:10.1364/AO.47.004633

[93] J. C. H. Spence, U Weierstall, H. N. Chapman: “X-ray lasers for structural and dynamic biology”, Reports on Progress in Physics **75**, 102601 (2012)

[94] L. Strüder, S. Epp, D. Rolles, et al.: “Large-format, high-speed, X-ray pnCCDs combined with electron and ion imaging spectrometers in a multipurpose chamber for experiments at 4th generation light sources”, Nuclear Instruments and Methods in Physics Research Section A: Accelerators, Spectrometers, Detectors and Associated Equipment **614**, 483–496 (2010) doi:10.1016/j.nima.2009.12.053

[95] G Suizdak: “Probing viruses with mass spectrometry. ”, J Mass Spectrom. **33**, 203–211 (1998)

[96] P. Thibault, M. Dierolf, O. Bunk, et al.: “Probe retrieval in ptychographic coherent diffractive imaging”, Ultramicroscopy **109**, 338–343 (2009) doi:10.1016/j.ultramic.2008.12.011

[97] P. Thibault, V. Elser, C. Jacobsen, et al.: “Reconstruction of a yeast cell from X-ray diffraction data”, Acta Crystallographica Section A **62**, 248–261 (2006) doi:10.1107/S0108767306016515

[98] K. Tiedtke, J. Feldhaus, U. Hahn, et al.: “Gas detectors for x-ray lasers”, Journal of Applied Physics **103**, 094511–094511–7 (2008) doi:10.1063/1.2913328

[99] K. Tono, T. Kudo, M. Yabashi, et al.: “Single-shot beam-position monitor for x-ray free electron laser”, Review of Scientific Instruments **82**, 023108–023108–6 (2011) doi:10.1063/1.3549133

[100] T. Tschentscher: “Layout of the X-Ray Systems at the European XFEL” (2011) doi:10.3204/XFEL.EU/TR-2011-001

[101] C. Uetrecht, A. J. R. Heck: “Modern Biomolecular Mass Spectrometry and its Role in Studying Virus Structure, Dynamics, and Assembly”, Angewandte Chemie International Edition **50**, 8248–8262 (2011)

[102] C. Uetrecht, R. J. Rose, E. van Duijn, et al.: “Ion mobility mass spectrometry of proteins and protein assemblies”, Chemical Society Reviews **39**, 1633 (2010)

[103] I Vartanyants, I Robinson, J Onken, et al.: “Coherent x-ray diffraction from quantum dots”, Physical Review B **71** (2005)

[104] I. A. Vartanyants, I. Robinson, I. Mcnulty, et al.: “Coherent X-ray scattering and lensless imaging at the European XFEL Facility”, Journal of Synchrotron Radiation **14**, 453–470 (2007)

[105] I. A. Vartanyants, A Singer, A. P. Mancuso, et al.: “Coherence Properties of Individual Femtosecond Pulses of an X-Ray Free-Electron Laser”, Physical Review Letters **107**, 144801 (2011)

[106] T. A. White, Personal communication, 2012

[107] T. A. White, A. Barty, F. Stellato, et al.: “Crystallographic data processing for free-electron laser sources”, Acta Crystallographica Section D **69**, 1231–1240 (2013) doi:10.1107/S0907444913013620

[108] T. A. White, R. A. Kirian, A. V. Martin, et al.: “CrystFEL: a software suite for snapshot serial crystallography”, Journal of Applied Crystallography **45**, 335–341 (2012)

[109] G. J. Williams, A. P. Mancuso, Personal communication, 2012

[110] M. Yabashi, J. B. Hastings, M. S. Zolotorev, et al.: “Single-Shot Spectrometry for X-Ray Free-Electron Lasers”, Physical Review Letters **97**, 084802 (2006) doi:10.1103/PhysRevLett.97.084802

[111] C. H. Yoon, P. Schwander, C. Abergel, et al.: “Unsupervised classification of single-particle X-ray diffraction snapshots by spectral clustering”, Optics Express **19**, 16542 (2011)

[112] H. Yumoto, H. Mimura, T. Koyama, et al.: “Focusing of X-ray free-electron laser pulses with reflective optics”, Nature Photonics **7**, 43–47 (2013) doi:10.1038/nphoton.2012.306

[113] D. Zhu, M. Cammarata, J. M. Feldkamp, et al.: “A single-shot transmissive spectrometer for hard x-ray free electron lasers”, Applied Physics Letters **101**, 034103–4 (2012) doi:10.1063/1.4736725